Dust-Enshrouded Star Formation at High Redshift

Susan Scott

Doctor of Philosophy
The University of Edinburgh
2003

This thesis is my own composition except where indicated in the text.

June 29, 2004

Acknowledgements

Well, it's been quite the challenge putting this thesis together. There have been laughs, tears, and huge amounts of swearing aimed at my computer screen, but it was all worth it. Astronomy research is definitely the coolest job ever. All that remains now is for me to thank those people who deserve it. So, a really big thanks to:

Jim Dunlop, my supervisor, for giving me such a good project and for all his help and support over the last four and a half years.

Steve Serjeant for always responding quickly and helpfully to all my screams for help regarding IDL (and being completely nuts when accompanying me on observing runs).

Elese Archibald, my good friend, for teaching me everything a person needs to know about SCUBA observing and data reduction, for taking me on fun days out around Hawaii, and lots and lots of games of pool (most of which I won, much to her disgust). May all of your dreams come true.

All of the other members of the "SCUBA 8 mJy Survey" Consortium; Michael Rowan-Robinson, Matt Fox, Seb Oliver, Rob Ivison, Malcolm Longair, Andrew Blain, Dave Hughes, Bob Mann, Andy Lawrence and John Peacock for their help and guidance.

All of the staff at the JAC, old and new, for looking after me so well during my stays in Hawaii.

Tom Lowe, Ed Lundin, Jonathan Kemp, and Jim Hoge, the JCMT telescope support scientists, for always managing to fix things when they go wrong at the

summit, particularly Tom Lowe and Jim Hoge who frequently went way beyond the call of duty in allowing extended observing. An extra special thanks and big hug goes to Jim Hoge, my newly adopted "dad", who has proved that not only is he one of the JCMT's finest assets, but can pull anyone out of the foulest mood within just a couple of minutes of his company.

Steve Rawlings and Katherine Blundell who taught me so much during my many vacation projects whilst I was an undergraduate in Oxford. I doubt I would have made it this far without their encouragement.

The "Old Bell" pub for keeping me well supplied with beer and having a number of really gorgeous dogs among their regular punters.

All of my friends from Oxford and Edinburgh for their bad influence. You know who you are....

Joss Whedon for creating the television series' "Buffy the Vampire Slayer" and "Angel". When thesis writing seemed truly bleak, watching a couple of episodes at the end of the day from either of these shows always managed to cheer me up.

Finally, my parents, Desmond and Pamela Catherine Scott. Sadly, both of them passed away during the course of my PHD but I think they'd be pleased with the end result.

Abstract

Since the advent of SCUBA, deep submillimetre surveys have succeeded in resolving the bulk of the far-infared extragalactic background into discrete sources, revealing a population of high-redshift ($z > 1$) heavily dust-enshrouded massive-starforming galaxies.

Here, the nature of the most luminous 850 μm sources ($S_{850} > 5$ mJy) are considered, in particular their link with the formation and evolution of the most massive elliptical galaxies visible in the present-day Universe.

The "SCUBA 8 mJy Survey" is the largest of the blank field submillimetre surveys completed to date, designed specifically with the aim of identifying the brightest 850 μm sources. It covers $\simeq 260$ square arcminutes of sky to a depth of $\sigma_{\rm rms} \simeq 2.5$ mJy/beam, evenly split between two areas of low galactic cirrus emission; the Lockman Hole East and ELAIS N2. The data have in part been reduced by the standard JCMT SURF procedures, but the primary reduction method was an alternative IDL-based pipeline which has the advantage of producing uncorrelated noise images. This latter approach has enabled me to develop a maximum-likelihood source extraction algorithm which simultaneously measures the statistical significance of every peak in a SCUBA map, leading to properly quantified errors on the flux densities of all potential sources. Applying the source extraction algorithm to these two fields has revealed 19 sources with S/N > 4.00, 40 sources with S/N > 3.50, and 85 sources with S/N > 3.00. Completeness, mean output vs. input flux density, and contamination from spurious / confused sources were quantified using extensive Monte Carlo simulations. Using deep 1.4 GHz imaging of the survey fields to determine the radio-to-submillimetre spectral indices for every 850 μm detection, all sources were constrained to lie at $z > 1$, with a median redshift $z_{\rm med} \simeq 2.4$. This being the case, the inferred star formation rates are $\sim 1000\,{\rm M}_\odot\ {\rm yr}^{-1}$, sufficient to form the most massive elliptical galaxies on timescales of ~ 1 Gyr, but heavily obscured by $10^8 - 10^9\,{\rm M}_\odot$ of dust. The comoving number density of high redshift galaxies forming stars at

$> 1000\,M_{\odot}\ yr^{-1}$ is $\simeq 10^{-5}\,Mpc^{-3}$, with only a weak dependence on the precise redshift distribution, also corresponding to the number density of massive ellipticals with $L > 3 - 4L*$ in the present-day Universe, as well as the co-moving number density of comparably massive, passively-evolving objects in the redshift band $1 < z < 2$ inferred from recent surveys of extremely red objects. This suggests that the bright submillimetre sources uncovered by this survey can plausibly account for the formation of all present-day massive spheroids.

Combining the data from the "SCUBA 8 mJy Survey" with other existing blank field surveys, re-reduced and analysed in an identical manner, approximately doubles the area of sky observed with SCUBA in an unbiased manner. The full source catalogue derived from combining these fields contains a sufficient number of significant detections to place meaningful constraints on the clustering properties of the bright submillimetre population. Measurements of angular correlation functions and nearest neighbour statistics for $S_{850} > 5$, 6, and 7 mJy sources, imply strong clustering on scales of ~ 1 arcminute at a significance level of $\sim 4\sigma$. The combined datasets also allow the determination of the most accurate source counts to date for $S_{850} > 2$ mJy. For $2 < S_{850} < 8$ mJy the differential source counts follow a power-law such that $dN(> S)/dS \propto S^{-1.5}$, but appear to steepen thereafter, possibly indicative of a high-mass cutoff. Reasonably successful modelling of the number counts can be achieved by strong pure luminosity evolution with redshift, of the local 850 μm luminosity function.

List of Abbreviations

- A.C. stands for Alternating Current.
- ACBAR stands for Arcminute Cosmology Bolometer Array Receiver.
- ACS stands for Advanced Camera for Surveys.
- AGN stands for Active Galactic Nucleus.
- BLAST stands for Balloon-borne Large Aperture Submillimetre Telescope.
- CADC stands for Canadian Astronomy Data Centre.
- CBI stands for Cosmic Background Imager.
- CCD stands for Charge-Coupled Device.
- CDM stands for Cold Dark Matter.
- CFRS stands for Canada France Redshift Survey.
- CM stands for Colour-Magnitude.
- CMB stands for Cosmic Microwave Background.
- COBE stands for Cosmic Background Explorer.
- CP stands for Charge-Parity.
- CSO stands for Caltech Submillimetre Observatory.
- D.C. stands for Direct Current.
- DEC stands for Declination.
- CUDSS stands for Canada UK Deep Submillimetre Survey.
- ELAIS stands for European Large Area ISO Survey.
- ERO stands for Extremely Red Object.
- FCF stands for Flux Conversion Factor.
- FIR stands for Far Infra-Red.
- FIRAS stands for Far Infra-Red Absolute Spectrophotometer.
- FWHM stands for Full Width at Half Maximum.
- GAIA stands for Graphical Astronomy and Image Analysis tool.
- GPS stands for Global Positioning Satellite.
- GUT stands for Grand Unified Theory.
- HDF stands for Hubble Deep Field.

- HFFS stands for Hawaii Flanking Fields Survey.
- HLIRG stands for Hyperluminous Infra-Red Galaxy.
- IDL stands for Interactive Data Language.
- IMF stands for Initial Mass Function.
- IRAS stands for Infra-Red Astronomical Satellite.
- ISM stands for Interstellar Medium.
- ISO stands for Infra-red Space Observatory.
- JCMT stands for James Clerk Maxwell Telescope.
- LBG stands for Lyman-Break Galaxy.
- LW stands for Long Wave.
- MACHO stands for Massive Compact Halo Object.
- MAMBO stands for Max-Planck Millimetre Bolometer array.
- M/L stands for Mass to Light ratio.
- MOPED stands for Multiple Optimised Parameter Estimation and Data compression.
- NEFD stands for Noise Equivalent Flux Density.
- PSF stands for Point Spread Function.
- QSO stands for Quasi-Stellar Object.
- RA stands for Right Ascension.
- SCUBA stands for Submillimetre Common-User Bolometer Array.
- SDSS stands for Sloan Digital Sky Survey.
- SED stands for Spectral Energy Distribution.
- SFR stands for Star Formation Rate.
- SFRD stands for Star Formation Rate Density.
- SHADES stands for SCUBA Half Degree Extragalactic Survey.
- SIRTF stands for Space Infra-Red Telescope Facility.
- SLUGS stands for SCUBA Local Universe Survey.
- S/N stands for Signal to Noise ratio.
- SURF stands for SCUBA User Reduction Facility.
- SW stands for Short Wave.
- SWIRE stands for SIRTF Wide-area Infra-Red Extragalactic survey.
- ULIRG stands for Ultraluminous Infra-Red Galaxy.
- UV stands for Ultra-Violet.
- VLA stands for Very Large Array.
- WDM stands for Warm Dark Matter.
- WIMP stands for Weakly Interacting Matter Particle.

- WMAP stands for Wilkinson Microwave Anisotropy Probe.
- XMM stands for X-ray Multi-Mirror satellite.

Contents

List of Figures

List of Tables

Chapter 1

Introduction

1.1 Modern-day Cosmology

Astronomy is the study of the components of the Universe and how they evolve. Humankind has been recording the positions and motions of the brightest stars and planets for many thousands of years, using this knowledge to predict tides and agricultural cycles and to navigate the oceans. However, it is really only in the last 100 years that the true extent of the Universe has been revealed.

The existence of galaxies outside our own was a matter of considerable debate until 1924, when Edwin Hubble identified Cepheid variable stars in the "spiral nebula" M31 (the Andromeda galaxy). The tight correlation between period and luminosity in Cepheid variables allowed Hubble to measure the distance to Andromeda, establishing that the Cepheid variables in M31 were much further away than any of those observed in the Milky Way, and thus identifying Andromeda as a separate galaxy for the first time. Immediately, the vast scale of the Universe was clear. Spirals similar to Andromeda could be seen in photographs all the way down to the faintest detectable images. Our perception of the Universe changed almost overnight, from one that was at most a million light years across to one that was at least billions of light years in scale.

During the same era, while the argument regarding the nature of spiral nebulae was still raging, V.M. Slipher began studying the radial velocities of these objects by means of measuring the Doppler shifts in the wavelengths of their absorption lines with respect to the laboratory values. By 1925, he had 40 reliable measurements from which he established that spectra showing redshifted lines were much more common than those exhibiting blueshifts, and therefore concluded that the vast majority of the galaxies were receding rapidly from us.

Hubble combined his distance measurements with Slipher's radial velocity measurements and in 1929 announced the discovery that the galaxies were receding away from Earth with a velocity directly proportional to their distance

$$v = H_0 d \tag{1.1}$$

where v is the recession velocity, d is the distance to the galaxy and H_0 is the constant of proportionality (known as the Hubble constant). This relation is known as Hubble's law, and tells us that not only are the galaxies moving away from Earth, but that they are also moving away from each other: the Universe is expanding.

Following these discoveries, our understanding of the nature and evolution of the Universe has increased by "leaps and bounds". The present-day "standard model" of physical cosmology provides a world picture which, although incomplete, has survived many observational tests and is consistent with the available evidence. This model asserts that the distribution of matter in the Universe is homogeneous and isotropic if smoothed on a sufficiently large scale, that the Universe is expanding, and that it was much hotter and denser in the past. It is based upon two fundamental assumptions and supported by a number of additional important observations.

The first assumption is that the laws of physics are the same on cosmological scales as they are on smaller scales; in particular, that general relativity is the correct description of gravity on large scales. The second assumption we make is often termed the "Copernican Principle" and simply states that there is nothing particularly special about the position we occupy in the Universe. How true this is on a sub-galactic scale is still open to question - to the best of our knowledge the presence of life requires a number of special conditions (such as the existence of liquid water) which are not omnipresent, however, there appears to be nothing particularly special about the Milky Way galaxy when compared with M31 or M101 for example, and there seems to be no good reason to suppose that our presence in this particular galaxy is due to anything other than chance.

The cosmic microwave background (CMB) provides some of the strongest evidence to date supporting an expanding and isotropic Universe. At early epochs the Universe was much hotter and denser, and the baryonic matter was fully ionised. Scattering was highly efficient and the Universe was in thermal equilibrium. By a redshift of $z \sim 1000$, the Universe had cooled sufficiently for electrons to combine with protons and form atoms. Following recombination, the optical

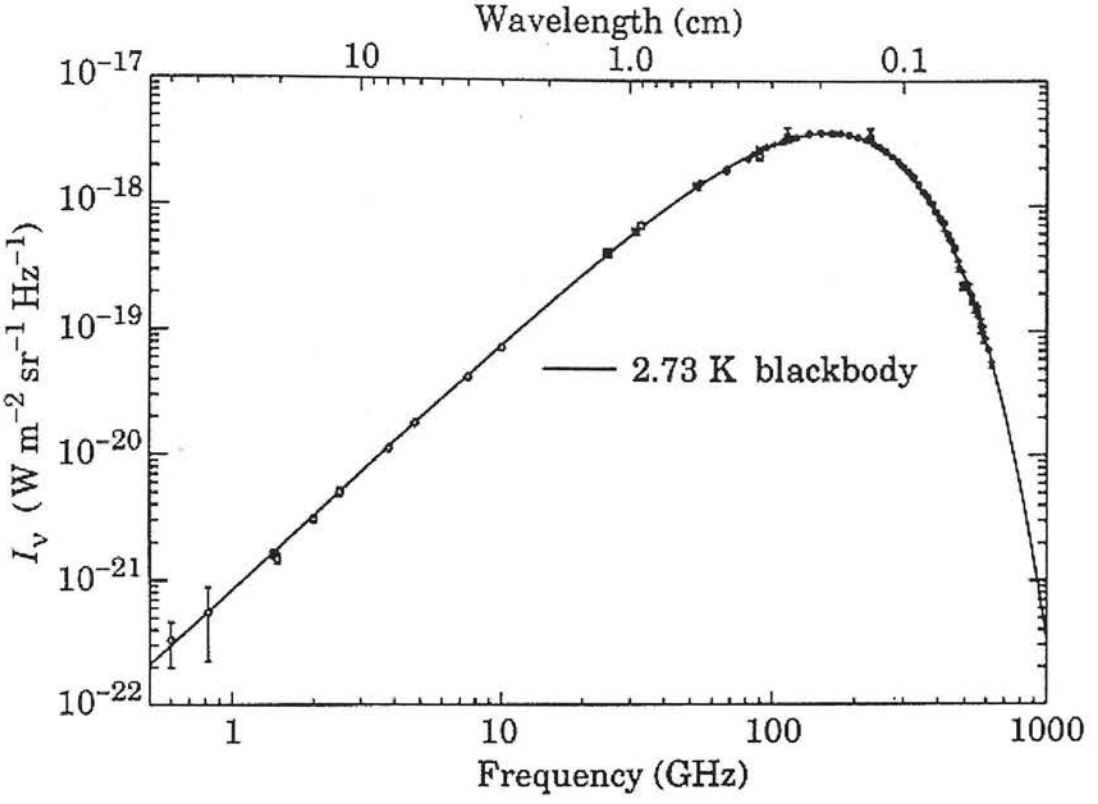

Figure 1.1: Intensity plot of the cosmic microwave background using data points measured by COBE-FIRAS. The curve is an isothermal blackbody with a temperature of 2.726 K. This figure is taken from
http://www.phy.duke.edu/ kolena/cmb.htm.

depth dropped sharply leaving the Universe transparent to CMB photons. Radiation from the surface of last scattering is observable today, albeit greatly redshifted due to universal expansion. Measurements by the "Far Infrared Absolute Spectrophotometer (FIRAS)" experiment on the "Cosmic Background Explorer (COBE)" satellite were the first to show that the spectrum of the CMB is an almost perfect black body with a temperature of 2.7 K, peaking at $\sim$ 1 mm, as shown in Figure 1.1. Furthermore the CMB is uniform to better than 1 part in 10000 (Figure 1.2) on all angular scales suggesting a highly isotropic Universe (Fixsen et al. 1996). This result has been confirmed more recently by the Wilkinson Microwave Anisotropy Probe (WMAP), which has 30 times the resolution of COBE (Figure 1.3) and is limited in the precision of its measurement by cosmic variance only. There have been many WMAP papers released in the last 6 months but Bennett et al. (2003) provide a comprehensive overview of the major results.

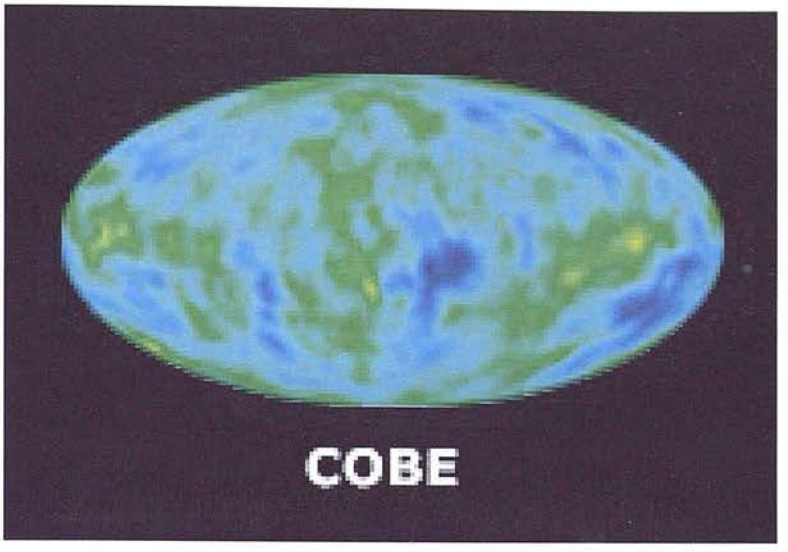

Figure 1.2: Anisotropies in the temperature in the CMB as measured by COBE. The dipole arising from the Earth's motion with respect to the CMB ($\sim 370\,\mathrm{km/s}$ in the direction of Virgo), as well as microwave emission from molecules (particularly CO) and dust from our galaxy have been removed. This figure is taken from http://map.gsfc.nasa.gov/m_mm.html.

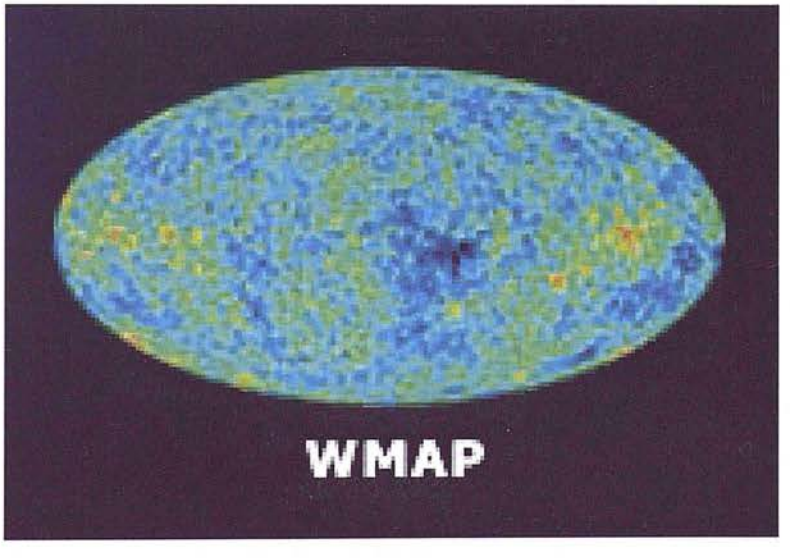

Figure 1.3: Anisotropies in the temperature in the CMB as measured by WMAP. The dipole arising from the Earth's motion with respect to the CMB ($\sim 370\,\mathrm{km/s}$ in the direction of Virgo), as well as microwave emission from molecules (particularly CO) and dust from our galaxy have been removed. This figure is taken from http://map.gsfc.nasa.gov/m_mm.html.

Galaxy counts may also be used to infer isotropy and homogeneity. Although structure is apparent on smaller scales (clusters, walls, voids etc.), smoothing the number counts towards larger scales, the Universe looks increasingly isotropic and homogeneous.

However, even with large investments of telescope time, there are a number of fundamental issues regarding the formation and evolution of galaxies that remain to be resolved. As will become clear, this thesis will address one of these controversial points; specifically the epoch and nature of formation of the most massive elliptical galaxies.

1.2 The "Standard" Cosmological Model

1.2.1 The Earliest Epochs

The generally accepted "standard" cosmological model amongst scientists today is that of the "Hot Big Bang". According to the Big Bang theory, the following sequence of events is believed to have occurred. The starting point for this timeline, 13.7 ± 0.2 billion years ago, is the time at which in general relativity there exists a gravitational singularity. At this time, general relativity is unable to make statements about what the Universe is like because the theory gives infinite values for the temperature and density of the universe.

It is believed that general relativity is insufficient to make predictions about the very beginning of the Universe and that a theory of quantum gravity will be needed to do so. Nevertheless the time at which general relativity predicts a singularity makes a convenient starting point to begin the timeline, despite the fact that this singularity may or may not actually have existed.

The "Big Bang" itself was a primaeval fireball from which the singularity expanded into the current space time continuum, creating not only fundamental subatomic particles and thus matter and energy, but space and time itself. We currently have no real understanding of what physics would be like at the energies prevailing between the occurrence of the Big Bang and the Planck time (10^{-43} seconds). Recent work on supersymmetric Grand Unified Theories (GUTs) suggests that prior to the Planck time the gravitational force may have been quantized, and that there could have been extra dimensions beyond the four that we experience as spacetime. It may be that the perturbations that would eventually become galaxies had their origins in quantum fluctuations right at the beginning

when gravity was quantised.

The "Planck Epoch" covers the time from 10^{-43} to 10^{-35} seconds after the Big Bang, during which time the temperature is estimated to have decreased from 10^{32} to 10^{27} K. At the Planck time of 10^{-43} seconds, the force of gravity separated from the other three fundamental forces (collectively known as the electronuclear force). The diameter of the currently observable Universe at this point in time is theorized as 10^{-35} m.

1.2.2 Inflation

The end of Grand Unification occurred 10^{-35} seconds after the Big Bang when the strong nuclear force separated from the electroweak force, initiating the inflationary epoch. Between 10^{-35} and 10^{-32} seconds, the Universe underwent a phase of strongly accelerated expansion, expanding by a factor of approximately 10^{20} to 10^{30}, increasing in diameter from the size of an atom to the size of a grapefruit, during which the temperature dropped from 10^{27} to 10^{25} K. The general idea behind inflation is that in the early Universe there exists some scalar field (called an *inflaton*) with a non-zero potential. The potential is a source of vacuum energy, acting as a large cosmological constant, and if sufficiently large will completely dominate the expansion. Although experimental particle physics provides no real motivation for the process of inflation, a period of strongly accelerated expansion in the Universe solves a number of long standing cosmological problems. The first of these is the so-called "flatness problem" ie. the fact that the observed density of the Universe is so close to the critical density ($\Omega_{\text{total}} = \Omega_{\text{M}} + \Omega_{\Lambda} = 1$). In the absence of inflation, the solution $\Omega = 1$ is unstable; any deviation from this value will become increasingly marked as time progresses, such that to observe a value of Ω so close to the critical density today would require a fine tuning of Omega at the Planck epoch to less than 1 part in 10^{60}. How could the Universe know that such fine tuning would be required in its initial conditions? The process of inflation, however, acts in the reverse, driving Ω so close to 1 on its completion that all subsequent expansion between the end of inflation and the present is insufficient to drive it away again.

The second of these issues is the "horizon problem". As mentioned briefly in the previous section, the CMB from all parts of the sky is at the same temperature to within one part in 10^5. Observations suggest thermal equilibrium which would make sense if different regions of the sky were in causal contact at some point in

the past. However, light has a finite speed and the CMB radiation we see from opposite sides of the sky has travelled to us uninterrupted from the surface of last scattering at which time the particle horizon had a size of order 100 Mpc. That is to say, points on the sky separated by more than 2 degrees are not causally connected. Inflation provides a simple solution to this problem: a region which is the same order of size as the particle horizon before inflation could encompass the entire observable horizon today.

A third problem solved by inflation, indeed the one which motivated its original invention, is the "monopole problem". GUT models predict that a large number density of monopoles (point like topological defects) should be produced during the breaking of the GUT symmetry in the early Universe. However, the predicted number density is orders of magnitude greater than the observational upper limit. Inflation can again produce a natural solution to this problem if the monopoles are generated prior to the period of accelerated expansion. In this case excessive monopoles are tidily swept beyond our observable horizon.

Finally, inflation is able to provide a solution to the "structure problem". The Heisenberg Uncertainty Principle tells us that small fluctuations in density must exist on very small scales. During a period of inflationary expansion, these quantum fluctuations will also expand, which given a sufficiently fast expansion rate they will reach super-horizon scales and become "frozen-in" before they can die away. As a result, small perturbations to the background over a wide range of scales are generated, in particular perturbations on scales larger than the particle horizon are possible. Such large scale perturbations are required to explain such large scale structures as observed today. In contrast, causal processes could not have generated such perturbations.

This period is also very important for the existence of matter in the Universe. Once inflation has ceased, the intense radiation field allows for the creation and annihilation of particle-antiparticle pairs; specifically quarks and antiquarks, neutrinos and antineutrinos, and electrons and positrons. Initially these processes are in thermal equilibrium but as the Universe continues to cool the radiation field is no longer hot enough for quark-antiquark pair production. It is at this point that those existing quarks and antiquarks annihilate one another. However, there exists an asymmetry between the production of matter and antimatter in the Universe due to charge-parity (CP) violation, resulting in the creation of an extra quark for every 10^9 quark-antiquark pair annihilations. Once the temperature drops to approximately 10^{25} K quark-antiquark freezeout begins. It is

still too hot for formation of protons and neutrons but now the quarks are sufficiently diffusely distributed that annihilations with any remaining antiquarks largely cease. This is the origin of the baryon-antibaryon asymmetry and is also the reason why baryons are so rare compared to photons.

1.2.3 Big Bang Nucleosynthesis

Between 10^{-32} and 10^{-12} seconds marks a bit of a desert regarding any changes in the physical processes governing the Universe's evolution. The next period of interest is the electroweak epoch, covering the time from 10^{-12} to 10^{-6} seconds after the Big Bang. During this era, the temperature drops from approximately 10^{15} to 10^{13} K. At 10^{-12} seconds the diameter of the Universe has increased to approximately 10^{13} m. The weak force which involves massive particles (the W and Z bosons) condenses and separates from the electromagnetic force for which the particle is massless (the photon), leaving the four separate fundamental forces we know today. Following the electroweak epoch, is the so-called hadron epoch, covering the time from 10^{-6} seconds to 1 second after the Big Bang. The temperature during this period is estimated to fall from 10^{13} to 10^{10} K. Electrons and positrons annihilate one another, eventually undergoing a freezeout when the Universe drops to 10^{10} K. Again the asymmetry between matter and antimatter leads to more residual electrons than positrons. Neutrinos break free and exist on their own. It is also during this time that quarks combine to form protons and neutrons. Any remaining antiquarks are also able to combine with their quark counterparts to produce mesons. After this period quarks and antiquarks can no longer exist as free particles.

The next epoch of importance is that of cosmic nucleosynthesis, when primordial baryons begin to fuse together to form the heavier elements. At very high temperatures ($\sim 10^{12}$ K), neutrons and protons were constantly being transformed into one another via the reactions

$$\mathrm{n} \rightleftharpoons \mathrm{p}^+ + \mathrm{e}^- + \bar{\nu}_\mathrm{e} \tag{1.2}$$

$$\mathrm{n} + \mathrm{e}^+ \rightleftharpoons \mathrm{p}^+ + \bar{\nu}_\mathrm{e} \tag{1.3}$$

$$\mathrm{n} + \nu_\mathrm{e} \rightleftharpoons \mathrm{p}^+ + \mathrm{e}^- \tag{1.4}$$

These constant conversions were easily accomplished because the mass difference between a proton and a neutron is only

$$(\mathrm{m_n} - \mathrm{m_p})\mathrm{c}^2 = 1.293\,\mathrm{MeV} \tag{1.5}$$

while the characteristic thermal energy of the particles at 10^{12} K is kT $\simeq$ 86 MeV. One has only protons and neutrons at these high temperatures, with abundances fixed by thermal equilibrium, such that

$$\frac{n_n}{n_p} = \exp\left(\frac{-(m_n - m_p)c^2}{kT}\right) \simeq \exp\left(\frac{-1.5 \times 10^{10}\,K}{T}\right) \tag{1.6}$$

Any heavier nucleii which form are rapidly dissociated. Initially the numbers of protons and neutrons are approximately the same (the ratio is 0.985 for T = 10^{12} K) since the mass difference between the two hadron particles is negligible in comparison to the thermal energy of the particles. However, as the Universe expanded and the temperature continued to fall, the balance began to shift in favour of the protons. If nothing else were to intervene, all of the neutrons would rapidly be converted to protons. This intervention occurred approximately 1 second after the Big Bang when the temperature had dropped to $\sim 10^{10}$ K and the time scale for these reactions exceeded the characteristic timescale of the expansion. At a little above 10^{10} K, the reaction rates decreased significantly for two reasons. Firstly, the expansion had reduced the energy of the neutrinos until they were unable to participate in the reactions 1.2 - 1.4. Secondly the cessation of electron-positron pair production meant that electrons and positrons annihilated each other without being replaced, leaving only a small remainder of excess electrons. For these reasons the neutrons could not be replenished as fast as they were destroyed and so there was insufficient time for these reactions to reach equilibrium. In a sense, that is to say that the creation of new neutrons could not keep up with the rate of expansion of the Universe. Consequently the relative number densities of neutrons to protons became frozen at approximately 0.34.

After the freeze-out, beta decay (the forward reaction of equation 1.2) continued to operate, converting neutrons to protons with a half-life of 617 seconds (or equivalently an e-folding timescale of 890 seconds). Around 3 minutes after this, however, and before beta decay could seriously deplete the number of remaining neutrons, the temperature dropped to 10^9 K at which point the protons and neutrons readily combined to produce as many deuterium nucleii as possible via the reaction

$$p^+ + n \rightarrow D + \gamma \tag{1.7}$$

The most efficient reactions leading to ^{4}He include the fusion of deuterium to ^{3}He

via

$$D + p^+ \rightarrow {}^3He + \gamma \tag{1.8}$$

$$D + D \rightarrow {}^3He + n \tag{1.9}$$

or to tritium (^{3}H) via

$$D + n \rightarrow {}^3H + \gamma \tag{1.10}$$

$$D + D \rightarrow {}^3H + p^+ \tag{1.11}$$

Subsequently, ^{4}He is formed via the reactions

$${}^3He + D \rightarrow {}^4He + p^+ \tag{1.12}$$

$${}^3H + D \rightarrow {}^4He + n \tag{1.13}$$

The binding energy per nucleon of the ^{4}He nucleus is substantially larger than that of deuterium, tritium or ^{3}He, so that any ^{4}He that forms is stable, and unlikely to be broken down. Consequently, nearly all of the neutrons become locked up in helium, and hence the abundances of the intermediate species at the end of nucleosynthesis are small. With the exception of very small traces of ^{7}Li and ^{7}Be, no elements heavier than ^{4}He form. Firstly, this is because nuclei with mass numbers 5 and 8 are unstable and rapidly decay back to their initial components, and secondly the triple-α process which is responsible for the first stages of heavy element production in stars

$${}^4He + {}^4He + {}^4He \rightarrow {}^{12}C + \gamma \tag{1.14}$$

occurs at a negligible rate. By 10^3 seconds after the Big Bang, the Universe is too cool for nuclear activity to continue, and these reactions stop. At this point the Universe consists of about 75% hydrogen and 25% ^{4}He by mass, with trace amounts of deuterium, ^{3}He, ^{7}Li and ^{7}Be. The relic abundances of D, ^{3}He, ^{7}Li and ^{7}Be are rate limited, determined by the competition between the early Universe expansion rate and the nucleon density. The precise abundances of these nucleii are controlled by a single free parameter, the baryon to photon ratio η where

$$\eta = 2.746 \times 10^{-8} \Omega_b h^2 \tag{1.15}$$

and Ω_b is the ratio (at present) of the baryon density to critical density, and h is the present value of the Hubble parameter in units of $100\,\mathrm{km\,s^{-1}\,Mpc^{-1}}$. In

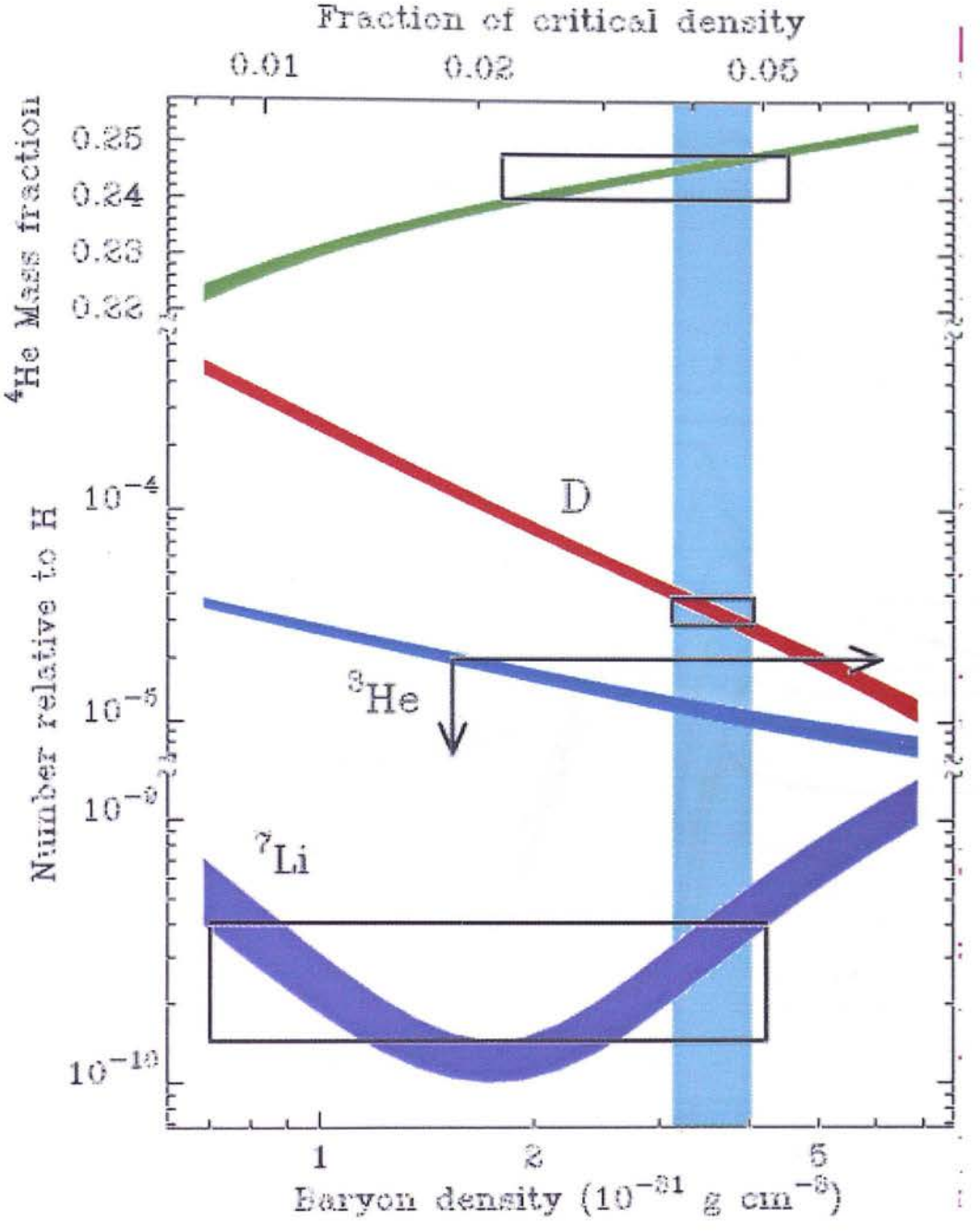

Figure 1.4: Plotted in the figure are the light element abundances predicted by primordial nucleosynthesis against its one free parameter, the baryon-to-photon ratio. The mass fraction of baryons in ^{4}He, and the number densities relative to hydrogen of D, ^{3}He and ^{7}Li are the abundances shown. The thickness of each curve represents the confidence in the abundance predictions at the 95% level. The boxes in the figure show the regions of parameter space the observationally determined abundances predict for the value of the baryon-to-photon ratio. The vertical band on the curve represents the determination of the baryon density from recent measurements of the cosmic background radiation fluctuations. This figure is taken from
http://nedwww.ipac.caltech.edu/level5/Tytler2/Tytler3_2.html.

contrast to the other light nuclides, once Big Bang nucleosynthesis begins, the reactions building ^{4}He are so rapid that its relic abundance is not rate limited. The primordial abundance of ^{4}He is limited by the availability of neutrons. To a very good approximation, its relic abundance is set by the neutron abundance at the beginning of Big Bang nucleosynthesis.

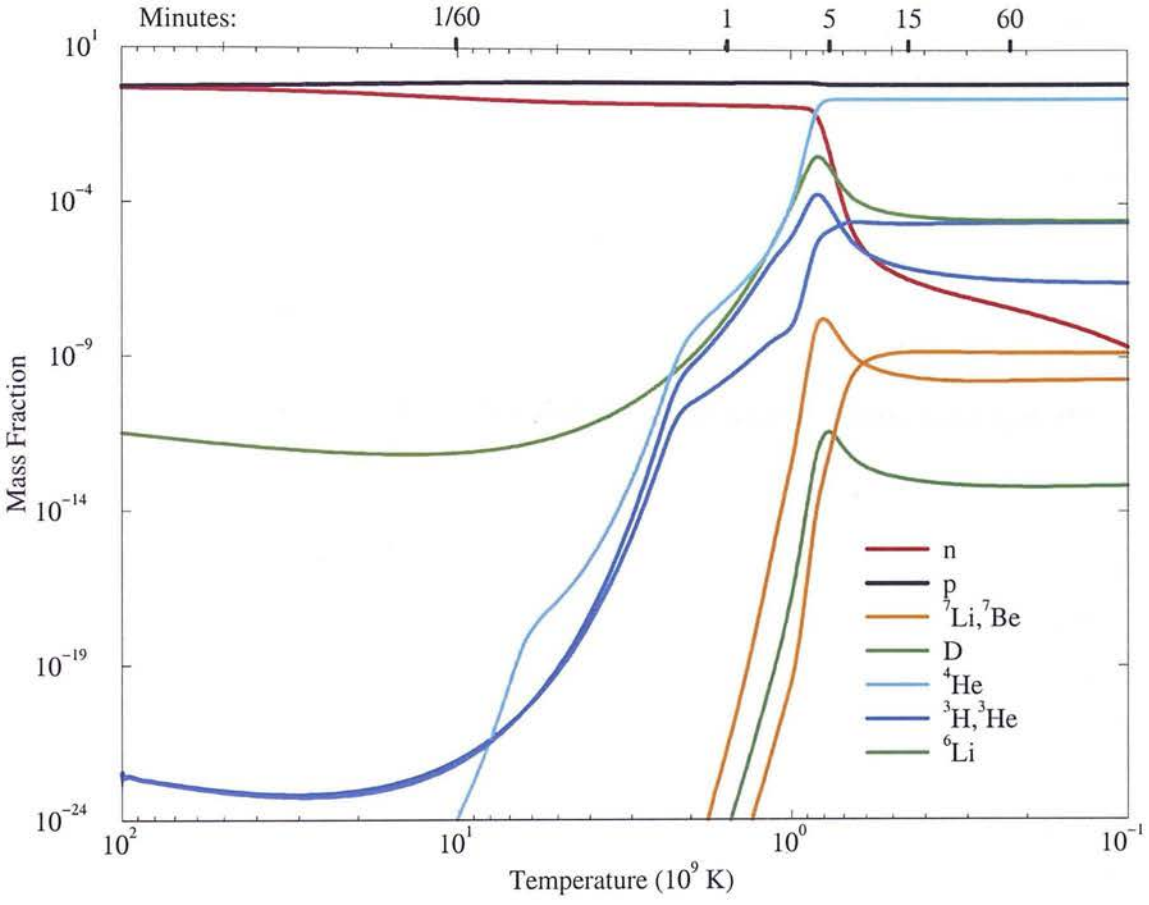

Figure 1.5: An example of the evolution of mass fraction versus temperature (or time) for BBN abundances for a baryon density consistent with current observational data. This figure is taken from
http://heseweb.nrl.navy.mil/gamma/dap-aps/astro/bbn/bbn5.htm.

Determination of the primordial abundance of any of the elements is substantially complicated by the fact that most of the gas we observe will have been contaminated by elements produced by stellar nucleosynthesis. The best technique to date for avoiding this problem involves determining the D/H ratio in absorption line systems of high redshift quasars. Deuterium is not produced dur-

ing stellar nucleosynthesis (although it can be destroyed) and thus the observed D/H ratio is thus a strong lower limit on the primordial ratio. Moreover the observed metal abundance of the absorption line systems allows one to estimate the fraction of gas that has been processed through stars, and thus the fraction of primordial deuterium that has been lost. Typical absorption line systems have $0.001 \leq Z/Z_{\odot} \leq 0.01$, corresponding to a loss of approximately 1 - 10% (Edmunds 1994) of the primordial deuterium. Recent measurements of the D/H ratio from absorption systems in the spectra of quasars (O'Meara et al. 2001 and references therein) give a value of $D/H = 3.0 \pm 0.4 \times 10^{-5}$ corresponding to a baryon density of $\Omega_b h^2 \simeq 0.021$, which is consistent with recent WMAP measurements from the CMB of $\Omega_b h^2 = 0.0224 \pm 0.0009$ (Bennett et al. 2003). The dependence of the abundances of the light elements relative to hydrogen with respect to the present density of baryonic matter are shown in Figure 1.4. Figure 1.5 goes on to show how the mass fraction of the elemental abundances evolves with temperature, and time after the Big Bang, when the baryon density is consistent with that measured observationally from the CMB and the D/H ratio in absorption systems of high redshift quasars.

1.2.4 Recombination

For several thousand years following the formation of helium nucleii, the Universe remained a hot broth of photons, neutrinos, hydrogen and helium nucleii, and electrons. The dynamics of the expansion were dominated by radiation and relativistc particles like neutrinos so that the scale factor of the Universe increased as $R \propto t^{1/2}$. Eventually, at $t \sim 10^{11}$ seconds after the Big Bang, the cosmic background radiation had become sufficiently diluted that the expansion became governed by the matter particles and the scale factor of the Universe now increased as $R \propto t^{2/3}$. The point at which the radiation era came to a close and the matter era began occured when the temperature was of order 10^5 K.

Being electrically charged, the protons and electrons continued to interact strongly with the high-energy photons of the electromagnetic radiation field. In this process, energy was exchanged between the particles and the photons, ensuring that the matter and radiation fields were closely linked. The two energy fields were in thermodynamic equilibrium and they remained in this state until the next milestone in the cosmic evolution, the recombination epoch, when radiation and matter became decoupled from each other.

This occurred approximately 300 000 years after the Big Bang, when the temperature had dropped to 3000 K. At this point electrons were able to combine with the nucleii to produce neutral atoms, and this is known as the recombination epoch. In a very short time the Universe went from being a predominately ionised state to a neutral state. The neutral gas no longer interacted with the radiation field and the matter and photon fields were free to evolve on their own. The Universe became transparent to the cosmic background radiation. It is this relic which is observed today by satellites such as COBE and WMAP, redshifted by a factor of 1000 into the microwave part of the electromagnetic spectrum, and commonly termed the cosmic microwave background (CMB). The radiation appears to have come from a spherical surface around the observer such that the radius of the shell is the distance each photon has travelled since it was last scattered at the epoch of recombination.

1.2.5 Dark Matter

Up until now, the evolution of the Universe has been discussed in terms of well known particles; photons, baryons (and of course the particles comprising the baryons at early epochs). However, there are good reasons for believing that the matter we see directly accounts for only a fraction of the matter in the Universe, the remainder termed "dark matter", since it manifests itself only via gravity. There exist several theories to account for the missing mass ranging from exotic subatomic particles, to a population of isolated black holes, to less exotic brown and white dwarfs.

Historically, the first detection of dark matter was made in 1933 by Zwicky, who was studying the motions of distant and massive clusters of galaxies, specifically the Coma cluster and the Virgo cluster. Zwicky estimated the mass of each galaxy in the cluster based on their luminosity, and added up all of the galaxy masses to get a total cluster mass. He then made a second, independent estimate of the cluster mass, based on measuring the spread in velocities of the individual galaxies in the cluster, finding that this second dynamical mass estimate was 400 times larger than the estimate based on the galaxy light. Although the evidence was strong at Zwicky's time, it was not until the 1970s that scientists began to explore this discrepancy comprehensively. It was at this time that the existence of dark matter began to be taken seriously. The existence of such matter would not only resolve the mass deficit in galaxy clusters; it would also have more far

reaching consequences for the evolution and fate of the universe itself.

The most dramatic evidence for the existence of large amounts of dark matter is that many galaxies show flat rotation curves, rather than the Keplerian fall-off $v \propto 1/\sqrt{r}$ that would be expected if the total mass inside r had converged. The observation of a roughly constant v implies a linearly divergent $M(< r) \propto r$. The implication is that the mass enclosed by larger-radius orbits increases, even for stars that are apparently near the edge of the galaxy. While they are near the edge of the luminous part of the galaxy, the galaxy has a mass profile that apparently continues well beyond the regions occupied by stars.

Several theories have surfaced in the literature to account for the missing mass such as WIMPs (Weakly Interacting Massive Particles), MACHOs (MAssive Compact Halo Objects), primordial black holes, massive neutrinos, although some of these can now be discounted as major halo dark matter constituents by recent research.

Limits already existed on much of the potential mass range of MACHOs from earlier studies. Lacey & Ostriker (1985) suggested a mechanism for disk heating by supermassive black holes and discussed that black holes with $M > 10^6 M_\odot$ could destroy the galactic disk. Nemiroff et al. (1993) searched for the "echoes" of gamma-ray bursts induced by gravitational lensing; that is to say they searched for multi-imaging associated with gravitational lensing which due to limited resolution could not be resolved spatially, but could still be resolved temporally. Their null results effectively excluded halo dark matter in the mass range $M \sim 10^{6.5} - 10^{8.5}$. Moore (1993) argued that massive black holes ($M > 10^3 M_\odot$) could disrupt low mass globular clusters. Although this argument is somewhat sensitive to assumptions about the initial population of globular clusters, it implies an upper limit of $M < 10^3 M_\odot$. At the lower mass end, microlensing experiments by the MACHO collaboration (Alcock et al. 2001) and the EROS collaboration (Afonso et al. 2003) found that MACHOs with $10^{-7.5} M_\odot < M < 30 M_\odot$ cannot account for the mass of the dark halo. De Rújula, Jetzer & Massó have investigated in detail the possibilty that the dark constituents of galactic halos may be brown dwarfs, compact hydrogenous objects of mass below the nuclear ignition threshold $M \simeq 0.08 M_\odot$. They demonstrated that these objects would have evaporated away in a galactic timescale if lighter than $\sim 10^{-7} M_\odot$. A recent study of halo dark matter by Yoo et al. (2003) has effectively put the final nail in the coffin on MACHOs being a major dark matter constituent. They investigated the evolution of halo wide binaries in the presence of MACHOs and estimated

upper limits of MACHO density as a function of their assumed mass by comparing simulations to the sample of wide binaries of Chanamé & Gould (2003). Their results were able to exclude MACHOs with $M > 43M_{\odot}$ at the standard local halo density at the 95% confidence level, effectively ruling out MACHOs as a significant dark matter constituent.

It has been suggested that if the neutrino, generally believed to be a massless particle, actually had an extremely small mass of order a few tens of eV, it could plausibly be a significant source of dark matter, simply due to the sheer number of the particles pervading the Universe. This scenario is an example of hot dark matter (HDM) and has been an attractive idea in the past since one does not need to introduce the concept of any new, more exotic particles. However, if the Universe were dominated by massive neutrinos, then fluctuations that contain a mass less than some critical mass would be wiped out because the neutrinos which move at relativistic speeds can "free-stream" from the over-dense regions into the under-dense regions. For a neutrino mass of 30 eV for example, this critical mass is $\sim 10^{16}M_{\odot}$ ie. supercluster scales. Somehow these would have to fragment for galaxies to form. Computer simulations have shown that in this "top down" structure formation scenario galaxies could only form at $z \sim 1$, and furthermore predict far too much condensation into large scale structure and huge voids. The situation is made worse for even smaller neutrino masses. Combining the extremely strong parametric constraints obtained from WMAP with large-scale structure data from the Sloan Digital Sky Survey (SDSS) (Tegmark et al. 2003), the sum of the masses of the three flavours of neutrino is constrained to $M_{\nu} < 1.7\,\mathrm{eV}$ at the 95% confidence level. These results would therefore suggest that massive neutrinos provide very little contribution (if any) to the dark matter.

The most favoured dark matter candidates to date are cold particles, often referred to as WIMPS. The candidates are non-baryonic eg. neutralinos and axions, and although no such particle has yet been directly detected there is some motivation for their existence from supersymmetry theories. In this case small scale structures are preserved at all times. Free-streaming of particles is unimportant since the dark matter is non-relativistic. In cold dark matter (CDM) models the structure formation is "bottom up". The first objects to form are low mass systems which assemble into larger systems by hierarchical clustering. Masses on small scales are able to begin collapse shortly after the recombination epoch.

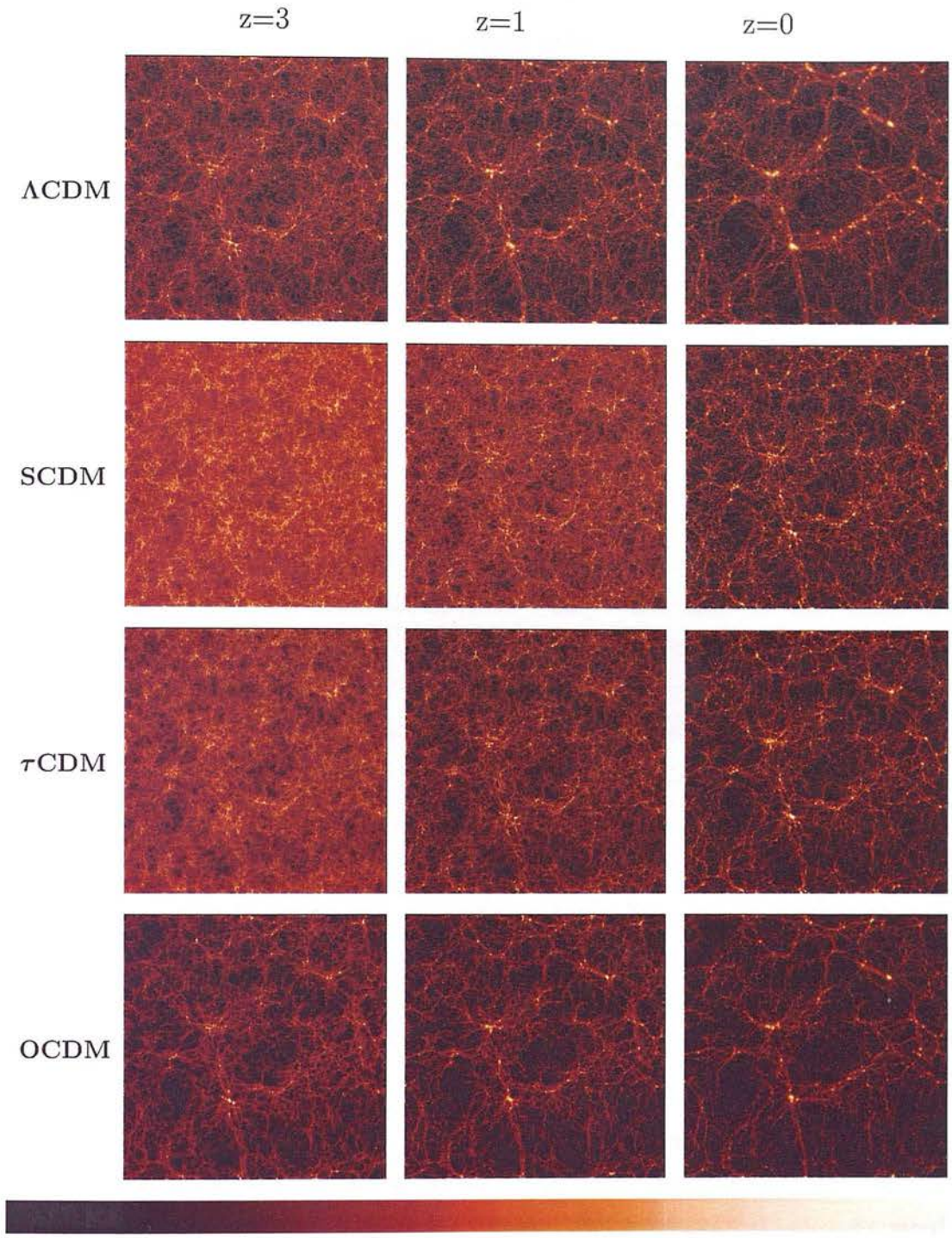

Figure 1.6: Snapshots of hierarchical CDM growth at $z = 3$, $z = 1$, and $z = 0$, for four different cosmologies (taken from Jenkins et al. (1998), courtesy of the VIRGO consortium). The brightness of the colours is proportional to the log of the density of the particles. The boxsize is 239.5/h Mpc, where $h = H_0/100$.

Figure 1.6 shows snapshots of hierarchical CDM growth at $z = 3$, $z = 1$, and $z = 0$, for four different cosmologies (taken from Jenkins et al. (1998), courtesy of the VIRGO consortium). The boxsize is 239.5/h Mpc, where $h = H_0/100$. The brightness of the colours is proportional to the log of the density of the particles. Note that the densest regions are the oldest since these mark the regions highest density peaks in the initial Gaussian fluctuations.

1.2.6 The Cosmological Constant

The cosmological constant is a term Einstein first introduced into his General Theory of Relativity in order to allow for static solutions of the field equations. Although he later retracted the suggestion following Hubble's discovery that the Universe was expanding, there is no physical reason for the cosmological constant Λ to be zero.

The idea that a cosmological constant could be explained in terms of a vacuum energy contribution was first introduced by Zeldovich (1967). The basic idea is that any energy density associated with space will have a negative equation of state. To see why this is so, consider the effects of expanding space by an infinitesimal amount dV. This increases the energy content by $dU = \rho_\Lambda c^2 dV$, which for an adiabatic change is $dU = -pdV$. The pressure must then be given by

$$p_\Lambda = -\rho_\Lambda c^2 \tag{1.16}$$

which further implies that

$$\frac{d\rho_\Lambda}{dt} = 0 \tag{1.17}$$

i.e. the vacuum energy density remains constant. At first sight the idea of empty space containing energy does seem rather abstract, however quantum theory tells us that there is no such thing as truly empty space. Rather, the vacuum state in quantum field theory is simply the minimum energy state. This value may be zero, but there does not appear to be anything in quantum field theory to force it to be so. A non-zero cosmological value for the cosmological constant would contribute to the energy-momentum tensor as a vacuum energy density.

Recent observational evidence is strongly supportive of a non-zero cosmological constant. Over the past decade, supernovae have emerged as some of the most powerful tools for measuring extragalactic distances. A well developed physical understanding of type Ia supernovae allow them to be used to measure distances independent of the extragalactic distance scale. Type Ia supernovae are empirical

tools whose precision and intrinsic brightness make them sensitive probes of the cosmological expansion. Two teams have used type Ia supernovae to trace the expansion of the Universe to a look-back time more than 60% of the age of the Universe. Perlmutter et al. (1999) and Riess et al. (1998) both found strong evidence for a non-zero cosmological constant, consistent with $\Omega_{\rm M} = 0.3$ and $\Omega_\Lambda = 0.7$.

Observations of the angular power spectrum of the anisotropies in the CMB can also be use for determining cosmological parameters. The powerful combination of WMAP data (Spergel et al. 2003, Verde et al. 2003) with data from CBI (Pearson et al. 2002) and ACBAR (Kuo et al. 2002) which probe the CMB temperature power spectrum at $l > 900$, very firmly indicates a non-zero cosmological constant, the best-fit model having a matter fraction $\Omega_{\rm M} = 0.27 \pm 0.04$ and dark energy fraction $\Omega_\Lambda = 0.73 \pm 0.04$.

1.3 The Evolutionary History of Galaxies

The standard model outlined above is a good description of the Universe on the largest scales where one can regard it as effectively homogeneous. However, looking at the Universe on smaller scales, the presence of galaxies, clusters and superclusters demonstrates an inhomogeneous distribution of matter. Initial density perturbations, observable today as very small temperature anisotropies (< 1 part in 10^5) in the cosmic microwave background, provided the seeds from which structure observable in the Universe today could begin to form. These small irregularities continued to grow under the influence of gravity, the regions with the highest density attracting more matter from the surrounding regions thus increasing their density further. An irregular distribution of matter is unstable under the influence of gravity, explaining the observation that the Universe is much more irregular now than at decoupling.

Gravity led to the accretion of primordial hydrogen and helium, created in big bang nucleosynthesis, to the higher density regions, producing massive clouds of gas from which the first stars could form. The initial star-forming clumps, however, were almost 30 times warmer than the molecular gas clouds that form stars today in the solar neighbourhood. They may have reached 500 to 800 Kelvin at the highest densities attained because they lacked dust grains and molecules with heavier elements that work much more efficiently to cool such clouds (Larson 1999). Hence, the minimum "Jeans mass" that a relatively warm,

primordial clump of gas needed to collapse under its gravity is hypothesized to be almost a thousand times what it is today (Bromm, Coppi & Larson 2002). These massive stars began synthesizing the heavier elements, resulting in the creation of dust grains composed of silicates and / or graphite, typically with diameters $\sim 0.01 - 0.1\,\mu$m. After three to four million years, these stars exploded as supernovae, infusing the interstellar medium with heavier elements and dust grains. Some of the metal-enriched material would feed back into new generations of stars which in their turn also evolve and die, and so on. Present day galaxies contain between $\sim 10^6$ and 10^{13} stars from dwarf to giant, along with gas and dust, the material from which they are composed having been through a number of stellar lifecycles previously.

Galaxies essentially come in three morphological classes; elliptical, spiral and irregular. The elliptical and spiral galaxies both show a symmetrical and regular structure, however, they display very different stellar populations and evolve on separate evolutionary tracks. An elliptical galaxy (or spheroid) comprises a group of stars showing more random than ordered three-dimensional motions. They contain old, red stellar populations, show very little evidence for recent star formation and tend to be devoid of gas and dust (Seeds 1990). Spiral galaxies (or disks) contain a central bulge with similar properties to that of a spheroid, however, they mainly comprise a flattened disk of stars and interstellar material rotating about the galactic centre in a two-dimensional ordered manner. The disk contains a young blue stellar population with significant levels of star formation ongoing as well as an interstellar medium rich in gas and dust (Seeds 1990). The remaining galaxies are classified as 'irregular' since they show no symmetrical or regular structure. In general they show signs of recent interactions, distorting their shape and often triggering fresh bouts of star formation activity. A survey of the region of space out to 9.1 Mpc shows that 13% of galaxies are ellipticals, 33% are spirals and 54% are irregulars.

The following two subsections will give a more detailed overview of the comparative evolutionary properties of disks and spheroids.

1.3.1 Spirals

Observations of ultraviolet continuum and Hα emission of the young stellar disk population of local spiral galaxies has shown that typical star formation rates are of order a few solar masses per year, although this ranges from almost zero to $\sim$

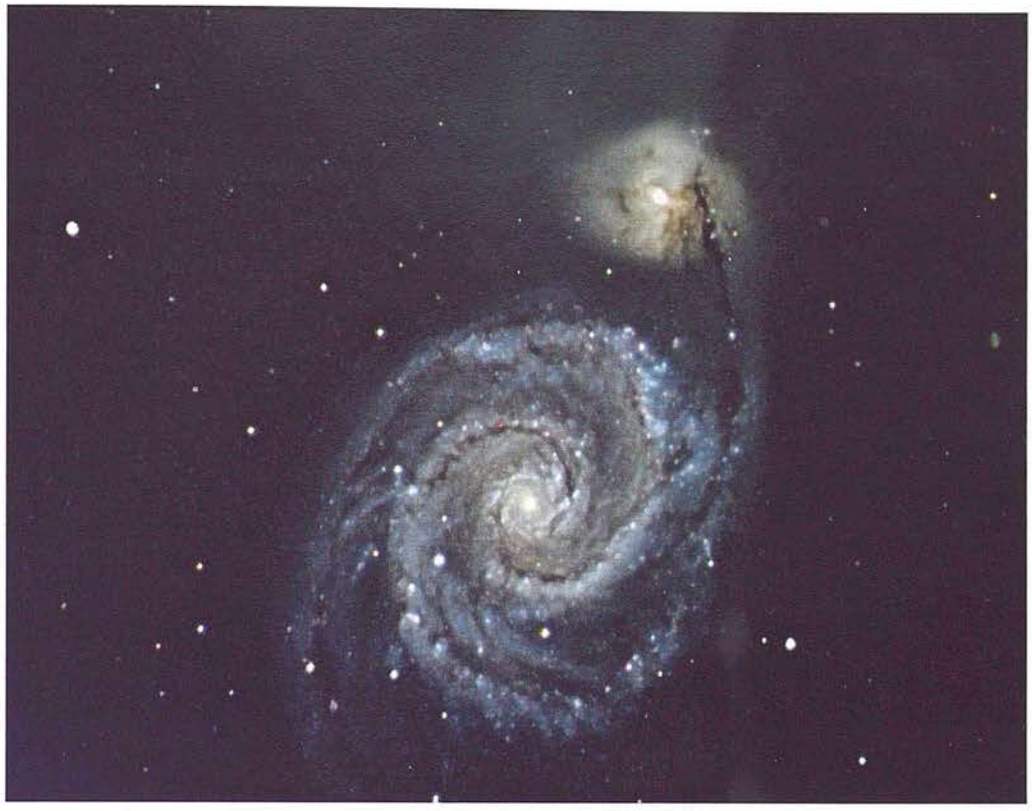

Figure 1.7: The spiral galaxy M51. This is a "true-colour" composite of B, V and R images obtained with the WHT Prime Focus Camera and. This image is taken from http://www.ing.iac.es/PR/newsletter/news3/crown.html.

$20\,M_{\odot}yr^{-1}$ in the largest spirals (Kennicutt 1983, Donas et al. 1987). Comparison of these star formation rates with the remaining supply of interstellar gas yields consumption timescales of a few Gyrs. Moreover, if one considers the past star formation rate estimated by dividing the current stellar content by the age of the disk, an almost constant star formation rate is implied throughout the lifetime of the disk (Kennicutt 1983). There is no initial intense burst of starburst to mark the beginning of formation.

The central bulges of spiral galaxies are believed to form in a similar manner to elliptical galaxies (described in the next subsection), with the disk being acquired at a later time via the infall of high angular momentum gas. Evidence supporting this idea comes from the age dating of our own Milky Way galactic disk, by means of cool white dwarf stars. The age estimate uses the idea that in a galaxy of finite age there will be a temperature beyond which the oldest, coolest white dwarfs have not had time to cool, which results in a break in their luminosity function. A multicolour proper motion survey for cool white dwarfs was conducted by Knox,

Hawkins & Hambly (1999), from which a white dwarf luminosity function was constructed. This survey showed no signs of incompleteness. By comparing the measured luminosity function to models of white dwarf cooling, they estimate the age of the Milky Way disk as 9-13 Gyr old. Cool white dwarfs are extremely faint and our distance from the galactic centre means that only a handful of these objects have been discovered in the galactic bulge to date. In order to estimate the age of the galactice bulge, therefore, one must use other methods such as globular clusters. A globular cluster is a dense spherical clump of mainly population II stars - very old stars with low metallicities, believed to form very early on in the galaxy's history. They are located in a spherical halo surrounding the galaxy and are part of the same spheroidal population of the bulge. Recent age dating of the stellar populations in globular clusters by Vandenberg (1998) has determined an age of 13-14 Gyr for the Milky Way's galactic bulge.

To summarise, the spiral disks appear to form quiescently, by means of a low but steady star formation rate over a long period of time. A picture of the spiral galaxy M51 is shown in Figure 1.7.

1.3.2 Ellipticals

There are two main families of models describing the formation of spheroids.

• The monolithic scenario, developed since the early work by Larson (1975), is characterized by an intense starburst and a consequent chemical enrichment at very early phases of the galaxy history, followed by a long period of quiescent evolution. Episodes of star formation may occur later in the lifetime of the galaxy, stimulated by either interactions with neighbours or accretion of gas from the intergalactic medium (Bertola et al. 1992).

• In the so called hierarchical scenario, ellipticals are formed from different merging episodes through the Hubble time, which trigger the star formation activity and the chemical enrichment of the system (White & Rees 1978). In this scenario massive ellipticals form at relatively low redshifts ($z \leq 1.5$) through the merging of spiral galaxies (Toomre 1977, Baugh et al. 1996, 1998).

As emphasised by Peebles (2002), the distinction between the two scenarios is more of historical rather then physical significance. Large objects may be formed by interaction and merging of a hierarchy of primeval "lumps" in a protogalaxy: this is practically equivalent to a monolithic scenario. On the other hand there is no doubt that galaxies do interact, with sometimes spectacular effects, and have

Figure 1.8: The elliptical galaxy M87. This is an optical image taken with the AAT. This image is taken from
http://www.seds.org/messier/more/m087_aat.html.

perhaps interacted still more at large z. The pivotal problem is to determine when the majority of the stars were formed and if the subsequent evolution was passive or modified by interactions.

There exist a large body of observations supporting the view that ellipticals were already formed at $z \simeq 2$ in about the same proportion as today, and have since evolved passively. Firstly the small scatter in the mass-to-light ratio derived from the Fundamental Plane (the correlation of luminosity with surface brightness and velocity dispersion), imposes tight constraints on the dynamics, initial mass function and ages of the stellar populations (Renzini & Ciotti 1993). Jorgensen et al. (1999) used photometric and kinematic data to derive the Fundamental Plane for two clusters near $z = 0.18$. Together with previous data published by van Dokkum & Franx (1996) and Kelson et al. (1997) for a series of higher redshift clusters, they found a gradual and slow evolution of the mass-to-light (M/L)

ratio with redshift. Using stellar population models, Jorgensen et al. (1999) were able to relate the change in the M/L ratio to the formation redshift, and found that their results were consistent with passive evolution of a stellar population formed at $z \simeq 5$. This is congruous with Ziegler et al. (1999) who examined the luminosity evolution of clusters in comparison to the local Coma cluster using the Kormendy relation (a correlation between the radius, r_e, that contains half of the luminosity in a de Vaucouleurs law fit to the surface brightness profile of an elliptical galaxy and the surface brightness at r_e).

One can also look to the colour-magnitude (CM) relation as a tracer of spheroid evolution. This is a remarkable correlation between colours and luminosities of the spheroid population, the brighter galaxies showing redder colours. The CM relation is best defined for clusters, and can be readily explained in terms of a single star formation episode. More massive galaxies would retain supernovae ejecta more effectively, resulting in higher metallicities for the succeeding generations of stars within the initial burst and hence in redder colours for more luminous galaxies (Larson 1975). Indeed, the CM relation in nearby clusters appears to imply a close tie between metallicity and galaxy mass, as seen in the tightness of the Mg_2 line index and central velocity dispersion ($Mg_2 - \sigma$) correlation (Bender, Burstein & Faber 1993). Furthermore, the scatter in the UVK colours of present-epoch cluster ellipticals is observed to be very small (Bower, Lucey & Ellis 1992a & 1992b). This is evidence for a high degree of synchronization in their star formation histories and relatively old ages. Late, episodic bursts of star formation, young galaxy ages, or a wide range in galaxy formation redshifts would be expected to lead to a much larger scatter in colour than is observed. An intense burst of star formation lasting ~ 1 Gyr at an early formation epoch coupled with passive evolution simply predicts the observed homogeneity in the colours of most elliptical galaxies in clusters today. Stanford et al. (1998) have studied the z variation of the CM diagram in clusters out to $z \simeq 1$. Their results are also in agreement with passive evolution of a population formed at $z > 2.5$.

Thomas et al. (2002) have studied the epochs of early-type galaxy formation in clusters and in the field by considering the role played by the so-called α-elements, represented largely by magnesium. They applied single stellar population (SSP) models with variable [α/Fe] ratios to a sample of 126 spheroidal galaxies, finding that [α/Fe] ratios correlated well with velocity dispersion σ, and also with the estimated mean population age. They concluded that the more massive ellipticals

had higher average ages and higher [α/Fe] ratios, because of earlier formation epochs and shorter formation timescales of their stellar populations: applying a boundary of $\sigma = 200\,\mathrm{km/s}$ to distinguish between "low" and "high" mass ellipticals they determined that 50% of low-mass ellipticals, but only 10% of the high-mass ellipticals, had average ages younger than 5 Gyr.

Finally, the lack of molecular gas and dust in spheroids suggests that the epoch of star formation of these galaxies is behind us. Observations of nearby ellipticals originally showed no evidence of an interstellar medium (ISM) and they were believed to be devoid of gas and dust (eg. Faber & Gallagher 1976). More recent observations carried out in the infrared and millimetre, however, have implied the presence of an ISM, similar in terms of colour and hydrogen abundances to that found in spirals but in much smaller quantities (Lees et al. 1991). Low levels of molecular gas are inferred $< 10^8\,\mathrm{M}_\odot$, insufficient for any major episodes of star formation in the future.

Perhaps one point of conjecture comes from recent analyses of the spectroscopic features and colours of elliptical galaxy spectra, indicating that some ellipticals contain an intermediate-age stellar population eg. James & Mobasher (1999). However, James & Mobasher also noted that this appears to be true for ellipticals clustered in small groups rather than those in isolated environments or dense clusters. Since it is small groups that are most conducive to merger activity due to their low velocity dispersion, it would seem likely that all ellipticals form coevally at high redshift, but those undergoing mergers with gas-rich galaxies in more recent epochs additionally contain a newer younger stellar population.

A wealth of observational evidence implies that elliptical galaxies and spheroidal bulges in spiral galaxies underwent a short ($\sim$ 1Gyr) and violent starbursting episode at high redshift, evolving passively from that point. The extremely high star formation rates would lead to the generation of huge amounts of dust, obscuring the optical and ultraviolet emission, particularly for the most massive objects. This, coupled with the huge distances involved, may explain why a massive elliptical galaxy in the throes of formation has yet to be detected directly by its starlight. An image of the elliptical galaxy M87 is shown in Figure 1.8.

1.4 Global Star Formation History - I. An Optical Perspective

1.4.1 Low Redshift ($z < 1$)

Young stars are very hot ($T > 10000\,K$), and hence emit strongly at optical and ultraviolet (UV) wavelengths. In order to determine the star formation rate (SFR) at low redshift one looks to the rest-frame UV luminosity density by means of large and deep multi-wavelength redshift surveys. Provided there is no substantial evolution of galaxy dust properties over the redshift range $0 < z < 1$, the shape of the rest-frame UV luminosity density should correlate directly with the SFR. The results of these surveys (described below) all agree that the co-moving star formation rate of the Universe is in decline. The rate of decline, however, is somewhat uncertain, the different analyses suggesting that the star formation rate has dropped by a factor of $3 - 30$ since $z = 1$, an order of magnitude discrepancy.

Optical / UV studies originally suggested a steep rise in the SFR as a function of redshift between $z = 0$ and $z = 1$ (Lilly et al. 1996) such that the star formation and metal production rates were of order 15 times greater at $z = 1$ than at $z = 0$. This was based on data from the "Canada France Redshift Survey (CFRS)" consisting of 730 $I-$band selected galaxies ($17.5 < I_{AB} < 22.5$), of which 591 had secure redshifts in the range $0 < z < 1.3$, with a median $< z > \sim 0.56$. All objects had V and I photometry, with a large proportion also having been observed in B and K.

An optical / UV analysis by Cowie et al. (1999), however, based on a large, deeper ($B_{AB} < 24.75$, $I_{AB} < 23.5$) and highly complete spectroscopic redshift survey of galaxies observed in seven colours (U', B, V, R, I, J and HK') of the "Hawaii Survey Fields" and "Hubble Deep Field" has implied a much gentler trend in the SFR density with epoch at $z < 1$, consistent with a slope of $(1+z)^{1.5}$ for an Einstein de Sitter cosmology (a drop in star formation rate by a factor of 3 since $z = 1$). They proposed that this survey had two advantages over the UV luminosity density analysis carried out by Lilly et al. (1996), as follows. Firstly, the CFRS is a red ($I-$band) selected sample with V and I photometry primarily, and only partial B and K coverage. At the lower end of the redshift range $0 < z < 1$ this requires a very substantial extrapolation across the 4000Å break to obtain a 2800Å rest-frame luminosity. Secondly, the CFRS is slightly

too shallow to address this issue ($I_{AB} < 22.5$), thus creating problems at the higher end of this redshift range near $z = 1$ because the sample does not probe deep enough in the luminosity function to allow a reliable extrapolation to a total luminosity density. Cowie et al. (1999) find a UV luminosity density at the lower end of this redshift range to be considerably higher than that found by Lilly et al. (1996), and in good agreement with the local UV luminosity density determined by Treyer et al. (1998). This would indicate that much of the integrated total of optically visible stars is still being assembled at the present time.

The most recent estimates of the star formation history in the low redshift Universe take an alternative approach. The measured spectrum of a galaxy contains, in principle, information about the processes which led to its formation and evolution. The quantity of gas transformed into stars, the metallicity and dust content at a given time all affect the integrated light of a galaxy. Therefore, using spectra from nearby galaxies one should be able to unlock the fossil record of the past history of the Universe. The vast quantities of data on the relatively nearby Universe collected from the Sloan Digital Sky Survey (SDSS) provides a unique tool for such an approach. In brief, the SDSS is a digital CCD survey in 5 optical wavebands (u, g, r, i and z) covering one quarter of the entire sky (York et al. 2000). The main galaxy sample is essentially a magnitude limited spectroscopic sample. It is selected as virtually all galaxies in the photometric area with a Petrosian magnitude $r < 17.7$. Ninety eight per cent of the galaxies span a redshift range of $0 < z < 0.25$ with a median redshift of 0.10.

Glazebrook et al. (2003) used an ensemble of all galaxies to construct the "Cosmic Optical Spectrum" of the local Universe which represents the luminosity-scaled spectra summed over all galaxies. The cosmic spectrum can be thought of as the total emission from all the objects in a representative volume of the Universe. Objects contribute to the cosmic spectrum according to their luminosity. As with an individual galaxy, this spectrum contains a luminosity-weighted mix of features from both young and old stars to which models of the star formation history may be fitted. Due to the fact that the cosmic spectrum represents an average, it will represent the end point of the average star formation history. This allows much simpler models to be fit to the cosmic spectrum than would be required for individual galaxies because the star formation history of the Universe as a whole is expected to vary smoothly with time. Using the standard power law star formation history model of the form $(1 + z)^{\beta}$ out to $z = 1$, Glazebrook et al. (2003) found that $\beta = 2 - 3$ (a drop of 4-8 in star formation activity from

$z = 1$ to the present day) is still the most likely model.

Panter, Heavens & Jimenez (2003) have also analysed the fossil record of galaxies from the SDSS, but instead of using the averaging approach of Glazebrook et al. (2003) they applied clever data compression techniques to allow each individual galaxy to be considered in turn. The approach of the Multiple Optimised Parameter Estimation and Data compression (MOPED; Heavens, Jimenez & Lahav 2000) chooses a relatively small number of linear combinations of the data, where the weightings are chosen carefully and automatically to preserve as much information as possible about the parameters one wants to know about; in this case placing emphasis on the star formation and metallicity histories and the dust content. In this manner it is possible in a practical way to recover virtually as much information as is theoretically possible, given the data and a theoretical model. Panter, Heavens & Jimenez (2003) found a considerable decrease is the star formation rate density of order a factor of 30 over the last 6 Gyr ($z < 1$), with tentative evidence for flattening before that time.

1.4.2 High Redshift ($z > 1$)

The earliest searches for high redshift star-forming galaxies were blank field surveys for Lyα emsision lines (eg. Pritchet & Hartwick 1990, Djorgovski & Thompson 1992 and refernces therein). Lyα emission in proto-galaxies can be powered primarily by photoionization by young, massive stars. Additional mechanisms include shock ionization from infalling and colliding protogalactic fragments, supernovae, cooling of the first stars, and photoionization by early active galactic nucleii (AGN), if any are present. However, these searches were largely unsuccessful, detecting only a handful of potentially high redshift objects, many of which were found to be at $z < 1$ in spectroscopic follow-up.

More successful in finding high-redshift star-forming galaxies was the Lyman-break technique. This method makes use of the Lyman-limit at a rest frame wavelength of 912Å. Very little flux is emitted from the blue side of the Lyman-limit since

- There are very few stars hot enough to produce such energetic photons.
- Photons at wavelengths shortwards of the Lyman-limit can ionize neutral hydrogen and hence stand a good chance of being absorbed.
- Such photons also may be absorbed by hydrogen clouds along the line of sight from the galaxy to Earth.

Lyman-break galaxies (LBGs) are selected by performing deep imaging in 3 broad-band filters; U, G and R when searching for galaxies at $z \sim 3$ or G, R and I when searching for galaxies at $z \sim 4$. Potential high-redshift sources are identified for spectroscopic follow-up if they are detected in the two longer wavelength filters but do not appear in the shortest wavelength image (as a result of the Lyman break having been redshifted into this waveband).

Based on imaging of the Hubble Deep Field (HDF), Madau et al. (1996) initially found that the global star formation rate declined beyond a redshift of $z \sim 1.5 - 2$ reaching a value at $z \simeq 4$ comparable to that Lilly et al. (1996) had inferred for the local Universe. However, as pointed out by Steidel et al. (1999) there are several reasons to be concerned about results based solely on the HDF. Firstly, the HDF, while one of the highest quality images of the sky ever obtained is after all only a small piece of sky (~ 5 sq. arcmin) and hence samples only a very small volume at any redshift. Since observations of the Lyman-break population at $z \sim 3$ in ground-based surveys have shown that at high redshift luminous star-forming galaxies are strongly clustered (Giavalisco et al. 1998), one must be concerned about sample variance. Moreover, even if the HDF represents a fair sample of the Universe, the redshift distributions of the F300W and F450W dropouts are not well known empirically. As a result, the effective volumes used by Madau et al. (1996) to calculate the star-formation densities at $< z >= 2.75$ and $< z >= 4$ were based upon models of the spectral-energy distributions and Lyman-continuum opacities of galaxies, and not on spectroscopic redshifts.

Steidel et al. (1999) have conducted a survey approximately 160 times larger than the HDF using both $U-$ and $G-$band dropouts of complemetary depths to search for luminous star-forming galaxies at $z \sim 3$ and $z \sim 4$ respectively. After correcting for extinction using the Calzetti (1997) reddening law (typical $E(B-V) = 0.15$), they find an almost constant star-formation rate density (SFRD) in the redshift range $1 < z < 4$.

In the past year, a number of groups have extended the Lyman-break technique to search for star-forming galaxies at redshifts $z \sim 5$ and $z \sim 6$. Iwata et al. (2003) have detected 305 candidate Lyman-break galaxies at $z \sim 5$ using ultra-deep V, I_c and z' imaging, taken with the Subaru Prime Focus Camera, of a 618 sq. arcmin field, including the Hubble Deep Field North. They found no signifiant difference between the luminosity function of LBGs at $z \sim 5$ and those at $z \sim 3$ and 4 obtained by Steidel et al. (1999) although there is some

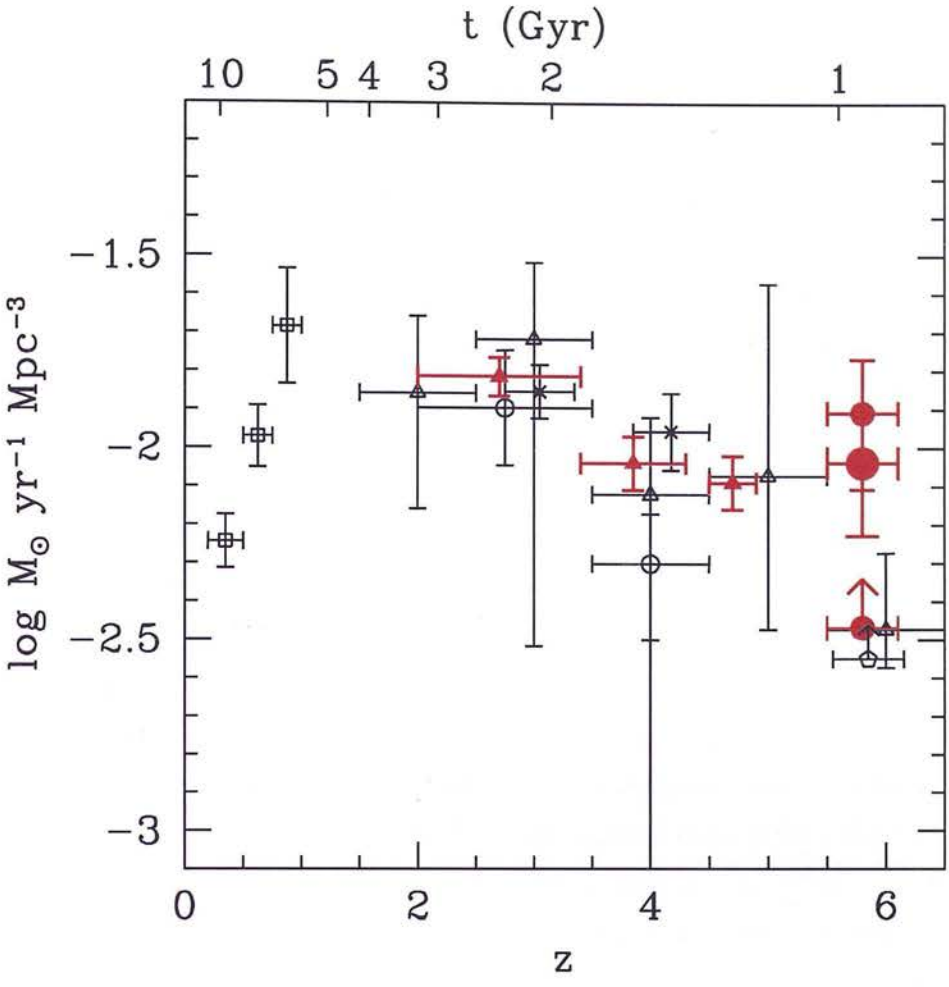

Figure 1.9: Figure taken from Bouwens et al. (2003a). A history of the star formation rate density assuming no extinction correction, integrated down to $0.5L_*$. The open squares are from Lilly et al. (1996), open circles from Madau et al. (1998), crosses from Steidel et al. (1999), open triangles from Thompson et al. (2001) and open pentagons from Stanway, Bunker & McMahon (2003). The solid red triangles are from Bouwens, Broadhurst & Illingworth (2003b), and the solid red circles are from Bouwens et al. (2003a). The lower solid red circle assumes no incompleteness correction and provides a reliable lower limit. The middle point is is based on a generalization of the formalism used in Steidel et al. (1999). The upper point is based on the differential evolution from $z \sim 6$ to $z \sim 5$ and is linked to $z \sim 3$ using the results of Bouwens, Broadhurst & Illingworth (2003b).

uncertainty at the fainter magnitudes. Furthermore, their best estimate for the co-moving star formation rate density at $z \sim 5$ is 60-70% of that estimated by Steidel et al. (1999) at $z \sim 3$, although they do make the point that with the uncertainty at the faint end of the LBG luminosity function of the $z \sim 5$ sample, their results are still consistent with a constant star formation rate density for the redshift range $1 < z < 5$.

The usual Lyman-break technique involves the use of three filters: one below

the Lyman-limit ($\lambda_{\rm rest} = 912\,$Å), one in the Lyman forest region and a third longwards of the Lyman-α line ($\lambda_{\rm rest} = 1216\,$Å). At $z \sim 6$, however, the integrated optical depth of the Lyman-α forest is $>> 1$, and hence the continuum break at the wavelength of Lyman-α is large and so the shortest wavelength filter below the Lyman-limit becomes redundant. Thus provided one has sufficiently high signal-to-noise imaging, i' dropouts can be safely identified through detection in a single redder band ie. z'. Using ultra-deep i' and z' imaging of the Chandra Deep Field South and Hubble Deep Field North, taken with the ACS camera on the Hubble Space Telescope, a handful of $z \sim 6$ LBGs have been identified (Bouwens et al. 2003a; Dickinson et al. 2003; Stanway, Bunker & McMahon 2003). All groups find fewer candidates than would be expected if the $z \sim 6$ luminosity function for LBGs were the same as the $z \sim 3$ Lyman break luminosity function. The preferred estimate for the rest-frame UV luminosity density and star formation rate density, however, implies only a 20-40% drop from $z \sim 3$ to $z \sim 6$.

Figure 1.9 (taken from Bouwens et al. 2003a) summarises the history of the star formation rate density of the Universe. The assumed cosmology is $\Omega_{\rm M} = 0.3$, $\Omega_\Lambda = 0.7$ and $\rm H_0 = 70\,km\,s^{-1}\,Mpc^{-1}$. The low-redshift data points (open squares) are taken from Lilly et al. (1996) and mark a rise in the SFRD of an order of magnitude from $z = 0$ to $z = 1$, which is approximately midway between the values quoted from the various studies outlined in Section 1.4.1. The data points at $z > 1$ are taken from Madau et al. (1998) (open circles), Steidel et al. (1999) (crosses), Thompson et al. (2001) (open triangles) and Stanway, Bunker & McMahon (2003) (open pentagons). The solid red triangles are from Bouwens, Broadhurst & Illingworth (2003b), and the solid red circles are from Bouwens et al. (2003a). The lower solid red circle assumes no incompleteness correction and provides a reliable lower limit. The middle point is based on a generalization of the formalism used in Steidel et al. (1999). The upper point is based on the differential evolution from $z \sim 6$ to $z \sim 5$ and is linked to $z \sim 3$ using the results of Bouwens, Broadhurst & Illingworth (2003b). None of the data points shown have been corrected for extinction, although application of the Calzetti reddening law would raise the $z > 1$ data points by a factor of 2-3, thus implying an almost uniform star formation rate density over the redshift range $1 < z < 6$.

It is at this point where we must ask whether the optical observations are telling us the whole story. Firstly, we must address the question of whether the applied extinction corrections to known high-redshift objects are appropriate. Direct measurements of the submillimetre / millimetre emission (a direct tracer

of thermal dust emission in high redshift galaxies - see next subsection) of the strongly-lensed Lyman-break galaxies MS 1512+36-cB58 (van der Werf et al. 2001, Baker et al. 2001, Sawicki 2000) and MS 1358+62-G1 (van der Werf et al. 2001) imply that the standard procedure based on the correlation of the ultraviolet spectral index and the ratio of far-infrared to ultraviolet flux used to predict the sub-millimetre emission of the Lyman-break population over-predicts the observed 850 μm flux densities by a factor of up to 14. A recent X-ray detection of MS 1512+36-cB58 (Almaini, Pettini & Steidel in prep.) also supports the view that corrections for dust have been exaggerated, the level of X-ray emission implying a much lower SFR than that derived from the "dust-corrected" UV spectrum, but consistent with the measured 850 μm flux density, for a typical starburst SED.

Secondly, it is possible that there exists an entire population of heavily dust-enshrouded high redshift objects that have gone completely undetected in optical / UV surveys. Even if the most optimistic corrections for dust extinction are made in Lyman-break galaxies, the typical inferred star formation rates are only a few tens of solar masses per year. Given the evidence outlined in Section 1.2.2, the most massive elliptical galaxies appear to form the majority of their stars on timescales of $\sim$ 1 Gyr, requiring star formation rates of a few hundred to a few thousand solar masses per year. The star formation rates observed in Lyman break galaxies fall short of this value by 1-2 orders of magnitude, suggesting they are young intermediate mass galaxies rather than the most massive ellipticals. Furthermore, since it is the most massive ellipticals which undergo the most vigorous starburst, one would expect huge quantities of dust to be produced, supporting the idea that the optical / UV emission from the young stars is almost completely absorbed in the progenitors of the most massive spheroids.

1.5 Thermal Dust Emission and the Submm Waveband

Once the dust has been heated to equilibrium temperature by the incident radiation field, it re-emits the aborbed radiation in the far-infrared (FIR) waveband. The emission is thermal and is normally described by greybody emission, essentially a blackbody spectrum modified by the wavelength dependence of the dust grains. For an isothermal source with dust temperature T_d, the rest frame flux

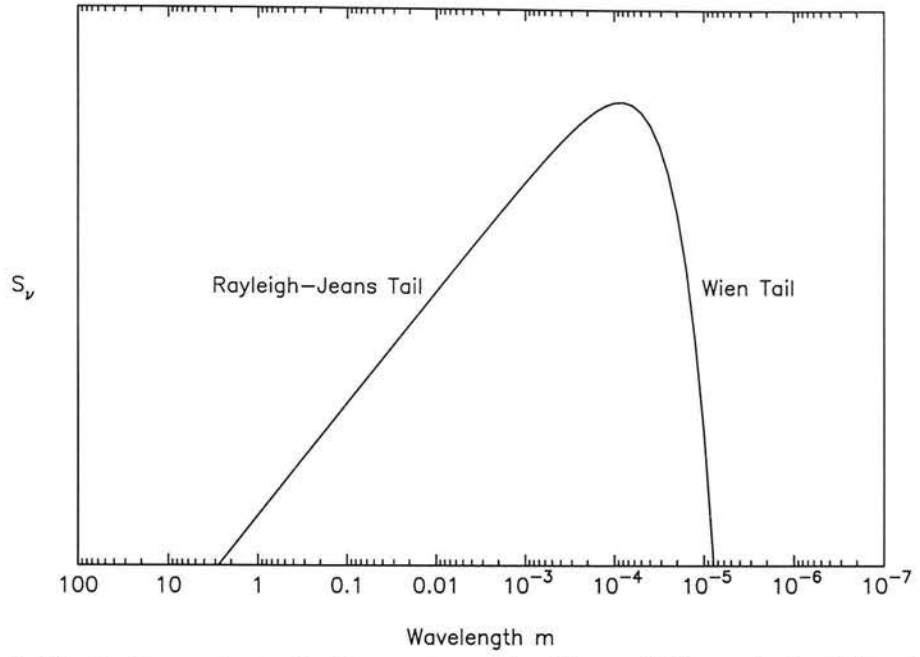

Figure 1.10: Isothermal greybody spectrum for $T_d = 40\,K$, typical of the dust temperatures of local starburst galaxies.

density takes the form

$$S_\nu = \frac{2\Omega h\nu^3}{c^2} \frac{(1 - e^{-\tau})}{(e^{\frac{h\nu}{kT_d}} - 1)} \tag{1.18}$$

where ν is the frequency at which the radiation is emitted, Ω is the solid angle of the source, h, k, and c are the Planck, Boltzmann and speed of light constants repectively, and τ is the optical depth of the source given by

$$\tau = \left(\frac{\nu}{\nu_0}\right)^\beta \tag{1.19}$$

where ν_0 is the wavelength at which the source becomes optically thick, and β is the strength of the wavelength dependence of the grain emissivity, generally taken to lie in the range $1 < \beta < 2$.

If the dust can be considered to be optically thin (ie. $\nu << \nu_0$) as is generally true at millimetre and submillimetre wavelengths, this expression simplifies to

$$S_\nu = \frac{2\Omega h}{c^2 \nu_0^\beta} \frac{\nu^{3+\beta}}{(e^{\frac{h\nu}{kT_d}} - 1)} \tag{1.20}$$

The spectrum turns over at a wavelength λ_{max} given by the Wien displacement law such that

$$\lambda_{max}(\mu m) = 2900/T_d(K) \tag{1.21}$$

For $\lambda < \lambda_{\rm max}$ the spectrum falls off exponentially on the Wien tail. For $\lambda > \lambda_{\rm max}$ the spectrum falls off as a steep power law on the Rayleigh-Jeans tail, asymptoting to $\nu^{2+\beta}$.

Surveys of local galaxies, such as the "SCUBA Local Universe Survey (SLUGS)" (Dunne et al. 2000a), have shown that dust temperatures in local star-forming galaxies eg. Arp 220 are typically $T_d \simeq 40\,K$. An example of a thermal dust emission spectrum for $T_d = 40\,K$ in the source's rest-frame is shown in Figure 1.10. The spectrum peaks in the far-infrared at $\lambda_{\rm max} \simeq 100\,\mu m$.

At high redshifts ($z \sim 1$) the strongly peaked FIR radiation emitted by the dust in star-formation regions of distant galaxies is redshifted into the submillimetre waveband. Furthermore, the steep spectral index of the thermal emission longwards of the peak at $\lambda \simeq 100\ \mu m$ results in a sufficiently large negative K-correction that the dimming effect of increasing cosmological distance is effectively cancelled over a wide range in redshift. Consequently, for a galaxy with fixed intrinsic FIR luminosity, we would expect to observe approximately the same 850 μm flux density for an object at $z = 8$ as at $z = 1$. The strength of this effect is obviously dependent on the assumed cosmology, as demonstrated in Figure 1.11 for an Arp 220 type galaxy with a SFR of $\simeq 300\,M_\odot yr^{-1}$. It is most pronounced in an Einstein-de Sitter universe (red-solid), in which the predicted flux density of an object of fixed luminosity actually increases slightly beyond $z \simeq 1$. If instead we adopt $\Omega_M = 0.3$, $\Omega_\Lambda = 0.7$, a very gentle decline in flux density is predicted over this same redshift range (blue-solid). At $450\,\mu m$, a similar but less pronounced effect may be seen (dashed red and blue lines for an Einstein de Sitter and $\Omega_M = 0.3$, $\Omega_\Lambda = 0.7$ cosmology respectively).

If one were to assume a different spectral energy distribution to that of Arp 220 eg. altering the values of the dust temperature and emissivity the following effects would be apparent on the observed flux density of a source with redshift:

- Increasing β increases the strength of the negative K-correction.
- Increasing T_d shifts the spectral peak to higher frequencies, allowing the K-correction to counteract the cosmological dimming over a larger range of redshift.
- If the spectrum were to become optically thick at $\sim 200\,\mu m$, the observed flux density would increase but continue to be almost independent of redshift for $z > 1$.

The mass of dust present in an object can be estimated directly from the submillimetre flux density if the following assumptions are made:

1) The dust is optically thin to submillimetre radiation.

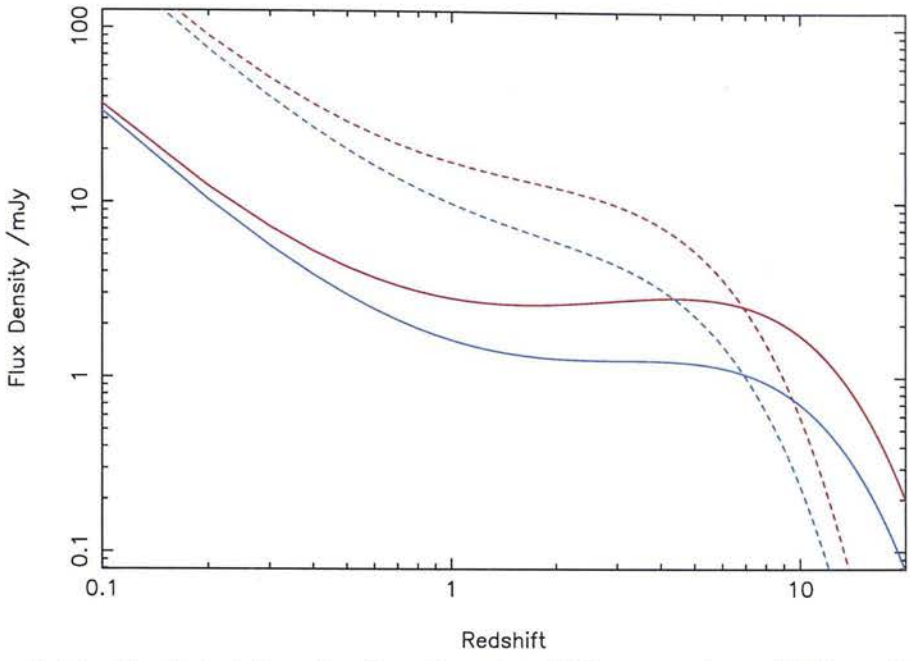

Figure 1.11: Predicted flux density of an Arp 220 type galaxy (SFR $\simeq 300\,M_{\odot}yr^{-1}$) at 850 μm (solid) and 450 μm (dashed). The red lines represent an Einstein de Sitter cosmology, whereas the blue lines represent an $\Omega_M = 0.3$, $\Omega_\Lambda = 0.7$ cosmology.

2) The dust grains radiate as an isothermal black body.

3) There is a single grain type.

4) The dust grains are spherical.

5) The dust is heated only by internal processes.

Assuming local thermodynamic equilibrium, one can write the emission from a single grain as:

$$f_{\nu_{rest}} = \Omega_{grain} Q_{\nu_{rest}} B_{\nu_{rest}}(T_d) \tag{1.22}$$

where $f_{\nu_{rest}}$ is the flux density contribution of a single grain at frequency ν_{rest}, Ω_{grain} is the solid angle of the dust grain as viewed along the line of sight, $Q_{\nu_{rest}}$ is the emissivity of the dust grain at ν_{rest}, and $B_{\nu_{rest}}(T_d)$ is the intensity of emission, in this case given by the blackbody function

$$B_{\nu_{rest}}(T_d) = \frac{2h}{c^2} \frac{\nu_{rest}^3}{(e^{\frac{h\nu_{rest}}{kT_d}} - 1)} \tag{1.23}$$

The size of the grain is much smaller than the distance to the dust cloud and so

$$\Omega_{grain} = \frac{\pi a^2}{D^2} \tag{1.24}$$

where a is the radius of the dust grain and D is the effective distance to the dust

cloud given by

$$D = \frac{c}{H_0} \int_0^{z_1} \frac{dz}{\sqrt{(1+z)^2(\Omega_M z + 1) - z(z+2)\Omega_\Lambda}} \tag{1.25}$$

for a source at redshift z_1 in a flat Universe.

Since the dust cloud is assumed to be optically thin, the total flux density $F_{\nu_{rest}}$ emitted by a cloud containing N dust grains is simply

$$F_{\nu_{rest}} = N f_{\nu_{rest}} \tag{1.26}$$

For a single grain type, the total mass of the dust cloud M_d is simply the number of grains multiplied by the mass of a single dust grain m_{grain}.

$$M_d = N m_{grain} \tag{1.27}$$

The observed flux density S_{obs} is related to the emitted flux density by

$$S_{obs} = \frac{F_{\nu_{rest}}}{(1+z)} \tag{1.28}$$

and the mass absorption coefficient κ_d is related to the emissivity by

$$\kappa_d(\nu) m_{grain} = Q_\nu \pi a^2 \tag{1.29}$$

Combining these equations, an estimate of the dust mass present is given by

$$M_d = \frac{S_{obs} D^2 (1+z)}{\kappa_d(\nu_{rest}) B_{\nu_{rest}}(T_d)} \tag{1.30}$$

The mass absorption coefficient $\kappa_d(\nu)$ varies with wavelength as $\lambda^{-\beta}$ where β is the dust emissivity index.

In fact, if one is using 850 μm observations to estimate the mass of dust in an object at $z > 1$, the very weak dependence of observed 850 μm flux density on redshift for a source of fixed intrinsic luminosity means that the measured flux density correlates almost linearly with the amount of dust present.

1.6 Global Star Formation History - II. A Submillimetre Perspective

Locally, all powerful radio sources reside in massive elliptical hosts, and so it would therefore seem natural to assume that high redshift radio galaxies are

younger versions of these local systems. Sub-millimetre detections of the $z \simeq 4$ radio galaxies 4C41.17 (Dunlop et al. 1994, Hughes, Dunlop & Rawlings 1997) and 8C1435+635 (Ivison 1995, Ivison et al. 1998) confirm that the Lyman-break population does not tell the full story. These extreme radio galaxies display the properties expected of youthful massive ellipticals, and have inferred dust masses $> 10^8 M_\odot$ and SFRs $> 1000\ M_\odot yr^{-1}$. Archibald et al. (2001) conducted the first major systematic submillimetre survey of 47 radio galaxies spanning the redshift range $1 < z < 5$, down to a consistent noise level of $\sigma_{850\,\mu m} = 1$ mJy. They found that the typical submillimetre luminosity (and hence dust mass) of a powerful radio galaxy was a strongly increasing function of redshift, the detection rate rising from $\simeq 15\%$ at $z < 2.5$ to $> 75\%$ at $z > 2.5$. If one assumes that the massive ellipticals housing powerful radio sources are typical of massive ellipticals in general this would imply that the bulk of star formation takes place at $z > 2.5$ and is highly obscured by large quantities of dust.

The total amount of optical / UV energy released from youthful stars and reprocessed into cool dust emission by the interstellar medium (ISM) may be constrained by the background detected at $\lambda > 150\,\mu$m (Puget et al. 1996, Schlegel, Finkbeiner & Davis 1998, Fixsen et al. 1998, Hauser et al. 1998). Since the advent of SCUBA, the Sub-millimetre Common User Bolometer Array, on the James Clerk Maxwell Telescope (JCMT) in Hawaii (Holland et al. 1999), a series of complementary deep 850 μm surveys (eg. Smail et al. 1997, Hughes et al. 1998, Barger et al. 1998, Barger, Cowie & Sanders 1999, Blain et al. 1999, Eales et al. 2000, Scott et al. 2002, Borys et al. 2002, Cowie et al. 2002, Webb et al. 2003a,) have successfully resolved the bulk of the far-infrared (FIR) extragalactic background into discrete sources, revealing a population of heavily dust-enshrouded high-redshift galaxies undergoing an intense period of massive star-forming activity. These surveys vary in size and depth from ultra-deep surveys exploiting gravitational lensing from intervening clusters to study the very faintest submm sources (Smail et al. 1997, Cowie et al. 2002), small and deep blank field surveys such as the HDF (6 sq. arcmin to a uniform noise level of $1\sigma_{\rm rms} \simeq 0.5$ mJy/beam; Hughes et al. 1998, Serjeant et al. 2002), through to moderate area and comparatively shallower blank field surveys such as the "SCUBA 8-mJy Survey" (a total of 250 sq. arcmin to a uniform noise level of $1\sigma_{\rm rms} \simeq 2.5$ mJy/beam; Scott et al. 2002). These sources, are believed to be analogous to the local ultraluminous infrared galaxies (ULIRGs) and undergoing a period of massive star-formation at rates of $10^2 - 10^3\,M_\odot yr^{-1}$. These submillimetre surveys have implied a star

formation rate up to an order of magnitude higher than that originally deduced from optical / UV data at high redshift.

1.7 Aim and Outline of this Thesis

The aim of this thesis is to present an unbiased study of the nature of bright 850 μm sources uncovered in blank field SCUBA surveys. In particular, the redshifted submillimetre thermal dust emision is used to estimate star formation rates and dust masses, and statistical properties such as source counts, clustering and co-moving number densities are used to investigate the link between the bright (> 5 mJy) submillimetre population and present-day massive elliptical galaxies.

Chapter 2 provides a detailed description of submillimetre observing, and data reduction, as well as a new source extraction algorithm based on a simultaneous maximum-likelihood fit to all the potential sources in the maps.

Chapter 3 presents results from extensive simulations which have been used to quantify completeness, the ratio of retrieved-to-input flux densities, positional uncertainties and the level of likely contamination form spurious /confused sources for every 850 μm survey field used in this thesis. These Monte-Carlo simulations fell into two different categories: a one-in, one-out technique where an individual source was added into the existing data and then retrieved using the source extraction algorithm, repeated many times, and also fully simulated realisations of the datasets based on a consistent number counts model.

Chapter 4 presents results from the 'SCUBA 8 mJy Survey', a wider-area, somewhat shallower survey than its earlier counterparts undertaken with the aim of constraining the brighter end of the 850 μm source counts in the region of 8 mJy. The almost linear correlation between the measured 850 μm flux density and intrinsic luminosity of sources lying in the redshift range $1 < z < 8$ is used to estimate star formation rates and dust masses. Source counts, clustering properties and co-moving number densities are used to place constraints on the formation and evolution of present-day massive elliptical galaxies.

In Chapter 5, existing submillimetre data from the blank field surveys of the Canada-France Redshift Survey Fields, Hawaii Flanking Fields and Hubble Deep Field are re-reduced in the same way as the '8 mJy Survey' observations and the new source lists compared with those published previously. All of the blank field datasets are then combined with the '8 mJy Survey' and clustering properties based on this larger source catalogue are re-addressed by means of 2-point angular

correlation functions and nearest-neighbour analyses. The most accurate 850 μm source counts are presented and compared with a variety of simple models.

Chapter 6 provides a summary of the key results from earlier chapters. It closes with a discussion of a major new blank field submillimetre survey currently in progress at the JCMT, motivated largely by the results presented in this thesis with the aim of addressing some of the remaining questions regarding the star formation history of the Universe and the clustering properties of bright SCUBA sources.

Two cosmologies have been adopted throughout this thesis; $\Omega_{\rm M} = 1.0$, $\Omega_{\Lambda} = 0.0$ (Einstein-de-Sitter cosmolgy) for easy comparisons with earlier publications, and $\Omega_{\rm M} = 0.3$, $\Omega_{\Lambda} = 0.7$ in line with the most recent cosmological parameter results from the supernova cosmology project (Perlmutter et al. 1999), X-ray clusters (Allen, Schmidt & Fabian 2002a, 2002b), and WMAP observations of the cosmic microwave background (Spergel et al. 2003). A value of $H_0 = 67\,{\rm km\,s^{-1}\,Mpc^{-1}}$ was assumed throughout.

Chapter 2

Observations, Data Reduction and Source Extraction

This Chapter describes the techniques used in submillimetre observing, as well as data reduction and source extraction methods. Section 2.1 gives a short description of the SCUBA instrument, the submillimetre continuum camera mounted on the JCMT in Hawaii which was used to take all of the observations described in subsequent chapters. In Section 2.2, the mapping technique known as "jiggle-mapping" is explained. Section 2.3 outlines the problems faced by submillimetre observing due to the Earth's atmosphere, and how these effects are compensated for in the observation and data reduction processes. Two independently designed data reduction pipelines are discussed and compared in Section 2.4, and lastly in Section 2.5 a new source extraction algorithm is presented which is able to provide a simultaneous maximum-likelihood fit to every peak in the images, thus partially accounting for source confusion.

2.1 The JCMT and SCUBA - a brief overview

The James Clerk Maxwell Telescope (JCMT) is a 15m Cassegrain telescope with an alt-azimuth mounting, located at a high dry site near the summit of Mauna Kea in Hawaii, and dedicated to observing at submillimetre wavelengths. Mounted on a Nasmyth platform at the telescope is a submillimetre continuum array receiver - the Submillimetre Common User Bolometer Array (SCUBA) (Holland et al 1999). SCUBA consists of two bolometer arrays, both of which are arranged in a close packed hexagon and have approximately a 2.3 arcminute field of view (slightly smaller on the short-wavelength array). The diffraction- limited beam sizes delivered by the JCMT have a full width at half maximum (FWHM) of

14.5 arcseconds at 850 μm and 7.5 arcseconds at 450 μm, and the bolometer feedhorns on the arrays are sized for optimal coupling to the respective beams. As a result, the long wavelength (LW) array consists of 37 bolometers, and the short-wavelength (SW) array consists of 91 bolometers. Observations may be made simultaneously with both arrays by means of a dichroic beamsplitter. SCUBA may also be used to undertake observations with a LW/SW combination of 750 and 350 μm respectively (when the filter wheel is in good repair). In addition there are three lone larger bolometers located at the edge of the LW array allowing photometry observations at 2 mm, 1.35 mm and 1.1 mm to be carried out. A ^{3}He / ^{4}He dilution refrigerator cools SCUBA down to $\sim$ 90mK, making the array background limited and not noise dominated from the detector itself. When using a cold load (specifically a reflector in front of the cryostat entrance window) to measure the basic system noise, the typical bolometer root-mean-square (rms) noise levels are in the range 40 – 50 nV, although it is not unusual for several bolometers to have rms noise levels over 100 nV, particularly those in the outer rings of the arrays.

2.2 Jiggle-mapping

There are two mapping techniques available on the JCMT; scan mapping and jiggle mapping. Both mapping modes have comparable observational efficiency at present. Jiggle-mapping is simpler and much better characterised than scan-mapping, and it is this observational method employed in the vast majority of deep SCUBA surveys which will be described here.

The arrangement of the bolometers means that at any instant observations of the sky are under-sampled. In order to obtain a fully sampled image, the gaps between the bolometers are filled-in by means of a series of 1 second exposures offset from one another in a hexagonal pattern. This offsetting is achieved by "jiggling" the secondary mirror. A 16-point jiggle-pattern is required if only the LW data is needed, whereas if data from both arrays is to be collected simultaneaously a 64-point pattern is required to fully sample the sky. The factor of four arises due to the fact that the size / spacing of the SW array feedhorns is smaller than on the LW array, and it is necessary to fill-in the gaps on the LW array at the resolution of the SW array.

Although data is taken at a rate of 128 Hz at the JCMT it is only actually recorded as a 1 second average. One jiggle-map "integration" corresponds to the

time taken to integrate for 1 second at each of the 64 jiggle positions, in both the positive and negative beams ie. 128 seconds. Overheads arising from chopping and nodding (see 2.3.1) mean that the actual amount of time required to execute this observation is about 1/3 as much again ie. ~ 171 seconds.

The current sensitivities of the arrays, give by the noise equivalent flux densities (NEFDs) are:

- 1400 mJyHz$^{-1/2}$ at 450 μm
- 90 mJyHz$^{-1/2}$ at 850 μm

2.3 Effects of the Earth's Atmosphere

The Earth's atmosphere has two important effects on the signal from a source. Firstly, the atmosphere and immediate surroundings of the telescope and observatory emit thermal radiation several orders of magnitude larger than the source signal (see 2.3.1). Secondly, the atmosphere is only partially transparent at submillimetre wavelengths and hence the source signal is attenuated (see 2.3.2).

2.3.1 Sky Subtraction - Chopping and Nodding

The sky emission varies with the wavelength being observed, both temporally and spatially, and completely overwhelms the source signal. The techniques applied to remove the background radiation are known as chopping and nodding. Together they are able to remove the bulk sky emission and diminish the variations in it.

• **Chopping.** The action of chopping is to tilt the secondary mirror back and forth so that alternately the source and a region of sky a specified distance away are brought into view. The measured sky signal is then subtracted from the source signal. The distance between the source and the reference region of sky is known as the chop throw, and should ideally be kept as small as possible otherwise poor sky cancellation and large beam shape distortions may result. It is important to chop faster than the rate at which the sky varies, although some compromise must be made between reliability, performance and vibrational noise induced; the standard chopping frequency is 7.8 Hz.

• **Nodding.** If the sky emission were spatially uniform then the act of chopping

alone should be sufficient, in theory, to recover the actual source flux. Gradual increases/decreases in sky brightness i.e. gradients in the sky emission, however, are not uncommon. Under such circumstances chopping on one region of sky only would lead to an over/under estimate of the actual source flux. In order to compensate for linear sky gradients the telescope also nods periodically. That is to say, the primary mirror now moves into an 'off' position where the source and a new region of sky, located the same distance away from the source, along a line joining all three sky areas, effectively trade roles. In the 'off' position the source is in the negative beam, and it is now the source signal subtracted from the sky emission that is recorded - a negative jiggle-map of the source is produced.

The action of nodding has the additional benefit of cancelling any asymmetries in the telescope environment. For example, since the internal electronics deal with the two beams separately, any electronic biasing effects are removed.

To move the primary 15m dish of the JCMT at a comparable rate to the chopping is highly impractical. Instead the telescope nods every 16 seconds in jiggle-map mode. In the case of a 16-point jiggle-map this is once every complete jiggle-sampling. For a 64-point jiggle-map, it is split into four Sections, each quadrant consisting of 16 jiggle positions. This rate was chosen as an optimal balance between observational overheads and the suppression of sky noise.

The overall consequence of chopping and nodding is that it can largely remove the thermal D.C. offset component of the sky emission and reduce the level of sky noise, although it is not able to entirely eradicate the quickly varying sky emission and gradients (although techniques in the data reduction can largely remove any residual - see Section 2.4.2).

The action of chopping and nodding leads to a rather distinctive beam pattern. If one chop throw, small enough to fall on the SCUBA array (under $\sim$ 70 arcseconds), and fixed in RA coordinates is used to observe a source, then the positive image will be accompanied by two negative sidelobes, one on either side of the source, each of which is half as deep as the positive peak flux (see Fig. 2.1). Recovering the signal in these sidelobes is important for blank field surveys as it boosts the signal-to-noise of the recovered sources and helps discriminate between real and spurious detections.

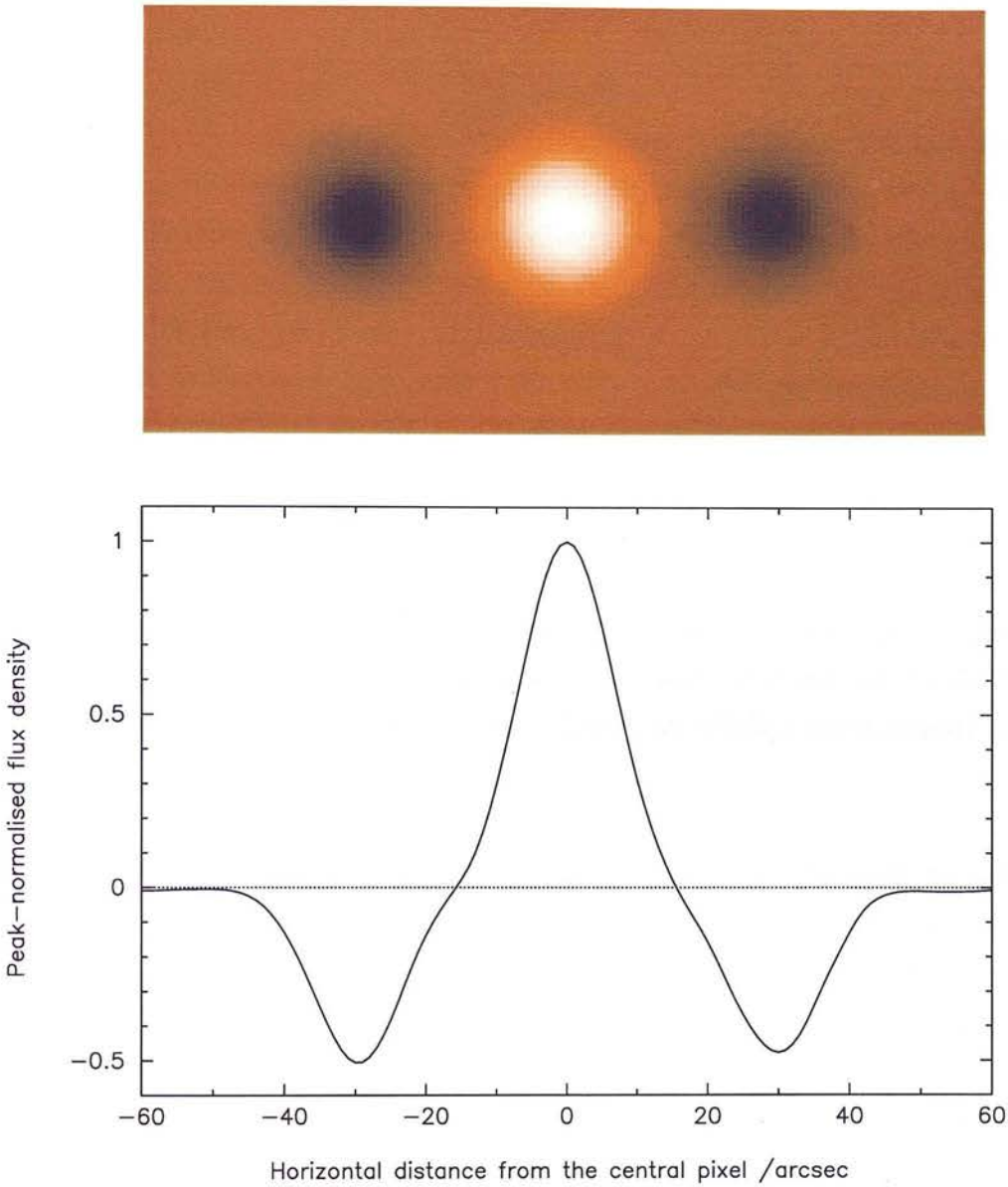

Figure 2.1: The peak-normalised beam profile of a source, observed with a 30 arcsecond chop throw, using a fixed position angle in the east-west direction.

2.3.2 Atmospheric Extinction

Atmospheric extinction reduces the observed source signal and must be accounted for when analysing the data recorded by the telescope. Assuming a plane parallel atmosphere,

$$V_0 = V_{meas} e^{\tau A} \tag{2.1}$$

where V_0 is the above atmosphere unattenuated signal, V_{meas} is the attenuated signal recorded at the telescope, A is the airmass(=cosec(angle of elevation)) and

τ is the zenith optical depth.

There are presently two methods with which the zenith sky opacity (τ) may be measured:

• **Skydip.** A skydip provides a direct measurement of the 850 and 450 μm opacities by measuring the sky brightness at different elevations. When performing a skydip SCUBA alternates between observing a hot load, the sky, and a cold load at each elevation. A chopper wheel in front of the cryostat entrance window has two blades (and two gaps), and is spun at a rate of $\sim$ 2 Hz. One of the blades is coated in Eccosorb and emits a blackbody at ambient temperature. The other blade is coated with a reflective surface so that the cryostat is seen by SCUBA. The temperature of the hot and cold loads may be measured, and adjusted to match the central wavelengths and bandwidths of the LW and SW filters. It is from these loads that the sky temperature may be calibrated. A model which describes both the system of optics and the atmosphere (assuming a plane parallel form) may be fitted to the data in order to determine the zenith sky opacity.

Given the observational overheads involved, skydips are normally only carried out every 1.5 - 2 hours.

• **Interpolation from $\tau_{225\mathrm{GHz}}$ measured at the Caltech Submillimetre Observatory (CSO).** The Caltech Submillimetre Observatory (next door to the JCMT) has an opacity meter recording the opacity at 225 GHz, at the CSO zenith, every 10mins (day and night). Although the individual observations taken with this device have a tendency to "spike" sometimes, Archibald et al. (2002a) have demonstrated that after smoothing the appropriate CSO data by means of polynomial fit, there is a well defined linear relation between the opacity at 225 GHz, and the opacities at 850 and 450 μm. This is currently the optimal method for measuring the atmospheric attenuation, and the relations are given below.

$$\tau_{850\mathrm{N}} = 3.96(\tau_{225\mathrm{GHz}} - 0.004) \tag{2.2}$$

$$\tau_{450\mathrm{N}} = 23.51(\tau_{225\mathrm{GHz}} - 0.012) \tag{2.3}$$

$$\tau_{850\mathrm{W}} = 4.17(\tau_{225\mathrm{GHz}} - 0.002) \tag{2.4}$$

$$\tau_{450\mathrm{W}} = 28.54(\tau_{225\mathrm{GHz}} - 0.015) \tag{2.5}$$

where the 'N' refers to the pre-upgrade narrow band filters, and the 'W' refers to the post-upgrade wideband filters, in use since October 1999.

2.4 Data Reduction

I have used two independent software packages to reduce SCUBA data in my thesis work: the SCUBA User Reduction Facility (SURF; Jenness et al. 1997), and an Interactive Data Language (IDL) based package, developed by Serjeant et al. (2003). The two mechanisms follow a very similar core reduction process, the main difference being in the techniques applied for deglitching and sky subtraction, and in the production of the final maps. Both data reduction procedures are discussed in detail here, however the IDL-based reduction routines were designed specifically with large jiggle-map surveys in mind and have an advantage that the noise levels in the final output images are much better characterised. This was therefore adopted as the primary method for data reduction and the results presented in subsequent chapters refer to data reduced by these IDL routines unless specifically stated otherwise. Much (but not all) of the "SCUBA 8 mJy Survey" map data has also been reduced using SURF.

2.4.1 Core Reduction

A basic reduction of the SCUBA jiggle-map data encompassed the following steps:

• **Combining the nods.** In order to take nodding into consideration, the off-position was subtracted from the on-position in the raw beam-switched data.

• **Flatfielding.** The relative sensitivities of the bolometers, with respect to a reference bolometer (the central bolometers H7 and C14, for the 850 and 450 μm arrays respectively) were accounted for by multiplying by the standard flatfield values.

• **Extinction Correction.** The atmospheric opacity was measured wherever possible using a 6th order polynomial fit to the CSO $\tau_{225\mathrm{GHz}}$, followed by a linear interpolation to 850 and 450 μm using the relations given in equations 2.2-2.5. On the occasions when the CSO opacity meter was out of service, or less than 7 reliable CSO observations were available within ± 1 hour of each observation, a linear interpolation between successive skydip values was used to determine $\tau_{850\mu\mathrm{m}}$ and $\tau_{450\mu\mathrm{m}}$. Equation 2.1 was then used to correct each jiggle for atmospheric attenuation.

2.4.2 Deglitching and Removal of Residual Sky Emission

The next steps in the data reduction process, are to remove spikes in the data resulting from cosmic-rays and bad bolometers, and to remove any residual sky emission. The two data reduction packages differ slightly in the techniques employed to do this, although the resulting improvements to the image quality are very similar.

In the case of SURF, the first deglitching step made use of the **scuclip** task. This routine considers each bolometer in turn, calculating the mean and removing any points lying more than $n\sigma$ from the mean. It is an iterative process, the mean being recalculated after each clip until no glitches remain. When considering the calibration data, the on-source bolometers jiggle on and off the source and therefore experience a large change in signal. Consequently only a 5σ clip was applied to the secondary / tertiary calibrators (see Section 2.4.3), and no clipping was applied to primary calibrators (Uranus or Mars) for fear of removing real source signal. A harder cut (5σ and then 3σ), however, was applied to the submm survey data, since this did not contain any sufficiently bright sources for real signal to be removed at this level.

Although the combination of chopping and nodding are largely able to compensate for slower-varying fluctuations in the submm sky, the practical limit to the rate at which the JCMT is able to nod means that there are still short-term temporal variations leaving residual sky-noise in the data. Jenness, Lightfoot & Holland (1998) developed a method of sky subtraction (employed in the SURF routine **remsky**) based on the fact that the scale size of the sky variations (> 1000 arcsec), are much larger than the size of the array ~ 140 arcsec. Consequently, the residual noise in the data is spatially correlated across the array, and is well approximated by calculating an average of all the bolometers observing sky for each jiggle, and subtracting this as a D.C. offset. In the survey data, the absence of any bright sources meant that all bolometers, with the exception of any showing abnormally high noise levels, were assumed to be observing sky emission.

The final SURF deglitching procedure used on the survey data was the **despike** routine, which was applied after the individual map data had been calibrated. The **despike** procedure compares points that lie within a cell of size one quarter of the beamwidth, removing any spikes lying $> n\sigma$ from the mean. A cut level of 3σ was again applied to the survey data. Prior to creating the final

maps, the **setbolwt** task was used to calculate the standard deviation on each of the bolometers, and for each jiggle-map to be combined in the final output. This assigned each bolometer a weight with reference to the central bolometer of the first input jiggle-map, thus allowing data from noisy bolometers to be down-weighted.

In the IDL reduction, deglitching and residual sky subtraction were undertaken by an iterative process, each iteration making a temporal noise estimate and deglitching, followed by a spatial sky subtraction. There were no bright sources in any of submm survey fields that would have been significantly detected in any single jigglemap, let alone in sub-dividing the data-stream into shorter timescale chunks and so the procedure was as follows:

- For each bolometer, noise estimates were made by fitting a Gaussian to the data-stream in chunks of 128 readout groups.
- These time dependent noise estimates were then used to remove any spikes by performing a 3σ clip on the data.
- Using the fits to all of the bolometers in the array, a modal residual sky level was determined for each of these 128 readout groups, and subtracted from this data.

With each consecutive iteration, the deglitching process makes a harder cut. Noisy bolometers were assigned a low inverse variance weight in this way. In the case of the calibration data, however, the presence of a bright source would likely lead to over-enthusiastic clipping of the data, and so in this case a timeline without object signal was constructed. This was created by calculating the mean of the timestream data points recorded immediately before and after the readout being considered, and subtracting this from the readout value.

2.4.3 Calibration

Each of the individual jiggle-maps comprising the submm survey data were calibrated prior to producing the final coadded images, in order to account for changes in the flux conversion factor (FCF) throughout the shift, and also to account for the mix of observations taken with the narrow-band (850N:450N) filters prior to October 1999, and the wider-band (850W:450W) filters since October 1999. The wide-band filters are more sensitive, resulting in lower flux conversion factors (typically 200 Jy/V/beam as compared with 240 Jy/V/beam at 850 μm, and 300

Jy/V/beam as compared with 700 Jy/V/beam at 450 μm).

There are currently two methods of calculating the FCF; the first of these calibrates on the peak flux density of a known calibration source in units of Jy/V/beam (ie. $FCF_{peak} = S_{beam}/V_{peak}$ where S_{beam} is the flux density contained within the beam, and V_{peak} is the measured peak voltage). The second method calibrates on the total flux density of a known calibration source contained within an aperture, in units of Jy/V/arcsec^2 (ie. $FCF_{aper} = S_{total}/(V_{int}A)$ where S_{total} is the total flux density of the calibration source, V_{int} is the integrated voltage within the aperture, and A is the area of the aperture).

Dunne & Eales (2001) and Jenness et al. (2002) have examined the issue of calibration errors in detail using the data from the "SCUBA Local Universe Galaxy Survey" (SLUGS), and an automated reduction of the extensive SCUBA calibration data stored in the Canadian Data Archive (CADC), respectively. Both groups found that the aperture calibration method generally produced more stable gains. For example, Dunne & Eales (2001) found that at 850 μm the standard deviation in the FCF determined using a 45 arcsecond aperture corresponded to an accuracy of 6%, compared with 8% when using peak FCFs. They found that this was more marked at 450 μm where the comparable accuracies were 9% and 18% for a 45 arcsecond aperture FCF and peak FCF respectively. In comparison, at 850 μm Jenness et al. (2002) found accuracies of 11% and 12% for a 40 arcsecond FCF and peak FCF using the narrow-band filter, and 5% and 6% for the wide-band filter. At 450 μm, Jenness et al. reported accuracies of 22% and 30% for a 40 arcsecond aperture FCF and peak FCF using the narrow-band filter, and 16% and 24% for the wide-band filter. The peak FCFs are less accurate than the aperture FCFs because the peak flux density measurements are sensitive to changes in the beam shape due to sky noise, pointing drifts, chop throw, and in particular the shape of the dish. This in turn translates through to variations in the determined flux conversion factors, particularly at 450 μm.

The IDL pipeline does, however, have the considerable advantage of producing accurate noise maps with uncorrelated pixels (see Section 2.4.5), which has allowed me to develop a maximum-likelihood method to measure the statistical significance of each peak in an image (see Section 2.5). The source-extraction algorthim provides a simultaneous fit to all peaks in the image, and is therefore able to decouple any partially-confused sources whilst still recovering the additional signal-to-noise yielded by the negative sidelobes. The resulting best-fit model therefore allows the flux densities of any significant detections ($> 3.00\sigma$) to be

measured directly, as well as yielding properly-quantified errors on this value. At 850 μm the accuracy gained by this approach more than compensates for the extra $\sim 1-2\%$ error in the calibration and the datasets when calibrated using a FCF system based on fitting to the peak values as opposed to the aperture method. For consistency, the same approach was adopted when considering the SW data.

In order to calibrate the data, each shift was divided in two and all available information was utilised to calculate the mean FCFs applicable to each half-shift by fitting to the calibrator peaks. Uranus and Mars were observed as primary calibrators when available, with the planetary flux densities taken from the JCMT FLUXES program. Additionally, the secondary calibrators CRL618, OH231.8, CRL2688 and IRC10216 were used. Since IRC10216 is variable with a period of 635 days, it was assumed to have constant flux density over an 8/9 night observing run, calculated using all other calibration data for that run. Beam maps of the pointing sources were used for tertiary calibration. The same chop-throw was used for observing both the survey areas and the calibrators, in order to cancel out the effects of beam distortion as far as possible. Recent work undertaken by Jenness et al. (2002), carried out since the submm survey datasets were fully reduced and analysed, has refined the accuracies of the flux densities and morphologies of the secondary calibrators used frequently at the JCMT, including an accurate 850 μm light curve for IRC10216. My calculated peak flux densities for IRC10216 agree well with the predicted flux density contained in the beam based on this light curve and the deconvolved size of the source, and also agree very well with earlier work undertaken by Sandell (1994). The exception is OH231.8 which was found to be variable by about 25%, and with a period of 630 days. This calibrator was used in determining the gains for only a small percentage of half-shifts and was always combined with other calibration information. In addition, the surveys affected by the discovery of variability in this calibrator were built up by many overlapping jiggle-maps, reducing any additional level of error introduced into the calibration. Taking into account the errors on the calibrator flux densities, the variation in the flux-conversion factor over half a shift, and errors in the measured atmospheric opacity, the average calibration error over the survey maps was found to be 10% at 850 μm, and 20% at 450 μm.

2.4.4 Pointing Problems

Over the period during which survey data were collected, three different pointing problems are now known to have afflicted the JCMT.

Firstly, prior to 28th July 1998, a bug in the chopping software of SCUBA meant that the chop direction was not updated once an observation had begun, and consequently the negative sidelobes accompanying a source in this data set will appear smeared and therefore shallower than expected. The effect however is small when compared to the sky noise and the length of an observation (never more than 1hr for any of the surveys), and affects only a small portion of the data collected.

Secondly, some of the jiggle-maps taken since June 1999 may have been affected by an elevation drive pointing glitch (Coulson 2000). Some observations appeared to suffer a 4 arcsecond jump in elevation when passing through transit. Additionally, pointing on the opposite side of the meridian to the survey field may have introduced a similar effect, of order 1.5-2 arcseconds in magnitude, since by pointing on the opposite side of the meridian the direction of the telescope drive is reversed on moving from the pointing source to the survey field. The fact that each area of sky is covered by several individual jiggle-maps significantly reduces the likelihood of a large increase in positional uncertainty and source smearing. It is not really possible to correct for this problem when conducting deep extragalactic blank field surveys such as these because:

1) The size and positioning of the jump in elevation were found to be non-constant.

2) None of the individual jiggle-maps contained any sources bright enough to be significantly detected, and hence could not be examined to see whether a jump in the elevation drive near transit had actually taken place.

3) When pointing in between sets of observations, it was not clear that slightly larger than average apparent pointing drifts (4-5 arcseconds as opposed to $<$ 3 arcseconds) hadn't in fact been introduced at the last minute by the action of returning to the pointing source.

Perhaps reassuringly, an examinination of which maps may have been affected in the "SCUBA 8 mJy Survey" under the most pessimistic assumptions, showed that a maximum of 15% of the overall data may have been affected by this pointing problem, and in any one region of sky no more than 25% of the jiggle-maps regridded would have been susceptible to pointing jumps.

Finally, data taken between the 15th July 1999 and 23rd May 2000, were affected by a non-synchronization of the GPS and SCUBA data acquisition computer clocks, leading to an incorrect time being stored in the data headers and hence causing the reduced jiggle-maps to appear rotated when regridded with respect to the actual observations. This problem has been corrected for in the data reduction by resurrecting the **scuba2mem** SURF routine (and an IDL reduction equivalent) to obtain the correct astrometry (Jenness 2000).

2.4.5 Producing the final images

To construct the final images in SURF, the task **rebin** outputs the reduced data onto a rectangular mesh, using a variety of methods. These methods use either a convolution with a linear, Bessel or Gaussian weighting function, or a spline interpolation and smoothing routine. The bolometer weights output from **setbolwt** noise-weight the final signal image.

In the IDL reduction, the final images were produced using an optimal noise-weighted drizzling algorithm (Fruchter & Hook, 2002) with a pixel size of 1 square arcsecond. Both output signal and noise maps were created, the signal in any one square-arcsecond pixel given by the noise-weighted average of the bolometer readouts at that position, and the corresponding noise value given by a noise-weighted average of the Gaussian fits to the readout histograms. Unlike a standard shift-and-add technique which takes the flux density in each detector pixel and places it into the final map over an area equivalent to one detector pixel projected on the sky, drizzling takes the flux density and places it into a smaller area in the final map. Although this almost minimises the signal-to-noise ratio in each pixel, simulations have shown that this helps preserve information on small angular scales, provided that there are enough observations to fill in the resulting gaps. The area in the coadded map receiving the flux from one detector pixel is termed the *footprint*. This method is an extreme example of drizzling; one takes the data from each 14.5 arcsecond bolometer and puts the flux density into a very small footprint (termed the 'zero-footprint'), one arcsecond square. Unlike in the standard SURF reduction, there is no intrinsic smoothing or interpolation between neighbouring pixels in this rebin procedure. Although there is some degree of correlation between pixels in the output zero-footprint *signal* maps in terms of the beam pattern, the corresponding pixel *noise* values represent individual measurements of the temporally varying sky noise averaged over the dataset integration

time, at a specific point on the sky, and are hence statistically independent from their neighbours. In essence this method produces a very oversampled image with statistically independent pixels. Statistical non-independence would refer to pixel-to-pixel crosstalk, which is not the case here. A final 4σ-clip on the signal-to-noise was carried out to remove any remaining 'hot pixels'. A noise-weighted convolution with a beam-sized Gaussian point spread function (PSF) produces realistic smoothed maps of the survey areas and is able to account for variable signal-to-noise between individual pixels.

Figures 2.2 - 2.9 show the examples of zero-footprint signal and noise images, and the corresponding noise-weighted Gaussian-convolved signal and noise images for two of the survey fields; the Lockman Hole East taken from the "SCUBA 8-mJy survey" and the Hubble Deep Field. These correspond to the shallowest and deepest of the submillimetre surveys analysed in this thesis respectively, and have been displayed with the minimum and maximum levels as given by a 95% auto-cut in the GAIA image analysis tool for clarity (specific values given in the figure captions). Note, when visually comparing the Lockman Hole and Hubble Deep Field images that the displayed dimensions on the page are not to scale - the Lockman Hole East has c. 130 square arcminutes of SCUBA data, whereas the Hubble Deep Field has only 6 square arcminutes of SCUBA data. In both fields, the unconvolved and convolved noise images show the increased noise levels in the areas towards the edge which have not been fully sampled. The deep strip of the Lockman Hole which saw roughly twice the integration time of the rest of the field is also clearly visible. In terms of the signal data, the two most significant Hubble Deep Field sources which are clearly visible in the smoothed image, are also just visible in the unconvolved signal map. The "speckling" in the edge regions of the smoothed images is simply a result of incomplete integration time here, and shows that quite a number of pixels in these regions contain no data. Further analysis of these fields may be found in Chapters 4 and 5.

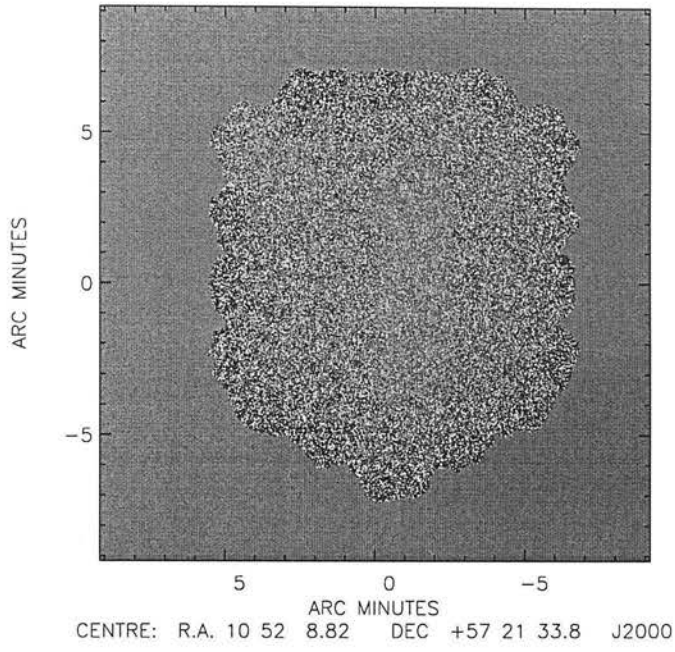

Figure 2.2: Zero-footprint signal map of the Lockman Hole East from the "SCUBA 8mJy Survey". Display levels are the 95% auto-cut levels from the GAIA image analysis tool (-82.8 - 89.1 mJy).

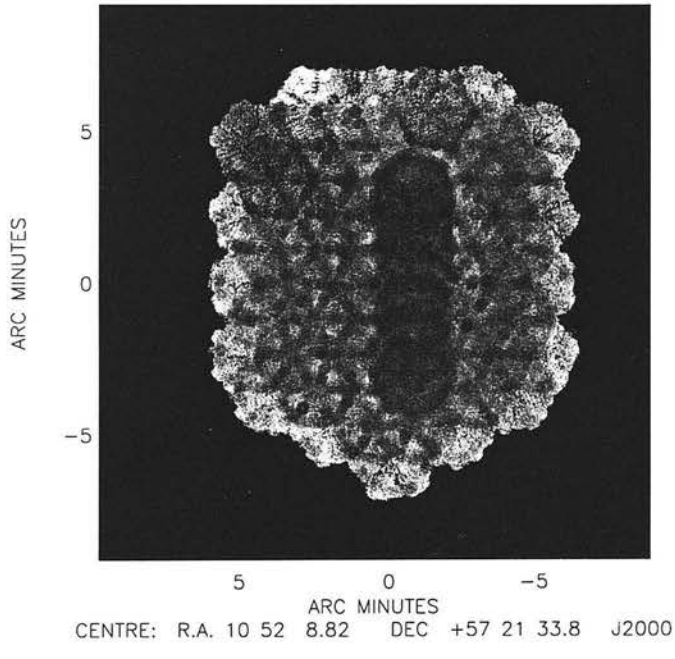

Figure 2.3: Zero-footprint noise map of the Lockman Hole East from the "SCUBA 8mJy Survey". Display levels are the 95% auto-cut levels from the GAIA image analysis tool (0.0 - 113.1 mJy).

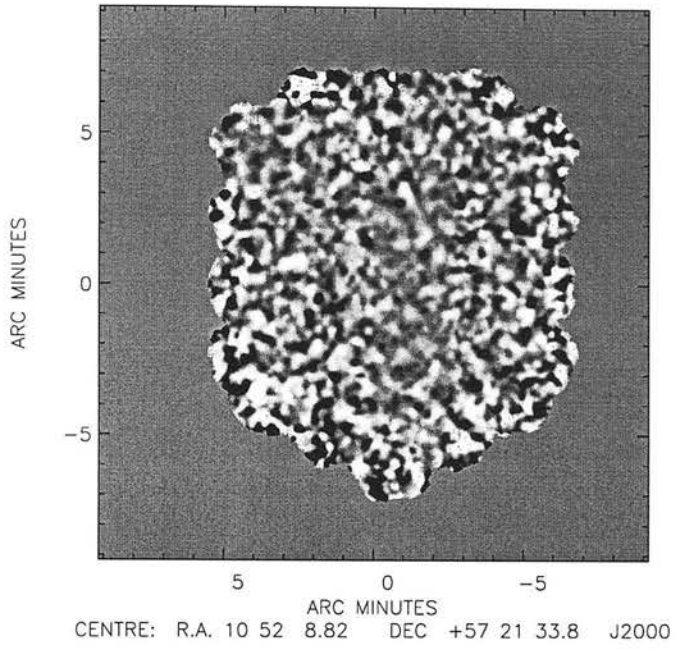

Figure 2.4: Gaussian-convolved signal map of the Lockman Hole East from the "SCUBA 8mJy Survey". Display levels are the 95% auto-cut levels from the GAIA image analysis tool (-7.5 - 7.8 mJy).

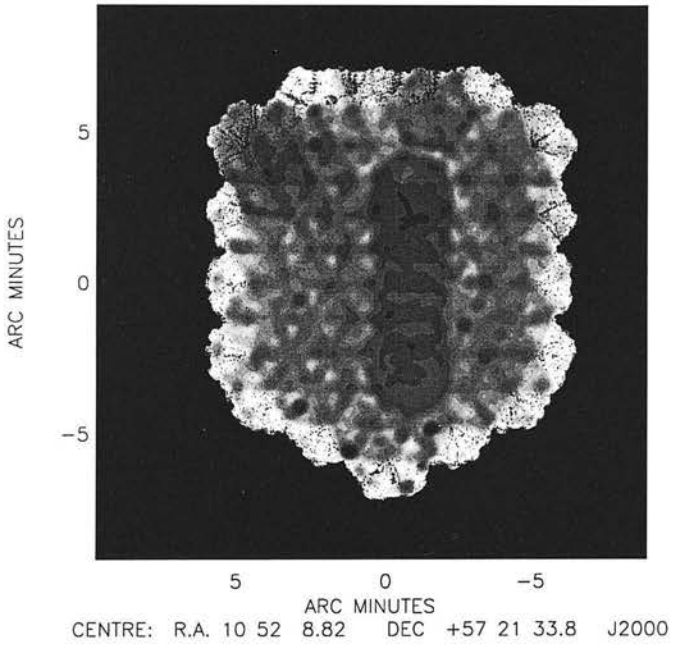

Figure 2.5: Gaussian-convolved noise map of the Lockman Hole East from the "SCUBA 8mJy Survey". Display levels are the 95% auto-cut levels from the GAIA image analysis tool (0.0 - 7.1 mJy).

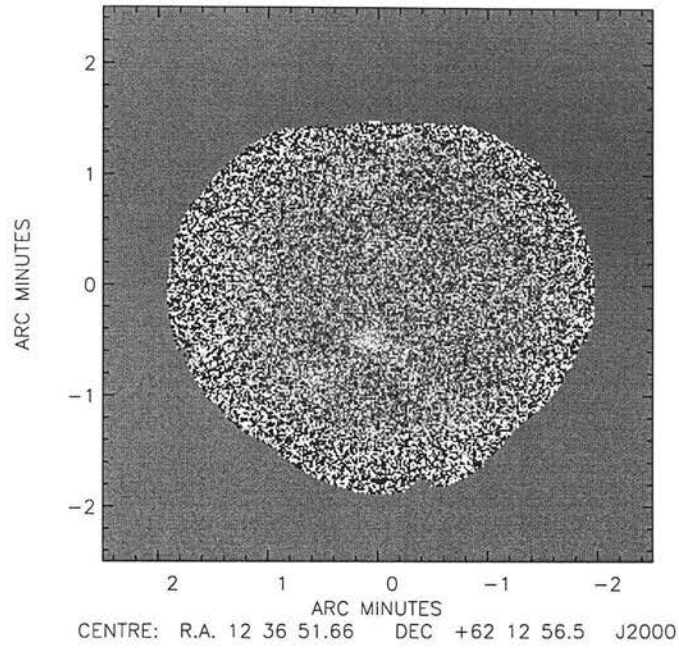

Figure 2.6: Zero-footprint signal map of the Hubble Deep Field. Display levels are the 95% auto-cut levels from the GAIA image analysis tool (-21.8 - 22.1 mJy).

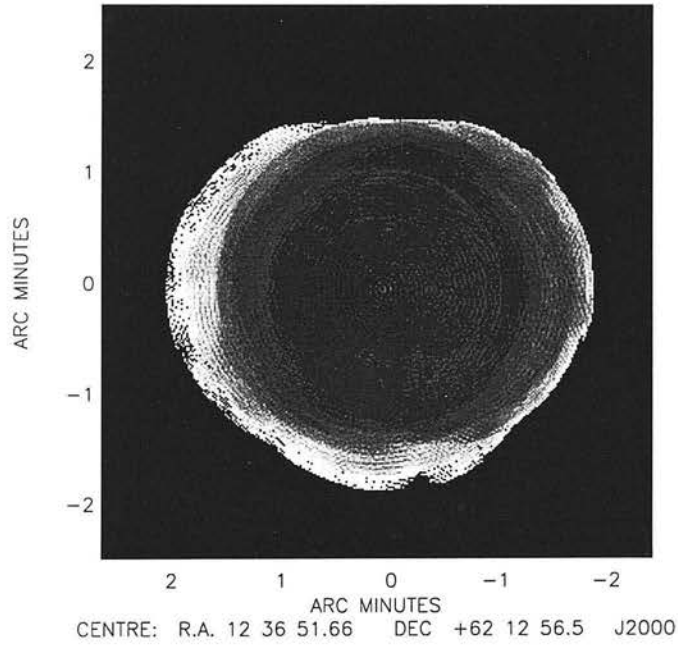

Figure 2.7: Zero-footprint noise map of the Hubble Deep Field. Display levels are the 95% auto-cut levels from the GAIA image analysis tool (0.0 - 41.1 mJy).

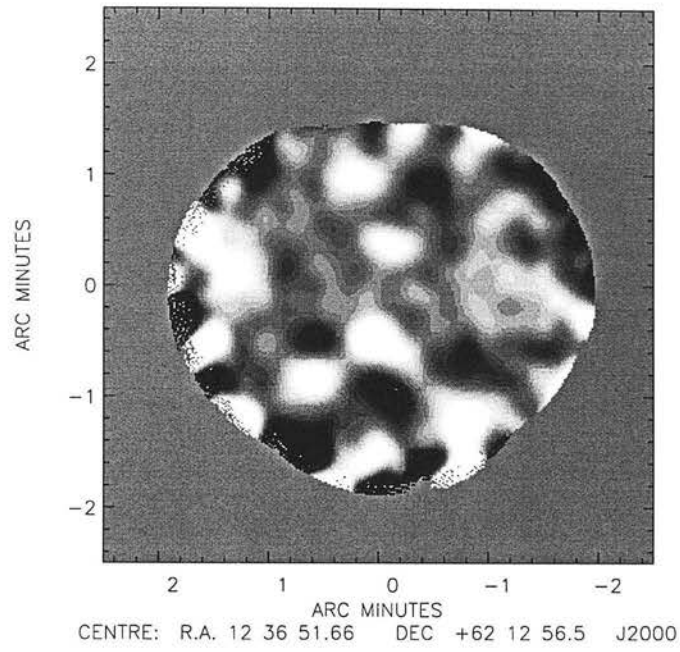

Figure 2.8: Gaussian-convolved signal map of the Hubble Deep Field. Display levels are the 95% auto-cut levels from the GAIA image analysis tool (-2.7 - 2.7 mJy).

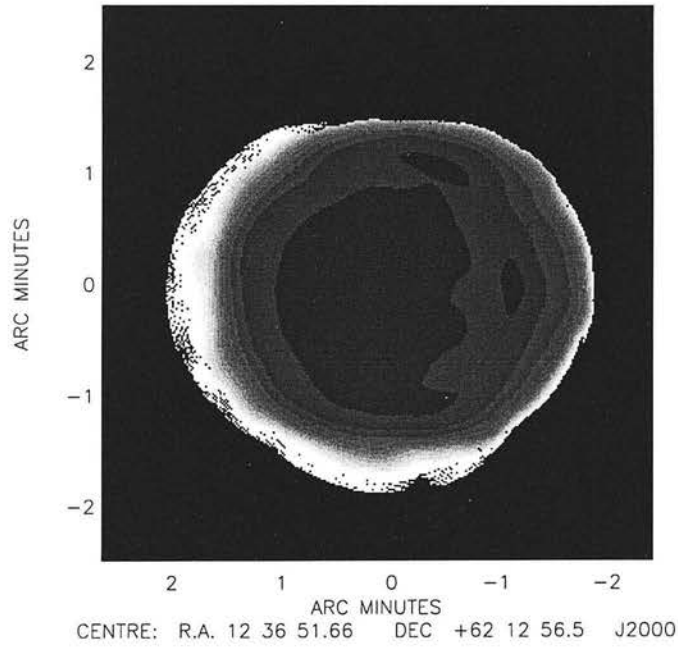

Figure 2.9: Gaussian-convolved noise map of the Hubble Deep Field. Display levels are the 95% auto-cut levels from the GAIA image analysis tool (0.0 - 3.5 mJy).

It is probably worth digressing a little at this point, to address the question of whether the SURF reduction process as it currently stands produces anything similar to the uncorrelated noise maps from the IDL reduction. In addition to the noise-weighted signal image produced by the SURF task **rebin**, a "variance" array is also output. As previously mentioned, SCUBA takes data at a rate of 128 Hz, recording the signal as a one second average. The value stored is derived from a linear least-squares fit of a model to the data, such that the measured values, MEAS(i), are given by:

$$\mathrm{MEAS(i)} = \mathrm{A.E(i)} + \mathrm{B.CHOP(i)} + \mathrm{C.CALIB(i)} + \mathrm{D} + \mathrm{ERROR(i)} \qquad (2.6)$$

where E(i) represents the slow exponential decay in mean signal which occurs when the chopped signal amplitude suddenly changes. Such a change is likely to happen each time a new jiggle position is started, and is caused by the electronics being A.C. coupled. CHOP(i) is a sine wave coinciding in period and phase with the expected chopped flux variation and B corresponds to the amplitude of the Fourier component at the chop period and phase after subtracting A.E(i). CALIB(i) is a sine wave coinciding in period and phase with the expected signal from the internal calibrator, with C corresponding to its Fourier amplitude. D allows for a zero offset in the system. The variance values are given by the formal values generated by the least-squares fit, and are propagated in the normal fashion throughout the SURF reduction process. One might assume that the final rebinned variance array would bear some resemblance to the Gaussian convolved noise maps (in the same way that the SURF signal map and Gaussian convolved IDL signal map are related), however, inital assessments (by myself and Rob Ivison) have suggested that this is NOT the case. One suspicion is that the variance values are artificially high as a result of microphonics and higher harmonics of the periodic signals, which are not included in the description of MEAS(i) (D. Kelly, priv comm). Whether the output variance arrays could be related to the actual variance by means of some "fudge" factor, or if they are useless for this purpose, is beyond the realms of this thesis (but an area of current and future work). The noise levels in the vicinity of a source in a SURF image may instead be estimated by placing beam-sized apertures on source-free sky areas and calculating the standard deviation of the enclosed ensemble of pixels. More sophisticated modifications to this procedure have been developed by other survey groups primarily using a SURF reduction (eg. Barger et al. 1999 and Eales et al. 2000), and these will be summarised in Chapter 5.

2.5 Source Extraction

The chopping-nodding mechanism of the telescope provides a valuable method of discriminating between real detections and spurious noise spikes in the data. All of the submm surveys discussed in this thesis were carried out using chop throws which were small enough to fall onto the SCUBA array (either 30" or 45"). With the exception of the Hubble Deep Field (HDF), each of the surveys used a single chop throw fixed in right ascension (RA), thus creating negative sidelobes, half the depth of the peak flux density, on either side of a real source. In the case of the HDF, this strategy was modified to use two chop throws fixed in RA, each chop throw used for approximately half of the total integration time. In all cases, this side-lobe signal can be recovered to boost the overall signal-to-noise ratio of a detection.

For well-separated sources, convolving the images with the beam is formally the best method of source extraction (Eales et al. 1999, 2000, Serjeant et al. 2003). However, following a careful examination of the reduced data it became clear that some of the potential sources were partially confused. This is particularly prominent in the map of ELAIS N2 (Chapter 4) where the negative sidelobes of individual sources have overlapped and are therefore somewhat deepened relative to both source peaks. Consequently, in order to decouple any confused sidelobes I have devised a source-extraction algorithm based on a simultaneous maximum-likelihood fit to the flux densities of all potentially significant peaks in the maps. This is made feasible by the independent data-points and errors yielded by the zero-footprint IDL-reduced maps. These peaks were identified as any positive peak in the noise-weighted Gaussian convolved signal maps. Using a peak-normalised beam-map as a source template (generated by binning together all of the observations of Uranus or CRL618 taken with the relevant chop throw), a basic model was constructed by centring a beam-map at the positions of every peak in the maps. The normalisation coefficients of each of the positioned beam-maps were then calculated simultaneously such that the final multi-source model provided the best description of the submm sky, as judged by a minimum χ^2 fit.

The fitting process is as follows. Suppose one considers a normalised beam-map $B(x, y)$ as a source template and that at position (i, j) in the unconvolved image the signal is $S(i, j)$ and the noise is $N(i, j)$. If n peaks above a specified flux threshold are located in the Gaussian-convolved image, one may construct a model to the unconvolved zero-footprint image such that beam-maps centred

on each peak position are simultaneously scaled to give an overall best fit to the entire image. Using a minimised χ^2 fit as the maximum likelihood estimator then

$$\chi^2 = \left(\sum_{i,j} \frac{S(i,j) - \sum_{k=1}^{n} a_k B_k(x-i, y-j)}{N(i,j)^2} \right)^2 \tag{2.7}$$

where a_k is the best fit flux to the kth peak. Minimising with respect to each a_k

$$\frac{d\chi^2}{da_m} = 2 \sum_{i,j} \frac{[S(i,j) - \sum_{k=1}^{n} a_k B_k(x-i, y-j)] B_m(x-i, y-i)}{N(i,j)^2} = 0 \tag{2.8}$$

and $m = 1 \cdots n$.

Rearranging, the matrix equation

$$\sum_{k=1}^{n} \left(\sum_{i,j} \frac{B_k(x-i, y-j) B_m(x-i, y-j)}{N(i,j)^2} \right) a_k = \sum_{i,j} \frac{S(i,j) B_m(x-i, y-j)}{N(i,j)^2} \tag{2.9}$$

is obtained, which may be written in the form

$$\sum_{k=1}^{n} \alpha_{mk} a_k = \beta_m \tag{2.10}$$

where

$$\alpha_{mk} = \sum_{i,j} \frac{B_k(x-i, y-j) B_m(x-i, y-j)}{N(i,j)^2} \tag{2.11}$$

an $n \times n$ matrix, and

$$\beta_m = \sum_{i,j} \frac{S(i,j) B_m(x-i, y-j)}{N(i,j)^2} \tag{2.12}$$

a vector of length n.

To recover the best fit values of a_k the matrix α is inverted such that

$$a_k = \sum_{m=1}^{n} [\alpha]_{km}^{-1} \beta_m \tag{2.13}$$

The variance associated with the estimate a_k is given by

$$N^2(a_k) = \sum_{i,j} N(i,j)^2 \left(\frac{\partial a_k}{\partial S(i,j)} \right) \tag{2.14}$$

Since α_{km} is independent of $S(i,j)$

$$\frac{\partial a_k}{\partial S(i,j)} = \sum_{m=1}^{n} \frac{[\alpha]_{km}^{-1} B_m(x-i, y-j)}{N(i,j)^2} \tag{2.15}$$

Consequently one finds,

$$N^2(a_k) = \sum_{k=1}^{n}\sum_{l=1}^{n}[\alpha]^{-1}_{km}[\alpha]^{-1}_{kl}\left(\sum_{i,j}\frac{B_m(x-i,y-j)B_l(x-i,y-j)}{N(i,j)^2}\right) \tag{2.16}$$

The final term in brackets is simply the matrix $[\alpha]$ and so this expression reduces to

$$N^2(a_k) = [\alpha]^{-1}_{kk} \tag{2.17}$$

The diagonal elements of $[\alpha]^{-1}$ are the variances of the fitted parameters a_k such that the significance of the peak detection

$$\sigma(a_k) = \frac{a_k}{\sqrt{[\alpha]^{-1}_{kk}}} \tag{2.18}$$

This method can also be modified to deal with surveys which have used more than one chop throw or position angle. The peaks are found in the same way as before, by regridding all of the individual observations together (regardless of the chop throw or position angle used) and carrying out a noise-weighted smoothing with a beam-sized Gaussian. When conducting the χ^2 fit, however, each particular combination of chop throw and position angle is binned separately. If r different chop configurations have been used then the expression for χ^2 becomes

$$\chi^2 = \sum_{p=1}^{r}\left(\sum_{i,j}\frac{S_p(i,j)-\sum_{k=1}^{n}a_kB_{p,k}(x_p-i,y_p-j)}{N_p(i,j)^2}\right)^2 \tag{2.19}$$

and the matrix equation generalises to

$$\sum_{k=1}^{n}\left(\sum_{p=1}^{r}\left(\sum_{i,j}\frac{B_{p,k}(x_p-i,y_p-j)B_{p,m}(x_p-i,y_p-j)}{N_p(i,j)^2}\right)\right)a_k =$$

$$\sum_{p=1}^{r}\left(\sum_{i,j}\frac{S_p(i,j)B_{p,m}(x_p-i,y_p-j)}{N_p(i,j)^2}\right) \tag{2.20}$$

Adopting the same notation as equation 2.10,

$$\alpha_{mk} = \sum_{p=1}^{r}\left(\sum_{i,j}\frac{B_{p,k}(x_p-i,y_p-j)B_{m,k}(x_p-i,y_p-j)}{N_p(i,j)^2}\right) \tag{2.21}$$

and

$$\beta_m = \sum_{p=1}^{r}\left(\sum_{i,j}\frac{S_p(i,j)B_{p,m}(x_p-i,y_p-j)}{N_p(i,j)^2}\right) \tag{2.22}$$

and the expressions for a_k and $N(a_k)$ are the same as equations 2.13 and 2.17 respectively.

One could, of course, attempt to fit a model of the sky consisting of a beam-map centred at every pixel, rather than just at those positions identified with a positive peak. This is essentially the technique applied in making maps of the cosmic microwave background (eg. Janssen & Gulkis 1992, Bennett et al. 2003), however, in this case a continuous map is required to measure the anisotropies over all of the angular scales appropriate to the telescope beamsize, thus requiring the data contained in every pixel to be considered in the matrix inversion. The difference with the SCUBA data is that the aim is to produce a discrete list of point sources for which a very acceptable fit ($\chi^2_\nu = 1$) to the sky can be obtained by centring the beam profile only at the positions of known peaks, certainly given the noise levels in these datasets. This has the advantage of requiring much smaller matrices to be inverted than if every pixel were considered, thus saving on cpu time and allowing an analytical method to be used rather than relying on numerical techniques. It is this which makes the simulations described in Chapter 3 tractable.

Chapter 3

Simulations

This Chapter describes the Monte Carlo simulations carried out to quantify the statistical effects of completeness, output-to-input flux-density ratio, positional error and spurious fraction. A preliminary introduction as to why simulations are required is given in Section 3.1. Sections 3.2 and 3.3 present results from the two different types of simulation method. The first of these methods builds on the real survey data, by adding in sources of known flux density at random positions throughout the signal maps, one source at a time so as not to significantly enhance source confusion, following which the source extraction algorithm is employed in an attempt to retrieve it. The latter of these two sections discusses results from fully simulated images of the survey fields, created by using a realistic source-counts model and noise properties from the actual data.

3.1 The need for simulations

In order to assess the effects of confusion and noise on the reliability of the source-extraction algorithm, Monte Carlo simulations were carried out on all of the survey fields. The individual fields vary widely in size and depth from small, deep surveys covering a few square arcminutes of sky down to the confusion limit (eg. the Hubble deep field), to wider, shallower surveys aimed at studying the most luminous sub-millimetre sources on scales of $\sim$ 100 square arcminutes (eg. the wide area Lockman Hole field from the "SCUBA 8-mJy Survey"). The typical noise levels and areas of each of the fields are given in Table 3.1. The dependences of positional error, completeness and error in reclaimed flux density, on input source flux density and noise in the maps, were determined by planting individual sources of known flux density into the real SCUBA maps. This has

Survey Field	Total area /sq. arcmins	Uniform noise area /sq. arcmins	1σ rms noise level mJy/beam
ELAIS N2	137	113	2.2 ± 0.7
Lockman Hole wide area	141*	88	2.7 ± 0.7
Lockman Hole deep strip		21	1.8 ± 0.2
03h wide area	69*	55	1.8 ± 0.5
03h deep area		8	1.1 ± 0.2
10h	10	8	1.3 ± 0.2
14h	61	57	1.5 ± 0.3
22h	7	5	1.5 ± 0.3
Hubble Deep Field	10	6	0.6 ± 0.1
SSA13 wide area	72*	45	2.5 ± 0.6
SSA13 deep area		8	0.7 ± 0.1
SSA17	24	21	1.6 ± 0.5
SSA22	26	21	0.9 ± 0.2
Lockman Hole deep area	11	8	0.8 ± 0.1

Table 3.1: Survey field areas and 1σ rms noise levels in the regions of uniform noise, as given by the mean and standard deviation measured directly from the 14.5" FWHM Gaussian convolved noise maps. Total areas marked with * refer to fields composed of a small deep region within a wider shallower survey area and correspond to the full area of that entire field (ie. both shallow and deep).

the advantage of testing the source-reclamation process against the real noise and confusion properties of the images, accounting for any clustering in the faint background source population, for example. However, these simulations do not allow assessment of the level to which false or confused sources can contaminate an extracted source list. I have therefore also created a number of fully-simulated images of the survey areas by assuming a reasonable 850 μm source-counts model, derived from a best-fit power-law to the source counts given in Chapter 5. The results of analyzing these sets of simulations are discussed in the following two sections.

3.2 Simulations building on the real survey data

A normalised beam-map, with the same chop throw and position angle as that used in the real data, was used as a source template. At flux density intervals of 0.5 mJy, spanning the entire range of flux densities for which real sources were recovered, fake sources were added into the unconvolved zero-footprint signal maps. This was done one fake source at a time, so as not to enhance significantly any existing real confusion noise within the image. The source-extraction algorithm

was then re-run. This exercise was repeated for 100 different randomly-selected positions on each image, at each flux density level, so that source reclamation could be monitored as a function of input flux density and position/noise-level within the maps. The source reclamation was deemed to have been successful if the source-extraction algorithm returned the fake source with signal-to-noise > 3.50 (a level selected as a compromise between recovering a reasonable number of sources and contamination with spurious / confused sources - see Section 3.3) within less than half a beam-width of the input position, but excluding from the analysis any fake sources which had fallen upon a position within half a beam-width of a brighter $> 3.00\sigma$ peak already detected in the map. This is because the flux densities of the recovered sources within the real data span a broad range ($\simeq 2-12\,\mathrm{mJy}$), and it is not possible to resolve two separate sources placed closer together than this - they would appear as one peak in the Gaussian-smoothed image. It is not realistic to consider, for example, a fake 2 mJy source to have been successfully recovered if it lies almost on top of an 8 mJy source already detected significantly in the map. Under this situation it is really the 8 mJy source already present in the image which is being recovered. Reversing the situation, however, the successful reclamation of a fake 8 mJy source planted into the map in the near vicinity of an already significantly detected 2 mJy source (a possible scenario in the very deep images such as that of the HDF) would be included in the analysis because the fake source is the dominating contribution to the combined flux density.

The Lockman Hole East field from the "SCUBA 8 mJy Survey", the 03h field from the "Canada UK Deep Submillimetre Survey (CUDSS)", and the SSA13 field from the "Hawaii Submillimetre Survey", contain sections of map which are markedly deeper than the rest of the data. In the case of the Lockman Hole this was due to an early change in survey mapping strategy, and in the 03h and SSA13 fields this resulted from a deep pencil beam survey being incorporated into the wider-area images. In each of these cases, separate sets of simulations were run on the deep and shallower sections of the fields.

Additionally, regions of uniform and non-uniform noise were defined for each field (again treating the deep parts of the Lockman Hole, 03h and SSA13 fields as separate fields from the wider-area shallower part), using the "GAIA" tool to manually cut out a template of the uniform noise area using the Gaussian-smoothed noise maps. The deep pencil beam surveys, such as the HDF and CUDSS 22h field, are comprised of a stack of jiggle-map observations centred on

Survey Field	Noise Region	a	b	χ^2
ELAIS N2	uniform	0.17043	2.3338	0.37425
Lockman Hole wide area	uniform	0.14800	3.2690	0.28300
Lockman Hole deep strip	uniform	0.20896	2.1064	0.22527
03h wide area	uniform	0.20081	2.0013	0.21037
03h deep area	uniform	0.28937	1.6500	0.39179
10h	uniform	0.22587	1.3248	0.42789
14h	uniform	0.21016	1.5467	0.31834
22h	uniform	0.26450	1.9359	0.12883
Hubble Deep Field	uniform	0.39711	0.6258	0.15015
SSA13 wide area	uniform	0.14627	2.6614	0.19068
SSA13 deep area	uniform	0.22037	0.8738	0.13963
SSA17	uniform	0.24248	1.9077	0.19140
SSA22	uniform	0.21362	0.4445	0.37697
Lockman Hole deep area	uniform	0.24862	0.8042	0.12062
ELAIS N2	non-uni	0.00588	0.0030	0.04114
Lockman Hole wide area	non-uni	0.01388	4.6093	0.05206

Table 3.2: Best fit values determined for a and b in equation 3.1, describing the percentage differential completeness against input source flux density for each of the survey fields and noise regions.

one or two positions only, and so the non-uniform edge regions in these images are largely the result of undersampling from the bolometers on the outer ring of the array. The wider-area images, however, were built up from a series of jiggle-pointings, offset from each other by some fraction of an array width. Hence, the pointings forming the outer-most regions of the survey field lack the next consecutive set of integrations from what would have been the neighbouring pointing, resulting in a border of shallower (and hence noisier) observations. In Chapters 4 and 5, which discuss the various survey fields in detail, any sources recovered in these poorer noise regions have been marked with the term "edge" in the source list tables.

3.2.1 Completeness

The differential completeness is given by the percentage of sources recovered with signal-to-noise ratio > 3.50 at each input flux density level, and was found to be described well by the functional form

$$\text{differential completeness} = 100(1 - e^{-a(x-b)}) \tag{3.1}$$

where x is the input flux density, and the values of a and b were determined by a minimised χ^2 fit to the simulation results for each 850 μm survey field. The

values of a and b determined from these fits are given in Table 3.2.

The primary goal in allowing a fit of this nature was to obtain a best-fit description of the overall shape of the curve, rather than a detailed analysis of possible combinations of free-parameters 'a' and 'b' in χ^2 space. However, even simple plots of the best fit values of a and b against the 1σ rms noise levels as measured from the beam-sized Gaussian convolved noise images (Figs. 3.1 and 3.2 respectively), show clear noise-dependent trends. The horizontal error bars reflect the standard deviation of the noise values about the mean, in the uniform regions of the map. The best-fit values of parameter 'a' show a general decrease with increasing rms noise levels, albeit with a fairly broad dispersion, particularly between the deep pencil beam surveys such as the Hubble deep field and the SSA13 deep area field. This is likely a combination of being at the confusion limit (generally high source density) and the variation in the number density of sources between these small area fields (cosmic variance and perhaps clustering effects also). The parameter 'b' defines a lower flux density cut-off below which no sources are successfully recovered, and shows a much tighter correlation, increasing roughly linearly with the rms noise as $b \simeq 1.25 \times$ noise.

Unfortunately, the scatter in parameter 'a' with rms noise is too large to allow for a general differential completeness formula applicable to any survey field to be developed, based on this data.

Figures 3.3, 3.4 and 3.5 show the completeness analysis for the uniform noise regions of the "SCUBA 8 mJy Survey" fields (ELAIS N2, Lockman Hole wide area and Lockman Hole deep strip). The error bars are given by the Poisson error on the number of sources planted into the field in each noise region, and at each flux density. These fields have the largest shallow border regions of all the survey fields discussed in this thesis, due to the survey strategy adopted to even out the noise (see Chapter 4). The corresponding completeness plots for the non-uniform regions of ELAIS N2 and the Lockman Hole wide area are shown in Figs. 3.6 and 3.7 respectively. It is immediately obvious in comparing plots of uniform and non-uniform noise that source recovery in the non-uniform edge regions is very much worse than in the fully observed central areas, reaching at best $\sim 10\%$ at 15 mJy as opposed to the $\sim 90\%$ in the uniform noise regions. The simulations carried out on the remaining smaller fields did not yield sufficiently good statistics in the non-uniform noise regions to allow any meaningful fit to be made, hence only plots for the uniform noise regions of the remaining fields have been presented (Figs. 3.8 to 3.18).

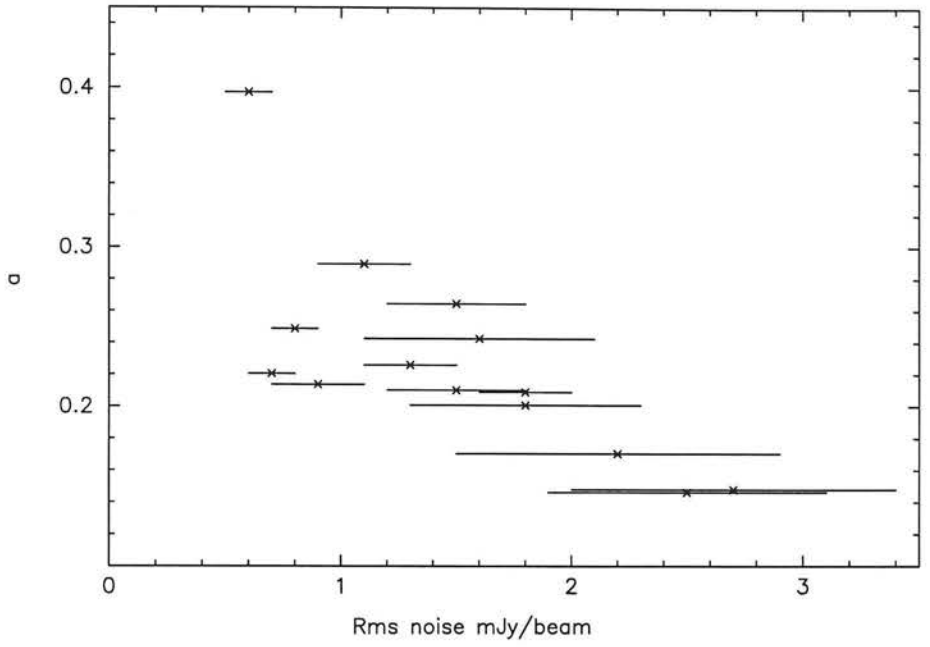

Figure 3.1: Best-fit values for the parameter "a" as given in Table 3.2, plotted against the 1σ rms noise levels as determined from the uniform regions of the 14.5" Gaussian convolved noise images (values given in Table 3.1). The horizontal error bars show the standard deviation of the noise about the mean level.

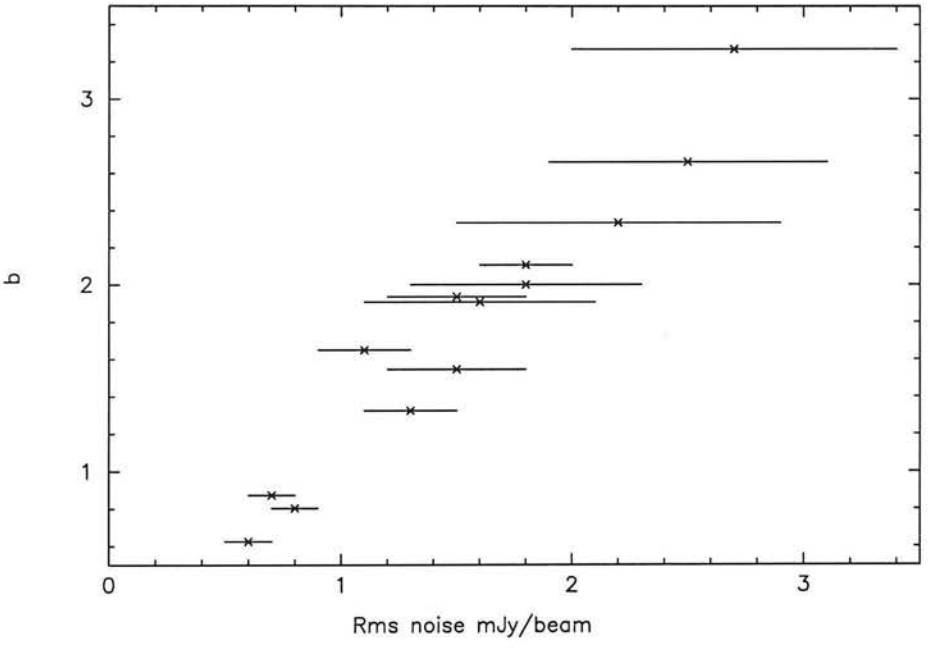

Figure 3.2: Best-fit values for the parameter "b" as given in Table 3.2, plotted against the 1σ rms noise levels as determined from the uniform regions of the 14.5" Gaussian convolved noise images (values given in Table 3.1). The horizontal error bars show the standard deviation of the noise about the mean level.

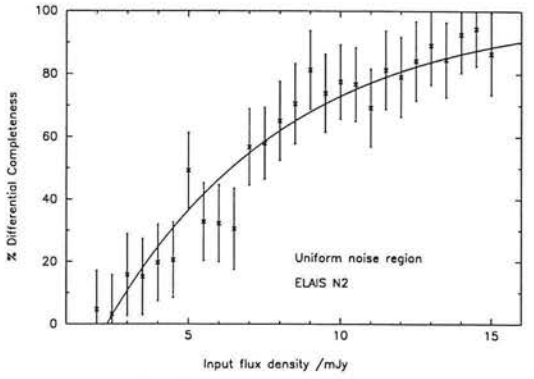

Figure 3.3: Percentage of sources recovered against input flux density, for the uniform noise regions of the ELAIS N2 field from the "SCUBA 8 mJy Survey".

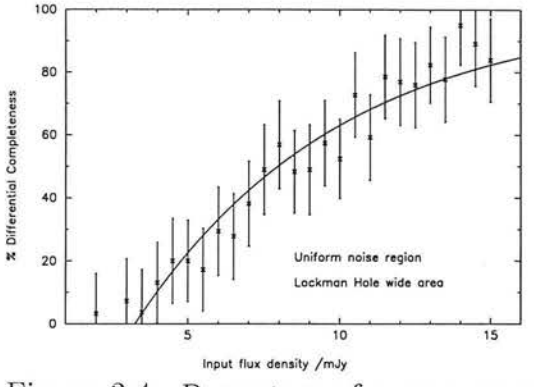

Figure 3.4: Percentage of sources recovered against input flux density, for the uniform noise regions of the Lockman Hole East wide area field from the "SCUBA 8 mJy Survey".

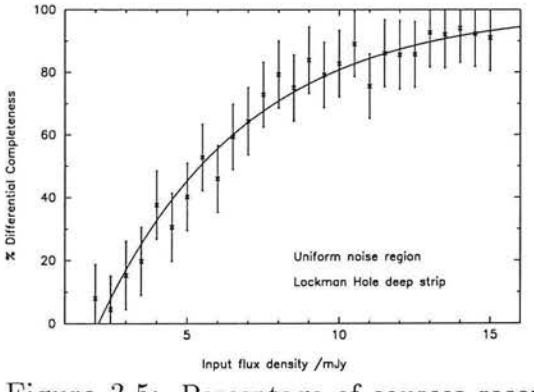

Figure 3.5: Percentage of sources recovered against input flux density, for the uniform noise regions of the Lockman Hole East deep strip from the "SCUBA 8 mJy Survey".

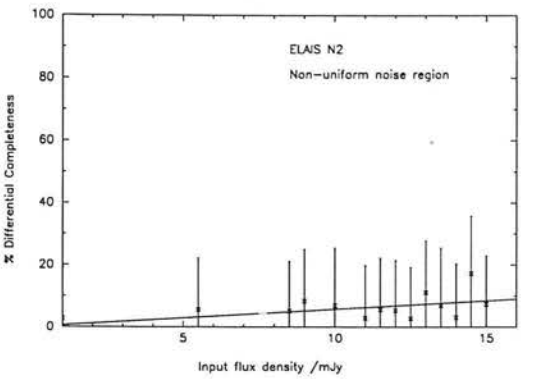

Figure 3.6: Percentage of sources recovered against input flux density, for the non-uniform noise regions of the ELAIS N2 field from the "SCUBA 8 mJy Survey".

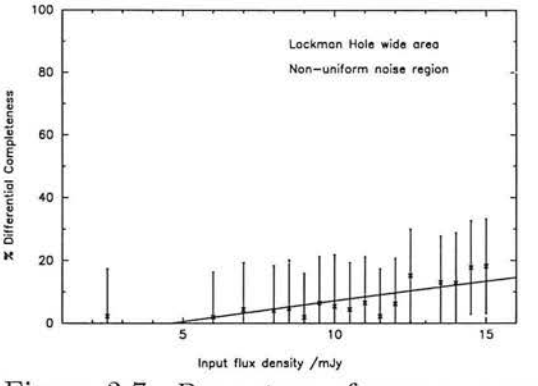

Figure 3.7: Percentage of sources recovered against input flux density, for the non-uniform noise regions of the Lockman Hole East wide area field from the "SCUBA 8 mJy Survey".

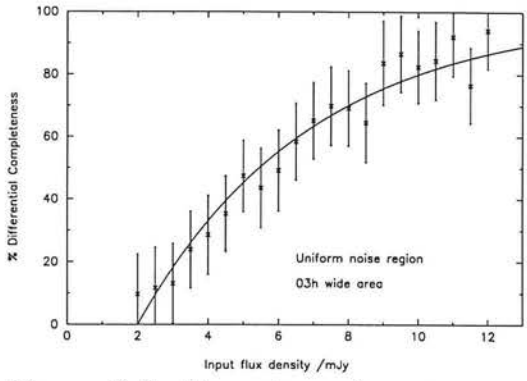

Figure 3.8: Percentage of sources recovered against input flux density, for the uniform noise regions of the 03 hour wide area field from the "CUDSS".

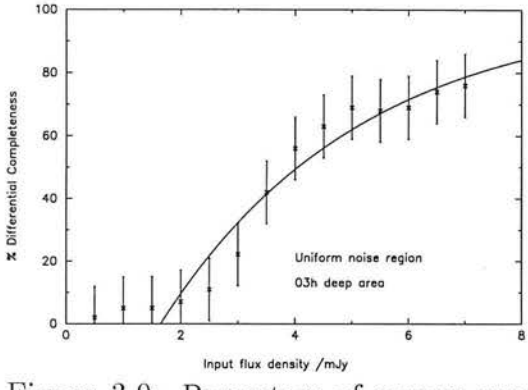

Figure 3.9: Percentage of sources recovered against input flux density, for the uniform noise regions of the 03 hour deep area from the "CUDSS".

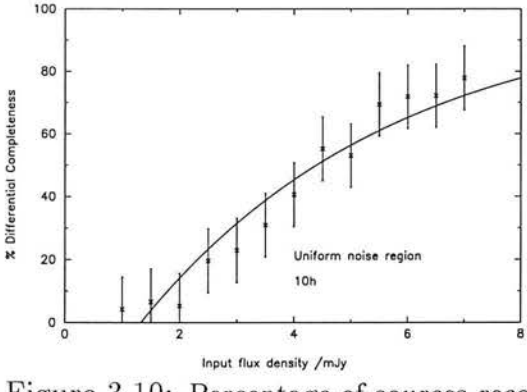

Figure 3.10: Percentage of sources recovered against input flux density, for the uniform noise regions of the 10 hour field from the "CUDSS".

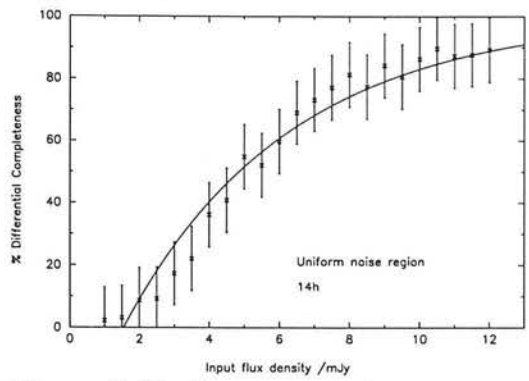

Figure 3.11: Percentage of sources recovered against input flux density, for the uniform noise regions of the 14 hour field from the "CUDSS".

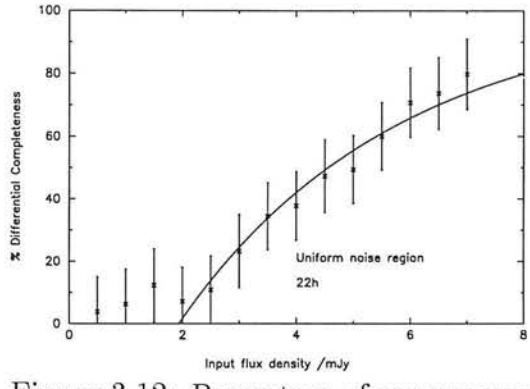

Figure 3.12: Percentage of sources recovered against input flux density, for the uniform noise regions of the 22 hour field from the 'CUDSS".

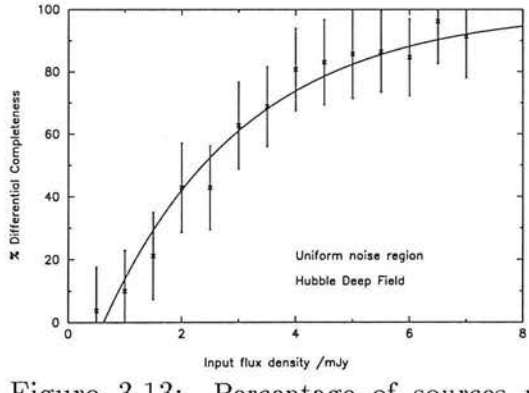

Figure 3.13: Percentage of sources recovered against input flux density, for the uniform noise regions of the Hubble Deep Field.

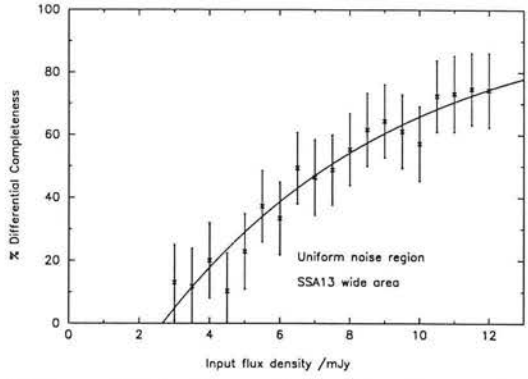

Figure 3.14: Percentage of sources recovered against input flux density, for the uniform noise regions of the SSA13 wide area field from the "Hawaii Submm Survey".

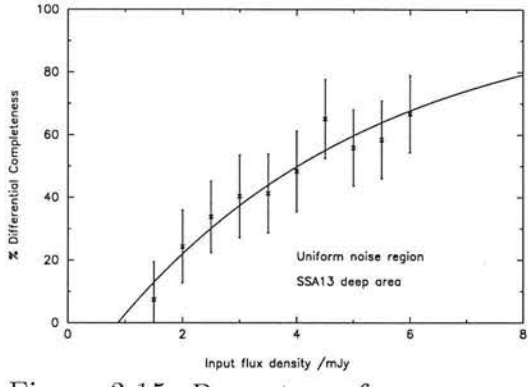

Figure 3.15: Percentage of sources recovered against input flux density, for the uniform noise regions of the SSA13 hour deep area from the "Hawaii Submm Survey".

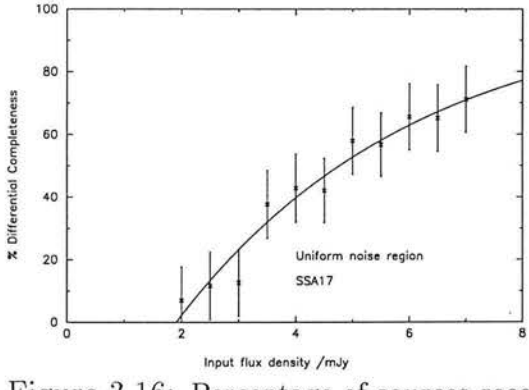

Figure 3.16: Percentage of sources recovered against input flux density, for the uniform noise regions of the SSA17 field from the "Hawaii Submm Survey".

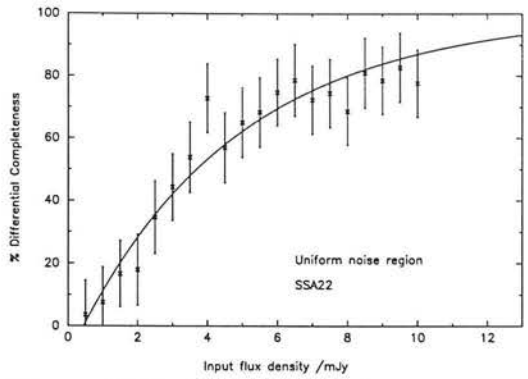

Figure 3.17: Percentage of sources recovered against input flux density, for the uniform noise regions of the SSA22 field from the "Hawaii Submm Survey".

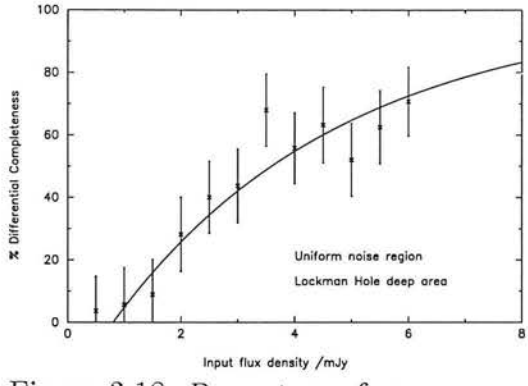

Figure 3.18: Percentage of sources recovered against input flux density, for the uniform noise regions of the Lockman Hole deep area from the "Hawaii Submm Survey".

Survey Field	Noise Region	C	d	f	χ^2
ELAIS N2	uniform	6.350	0.4813	1.0150	1.11683
Lockman Hole wide area	uniform	5.555	0.3591	1.0246	1.08116
Lockman Hole deep strip	uniform	6.543	0.5313	1.0154	1.34420
03h wide area	uniform	6.587	0.5667	1.0603	1.05373
03h deep area	uniform	13.575	1.1842	1.0537	1.67181
10h	uniform	8.786	0.9443	1.0439	0.76535
14h	uniform	8.086	0.7701	1.0325	1.71510
22h	uniform	9.815	0.8236	1.1301	1.51353
Hubble Deep Field	uniform	12.106	1.6358	1.0513	1.80567
SSA13 wide area	uniform	4.606	0.4312	1.0430	1.52413
SSA13 deep area	uniform	2.726	0.8049	1.0516	1.22079
SSA17	uniform	6.769	0.8624	1.0965	1.60692
SSA22	uniform	8.262	1.2241	1.0168	1.23946
Lockman Hole deep area	uniform	9.712	1.5104	1.0422	0.68671
ELAIS N2	non-uni	3.686	0.2283	1.1805	1.84850
Lockman Hole wide area	non-uni	112.821	0.6582	1.2593	3.39015

Table 3.3: Best fit values determined for C, d and f in equation 3.2, describing the output to input flux density ratio against input flux density for each of the survey fields and noise regions.

3.2.2 Output versus Input Flux Density

Using these simulations, it is also possible to determine the dependence of the mean output-to-input flux density ratio as a function of the input flux density, for those sources identified with signal-to-noise ratio > 3.50. This relation was found to be well described by the expression

$$\frac{\text{output flux density}}{\text{input flux density}} = Ce^{-dx} + f \tag{3.2}$$

where x is the input flux density, and the values of C, d and f were determined by a minimised χ^2 fit to the simulation results for each 850 μm survey field and are given in Table 3.3.

The plots of mean output/input flux density ratio against input flux density are shown in Figs. 3.22 to 3.37. The error bars are the standard error on the mean. One of the first things to notice about the subsequent ratio plots, is that the effect of noise and confusion is to produce systematic 'flux-boosting', the mean retrieved flux density always being greater than the input value. This effect is apparent in any flux limited survey where a specific signal-to-noise threshold is employed. The presence of noise and confusion from the faint background population will vary the flux densities with which a source of specified input flux density is retrieved. If, for

example, one considers a very simple case of pure Gaussian noise on a fake source, the measured flux densities would be expected to have a symmetric distribution about the actual source flux density, the exact characteristics of the distribution dependent on the level of noise applied. However, if a fixed signal-to-noise ratio is applied to the source extraction procedure, one will preferentially select those sources which have been retrieved with a brighter flux density, as some of the fainter measured values will fail to make the signal-to-noise cutoff. Consequently, the mean retrieved flux density will always be larger than the input flux density. Applying the same noise characteristics to input sources of increasing brightness, the mean boosting ratio is reduced, because only the larger negative fluctuations on the tail of the Gaussian noise distribution will allow the brighter sources to fall below the signal-to-noise threshold. For very bright sources the output-to-input flux density ratio approaches 1. Non-Gaussian noise and confusion will of course affect the distribution of the retrieved flux densities - in particular confusion of faint background sources may lead to a more asymmetric distribution, especially if the SCUBA population is found to strongly cluster. Simulations such as these, however, allow for an empirical numerical description on a field by field basis.

Trends in the properties of parameters 'C', 'd' and 'f' with rms noise are shown in Figs. 3.19 to 3.21. Both parameters 'C' and 'd' decrease with increasing rms noise. The decline is steep at low rms noise levels, but becomes more shallow above $1\sigma_{\rm rms} \simeq 1.5-2\,{\rm mJy}$. Parameter 'd' shows a fairly tight correlation, however 'C' shows too great a level of scatter to allow a general formula, based solely on rms noise, to be developed for the output-to-input flux density ratio. The parameter 'f' represents the ratio of output-to-input flux density for very bright sources with a constant value of ~ 1 expected for all fields, regardless of noise level (the median value is in fact 1.04).

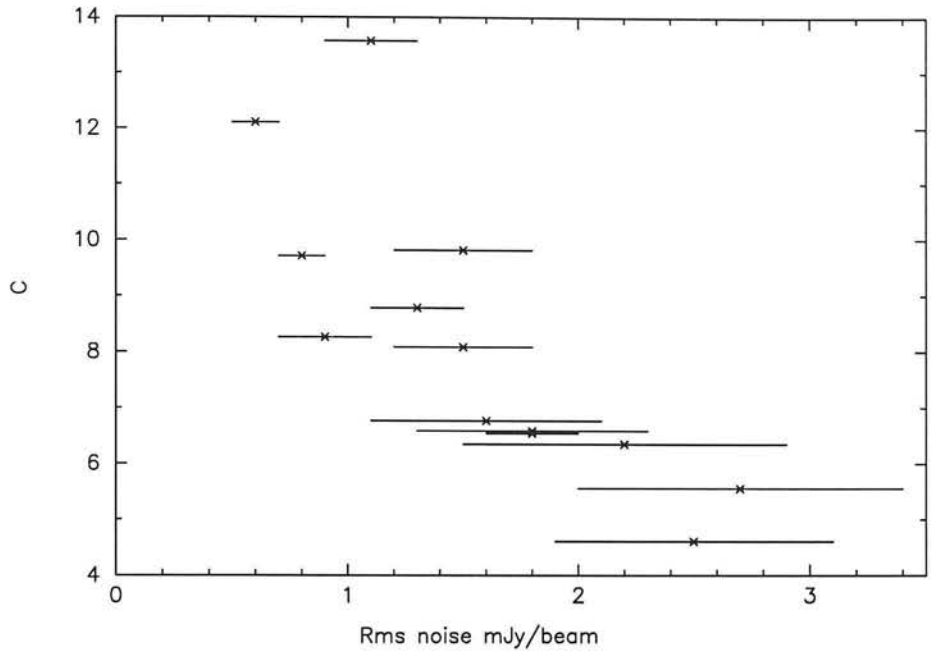

Figure 3.19: Best-fit values for the parameter "C" as given in Table 3.3, plotted against the 1σ rms noise levels as determined from the uniform regions of the 14.5" Gaussian convolved noise images (values given in Table 3.1). The horizontal error bars show the standard deviation of the noise about the mean level.

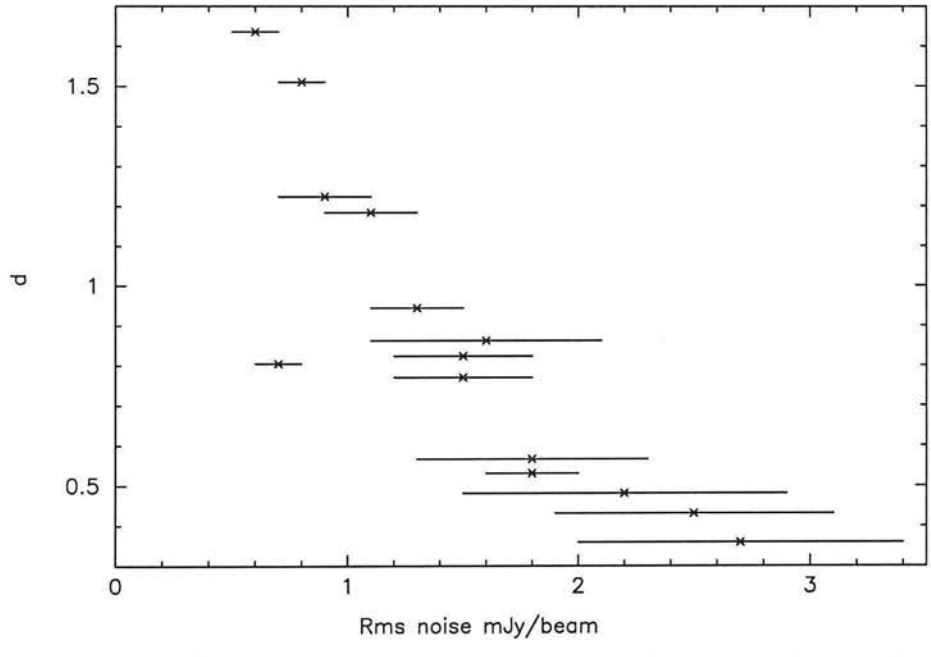

Figure 3.20: Best-fit values for the parameter "d" as given in Table 3.3, plotted against the 1σ rms noise levels as determined from the uniform regions of the 14.5" Gaussian convolved noise images (values given in Table 3.1). The horizontal error bars show the standard deviation of the noise about the mean level.

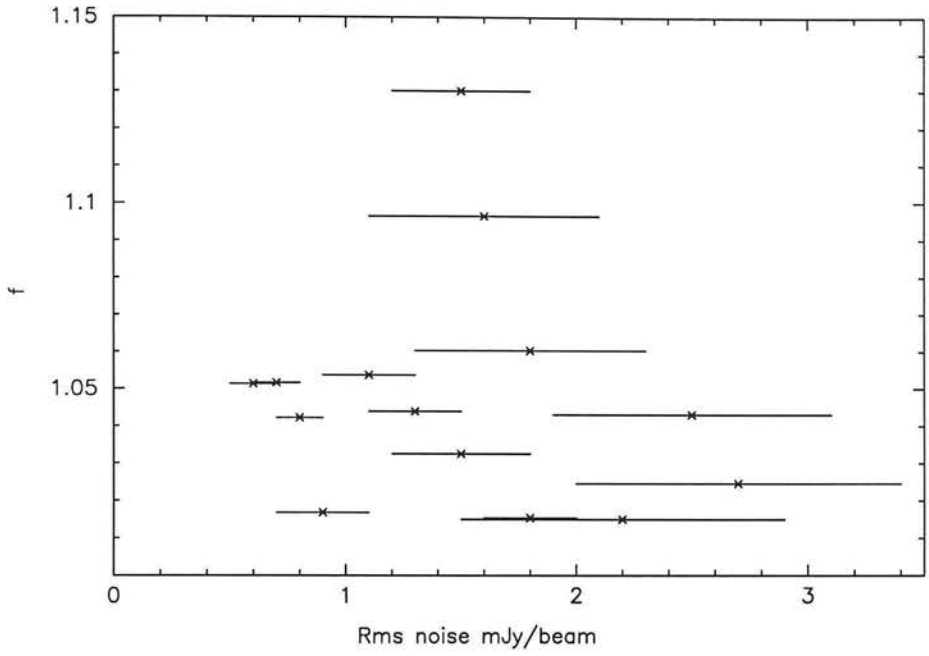

Figure 3.21: Best-fit values for the parameter "f" as given in Table 3.3, plotted against the 1σ rms noise levels as determined from the uniform regions of the 14.5" Gaussian convolved noise images (values given in Table 3.1). The horizontal error bars show the standard deviation of the noise about the mean level.

It can also be readily seen from comparing Figs. 3.22 and 3.23, with 3.25 and 3.26, that the level of flux-boosting is much greater in the non-uniform noise regions and with a much larger degree of scatter in the data points. For example, a source input to the ELAIS N2 or Lockman Hole fields ("from the SCUBA 8-mJy Survey") would appear boosted on average by a factor of 1.2−1.3 if extracted from the uniform noise regions. In the non-uniform regions though, the mean level of boosting is by a factor 2. Due to the combination of a poor level of retrieval and large flux boosting factors, any sources recovered in the non-uniform noise regions (marked as "edge" in subsequent chapters) have been excluded from statistical analyses such as source counts, and clustering measures etc.

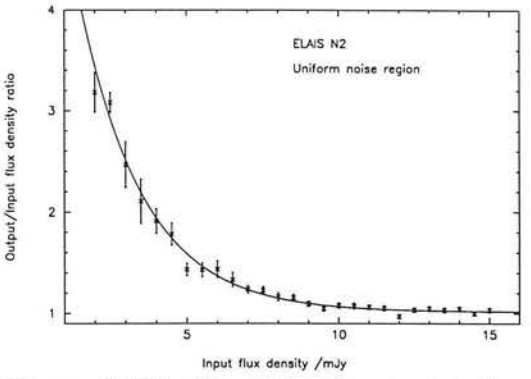

Figure 3.22: The ratio of output to input flux density against input flux density, for the uniform noise regions of the ELAIS N2 field from the "SCUBA 8 mJy Survey".

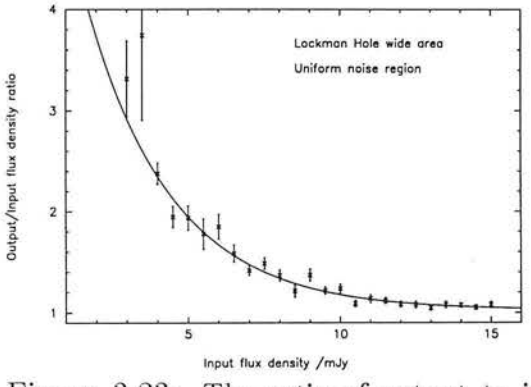

Figure 3.23: The ratio of output to input flux density against input flux density, for the uniform noise regions of the Lockman Hole East wide area field from the "SCUBA 8 mJy Survey".

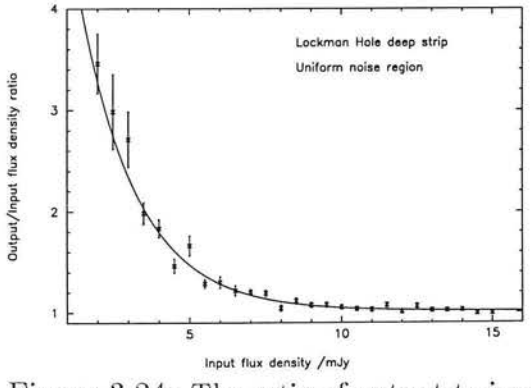

Figure 3.24: The ratio of output to input flux density against input flux density, for the uniform noise regions of the Lockman Hole East deep strip from the "SCUBA 8 mJy Survey".

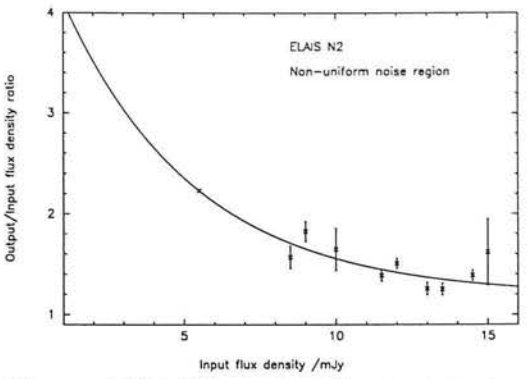

Figure 3.25: The ratio of output to input flux density against input flux density, for the non-uni noise regions of the ELAIS N2 field from the "SCUBA 8 mJy Survey".

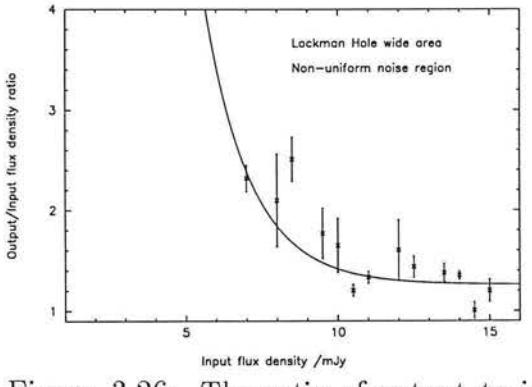

Figure 3.26: The ratio of output to input flux density against input flux density, for the non-uni noise regions of the Lockman Hole East wide area field from the "SCUBA 8 mJy Survey".

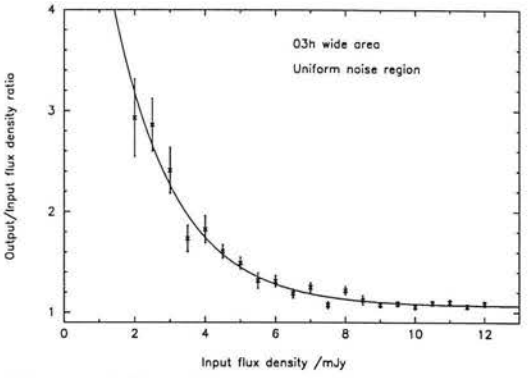

Figure 3.27: The ratio of output to input flux density against input flux density, for the uniform noise regions of the 03 hour wide area field from the "CUDSS".

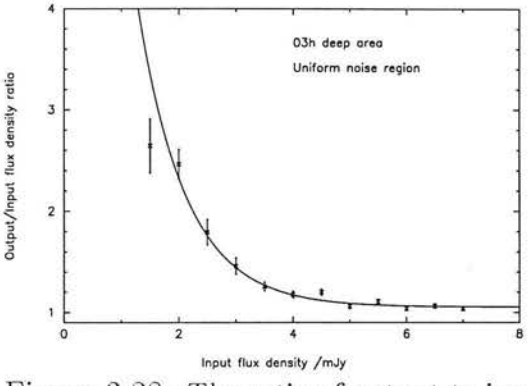

Figure 3.28: The ratio of output to input flux density against input flux density, for the uniform noise regions of the 03 hour deep area from the "CUDSS".

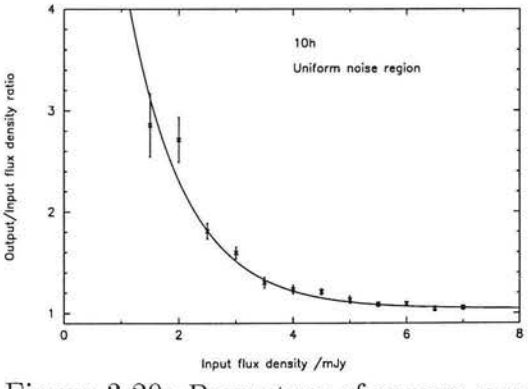

Figure 3.29: Percentage of sources recovered against input flux density, for the uniform noise regions of the 10 hour field from the "CUDSS".

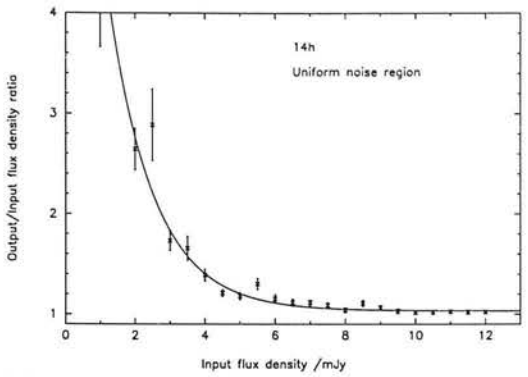

Figure 3.30: The ratio of output to input flux density against input flux density, for the uniform noise regions of the 14 hour field from the "CUDSS".

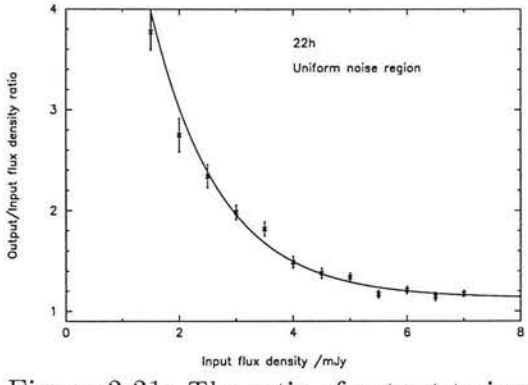

Figure 3.31: The ratio of output to input flux density against input flux density, for the uniform noise regions of the 22 hour field from the 'CUDSS".

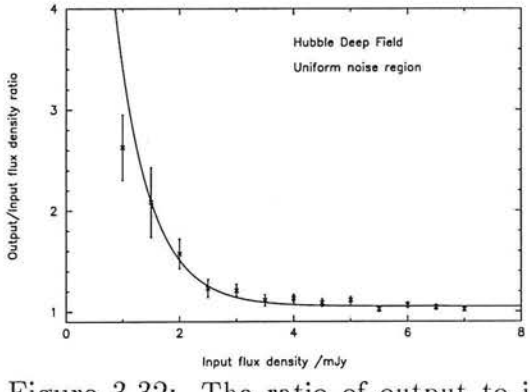

Figure 3.32: The ratio of output to input flux density against input flux density, for the uniform noise regions of the Hubble Deep Field.

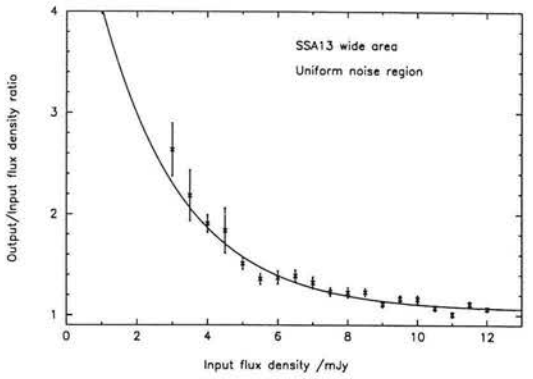

Figure 3.33: The ratio of output to input flux density against input flux density, for the uniform noise regions of the SSA13 wide area field from the "Hawaii Submm Survey".

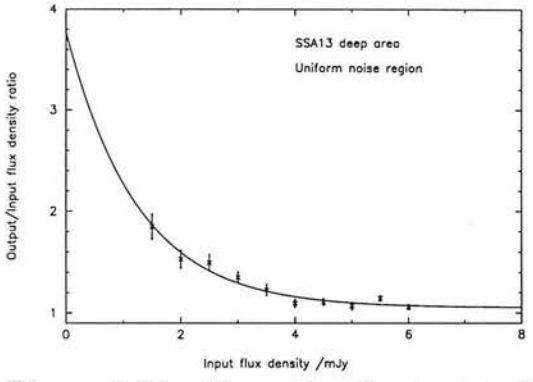

Figure 3.34: The ratio of output to input flux density against input flux density, for the uniform noise regions of the SSA13 hour deep area from the "Hawaii Submm Survey".

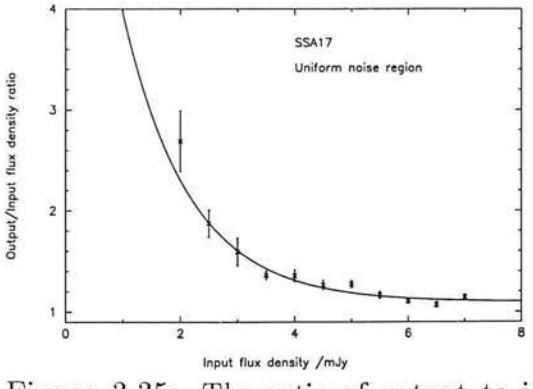

Figure 3.35: The ratio of output to input flux density against input flux density, for the uniform noise regions of the SSA17 field from the "Hawaii Submm Survey".

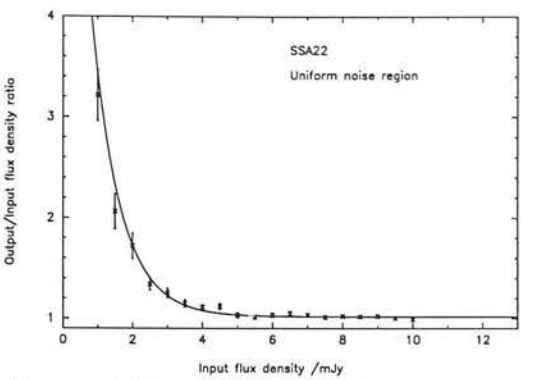

Figure 3.36: The ratio of output to input flux density against input flux density, for the uniform noise regions of the SSA22 field from the "Hawaii Submm Survey".

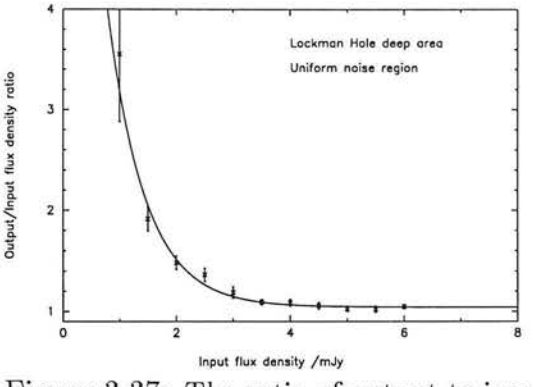

Figure 3.37: The ratio of output to input flux density against input flux density, for the uniform noise regions of the Lockman Hole deep area from the "Hawaii Submm Survey".

Survey Field	Noise Region	g arcsec/mJy	h arcsec	χ^2
ELAIS N2	uniform	0.17364	4.6693	1.45445
Lockman Hole wide area	uniform	0.12235	4.5791	0.90109
Lockman Hole deep strip	uniform	0.16592	4.2357	1.65490
03h wide area	uniform	0.13772	4.2672	1.05487
03h deep area	uniform	0.46026	5.2313	2.22813
10h	uniform	0.36036	4.8814	2.04834
14h	uniform	0.20604	4.2997	0.52830
22h	uniform	0.33656	5.6634	0.76516
Hubble Deep Field	uniform	0.42609	5.0274	1.11186
SSA13 wide area	uniform	0.11505	4.2934	0.76635
SSA13 deep area	uniform	0.43070	5.1689	0.36683
SSA17	uniform	0.37809	5.1600	0.65348
SSA22	uniform	0.29406	4.3191	1.79829
Lockman Hole deep area	uniform	0.33253	4.2634	0.54652
ELAIS N2	non-uni	0.51966	9.4885	4.09028
Lockman Hole wide area	non-uni	0.00000	4.1870	1.88165

Table 3.4: Best fit values determined for g and h in equation 3.3, describing the mean positional error against input flux density for each of the survey fields and noise regions.

3.2.3 Positional Uncertainty

The mean positional uncertainty in retrieving the fake sources was found to be well approximated by a linear dependence on the input flux density such that

$$\text{positional error} = -\text{g}x + \text{h} \tag{3.3}$$

where x is the input flux density, the values of g and h for each 850 μm survey field were determined by a minimised χ^2 fit to the simulation results (given in Table 3.4), and the positional uncertainty is given in arcseconds. Figs. 3.38 and 3.39 show the dependence of parameters 'g' and 'h' on rms noise. One might expect a general formula for positional error to depend on the ratio of input flux density to rms noise such that $\text{g}_{\text{general}} \propto 1\sigma_{\text{rms}}^{-1}$ in this straight line desription. The data points are consistent with $\text{g}_{\text{general}} \times 1\sigma_{\text{rms}} \sim 0.35$ arcseconds, but the large scatter means that a simple straight line with negative gradient provides a similarly good description. The values of parameter 'h' have a median of ~ 4.65 between all the survey fields, and there is no obvious trend with rms noise.

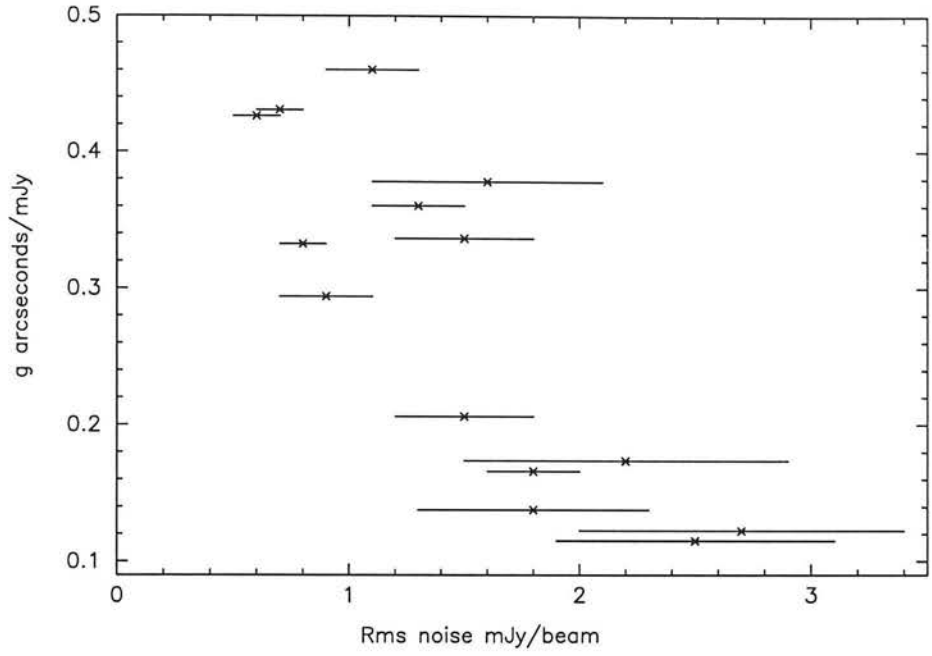

Figure 3.38: Best-fit values for the parameter "g" as given in Table 3.4, plotted against the 1σ rms noise levels as determined from the uniform regions of the 14.5" Gaussian convolved noise images (values given in Table 3.1). The horizontal error bars show the standard deviation of the noise about the mean level.

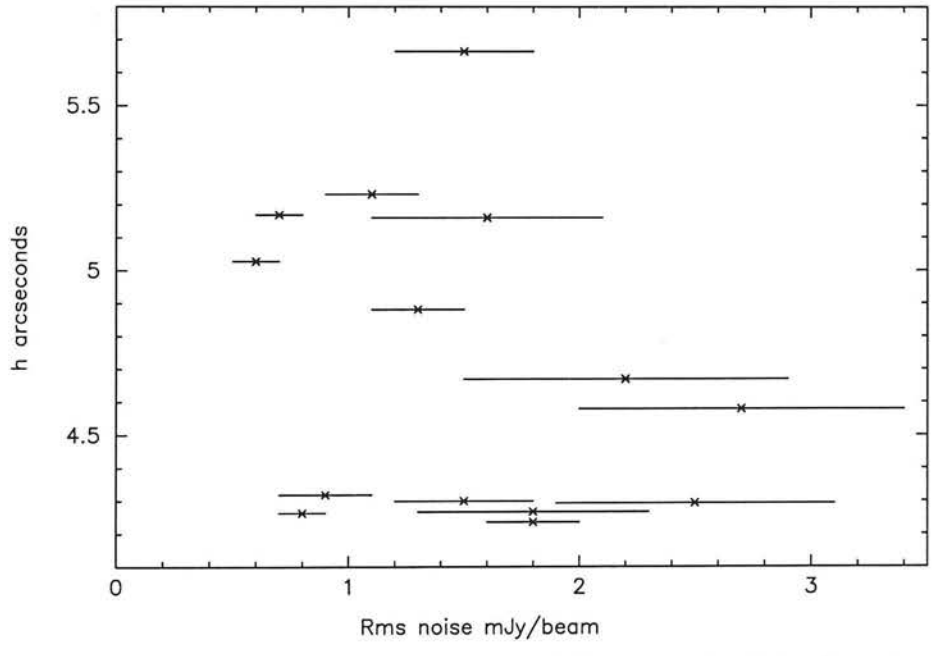

Figure 3.39: Best-fit values for the parameter "h" as given in Table 3.4, plotted against the 1σ rms noise levels as determined from the uniform regions of the 14.5" Gaussian convolved noise images (values given in Table 3.1). The horizontal error bars show the standard deviation of the noise about the mean level.

Figures 3.40 through to 3.55 show the mean positional error of the retrieved fake sources against input flux density. The error bars are the standard error on the mean. Again, one can see that the data from the "SCUBA 8 mJy Survey" fields (Figs. 3.40 to 3.44) show a greater scatter in the non-uniform noise regions than the central uniform noise parts, with a generally greater positional uncertainty in these border areas $4-5$ arcseconds, as compared with $2-4$ arcseconds in the uniform noise regions). The positional accuracy improves with higher flux density sources (and hence better signal-to-noise). Such estimates of positional error do not include any pointing errors arising whilst the data is being taken at the telescope. The pointing of the JCMT is known to be very accurate for such a large dish; typical pointing errors are less than 3 arcseconds, much less than the 850 μm beam size of 14.5 arcseconds FWHM. Several pointing problems have been discovered during the period in which these deep submillimetre surveys were undertaken (as discussed in section 2.4.4), however, the fact that each map is built up from many shorter integration datasets limits the impact which these pointing inaccuracies can have on the final image. Overall, the uniform noise regions of all the survey areas suggest likely positional errors of $2-4$ arcseconds in source retrieval, arising from the effects of noise and confusion.

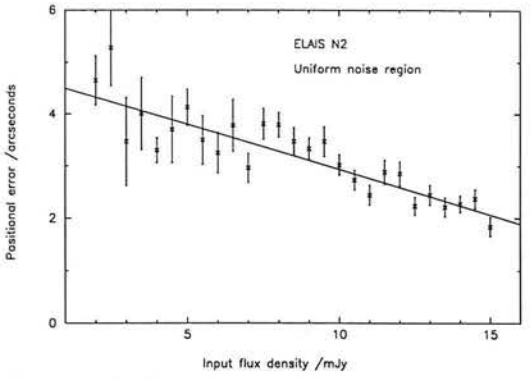

Figure 3.40: Mean positional uncertainty against input flux density, for the uniform noise regions of the ELAIS N2 field from the "SCUBA 8 mJy Survey".

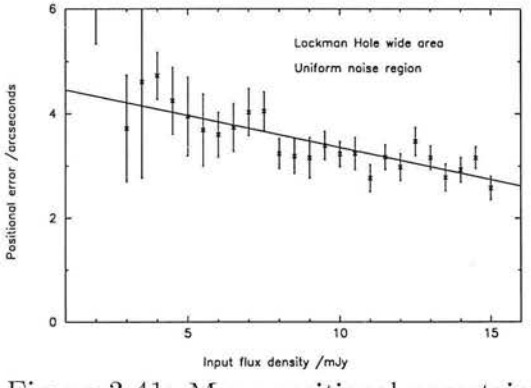

Figure 3.41: Mean positional uncertainty against input flux density, for the uniform noise regions of the Lockman Hole East wide area field from the "SCUBA 8 mJy Survey".

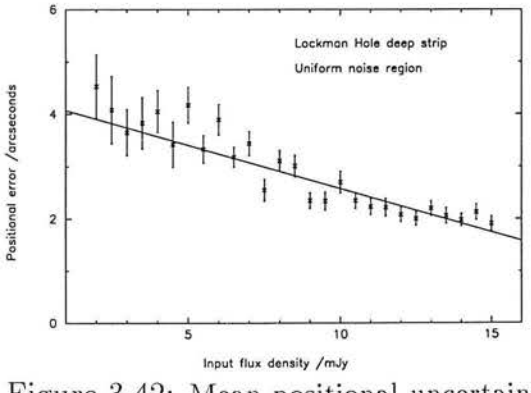

Figure 3.42: Mean positional uncertainty against input flux density, for the uniform noise regions of the Lockman Hole East deep strip from the "SCUBA 8 mJy Survey".

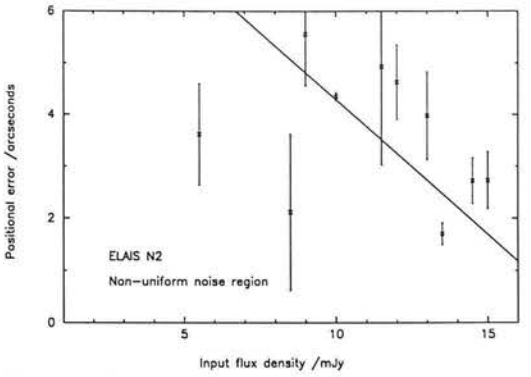

Figure 3.43: Mean positional uncertainty against input flux density, for the non-uniform noise regions of the ELAIS N2 field from the "SCUBA 8 mJy Survey".

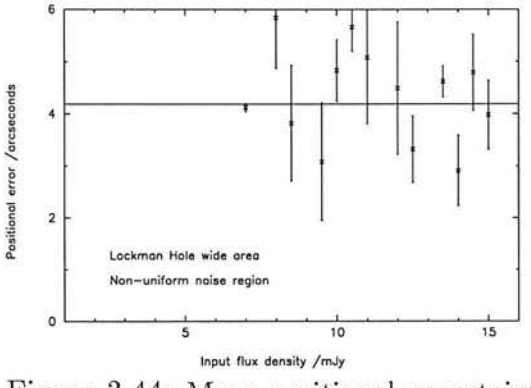

Figure 3.44: Mean positional uncertainty against input flux density, for the non-uniform noise regions of the Lockman Hole East wide area field from the "SCUBA 8 mJy Survey".

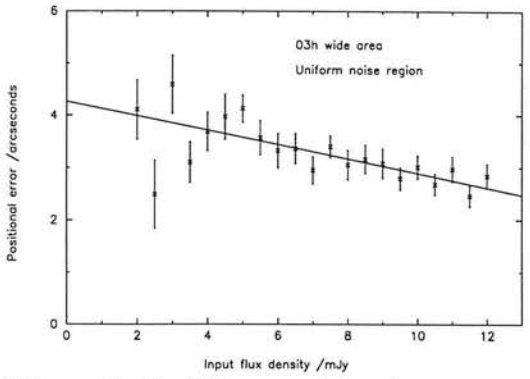

Figure 3.45: Mean positional uncertainty against input flux density, for the uniform noise regions of the 03 hour wide area field from the "CUDSS".

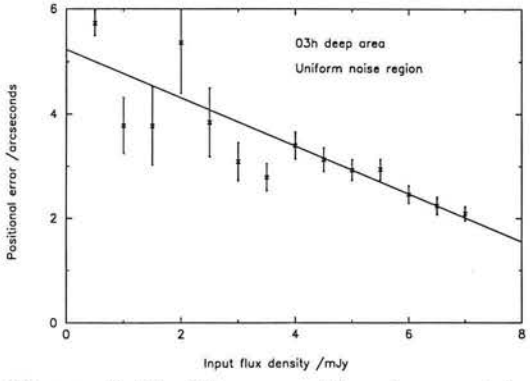

Figure 3.46: Mean positional uncertainty against input flux density, for the uniform noise regions of the 03 hour deep area from the "CUDSS".

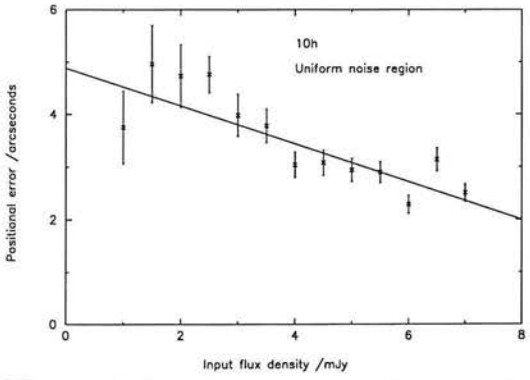

Figure 3.47: Mean positional uncertainty against input flux density, for the uniform noise regions of the 10 hour field from the "CUDSS".

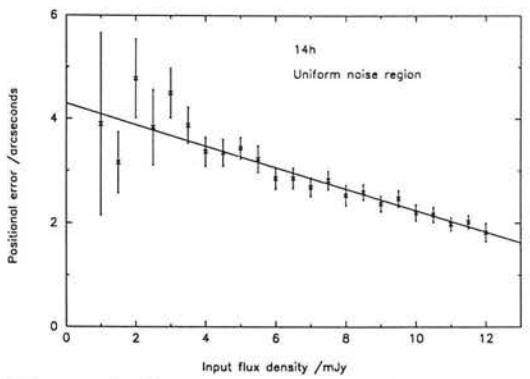

Figure 3.48: Mean positional uncertainty against input flux density, for the uniform noise regions of the 14 hour field from the "CUDSS".

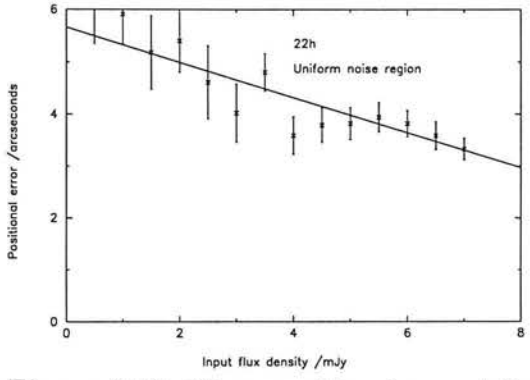

Figure 3.49: Mean positional uncertainty against input flux density, for the uniform noise regions of the 22 hour field from the 'CUDSS".

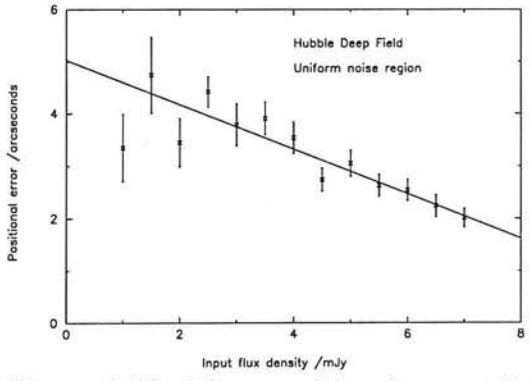

Figure 3.50: Mean positional uncertainty against input flux density, for the uniform noise regions of the Hubble Deep Field.

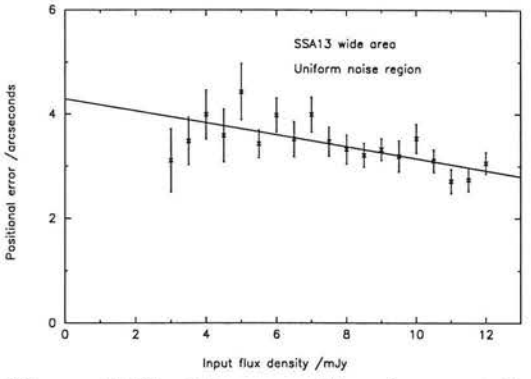

Figure 3.51: Mean positional uncertainty against input flux density, for the uniform noise regions of the SSA13 wide area field from the "Hawaii Submm Survey".

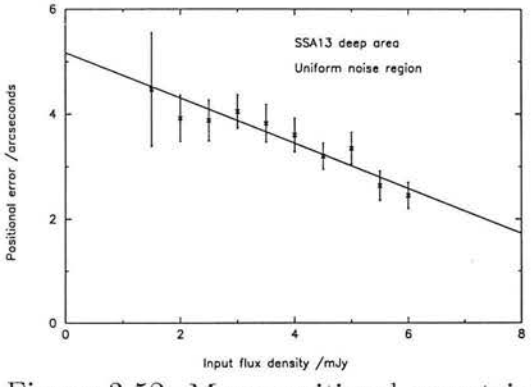

Figure 3.52: Mean positional uncertainty against input flux density, for the uniform noise regions of the SSA13 hour deep area from the "Hawaii Submm Survey".

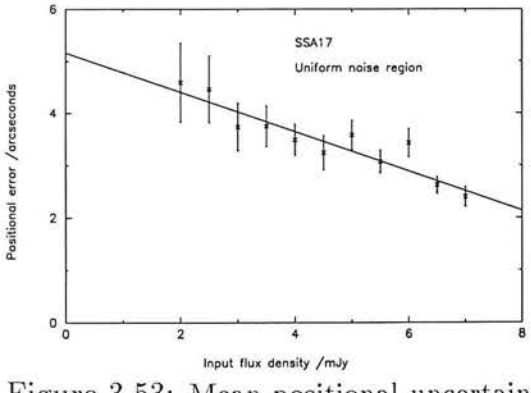

Figure 3.53: Mean positional uncertainty against input flux density, for the uniform noise regions of the SSA17 field from the "Hawaii Submm Survey".

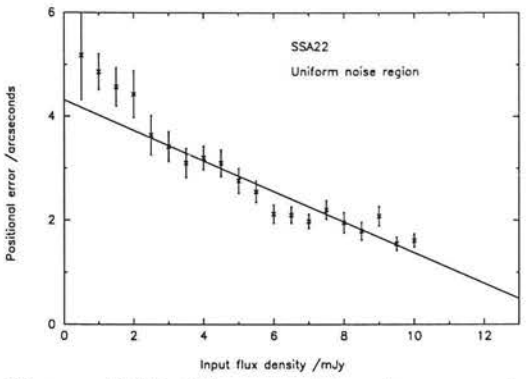

Figure 3.54: Mean positional uncertainty against input flux density, for the uniform noise regions of the SSA22 field from the "Hawaii Submm Survey".

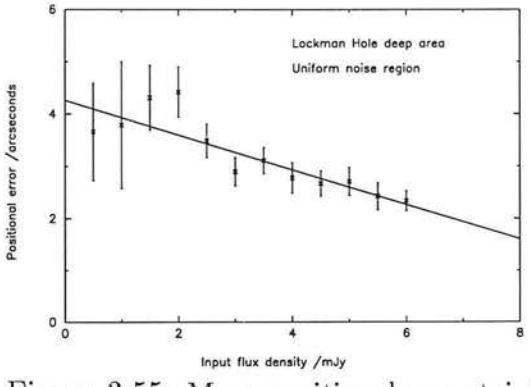

Figure 3.55: Mean positional uncertainty against input flux density, for the uniform noise regions of the Lockman Hole deep area from the "Hawaii Submm Survey".

3.3 Completely simulated maps

In order to obtain constraints on the fraction of recovered 850 μm sources arising from confusion and noise, as well as integrated completeness and count correction factors, 100 simulated images of each of the survey fields were generated. The assumed source counts were taken from the best fit of a simple power-law model (in the format first employed by Barger et al., 1999) to the differential counts given in Chapter 5, which were corrected for completeness and flux-boosting at the $> 3.50\sigma$ level using the simulation results of Section 3.2. Specifically, the differential counts are given by:

$$\frac{dN(S)}{dS} = \frac{N_0}{(a + S^{\alpha})} \tag{3.4}$$

where $N_0 = 2.67 \times 10^4$, a = 0.49 and $\alpha = 3.14$, which predicts a total 850 μm background of 3.8×10^4 mJy deg^{-2}, consistent with the value of 4.4×10^4 mJy deg^{-2} measured by Fixsen et al. (1998). A realistic model of the background counts was produced , by randomising the number of sources placed into each simulated field at 0.1 mJy intervals, from 0.1 – 14.0 mJy, according to a normal distribution about the number expected. Each source was then allocated a random position and the whole image was convolved with the beam. The simulated field is initially created to be larger than the actual field, allowing for the negative sidelobes of sources centred off-field in the final image to appear in it. The clustering properties of the SCUBA population are, at present, not well characterised. Results presented in Chapter 5 suggest that at least the very brightest SCUBA sources (> 5 mJy) are strongly clustered on arcminute scales, consistent with the idea that these objects are progenitors of present day massive ellipticals, but there is insufficient blank field survey data available to allow a realistic clustering component to be added into the selection of positions within the simulations. This means that these simulations which make the assumption of a random distribution (ie. no clustering) can only be used as a first approximation in determining the level of spurious / confused source contamination.

Noise overlays were constructed by subtracting the full minimised χ^2 fit model (i.e. the model representation of the full sky region comprised of the best-fit beam profiles to all of the peaks in the image) from the zero-footprint signal maps of the actual survey data. The source-extraction algorithm was then re-run on these residual images to determine the number of sources which could be recovered from

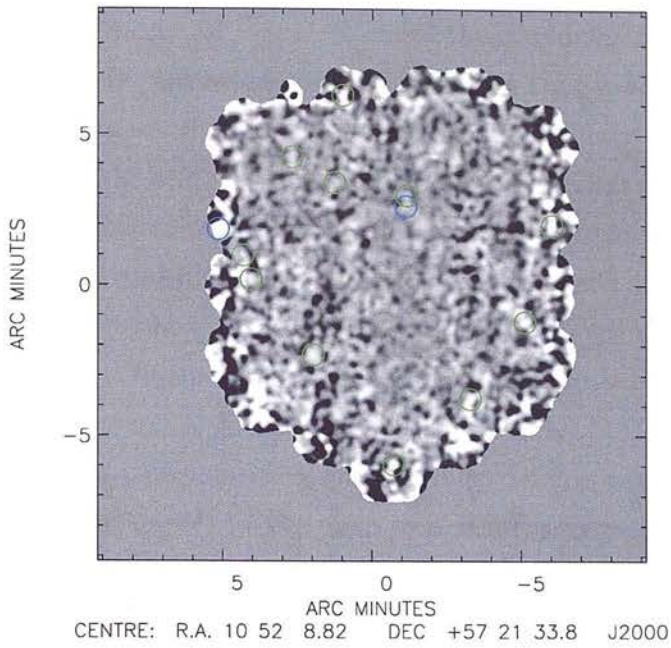

Figure 3.56: Gaussian smoothed residual signal map of the Lockman Hole East from the "SCUBA 8mJy Survey". Display levels are the 95% auto-cut levels from the GAIA image analysis tool (-7.0 - 7.0 mJy). Any residual peaks recovered with S/N > 4.00 are circled in red, 3.50 < S/N < 3.99 are circled in blue, and 3.00 < S/N < 3.49 are circled in green.

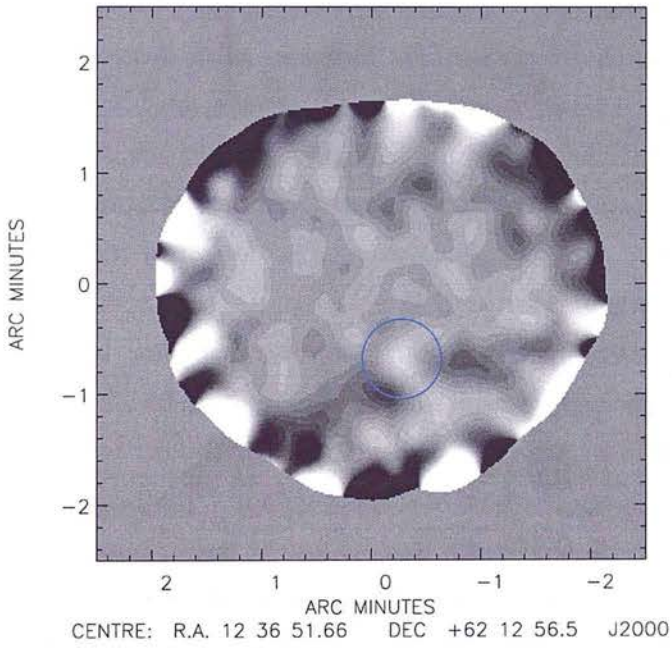

Figure 3.57: Gaussian smoothed residual signal map of the Hubble Deep Field. Display levels are the 95% auto-cut levels from the GAIA image analysis tool (-4.5 - 4.5 mJy). Any residual peaks recovered with S/N > 4.00 are circled in red, 3.50 < S/N < 3.99 are circled in blue, and 3.00 < S/N < 3.49 are circled in green.

the noise overlays alone, at signal-to-noise thresholds of $1.50 - 4.00\sigma$, spaced regularly at 0.5σ levels. Gaussian statistics predict that given the number of beams in the 464 sq. arcmin of uniform noise, there are likely to be ~ 24 noise peaks recovered at $> 3.00\sigma$ and ~ 0.5 noise peaks recovered at $> 4.00\sigma$ (in fact slightly less than this, as this calculation does not account for the recovery of the negative sidelobes). The actual numbers recovered are 24 and 1 at $> 3.00\sigma$ and $> 4.00\sigma$ respectively, comparing reasonably well with the Gaussian estimates. Additional sources of high-significance ($> 3.00\sigma$) peaks in the residuals might be:

1) A non-Gaussian component in the noise eg. microphonics.
2) A poor fit of the model to the data in a small sub-region of the full dataset.
3) Incomplete source removal, for example a faint source confused with a bright source such that only the brighter of the two sources could be identified by the presence of a peak.

Future improvements to the source extraction algorithm will address points (2) and (3). Currently, however, a poor model-fit to sub-sections of the original map or the presence of any remaining real sources in the residual images will lead to an over-estimate of the level of spurious/confused source contamination, and so the results presented in subsequent tables may be considered an upper limit. Examples of the residual images (smoothed with a 14.5" FWHM Gaussian) for the Lockman Hole East ("SCUBA 8mJy Survey") and HDF may be seen in Figs. 3.56 and 3.57, with any "sources" recovered with signal-to-noise ratio > 4.00 circled in red, signal-to-noise ratio in the range $3.50 - 3.99$ circled in blue, and signal-to-noise ratio in the range $3.00 - 3.49$ circled in green.

The final signal images were constructed by adding the unsmoothed noise-overlay to the simulated background counts, and trimming to the correct size and shape. The original zero-footprint noise maps were used as noise maps for the simulated images, and any "hot" pixels identified with signal-to-noise ratio > 4.00 were re-assigned large noise levels, as was done with the real data. The source extraction algorithm was then applied to each simulated image in an identical way to the actual survey maps. Two examples of the generated images, smoothed with a beam-sized (14.5" FWHM) Gaussian, for both the Lockman Hole East and HDF, are shown in Figs. 3.58 and 3.59. The sources retrieved with signal-to-noise ratio > 4.00 are circled in red, signal-to-noise ratio in the range $3.50 - 3.99$ are circled in blue, and signal-to-noise ratio in the range $3.00 - 3.49$ are circled in

green.

Simulated images of the 03h (CUDSS), SSA13 (Hawaii Survey) and Lockman Hole wide area (8 mJy Survey) fields were created with the small deep regions combined into the wider area surveys, however, in the same way as the adding of one source into the real data and attempting to retrieve it (Section 3.2) the results for the deep and shallower areas were treated separately. The regions of uniform and non-uniform noise were also treated individually, as before.

These simulations differ slightly to those presented in Scott et al. (2002), and this is reflected in the results presented for the "SCUBA 8 mJy Survey" fields (ELAIS N2 and the Lockman Hole East wide area field). Combining the data from the various surveys improves the constraints on the 850 μm source counts (as discussed in Chapter 5), and a steeper source counts model, fit to the combined counts, has been used to create these mock images. This leads to higher densities of fainter sources, and hence increases the fraction of significant detections arising from confusion. The second difference is that a lower flux density cut-off of 14 mJy has been applied, corresponding to the retrieved flux density of the brightest source detected in the uniform regions of any of the survey fields, as opposed to the 20 mJy cut-off employed in the earlier simulations. The presence of sources with artificially high input flux densities increases the fraction of objects retrieved with high signal-to-noise ratios, which in turn overestimates the integral completeness at a given signal-to-noise threshold, particularly in the non-uniform areas where the noise levels are higher. The third difference is the noise overlay added on to the background sources. In previous simulations this was created by rebinning the individual datasets with randomised bolometer astrometry so as to smear out any sources present. This approach was found to have problems in regions with several significant bright sources, which would become smeared together on scrambling, creating a patch of excessive noise. For this reason, and in order to preserve the noise properties of the real data as far as possible, the residual signal maps were adopted as the overlaid noise. These residual maps are the difference between the pixel values of the actual unconvolved signal maps, and the best-fit model of the full sky region as constructed from a series of idealised beam-profiles centred on every peak in the convolved signal image. Hence, the residual maps represent the excess noise levels superimposed on top of the real data. The final difference is in the flux densities of peaks in the convolved maps, considered as potential sources. In Scott et al. (2002), peaks identified at > 3 mJy were considered as possible sources and included in the source extraction matrix,

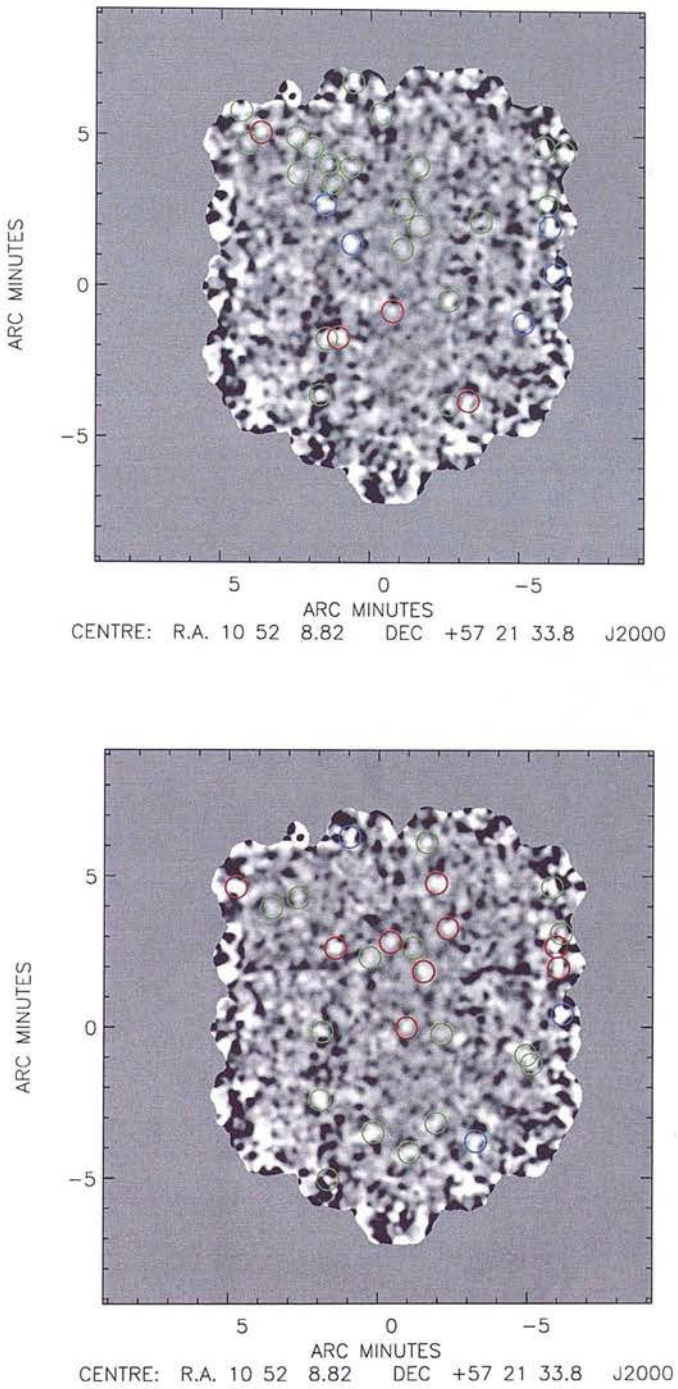

Figure 3.58: Two examples of the fully simulated Lockman Hole East images from the "SCUBA 8 mJy Survey". The images have been convolved with a 14.5" FWHM Gaussian. Display levels are -7.0 – 7.0 mJy, for comparison with the residual image. Sources recovered with S/N > 4.00 are circled in red, 3.50 < S/N < 3.99 are circled in blue, and 3.00 < S/N < 3.49 are circled in green.

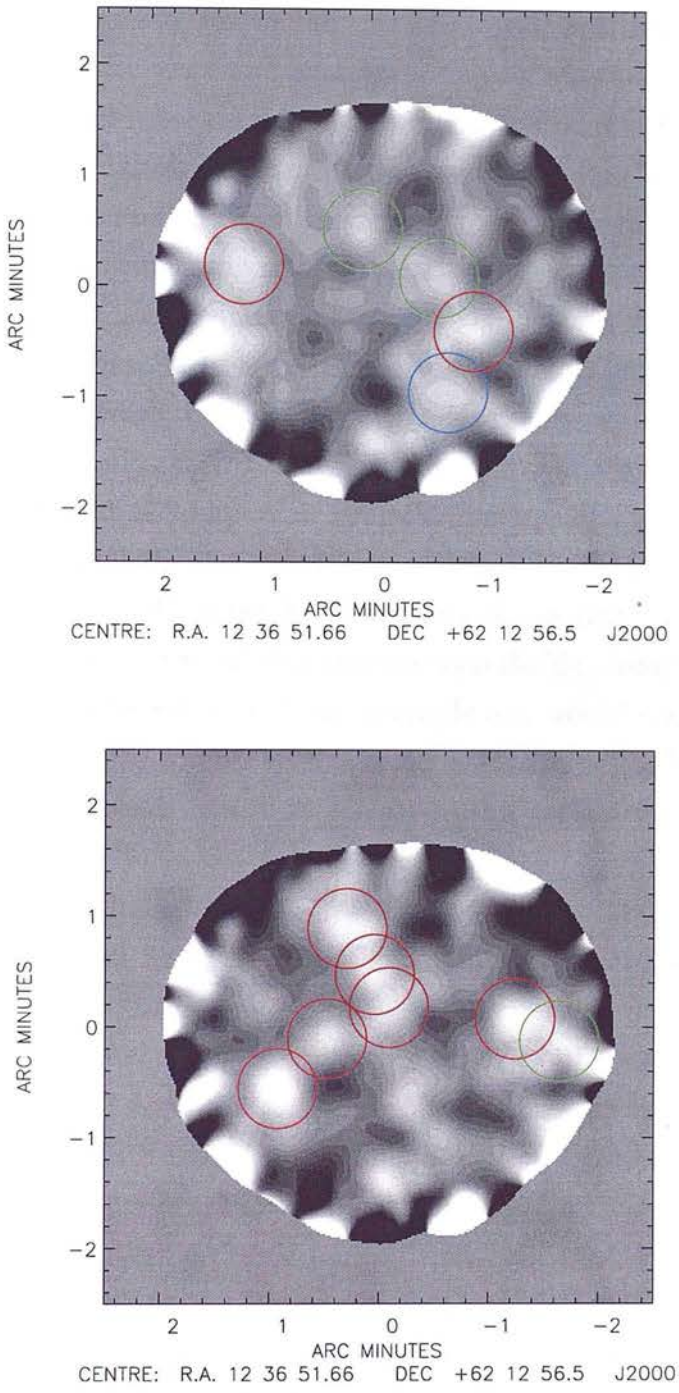

Figure 3.59: Two examples of the fully simulated Hubble Deep Field images. The images have been convolved with a 14.5" FWHM Gaussian. Display levels are -4.5 – 4.5 mJy, for comparison with the residual image. Sources recovered with S/N > 4.00 are circled in red, 3.50 < S/N < 3.99 are circled in blue, and 3.00 < S/N < 3.49 are circled in green.

whereas in these simulations all positive peaks were included in the maximum likelihood fit.

The extracted sources were each identified with the brightest input source, located within 8 arcseconds of the retrieved peak position. Regions of uniform or non-uniform noise were assigned according to whether the input position lay within the uniform noise cutouts. This raises the possibility of a source located very close to the uniform/non-uniform boundary being input and assigned one noise area, but extracted a few arcseconds away under a different noise classification. In these circumstances, both locations were allocated the input position classification so as not to underestimate the completeness. The subsequent simulation analyses were conducted at various signal-to-noise levels down to very low significance levels ($> 1.50\sigma$), even though the source catalogues presented in Chapters 4 and 5 only reach $> 3.00\sigma$. This was to allow an assessment of whether sources recovered at $> 3\sigma$ by other submillimetre groups using different reduction and extraction methods, but which were recovered at lower signal-to-noise in the analysis presented in Chapter 5, were likely to be real. The tabulated results also reflect a broad range of flux density thresholds, some of which are not of particular interest to every field, for example one would not expect to recover a 2 mJy source in a field where the rms noise levels are > 2 mJy. These values were included to allow trends with flux density in the various quantified properties to be identified.

The results of the integral completeness analyses are given in Tables 3.5 to 3.20, for the uniform noise regions of each individual field, and the non-uniform noise regions of the "8 mJy Survey" fields. Flux density thresholds of $2-10$ mJy at 2 mJy intervals, and signal-to-noise thresholds of $1.50-4.00\sigma$ at 0.50σ intervals were considered. The quoted errors are the 1σ Poisson error on the number of sources input to the fields. Comparing the values given in Tables 3.5 and 3.7 with 3.6 and 3.8, there is a marked contrast in the fraction of sources successfully retrieved in the uniform and non-uniform noise regions. For example, at $S_{850} > 8$ mJy and a significance of 3.50σ the uniform noise regions of the Lockman Hole East and ELAIS N2 are $70-75\%$ complete, whereas the non-uniform noise regions are only $10-15\%$ complete. As the flux density threshold drops to reach the faint limit at which significant ($> 3.00\sigma$) sources can still be detected in the uniform noise regions of the respective surveys (corresponding to an integral completeness of $65-75\%$), there is a drop of $5-10\%$ in the fraction of sources recovered for every increase of 0.50σ in the signal-to-noise threshold. The estimated completeness

ELAIS N2 field, uniform noise region						
Flux Density	% Integral Completeness					
	$> 1.50\sigma$	$> 2.00\sigma$	$> 2.50\sigma$	$> 3.00\sigma$	$> 3.50\sigma$	$> 4.00\sigma$
$>$ 2 mJy	45.7 ± 0.5	36.3 ± 0.4	25.6 ± 0.3	17.6 ± 0.2	11.5 ± 0.1	7.6 ± 0.1
$>$ 4 mJy	71.2 ± 1.7	68.9 ± 1.6	60.8 ± 1.4	50.9 ± 1.2	38.7 ± 0.9	28.8 ± 0.7
$>$ 6 mJy	79.9 ± 3.1	79.6 ± 3.1	77.3 ± 3.0	72.8 ± 2.8	64.7 ± 2.5	55.4 ± 2.2
$>$ 8 mJy	76.4 ± 4.4	76.4 ± 4.4	76.1 ± 4.4	74.4 ± 4.3	71.1 ± 4.1	65.2 ± 3.7
$>$ 10 mJy	76.8 ± 6.4	76.8 ± 6.4	76.8 ± 6.4	76.8 ± 6.4	74.6 ± 6.3	71.1 ± 6.0

Table 3.5: Percentage integral completeness results for the uniform noise region of the ELAIS N2 field, over the flux density range 2 – 10 mJy, and for signal-to-noise thresholds of $> 1.50\sigma$ to $> 4.00\sigma$.

ELAIS N2 field, non-uniform noise region						
Flux Density	% Integral Completeness					
	$> 1.50\sigma$	$> 2.00\sigma$	$> 2.50\sigma$	$> 3.00\sigma$	$> 3.50\sigma$	$> 4.00\sigma$
$>$ 2 mJy	12.6 ± 0.3	8.2 ± 0.2	4.7 ± 0.1	2.4 ± 0.1	1.0 ± 0.1	0.4 ± 0.1
$>$ 4 mJy	24.2 ± 1.1	18.3 ± 0.8	12.7 ± 0.6	7.7 ± 0.3	4.0 ± 0.2	1.9 ± 0.1
$>$ 6 mJy	35.6 ± 2.7	31.6 ± 2.4	24.9 ± 1.9	14.7 ± 1.1	9.6 ± 0.7	5.6 ± 0.4
$>$ 8 mJy	37.8 ± 4.4	33.8 ± 3.9	31.1 ± 3.6	23.0 ± 2.7	14.9 ± 1.7	10.8 ± 1.3
$>$ 10 mJy	38.1 ± 5.9	35.7 ± 5.5	33.3 ± 5.1	28.6 ± 4.4	19.0 ± 2.9	11.9 ± 1.8

Table 3.6: Percentage integral completeness results for the non-uniform noise region of the ELAIS N2 field, over the flux density range 2 – 10 mJy, and for signal-to-noise thresholds of $> 1.50\sigma$ to $> 4.00\sigma$.

Lockman Hole wide area field, uniform noise region						
Flux Density	% Integral Completeness					
	$> 1.50\sigma$	$> 2.00\sigma$	$> 2.50\sigma$	$> 3.00\sigma$	$> 3.50\sigma$	$> 4.00\sigma$
$>$ 2 mJy	41.8 ± 0.5	30.0 ± 0.4	19.2 ± 0.2	11.9 ± 0.1	7.1 ± 0.1	4.3 ± 0.1
$>$ 4 mJy	72.0 ± 2.0	65.3 ± 1.8	52.7 ± 1.4	38.8 ± 1.1	26.9 ± 0.7	18.2 ± 0.5
$>$ 6 mJy	78.1 ± 3.5	77.6 ± 3.4	74.4 ± 3.3	64.0 ± 2.8	51.4 ± 2.3	38.2 ± 1.7
$>$ 8 mJy	81.3 ± 5.4	81.3 ± 5.4	80.9 ± 5.4	79.6 ± 5.3	73.8 ± 4.9	60.9 ± 4.1
$>$ 10 mJy	73.0 ± 6.8	73.0 ± 6.8	73.0 ± 6.8	73.0 ± 6.8	72.2 ± 6.7	67.0 ± 6.2

Table 3.7: Percentage integral completeness results for the uniform noise region of the Lockman Hole wide area field, over the flux density range 2 – 10 mJy, and for signal-to-noise thresholds of $> 1.50\sigma$ to $> 4.00\sigma$.

Lockman Hole wide area field, non-uniform noise region						
Flux Density	% Integral Completeness					
	$> 1.50\sigma$	$> 2.00\sigma$	$> 2.50\sigma$	$> 3.00\sigma$	$> 3.50\sigma$	$> 4.00\sigma$
$>$ 2 mJy	19.2 ± 0.3	13.1 ± 0.2	7.9 ± 0.1	3.8 ± 0.1	1.8 ± 0.1	0.7 ± 0.1
$>$ 4 mJy	34.6 ± 1.2	25.7 ± 0.9	18.0 ± 0.6	9.8 ± 0.4	5.4 ± 0.2	2.5 ± 0.1
$>$ 6 mJy	39.6 ± 2.3	34.0 ± 2.0	25.4 ± 1.5	16.2 ± 0.9	8.6 ± 0.5	4.0 ± 0.2
$>$ 8 mJy	36.8 ± 3.1	34.7 ± 2.9	29.9 ± 2.5	19.4 ± 1.6	10.4 ± 0.9	4.9 ± 0.4
$>$ 10 mJy	30.3 ± 3.5	30.3 ± 3.5	28.9 ± 3.3	21.1 ± 2.4	14.5 ± 1.7	7.9 ± 0.9

Table 3.8: Percentage integral completeness results for the non-uniform noise region of the Lockman Hole wide area field, over the flux density range 2 – 10 mJy, and for signal-to-noise thresholds of $> 1.50\sigma$ to $> 4.00\sigma$.

Lockman Hole deep strip field, uniform noise region						
Flux Density	% Integral Completeness					
	$> 1.50\sigma$	$> 2.00\sigma$	$> 2.50\sigma$	$> 3.00\sigma$	$> 3.50\sigma$	$> 4.00\sigma$
$>$ 2 mJy	57.2 ± 1.5	48.6 ± 1.2	38.0 ± 1.0	29.6 ± 0.8	21.7 ± 0.6	15.0 ± 0.4
$>$ 4 mJy	82.3 ± 4.7	82.3 ± 4.7	80.0 ± 4.6	76.1 ± 4.4	63.3 ± 3.6	50.2 ± 2.9
$>$ 6 mJy	85.2 ± 7.9	85.2 ± 7.9	85.2 ± 7.9	85.2 ± 7.9	83.5 ± 7.8	78.3 ± 7.3
$>$ 8 mJy	84.6 ± 11.7	84.6 ± 11.7	84.6 ± 11.7	84.6 ± 11.7	84.6 ± 11.7	84.6 ± 11.7
$>$ 10 mJy	65.4 ± 12.8	65.4 ± 12.8	65.4 ± 12.8	65.4 ± 12.8	65.4 ± 12.8	65.4 ± 12.8

Table 3.9: Percentage integral completeness results for the uniform noise region of the Lockman Hole deep strip, over the flux density range 2 – 10 mJy, and for signal-to-noise thresholds of $> 1.50\sigma$ to $> 4.00\sigma$.

03h deep area field, uniform noise region						
Flux Density	% Integral Completeness					
	$> 1.50\sigma$	$> 2.00\sigma$	$> 2.50\sigma$	$> 3.00\sigma$	$> 3.50\sigma$	$> 4.00\sigma$
$>$ 2 mJy	58.7 ± 2.6	58.5 ± 2.5	57.2 ± 2.5	53.8 ± 2.3	46.6 ± 2.0	38.4 ± 1.7
$>$ 4 mJy	82.2 ± 7.6	82.2 ± 7.6	82.2 ± 7.6	82.2 ± 7.6	82.2 ± 7.6	82.2 ± 7.6
$>$ 6 mJy	88.6 ± 13.4	88.6 ± 13.4	88.6 ± 13.4	88.6 ± 13.4	88.6 ± 13.4	88.6 ± 13.4
$>$ 8 mJy	82.6 ± 17.2	82.6 ± 17.2	82.6 ± 17.2	82.6 ± 17.2	82.6 ± 17.2	82.6 ± 17.2
$>$ 10 mJy	90.0 ± 28.5	90.0 ± 28.5	90.0 ± 28.5	90.0 ± 28.5	90.0 ± 28.5	90.0 ± 28.5

Table 3.10: Percentage integral completeness results for the uniform noise region of the 03h deep area field, over the flux density range 2 – 10 mJy, and for signal-to-noise thresholds of $> 1.50\sigma$ to $> 4.00\sigma$.

03h wide area field, uniform noise region						
Flux Density	% Integral Completeness					
	$> 1.50\sigma$	$> 2.00\sigma$	$> 2.50\sigma$	$> 3.00\sigma$	$> 3.50\sigma$	$> 4.00\sigma$
$>$ 2 mJy	43.8 ± 0.6	35.5 ± 0.5	26.5 ± 0.4	19.2 ± 0.3	13.1 ± 0.2	8.9 ± 0.1
$>$ 4 mJy	68.4 ± 2.2	65.8 ± 2.1	60.4 ± 2.0	52.9 ± 1.7	42.3 ± 1.4	32.6 ± 1.1
$>$ 6 mJy	73.8 ± 4.0	73.2 ± 4.0	70.9 ± 3.8	66.8 ± 3.6	60.3 ± 3.3	52.4 ± 2.8
$>$ 8 mJy	71.5 ± 6.0	71.5 ± 6.0	71.5 ± 6.0	71.5 ± 6.0	68.8 ± 5.7	63.9 ± 5.3
$>$ 10 mJy	69.1 ± 8.4	69.1 ± 8.4	69.1 ± 8.4	69.1 ± 8.4	69.1 ± 8.4	67.6 ± 8.2

Table 3.11: Percentage integral completeness results for the uniform noise region of the 03h wide area field, over the flux density range 2 – 10 mJy, and for signal-to-noise thresholds of $> 1.50\sigma$ to $> 4.00\sigma$.

10h field, uniform noise region						
Flux Density	% Integral Completeness					
	$> 1.50\sigma$	$> 2.00\sigma$	$> 2.50\sigma$	$> 3.00\sigma$	$> 3.50\sigma$	$> 4.00\sigma$
$>$ 2 mJy	44.4 ± 1.7	39.0 ± 1.5	33.6 ± 1.3	26.5 ± 1.0	19.4 ± 0.8	14.8 ± 0.6
$>$ 4 mJy	57.1 ± 5.0	56.4 ± 4.9	55.6 ± 4.8	52.6 ± 4.6	50.4 ± 4.4	47.4 ± 4.1
$>$ 6 mJy	68.1 ± 9.9	68.1 ± 9.9	68.1 ± 9.9	66.0 ± 9.6	66.0 ± 9.6	63.8 ± 9.3
$>$ 8 mJy	70.0 ± 15.7	70.0 ± 15.7	70.0 ± 15.7	70.0 ± 15.7	70.0 ± 15.7	70.0 ± 15.7
$>$ 10 mJy	72.7 ± 21.9	72.7 ± 21.9	72.7 ± 21.9	72.7 ± 21.9	72.7 ± 21.9	72.7 ± 21.9

Table 3.12: Percentage integral completeness results for the uniform noise region of the 10h field, over the flux density range 2 – 10 mJy, and for signal-to-noise thresholds of $> 1.50\sigma$ to $> 4.00\sigma$.

14h field, uniform noise region						
Flux Density	% Integral Completeness					
	$> 1.50\sigma$	$> 2.00\sigma$	$> 2.50\sigma$	$> 3.00\sigma$	$> 3.50\sigma$	$> 4.00\sigma$
$>$ 2 mJy	51.0 ± 0.8	45.1 ± 0.7	36.2 ± 0.5	27.5 ± 0.4	20.6 ± 0.3	15.3 ± 0.2
$>$ 4 mJy	70.3 ± 2.3	69.1 ± 2.2	65.9 ± 2.1	61.5 ± 2.0	55.4 ± 1.8	48.8 ± 1.6
$>$ 6 mJy	74.5 ± 3.9	74.2 ± 3.9	73.4 ± 3.8	70.9 ± 3.7	69.0 ± 3.6	67.4 ± 3.5
$>$ 8 mJy	77.8 ± 6.0	77.8 ± 6.0	77.8 ± 6.0	76.0 ± 5.9	75.4 ± 5.8	74.9 ± 5.8
$>$ 10 mJy	78.3 ± 9.4	78.3 ± 9.4	78.3 ± 9.4	76.8 ± 9.2	76.8 ± 9.2	75.4 ± 9.1

Table 3.13: Percentage integral completeness results for the uniform noise region of the 14h field, over the flux density range 2 – 10 mJy, and for signal-to-noise thresholds of $> 1.50\sigma$ to $> 4.00\sigma$.

22h field, uniform noise region						
Flux Density	% Integral Completeness					
	$> 1.50\sigma$	$> 2.00\sigma$	$> 2.50\sigma$	$> 3.00\sigma$	$> 3.50\sigma$	$> 4.00\sigma$
$>$ 2 mJy	49.9 ± 2.4	45.1 ± 2.2	36.8 ± 1.8	27.7 ± 1.4	20.5 ± 1.0	14.3 ± 0.7
$>$ 4 mJy	72.2 ± 8.1	72.2 ± 8.1	72.2 ± 8.1	72.2 ± 8.1	65.8 ± 7.4	55.7 ± 6.3
$>$ 6 mJy	80.0 ± 16.0	80.0 ± 16.0	80.0 ± 16.0	80.0 ± 16.0	80.0 ± 16.0	80.0 ± 16.0
$>$ 8 mJy	60.0 ± 15.5	60.0 ± 15.5	60.0 ± 15.5	60.0 ± 15.5	60.0 ± 15.5	60.0 ± 15.5
$>$ 10 mJy	75.0 ± 37.5	75.0 ± 37.5	75.0 ± 37.5	75.0 ± 37.5	75.0 ± 37.5	75.0 ± 37.5

Table 3.14: Percentage integral completeness results for the uniform noise region of the 22h field, over the flux density range 2 – 10 mJy, and for signal-to-noise thresholds of $> 1.50\sigma$ to $> 4.00\sigma$.

SSA13 deep area field, uniform noise region						
Flux Density	% Integral Completeness					
	$> 1.50\sigma$	$> 2.00\sigma$	$> 2.50\sigma$	$> 3.00\sigma$	$> 3.50\sigma$	$> 4.00\sigma$
$>$ 2 mJy	51.3 ± 2.0	50.6 ± 1.9	48.4 ± 1.9	47.1 ± 1.8	42.9 ± 1.6	38.8 ± 1.5
$>$ 4 mJy	67.9 ± 5.9	67.9 ± 5.9	67.2 ± 5.8	67.2 ± 5.8	67.2 ± 5.8	67.2 ± 5.8
$>$ 6 mJy	84.1 ± 12.7	84.1 ± 12.7	84.1 ± 12.7	84.1 ± 12.7	84.1 ± 12.7	84.1 ± 12.7
$>$ 8 mJy	68.0 ± 13.6	68.0 ± 13.6	68.0 ± 13.6	68.0 ± 13.6	68.0 ± 13.6	68.0 ± 13.6
$>$ 10 mJy	75.0 ± 21.7	75.0 ± 21.7	75.0 ± 21.7	75.0 ± 21.7	75.0 ± 21.7	75.0 ± 21.7

Table 3.15: Percentage integral completeness results for the uniform noise region of the SSA13 deep area field, over the flux density range 2 – 10 mJy, and for signal-to-noise thresholds of $> 1.50\sigma$ to $> 4.00\sigma$.

SSA13 wide area field, uniform noise region						
Flux Density	% Integral Completeness					
	$> 1.50\sigma$	$> 2.00\sigma$	$> 2.50\sigma$	$> 3.00\sigma$	$> 3.50\sigma$	$> 4.00\sigma$
$>$ 2 mJy	38.6 ± 0.6	29.2 ± 0.5	21.0 ± 0.3	14.2 ± 0.2	9.4 ± 0.2	6.2 ± 0.1
$>$ 4 mJy	61.2 ± 2.1	56.6 ± 1.9	49.5 ± 1.7	39.3 ± 1.4	29.2 ± 1.0	21.8 ± 0.7
$>$ 6 mJy	70.7 ± 3.9	67.0 ± 3.7	63.6 ± 3.5	59.6 ± 3.3	50.6 ± 2.8	42.0 ± 2.3
$>$ 8 mJy	77.0 ± 6.5	76.3 ± 6.5	73.4 ± 6.2	72.7 ± 6.2	66.2 ± 5.6	60.4 ± 5.1
$>$ 10 mJy	73.0 ± 9.2	73.0 ± 9.2	73.0 ± 9.2	73.0 ± 9.2	69.8 ± 8.8	65.1 ± 8.2

Table 3.16: Percentage integral completeness results for the uniform noise region of the SSA13 wide area field, over the flux density range 2 – 10 mJy, and for signal-to-noise thresholds of $> 1.50\sigma$ to $> 4.00\sigma$.

SSA17 field, uniform noise region						
Flux Density	% Integral Completeness					
	$> 1.50\sigma$	$> 2.00\sigma$	$> 2.50\sigma$	$> 3.00\sigma$	$> 3.50\sigma$	$> 4.00\sigma$
$>$ 2 mJy	49.6 ± 1.2	42.7 ± 1.1	35.3 ± 0.9	29.2 ± 0.7	22.9 ± 0.6	18.3 ± 0.5
$>$ 4 mJy	70.9 ± 3.6	69.0 ± 3.6	68.3 ± 3.5	65.1 ± 3.3	57.1 ± 2.9	50.3 ± 2.6
$>$ 6 mJy	78.9 ± 6.5	78.9 ± 6.5	78.9 ± 6.5	78.2 ± 6.5	74.1 ± 6.1	67.3 ± 5.6
$>$ 8 mJy	71.8 ± 8.5	71.8 ± 8.5	71.8 ± 8.5	71.8 ± 8.5	71.8 ± 8.5	71.8 ± 8.5
$>$ 10 mJy	69.7 ± 12.1	69.7 ± 12.1	69.7 ± 12.1	69.7 ± 12.1	69.7 ± 12.1	69.7 ± 12.1

Table 3.17: Percentage integral completeness results for the uniform noise region of the SSA17 field, over the flux density range 2 – 10 mJy, and for signal-to-noise thresholds of $> 1.50\sigma$ to $> 4.00\sigma$.

SSA22 field, uniform noise region						
Flux Density	% Integral Completeness					
	$> 1.50\sigma$	$> 2.00\sigma$	$> 2.50\sigma$	$> 3.00\sigma$	$> 3.50\sigma$	$> 4.00\sigma$
$>$ 2 mJy	50.3 ± 1.2	49.0 ± 1.2	46.3 ± 1.2	43.1 ± 1.1	39.0 ± 1.0	34.6 ± 0.9
$>$ 4 mJy	65.7 ± 3.6	65.4 ± 3.6	64.8 ± 3.5	64.2 ± 3.5	62.7 ± 3.4	60.9 ± 3.3
$>$ 6 mJy	73.9 ± 6.8	73.9 ± 6.8	73.9 ± 6.8	73.1 ± 6.7	73.1 ± 6.7	73.1 ± 6.7
$>$ 8 mJy	69.6 ± 9.3	69.6 ± 9.3	69.6 ± 9.3	69.6 ± 9.3	69.6 ± 9.3	69.6 ± 9.3
$>$ 10 mJy	78.3 ± 16.3	78.3 ± 16.3	78.3 ± 16.3	78.3 ± 16.3	78.3 ± 16.3	78.3 ± 16.3

Table 3.18: Percentage integral completeness results for the uniform noise region of the SSA22 field, over the flux density range 2 – 10 mJy, and for signal-to-noise thresholds of $> 1.50\sigma$ to $> 4.00\sigma$.

Lockman Hole deep field, uniform noise region						
Flux Density	% Integral Completeness					
	$> 1.50\sigma$	$> 2.00\sigma$	$> 2.50\sigma$	$> 3.00\sigma$	$> 3.50\sigma$	$> 4.00\sigma$
$>$ 2 mJy	45.9 ± 1.8	45.5 ± 1.8	43.6 ± 1.7	41.8 ± 1.6	37.9 ± 1.5	33.6 ± 1.3
$>$ 4 mJy	60.4 ± 5.0	60.4 ± 5.0	60.4 ± 5.0	60.4 ± 5.0	59.7 ± 5.0	59.0 ± 4.9
$>$ 6 mJy	68.5 ± 9.3	68.5 ± 9.3	68.5 ± 9.3	68.5 ± 9.3	68.5 ± 9.3	68.5 ± 9.3
$>$ 8 mJy	64.3 ± 12.1	64.3 ± 12.1	64.3 ± 12.1	64.3 ± 12.1	64.3 ± 12.1	64.3 ± 12.1
$>$ 10 mJy	70.6 ± 17.1	70.6 ± 17.1	70.6 ± 17.1	70.6 ± 17.1	70.6 ± 17.1	70.6 ± 17.1

Table 3.19: Percentage integral completeness results for the uniform noise region of the Lockman Hole deep field, over the flux density range 2 – 10 mJy, and for signal-to-noise thresholds of $> 1.50\sigma$ to $> 4.00\sigma$.

Hubble deep field, uniform noise region						
Flux Density	% Integral Completeness					
	$> 1.50\sigma$	$> 2.00\sigma$	$> 2.50\sigma$	$> 3.00\sigma$	$> 3.50\sigma$	$> 4.00\sigma$
$>$ 2 mJy	61.6 ± 2.9	61.6 ± 2.9	61.6 ± 2.9	61.3 ± 2.9	59.8 ± 2.8	57.1 ± 2.7
$>$ 4 mJy	77.3 ± 7.9	77.3 ± 7.9	77.3 ± 7.9	77.3 ± 7.9	77.3 ± 7.9	77.3 ± 7.9
$>$ 6 mJy	93.0 ± 14.2	93.0 ± 14.2	93.0 ± 14.2	93.0 ± 14.2	93.0 ± 14.2	93.0 ± 14.2
$>$ 8 mJy	82.4 ± 20.0	82.4 ± 20.0	82.4 ± 20.0	82.4 ± 20.0	82.4 ± 20.0	82.4 ± 20.0
$>$ 10 mJy	100 ± 40.8	100 ± 40.8	100 ± 40.8	100 ± 40.8	100 ± 40.8	100 ± 40.8

Table 3.20: Percentage integral completeness results for the uniform noise region of the Hubble deep field, over the flux density range 2 – 10 mJy, and for signal-to-noise thresholds of $> 1.50\sigma$ to $> 4.00\sigma$.

percentages in the small deep surveys (such as the 10h and SSA13 deep fields) should be considered as lower limits due to their small area in relation to the beam size. The undersampling in the jiggle pattern affects the data taken up to a beam-width into the field. These elevated noise levels in turn can mask the identification of a potential source located up to a further half a beam-width into the map, despite that region being fully sampled and hence uniform noise. A greater proportion of the field area in a small SCUBA map is affected by this problem than in a wider-area field and may artificially increase the number of bright sources which fail to be recovered. The error bars on the integral completeness measurements at bright flux densities (8 or 10 mJy) are also generally large ($\pm 20\%$) in the smaller fields due to a low source density and hence fewer bright sources being entered into the pencil-beam maps.

Tables 3.21 to 3.26 give the percentage count correction factors, above a specific flux density level, and at a given signal-to-noise ratio threshold, for the uniform noise regions of each individual field, and the non-uniform noise regions of the "8 mJy Survey" fields. Count correction factors at 2 mJy intervals from $S_{850} > 2$ mJy to $S_{850} > 10$ mJy, and significances of better than $1.50 - 4.00\sigma$ at 0.50σ intervals were considered. The first point of note is that the percentage count corrections in the non-uniform noise regions of the "SCUBA 8 mJy Survey" fields (Tables 3.22 and 3.24) are in most cases greater than 100% for the 3.50 and 4.00 significance levels at all flux densities, reflecting the poor levels of completeness in these regions. The converse, however, is true in the regions of uniform noise, implying that the effects of flux-boosting (discussed in Section 3.2) have a stronger effect on the source counts than incompleteness. In the Lockman Hole East and ELAIS N2 fields, the correction factors applied to the bright counts (8 or 10 mJy) is $30 - 40\%$ at S/N > 3.00, $50 - 60\%$ at S/N > 3.50, and $70 - 90\%$ at S/N > 4.00, the trend in signal-to-noise ratio indicative of an increase in the contamination of spurious/confused sources in the raw catalogues as the significance threshold is lowered. The count corrections become less severe with decreasing noise levels. The intermediate depth and sized areas such as the 03h wide area field ("CUDSS"), Lockman Hole deep strip ("8 mJy Survey"), and SSA17 and SSA22 ("Hawaii Survey") require a $70 - 80\%$ correction to the raw counts at S/N > 3.50, and $80 - 90\%$ at S/N > 4.00. The deep single-pointing SCUBA maps such as the 10h and 22h fields ("CUDSS") and the Lockman Hole deep field and SSA13 deep field ("Hawaii Survey") require no count correction

ELAIS N2 field, uniform noise region						
Flux Density	% Count Correction					
	$> 1.50\sigma$	$> 2.00\sigma$	$> 2.50\sigma$	$> 3.00\sigma$	$> 3.50\sigma$	$> 4.00\sigma$
> 2 mJy	44.0 ± 0.3	78.9 ± 0.7	160.5 ± 2.2	334.8 ± 6.5	652.6 ± 17.7	> 1000
> 4 mJy	14.8 ± 0.1	20.8 ± 0.2	36.5 ± 0.5	71.1 ± 1.4	137.3 ± 3.7	245.5 ± 8.9
> 6 mJy	13.3 ± 0.2	16.6 ± 0.3	24.8 ± 0.5	38.5 ± 0.9	61.0 ± 1.8	94.3 ± 3.6
> 8 mJy	17.1 ± 0.4	18.7 ± 0.5	25.4 ± 0.7	37.9 ± 1.3	54.7 ± 2.3	75.7 ± 3.8
> 10 mJy	26.4 ± 1.1	27.1 ± 1.2	33.0 ± 1.6	45.1 ± 2.5	59.7 ± 3.9	75.9 ± 5.6

Table 3.21: Percentage count correction results for the uniform noise region of the ELAIS N2 field, over the flux density range 2 – 10 mJy, and for signal-to-noise thresholds of $> 1.50\sigma$ to $> 4.00\sigma$.

ELAIS N2 field, non-uniform noise region						
Flux Density	% Count Correction					
	$> 1.50\sigma$	$> 2.00\sigma$	$> 2.50\sigma$	$> 3.00\sigma$	$> 3.50\sigma$	$> 4.00\sigma$
> 2 mJy	83.0 ± 1.5	158.4 ± 4.0	467.8 ± 20.5	> 1000	> 1000	> 1000
> 4 mJy	17.8 ± 0.3	33.9 ± 0.9	100.2 ± 4.4	366.2 ± 30.7	> 1000	> 1000
> 6 mJy	6.8 ± 0.1	11.6 ± 0.3	34.1 ± 1.5	124.6 ± 10.5	491.7 ± 81.9	> 1000
> 8 mJy	4.0 ± 0.1	5.8 ± 0.2	14.7 ± 0.7	52.1 ± 4.4	205.6 ± 34.3	616.7 ± 178.0
> 10 mJy	4.7 ± 0.2	6.6 ± 0.3	14.6 ± 0.9	42.0 ± 4.2	120.0 ± 20.3	350.0 ± 101.0

Table 3.22: Percentage count correction results for the non-uniform noise region of the ELAIS N2 field, over the flux density range 2 – 10 mJy, and for signal-to-noise thresholds of $> 1.50\sigma$ to $> 4.00\sigma$.

Lockman Hole wide area field, uniform noise region						
Flux Density	% Count Correction					
	$> 1.50\sigma$	$> 2.00\sigma$	$> 2.50\sigma$	$> 3.00\sigma$	$> 3.50\sigma$	$> 4.00\sigma$
> 2 mJy	45.7 ± 0.4	93.8 ± 1.1	207.2 ± 3.7	459.8 ± 12.3	> 1000	> 1000
> 4 mJy	11.4 ± 0.1	20.7 ± 0.3	44.1 ± 0.8	96.6 ± 2.6	230.5 ± 9.5	448.0 ± 25.8
> 6 mJy	9.7 ± 0.1	12.3 ± 0.2	20.9 ± 0.4	41.2 ± 1.2	91.7 ± 3.9	171.0 ± 9.9
> 8 mJy	12.3 ± 0.3	13.5 ± 0.3	18.1 ± 0.5	26.6 ± 0.9	52.2 ± 2.5	88.6 ± 5.6
> 10 mJy	22.1 ± 1.0	22.7 ± 1.0	28.8 ± 1.4	36.4 ± 2.0	46.9 ± 3.0	65.0 ± 4.9

Table 3.23: Percentage count correction results for the uniform noise region of the Lockman Hole wide area field, over the flux density range 2 – 10 mJy, and for signal-to-noise thresholds of $> 1.50\sigma$ to $> 4.00\sigma$.

Lockman Hole wide area field, non-uniform noise region						
Flux Density	% Count Correction					
	$> 1.50\sigma$	$> 2.00\sigma$	$> 2.50\sigma$	$> 3.00\sigma$	$> 3.50\sigma$	$> 4.00\sigma$
> 2 mJy	59.3 ± 0.8	102.7 ± 1.7	191.8 ± 4.4	441.5 ± 15.2	> 1000	> 1000
> 4 mJy	12.6 ± 0.2	21.8 ± 0.4	40.7 ± 0.9	93.6 ± 3.2	312.7 ± 19.7	> 1000
> 6 mJy	5.3 ± 0.1	8.5 ± 0.1	15.7 ± 0.4	36.1 ± 1.2	120.7 ± 7.6	673.3 ± 100.4
> 8 mJy	3.1 ± 0.1	4.4 ± 0.1	7.6 ± 0.2	17.2 ± 0.6	57.4 ± 3.6	320.0 ± 47.7
> 10 mJy	2.3 ± 0.1	2.9 ± 0.1	4.5 ± 0.1	9.8 ± 0.4	31.4 ± 2.0	172.7 ± 26.0

Table 3.24: Percentage count correction results for the nonuniform noise region of the Lockman Hole wide area field, over the flux density range 2 – 10 mJy, and for signal-to-noise thresholds of $> 1.50\sigma$ to $> 4.00\sigma$.

Lockman Hole deep strip field, uniform noise region						
Flux Density	% Count Correction					
	$> 1.50\sigma$	$> 2.00\sigma$	$> 2.50\sigma$	$> 3.00\sigma$	$> 3.50\sigma$	$> 4.00\sigma$
$>$ 2 mJy	41.5 ± 0.7	65.2 ± 1.3	113.3 ± 3.1	205.5 ± 7.5	352.7 ± 16.9	606.0 ± 38.2
$>$ 4 mJy	26.5 ± 0.8	27.2 ± 0.8	32.5 ± 1.1	45.3 ± 1.7	71.6 ± 3.5	121.0 ± 7.6
$>$ 6 mJy	50.2 ± 3.3	50.2 ± 3.3	50.2 ± 3.3	51.8 ± 3.5	56.1 ± 3.9	63.9 ± 4.8
$>$ 8 mJy	83.9 ± 10.7	83.9 ± 10.7	83.9 ± 10.7	83.9 ± 10.7	83.9 ± 10.7	83.9 ± 10.7
$>$ 10 mJy	81.2 ± 14.4	81.2 ± 14.4	81.2 ± 14.4	81.2 ± 14.4	81.2 ± 14.4	81.2 ± 14.4

Table 3.25: Percentage count correction results for the uniform noise region of the Lockman Hole deep strip field, over the flux density range 2 – 10 mJy, and for signal-to-noise thresholds of $> 1.50\sigma$ to $> 4.00\sigma$.

03h deep area field, uniform noise region						
Flux Density	% Count Correction					
	$> 1.50\sigma$	$> 2.00\sigma$	$> 2.50\sigma$	$> 3.00\sigma$	$> 3.50\sigma$	$> 4.00\sigma$
$>$ 2 mJy	62.3 ± 2.1	64.9 ± 2.3	76.5 ± 2.9	100.4 ± 4.4	140.1 ± 7.2	199.2 ± 12.2
$>$ 4 mJy	58.7 ± 4.1	59.9 ± 4.3	62.8 ± 4.6	64.8 ± 4.8	67.8 ± 5.1	72.8 ± 5.7
$>$ 6 mJy	62.9 ± 7.5	63.8 ± 7.7	63.8 ± 7.7	64.7 ± 7.8	65.7 ± 8.0	65.7 ± 8.0
$>$ 8 mJy	88.5 ± 17.3	88.5 ± 17.3	88.5 ± 17.3	92.0 ± 18.4	92.0 ± 18.4	92.0 ± 18.4
$>$ 10 mJy	71.4 ± 19.1	71.4 ± 19.1	71.4 ± 19.1	76.9 ± 21.3	76.9 ± 21.3	76.9 ± 21.3

Table 3.26: Percentage count correction results for the uniform noise region of the 03h deep area field, over the flux density range 2 – 10 mJy, and for signal-to-noise thresholds of $> 1.50\sigma$ to $> 4.00\sigma$.

03h wide area field, uniform noise region						
Flux Density	% Count Correction					
	$> 1.50\sigma$	$> 2.00\sigma$	$> 2.50\sigma$	$> 3.00\sigma$	$> 3.50\sigma$	$> 4.00\sigma$
$>$ 2 mJy	52.8 ± 0.6	89.2 ± 1.2	165.6 ± 3.2	308.9 ± 8.0	553.0 ± 19.3	919.8 ± 41.3
$>$ 4 mJy	20.4 ± 0.3	27.7 ± 0.5	44.0 ± 0.9	71.4 ± 2.0	116.9 ± 4.1	190.5 ± 8.6
$>$ 6 mJy	20.7 ± 0.5	24.4 ± 0.7	33.1 ± 1.0	51.9 ± 2.0	75.4 ± 3.5	101.8 ± 5.6
$>$ 8 mJy	24.7 ± 1.0	25.6 ± 1.1	35.4 ± 1.8	53.5 ± 3.3	70.6 ± 4.9	87.8 ± 6.9
$>$ 10 mJy	32.2 ± 2.2	32.5 ± 2.3	34.2 ± 2.4	49.3 ± 4.2	68.0 ± 6.8	85.0 ± 9.5

Table 3.27: Percentage count correction results for the uniform noise region of the 03h wide area field, over the flux density range 2 – 10 mJy, and for signal-to-noise thresholds of $> 1.50\sigma$ to $> 4.00\sigma$.

10h field, uniform noise region						
Flux Density	% Count Correction					
	$> 1.50\sigma$	$> 2.00\sigma$	$> 2.50\sigma$	$> 3.00\sigma$	$> 3.50\sigma$	$> 4.00\sigma$
$>$ 2 mJy	77.4 ± 2.6	100.5 ± 3.9	147.9 ± 7.0	231.4 ± 13.7	379.4 ± 28.7	558.0 ± 51.2
$>$ 4 mJy	58.8 ± 3.9	63.0 ± 4.3	73.1 ± 5.4	88.7 ± 7.2	104.7 ± 9.3	129.1 ± 12.7
$>$ 6 mJy	64.4 ± 7.5	65.3 ± 7.7	78.3 ± 10.1	90.4 ± 12.5	92.2 ± 12.9	94.0 ± 13.3
$>$ 8 mJy	66.7 ± 12.2	66.7 ± 12.2	69.0 ± 12.8	76.9 ± 15.1	80.0 ± 16.0	80.0 ± 16.0
$>$ 10 mJy	122.2 ± 40.7	122.2 ± 40.7	122.2 ± 40.7	122.2 ± 40.7	122.2 ± 40.7	122.2 ± 40.7

Table 3.28: Percentage count correction results for the uniform noise region of the 10h field, over the flux density range 2 – 10 mJy, and for signal-to-noise thresholds of $> 1.50\sigma$ to $> 4.00\sigma$.

14h field, uniform noise region						
Flux Density	% Count Correction					
	$> 1.50\sigma$	$> 2.00\sigma$	$> 2.50\sigma$	$> 3.00\sigma$	$> 3.50\sigma$	$> 4.00\sigma$
$>$ 2 mJy	55.5 ± 0.6	83.6 ± 1.1	146.4 ± 2.6	248.4 ± 5.8	394.8 ± 11.6	584.9 ± 21.0
$>$ 4 mJy	34.2 ± 0.6	42.3 ± 0.9	55.4 ± 1.3	71.9 ± 2.0	96.3 ± 3.1	126.9 ± 4.6
$>$ 6 mJy	39.0 ± 1.3	50.2 ± 1.9	69.0 ± 3.0	80.2 ± 3.7	89.5 ± 4.4	96.8 ± 5.0
$>$ 8 mJy	45.9 ± 2.4	52.8 ± 3.0	69.3 ± 4.5	84.3 ± 6.0	92.8 ± 6.9	96.5 ± 7.3
$>$ 10 mJy	61.1 ± 5.7	61.6 ± 5.8	71.1 ± 7.2	80.2 ± 8.7	87.3 ± 9.8	90.8 ± 10.4

Table 3.29: Percentage count correction results for the uniform noise region of the 14h field, over the flux density range 2 – 10 mJy, and for signal-to-noise thresholds of $> 1.50\sigma$ to $> 4.00\sigma$.

22h field, uniform noise region						
Flux Density	% Count Correction					
	$> 1.50\sigma$	$> 2.00\sigma$	$> 2.50\sigma$	$> 3.00\sigma$	$> 3.50\sigma$	$> 4.00\sigma$
$>$ 2 mJy	52.4 ± 1.9	82.6 ± 3.7	138.7 ± 8.0	246.5 ± 18.9	395.3 ± 38.4	634.8 ± 78.1
$>$ 4 mJy	40.7 ± 2.9	42.9 ± 3.2	50.3 ± 4.0	59.8 ± 5.2	76.0 ± 7.4	119.7 ± 14.7
$>$ 6 mJy	56.8 ± 8.6	56.8 ± 8.6	56.8 ± 8.6	61.0 ± 9.5	67.6 ± 11.1	78.1 ± 13.8
$>$ 8 mJy	115.4 ± 32.0	115.4 ± 32.0	115.4 ± 32.0	115.4 ± 32.0	115.4 ± 32.0	125.0 ± 36.1
$>$ 10 mJy	100.0 ± 50.0	100.0 ± 50.0	100.0 ± 50.0	100.0 ± 50.0	100.0 ± 50.0	100.0 ± 50.0

Table 3.30: Percentage count correction results for the uniform noise region of the 22h field, over the flux density range 2 – 10 mJy, and for signal-to-noise thresholds of $> 1.50\sigma$ to $> 4.00\sigma$.

SSA13 deep area field, uniform noise region						
Flux Density	% Count Correction					
	$> 1.50\sigma$	$> 2.00\sigma$	$> 2.50\sigma$	$> 3.00\sigma$	$> 3.50\sigma$	$> 4.00\sigma$
$>$ 2 mJy	74.6 ± 2.5	79.0 ± 2.7	89.3 ± 3.2	102.0 ± 4.0	125.8 ± 5.4	154.4 ± 7.4
$>$ 4 mJy	69.1 ± 5.0	69.4 ± 5.0	70.5 ± 5.1	71.7 ± 5.2	72.8 ± 5.4	74.0 ± 5.5
$>$ 6 mJy	73.3 ± 9.5	73.3 ± 9.5	73.3 ± 9.5	73.3 ± 9.5	73.3 ± 9.5	74.6 ± 9.7
$>$ 8 mJy	119.0 ± 26.0	119.0 ± 26.0	119.0 ± 26.0	119.0 ± 26.0	119.0 ± 26.0	119.0 ± 26.0
$>$ 10 mJy	100.0 ± 28.9	100.0 ± 28.9	100.0 ± 28.9	100.0 ± 28.9	100.0 ± 28.9	100.0 ± 28.9

Table 3.31: Percentage count correction results for the uniform noise region of the SSA13 deep area field, over the flux density range 2 – 10 mJy, and for signal-to-noise thresholds of $> 1.50\sigma$ to $> 4.00\sigma$.

SSA13 wide area field, uniform noise region						
Flux Density	% Count Correction					
	$> 1.50\sigma$	$> 2.00\sigma$	$> 2.50\sigma$	$> 3.00\sigma$	$> 3.50\sigma$	$> 4.00\sigma$
$>$ 2 mJy	59.7 ± 0.8	111.6 ± 1.9	215.8 ± 5.2	423.2 ± 14.2	841.6 ± 39.7	> 1000
$>$ 4 mJy	20.0 ± 0.3	30.0 ± 0.6	51.7 ± 1.3	96.6 ± 3.3	189.0 ± 8.9	327.5 ± 20.4
$>$ 6 mJy	20.4 ± 0.5	26.1 ± 0.7	35.9 ± 1.2	54.4 ± 2.2	91.0 ± 4.8	138.5 ± 9.1
$>$ 8 mJy	29.7 ± 1.4	34.5 ± 1.7	41.4 ± 2.3	49.5 ± 3.0	70.6 ± 5.0	96.5 ± 8.0
$>$ 10 mJy	50.0 ± 4.5	54.8 ± 5.1	59.4 ± 5.8	61.8 ± 6.1	70.8 ± 7.5	80.8 ± 9.1

Table 3.32: Percentage count correction results for the uniform noise region of the SSA13 wide area field, over the flux density range 2 – 10 mJy, and for signal-to-noise thresholds of $> 1.50\sigma$ to $> 4.00\sigma$.

SSA17 field, uniform noise region						
Flux Density	% Count Correction					
	$> 1.50\sigma$	$> 2.00\sigma$	$> 2.50\sigma$	$> 3.00\sigma$	$> 3.50\sigma$	$> 4.00\sigma$
$>$ 2 mJy	66.5 ± 1.3	96.1 ± 2.3	148.3 ± 4.5	226.3 ± 8.4	329.7 ± 14.8	464.7 ± 24.7
$>$ 4 mJy	41.1 ± 1.4	46.2 ± 1.6	56.1 ± 2.2	69.9 ± 3.0	88.7 ± 4.3	113.9 ± 6.2
$>$ 6 mJy	53.6 ± 3.2	57.0 ± 3.5	62.8 ± 4.1	71.0 ± 4.9	77.0 ± 5.6	86.0 ± 6.6
$>$ 8 mJy	76.3 ± 7.9	76.3 ± 7.9	79.8 ± 8.5	83.5 ± 9.1	85.5 ± 9.4	87.7 ± 9.7
$>$ 10 mJy	84.6 ± 13.5	84.6 ± 13.5	89.2 ± 14.7	89.2 ± 14.7	91.7 ± 15.3	91.7 ± 15.3

Table 3.33: Percentage count correction results for the uniform noise region of the SSA17 field, over the flux density range 2 – 10 mJy, and for signal-to-noise thresholds of $> 1.50\sigma$ to $> 4.00\sigma$.

SSA22 field, uniform noise region						
Flux Density	% Count Correction					
	$> 1.50\sigma$	$> 2.00\sigma$	$> 2.50\sigma$	$> 3.00\sigma$	$> 3.50\sigma$	$> 4.00\sigma$
$>$ 2 mJy	84.3 ± 1.9	94.7 ± 2.3	107.4 ± 2.8	126.1 ± 3.5	155.9 ± 4.8	196.2 ± 6.8
$>$ 4 mJy	65.6 ± 2.9	68.6 ± 3.1	71.2 ± 3.3	76.1 ± 3.6	80.3 ± 3.9	84.5 ± 4.2
$>$ 6 mJy	77.3 ± 6.2	77.3 ± 6.2	78.8 ± 6.4	80.4 ± 6.6	82.1 ± 6.8	85.0 ± 7.2
$>$ 8 mJy	94.9 ± 12.4	94.9 ± 12.4	94.9 ± 12.4	94.9 ± 12.4	94.9 ± 12.4	98.2 ± 13.0
$>$ 10 mJy	92.0 ± 18.4	92.0 ± 18.4	92.0 ± 18.4	92.0 ± 18.4	92.0 ± 18.4	92.0 ± 18.4

Table 3.34: Percentage count correction results for the uniform noise region of the SSA22 field, over the flux density range 2 – 10 mJy, and for signal-to-noise thresholds of $> 1.50\sigma$ to $> 4.00\sigma$.

Lockman Hole deep field, uniform noise region						
Flux Density	% Count Correction					
	$> 1.50\sigma$	$> 2.00\sigma$	$> 2.50\sigma$	$> 3.00\sigma$	$> 3.50\sigma$	$> 4.00\sigma$
$>$ 2 mJy	88.2 ± 3.3	98.0 ± 3.8	113.1 ± 4.7	129.5 ± 5.8	155.6 ± 7.6	203.4 ± 11.4
$>$ 4 mJy	63.2 ± 4.2	66.7 ± 4.5	72.4 ± 5.1	77.8 ± 5.7	82.8 ± 6.3	91.1 ± 7.3
$>$ 6 mJy	74.0 ± 8.7	74.0 ± 8.7	78.3 ± 9.4	87.1 ± 11.1	88.5 ± 11.3	88.5 ± 11.3
$>$ 8 mJy	96.6 ± 17.9	96.6 ± 17.9	96.6 ± 17.9	96.6 ± 17.9	96.6 ± 17.9	96.6 ± 17.9
$>$ 10 mJy	113.3 ± 29.3	113.3 ± 29.3	113.3 ± 29.3	113.3 ± 29.3	113.3 ± 29.3	113.3 ± 29.3

Table 3.35: Percentage count correction results for the uniform noise region of the Lockman Hole deep field, over the flux density range 2 – 10 mJy, and for signal-to-noise thresholds of $> 1.50\sigma$ to $> 4.00\sigma$.

Hubble deep field, uniform noise region						
Flux Density	% Count Correction					
	$> 1.50\sigma$	$> 2.00\sigma$	$> 2.50\sigma$	$> 3.00\sigma$	$> 3.50\sigma$	$> 4.00\sigma$
$>$ 2 mJy	102.5 ± 4.9	102.5 ± 4.9	102.7 ± 4.9	104.7 ± 5.0	108.7 ± 5.3	118.1 ± 6.1
$>$ 4 mJy	80.8 ± 7.4	80.8 ± 7.4	80.8 ± 7.4	80.8 ± 7.4	80.8 ± 7.4	80.8 ± 7.4
$>$ 6 mJy	82.7 ± 11.5	82.7 ± 11.5	82.7 ± 11.5	82.7 ± 11.5	82.7 ± 11.5	82.7 ± 11.5
$>$ 8 mJy	81.0 ± 17.7	81.0 ± 17.7	81.0 ± 17.7	81.0 ± 17.7	81.0 ± 17.7	81.0 ± 17.7
$>$ 10 mJy	85.7 ± 32.4	85.7 ± 32.4	85.7 ± 32.4	85.7 ± 32.4	85.7 ± 32.4	85.7 ± 32.4

Table 3.36: Percentage count correction results for the uniform noise region of the Hubble deep field, over the flux density range 2 – 10 mJy, and for signal-to-noise thresholds of $> 1.50\sigma$ to $> 4.00\sigma$.

in the 8−10 mJy range, and a 70−90% correction at $S_{850} > 4$ mJy to $S_{850} > 6$ mJy, for applied signal-to-noise thresholds of 3.00 or higher. At 2 or 3 mJy, the very faintest source flux density levels accessible in a blank field survey due to the confusion limit being reached, the count correction factor again exceeds 100%. This is because the extraction of sources becomes less complete as confusion worsens, and begins to offset and even exceed the effect of flux-boosting which dominated at the brighter end of the counts. These simulations show that the raw source counts will be an overestimate of the true source counts, and this will be readdressed in Section 5.3 where the 850 μm source counts are considered in greater detail.

The final property of the survey data investigated by these simulations is the relationship of the output-to-input flux densities of the sources, with signal-to-noise ratio. The results for the uniform noise regions of each individual field, and the non-uniform noise regions of the "8 mJy Survey" fields are given in Tables 3.37 to 3.52, for significances in the range $> 1.50\sigma$ to $> 4.00\sigma$ at 0.50σ intervals. The first quantity to be considered was the fraction of "sources" recovered above a specific signal-to-noise threshold which could be attributed to noise only, by running the source extraction algorithm purely on the residual signal maps with no background counts added in (Column 2 in the tables). Each source recovered from the simulated images was then classified according to the relation between the output and identified input flux density. The classes were:

1) Fainter. The retrieved flux density was fainter than the input source with which it had been identified ($S_{in} > S_{out}$).
2) Within error bars. The input flux density lay within the $1\sigma_{rms}$ error bars of the retrieved value ($S_{out} - err_{out} < S_{in} < S_{out} + err_{out}$).
3) Boosted. The input flux density was less than the lower error boundary on the output value, but was still within a factor of 2 of the measured flux density ($S_{out}/2 < S_{in} < S_{out} - err_{out}$).
4) Spurious / confused. The fitted flux density to the peak could not be identified with a source in the input catalogue, located within 8 arcseconds and a factor 2 in brightness ($S_{in} < S_{out}/2$).

The percentage of sources classified as (1), (2), (3) and (4) are given in Columns 3, 4, 5 and 6 respectively. As a point of note, the peaks identified

in the residual signal image do not just contribute to the confused / spurious fraction, but may affect any of the classifications of source to some extent. In all cases, the fraction of sources which are recovered at a fainter flux density than they were input is $< 10\%$. In the uniform noise regions, $\sim 65 - 70\%$ of the sources recovered with S/N > 4.00 may be identified as boosted or within the error bars. In the wider-area shallower surveys, this number drops to $\sim 55 - 65\%$ for S/N > 3.50 and $\sim 40 - 55\%$ for S/N > 3.00. The decline with signal-to-noise ratio is less marked in the fields with lower rms noise levels, and in fact remains approximately constant at the $65 - 70\%$ level in the deep single-pointing SCUBA fields. The number of sources categorised as boosted is approximately the same as the number for which the identified input object fell within the extracted $1\sigma_{\rm rms}$ error bars. The confused / spurious fraction of sources in the non-uniform regions of the "8 mJy Survey" fields are markedly higher than their uniform region counterparts, even cutting at high signal-to-noise levels. The Lockman Hole East is the worst of the two, with $\sim 90\%$ of the recovered "sources" unidentified with an input source at least 1/2 as bright, even at $> 4.00\sigma$. The ELAIS N2 field is not quite as severe, but still $\sim 40\%$ of the recovered $> 4.00\sigma$ peaks fall into the spurious / confused category, rising to $\sim 90\%$ at $> 3.00\sigma$. This casts severe doubt on the reality of any $> 3.00\sigma$ objects identified in the high noise regions near the edge of the maps. The simulations imply that up to $20 - 30\%$ of the $> 4.00\sigma$ peaks may the result of confusion or noise, increasing to $30 - 40\%$ at $> 3.50\sigma$. and $\sim 30 - 60\%$ at $> 3.00\sigma$. The fields with the highest noise levels (Lockman Hole wide area field, ELAIS N2, and the SSA13 wide area field) show the highest levels of contamination and the deepest surveys the least at both S/N > 3.00 and S/N > 3.50, however, there is no obvious trend of spurious / confused fraction with noise at $> 4.00\sigma$. I reiterate that without particularly tight constraints on the number density of the faint SCUBA population, and without knowing the clustering properties, these quantities should be considered a rough guideline only.

The opposing effects of increasing the completeness of a catalogue by dropping to lower signal-to-noise thresholds, while at the same time also introducing a larger fraction of spurious / confused sources suggests that setting a cut-off of $> 3.50\sigma$ is a good compromise for selecting SCUBA sources to follow-up. Unless otherwise stated, subsequent analyses in Chapters 4 and 5 are based on the S/N > 3.50 lists.

Simulations of a similar nature to these have been carried out by Eales et al.

ELAIS N2 field, uniform noise region					
	Output vs. input flux density statistics				
S/N threshold	% noise only	% fainter	% within 1σ errors	% boosted	% confused/ spurious
$> 1.50\sigma$	100.7 ± 0.7	0.4 ± 0.1	15.0 ± 0.1	4.1 ± 0.1	80.6 ± 0.6
$> 2.00\sigma$	81.4 ± 1.0	0.6 ± 0.1	13.8 ± 0.1	7.3 ± 0.1	78.4 ± 0.7
$> 2.50\sigma$	60.0 ± 0.8	0.9 ± 0.1	16.4 ± 0.2	12.6 ± 0.2	70.1 ± 0.9
$> 3.00\sigma$	26.6 ± 0.5	1.6 ± 0.1	21.8 ± 0.4	19.8 ± 0.4	56.8 ± 1.1
$> 3.50\sigma$	14.8 ± 0.4	2.1 ± 0.1	28.6 ± 0.8	27.5 ± 0.7	41.8 ± 1.1
$> 4.00\sigma$	0.0 ± 0.0	3.4 ± 0.1	35.4 ± 1.3	35.1 ± 1.3	26.1 ± 0.9

Table 3.37: Output versus input flux density statistics for the uniform noise region of the ELAIS N2 field, for signal-to-noise thresholds in the range $> 1.50\sigma$ to $> 4.00\sigma$.

ELAIS N2 field, non-uniform noise region					
	Output vs. input flux density statistics				
S/N threshold	% noise only	% fainter	% within 1σ errors	% boosted	% confused/ spurious
$> 1.50\sigma$	95.8 ± 1.8	0.0 ± 0.0	3.4 ± 0.1	0.6 ± 0.1	96.0 ± 1.8
$> 2.00\sigma$	84.8 ± 2.4	0.0 ± 0.0	2.6 ± 0.1	1.2 ± 0.1	96.2 ± 2.5
$> 2.50\sigma$	38.5 ± 1.7	0.0 ± 0.0	4.0 ± 0.2	3.5 ± 0.2	92.5 ± 4.1
$> 3.00\sigma$	70.4 ± 5.9	0.0 ± 0.0	7.7 ± 0.7	7.0 ± 0.6	85.2 ± 7.2
$> 3.50\sigma$	0.0 ± 0.0	0.0 ± 0.0	13.9 ± 2.3	25.0 ± 4.2	61.1 ± 10.2
$> 4.00\sigma$	0.0 ± 0.0	0.0 ± 0.0	8.3 ± 2.4	50.0 ± 14.4	41.7 ± 12.0

Table 3.38: Output versus input flux density statistics for the non-uniform noise region of the ELAIS N2 field, for signal-to-noise thresholds in the range $> 1.50\sigma$ to $> 4.00\sigma$.

Lockman Hole wide area field, uniform noise region					
	Output vs. input flux density statistics				
S/N threshold	% noise only	% fainter	% within 1σ errors	% boosted	% confused/ spurious
$> 1.50\sigma$	89.3 ± 0.8	0.3 ± 0.1	12.2 ± 0.1	2.6 ± 0.1	84.9 ± 0.7
$> 2.00\sigma$	69.8 ± 1.1	0.5 ± 0.1	11.7 ± 0.1	5.3 ± 0.1	82.5 ± 1.0
$> 2.50\sigma$	64.3 ± 1.2	0.7 ± 0.1	14.8 ± 0.3	9.7 ± 0.2	74.7 ± 1.3
$> 3.00\sigma$	35.7 ± 1.0	1.1 ± 0.1	20.5 ± 0.5	15.0 ± 0.4	63.3 ± 1.7
$> 3.50\sigma$	0.0 ± 0.0	2.4 ± 0.1	32.7 ± 1.4	23.3 ± 1.0	41.6 ± 1.7
$> 4.00\sigma$	0.0 ± 0.0	3.0 ± 0.2	40.7 ± 2.3	32.5 ± 1.9	23.8 ± 1.4

Table 3.39: Output versus input flux density statistics for the uniform noise region of the Lockman Hole wide area field, for signal-to-noise thresholds in the range $> 1.50\sigma$ to $> 4.00\sigma$.

Lockman Hole wide area field, non-uniform noise region					
	Output vs. input flux density statistics				
S/N threshold	% noise only	% fainter	% within 1σ errors	% boosted	% confused/ spurious
$> 1.50\sigma$	88.1 ± 1.1	0.1 ± 0.1	3.7 ± 0.1	0.5 ± 0.1	95.7 ± 1.2
$> 2.00\sigma$	94.3 ± 1.5	0.1 ± 0.1	2.6 ± 0.1	0.9 ± 0.1	96.4 ± 1.6
$> 2.50\sigma$	82.9 ± 1.9	0.1 ± 0.1	2.6 ± 0.1	1.4 ± 0.1	96.0 ± 2.2
$> 3.00\sigma$	83.4 ± 2.9	0.1 ± 0.1	2.3 ± 0.1	1.9 ± 0.1	95.7 ± 3.3
$> 3.50\sigma$	79.7 ± 5.0	0.0 ± 0.0	3.2 ± 0.2	3.6 ± 0.2	93.2 ± 5.9
$> 4.00\sigma$	0.0 ± 0.0	0.0 ± 0.0	2.2 ± 0.3	11.1 ± 1.7	86.7 ± 12.9

Table 3.40: Output versus input flux density statistics for the non-uniform noise region of the Lockman Hole wide area field, for signal-to-noise thresholds in the range $> 1.50\sigma$ to $> 4.00\sigma$.

Lockman Hole deep strip field, uniform noise region					
	Output vs. input flux density statistics				
S/N threshold	% noise only	% fainter	% within 1σ errors	% boosted	% confused/ spurious
$> 1.50\sigma$	83.3 ± 1.4	0.8 ± 0.1	22.7 ± 0.4	6.6 ± 0.1	69.9 ± 1.1
$> 2.00\sigma$	59.8 ± 1.7	1.2 ± 0.1	18.8 ± 0.4	10.5 ± 0.2	69.6 ± 1.4
$> 2.50\sigma$	44.5 ± 1.2	1.7 ± 0.1	19.9 ± 0.5	16.1 ± 0.4	62.3 ± 1.7
$> 3.00\sigma$	26.9 ± 1.0	2.6 ± 0.1	25.2 ± 0.9	23.3 ± 0.9	49.0 ± 1.8
$> 3.50\sigma$	23.1 ± 1.1	3.9 ± 0.2	30.7 ± 1.5	29.8 ± 1.4	35.6 ± 1.7
$> 4.00\sigma$	0.0 ± 0.0	5.2 ± 0.3	36.9 ± 2.3	35.3 ± 2.2	22.6 ± 1.4

Table 3.41: Output versus input flux density statistics for the uniform noise region of the Lockman Hole deep strip field, for signal-to-noise thresholds in the range $> 1.50\sigma$ to $> 4.00\sigma$.

03h deep area field, uniform noise region					
	Output vs. input flux density statistics				
S/N threshold	% noise only	% fainter	% within 1σ errors	% boosted	% confused/ spurious
$> 1.50\sigma$	62.0 ± 1.7	3.1 ± 0.1	35.9 ± 1.0	15.9 ± 0.4	45.1 ± 1.3
$> 2.00\sigma$	61.5 ± 2.0	3.4 ± 0.1	30.5 ± 1.0	21.0 ± 0.7	45.1 ± 1.4
$> 2.50\sigma$	41.6 ± 1.5	4.0 ± 0.1	29.1 ± 1.1	26.8 ± 1.0	40.1 ± 1.5
$> 3.00\sigma$	0.0 ± 0.0	5.1 ± 0.2	30.9 ± 1.3	30.9 ± 1.3	33.0 ± 1.4
$> 3.50\sigma$	0.0 ± 0.0	5.8 ± 0.3	31.8 ± 1.6	35.8 ± 1.8	26.5 ± 1.4
$> 4.00\sigma$	0.0 ± 0.0	7.5 ± 0.5	34.0 ± 2.1	38.5 ± 2.4	20.0 ± 1.2

Table 3.42: Output versus input flux density statistics for the uniform noise region of the 03h deep area field, for signal-to-noise thresholds in the range $> 1.50\sigma$ to $> 4.00\sigma$.

03h wide area field, uniform noise region					
	Output vs. input flux density statistics				
S/N threshold	% noise only	% fainter	% within 1σ errors	% boosted	% confused/ spurious
$> 1.50\sigma$	89.4 ± 1.0	0.7 ± 0.1	19.5 ± 0.2	5.2 ± 0.1	74.5 ± 0.8
$> 2.00\sigma$	74.2 ± 1.2	1.0 ± 0.1	18.2 ± 0.3	9.0 ± 0.1	71.7 ± 1.0
$> 2.50\sigma$	54.4 ± 1.0	1.6 ± 0.1	20.7 ± 0.4	14.5 ± 0.3	63.2 ± 1.2
$> 3.00\sigma$	27.1 ± 0.7	2.4 ± 0.1	26.3 ± 0.7	19.8 ± 0.5	51.5 ± 1.3
$> 3.50\sigma$	12.1 ± 0.4	4.1 ± 0.1	30.4 ± 1.1	25.3 ± 0.9	40.1 ± 1.4
$> 4.00\sigma$	20.2 ± 0.9	5.4 ± 0.2	34.7 ± 1.6	30.0 ± 1.3	29.8 ± 1.3

Table 3.43: Output versus input flux density statistics for the uniform noise region of the 03h wide area field, for signal-to-noise thresholds in the range $> 1.50\sigma$ to $> 4.00\sigma$.

10h field, uniform noise region					
	Output vs. input flux density statistics				
S/N threshold	% noise only	% fainter	% within 1σ errors	% boosted	% confused/ spurious
$> 1.50\sigma$	58.7 ± 1.8	1.8 ± 0.1	35.5 ± 1.1	10.5 ± 0.3	52.3 ± 1.6
$> 2.00\sigma$	59.4 ± 2.3	2.1 ± 0.1	31.1 ± 1.2	15.9 ± 0.6	51.0 ± 2.0
$> 2.50\sigma$	66.8 ± 3.2	2.4 ± 0.1	31.4 ± 1.5	21.4 ± 1.0	44.8 ± 2.1
$> 3.00\sigma$	0.0 ± 0.0	3.8 ± 0.2	32.1 ± 1.9	26.8 ± 1.6	37.3 ± 2.2
$> 3.50\sigma$	0.0 ± 0.0	5.7 ± 0.4	34.3 ± 2.6	29.1 ± 2.2	30.9 ± 2.3
$> 4.00\sigma$	0.0 ± 0.0	6.7 ± 0.6	36.1 ± 3.3	32.8 ± 3.0	24.4 ± 2.2

Table 3.44: Output versus input flux density statistics for the uniform noise region of the 10h field, for signal-to-noise thresholds in the range $> 1.50\sigma$ to $> 4.00\sigma$.

14h field, uniform noise region					
	Output vs. input flux density statistics				
S/N threshold	% noise only	% fainter	% within 1σ errors	% boosted	% confused/ spurious
$> 1.50\sigma$	88.6 ± 0.9	1.3 ± 0.1	28.5 ± 0.3	7.9 ± 0.1	62.4 ± 0.7
$> 2.00\sigma$	57.9 ± 1.2	1.7 ± 0.1	27.7 ± 0.4	12.9 ± 0.2	57.8 ± 0.8
$> 2.50\sigma$	28.9 ± 0.5	2.5 ± 0.1	30.3 ± 0.5	19.8 ± 0.4	47.3 ± 0.8
$> 3.00\sigma$	10.9 ± 0.3	3.4 ± 0.1	33.7 ± 0.8	26.6 ± 0.6	36.3 ± 0.8
$> 3.50\sigma$	0.0 ± 0.0	4.7 ± 0.1	38.3 ± 1.1	29.8 ± 0.9	27.2 ± 0.8
$> 4.00\sigma$	0.0 ± 0.0	5.6 ± 0.2	40.7 ± 1.5	33.4 ± 1.2	20.3 ± 0.7

Table 3.45: Output versus input flux density statistics for the uniform noise region of the 14h field, for signal-to-noise thresholds in the range $> 1.50\sigma$ to $> 4.00\sigma$.

22h field, uniform noise region					
	Output vs. input flux density statistics				
S/N threshold	% noise only	% fainter	% within 1σ errors	% boosted	% confused/ spurious
$> 1.50\sigma$	94.8 ± 3.3	1.3 ± 0.1	28.9 ± 1.0	7.8 ± 0.3	62.0 ± 2.1
$> 2.00\sigma$	39.4 ± 4.2	1.6 ± 0.1	26.6 ± 1.2	13.0 ± 0.6	58.8 ± 2.6
$> 2.50\sigma$	33.1 ± 1.9	2.6 ± 0.2	27.8 ± 1.	19.2 ± 1.1	50.3 ± 2.9
$> 3.00\sigma$	0.0 ± 0.0	3.5 ± 0.3	34.1 ± 2.6	22.9 ± 1.8	39.4 ± 3.0
$> 3.50\sigma$	0.0 ± 0.0	5.7 ± 0.5	40.6 ± 3.9	23.6 ± 2.3	30.2 ± 2.9
$> 4.00\sigma$	0.0 ± 0.0	9.1 ± 1.1	45.5 ± 5.6	25.8 ± 3.2	19.7 ± 2.4

Table 3.46: Output versus input flux density statistics for the uniform noise region of the 22h field, for signal-to-noise thresholds in the range $> 1.50\sigma$ to $> 4.00\sigma$.

SSA13 deep area field, uniform noise region					
	Output vs. input flux density statistics				
S/N threshold	% noise only	% fainter	% within 1σ errors	% boosted	% confused/ spurious
$> 1.50\sigma$	122.0 ± 3.2	4.3 ± 0.1	30.6 ± 0.8	18.0 ± 0.5	47.1 ± 1.2
$> 2.00\sigma$	40.8 ± 3.5	4.2 ± 0.1	27.6 ± 0.8	21.6 ± 0.6	46.6 ± 1.3
$> 2.50\sigma$	42.4 ± 1.4	4.4 ± 0.1	24.6 ± 0.8	26.9 ± 0.9	44.1 ± 1.4
$> 3.00\sigma$	0.0 ± 0.0	5.3 ± 0.2	24.4 ± 0.9	29.6 ± 1.1	40.7 ± 1.5
$> 3.50\sigma$	0.0 ± 0.0	5.7 ± 0.2	24.2 ± 1.0	33.9 ± 1.5	36.3 ± 1.6
$> 4.00\sigma$	0.0 ± 0.0	6.4 ± 0.3	23.5 ± 1.1	37.1 ± 1.8	33.0 ± 1.6

Table 3.47: Output versus input flux density statistics for the uniform noise region of the SSA13 deep area field, for signal-to-noise thresholds in the range $> 1.50\sigma$ to $> 4.00\sigma$.

SSA13 wide area field, uniform noise region					
	Output vs. input flux density statistics				
S/N threshold	% noise only	% fainter	% within 1σ errors	% boosted	% confused/ spurious
$> 1.50\sigma$	96.1 ± 1.2	0.7 ± 0.1	16.7 ± 0.2	3.9 ± 0.1	78.7 ± 1.0
$> 2.00\sigma$	67.9 ± 1.7	1.1 ± 0.1	15.7 ± 0.3	7.3 ± 0.1	75.9 ± 1.3
$> 2.50\sigma$	51.4 ± 1.2	1.7 ± 0.1	18.8 ± 0.5	12.2 ± 0.3	67.3 ± 1.6
$> 3.00\sigma$	11.2 ± 0.4	2.1 ± 0.1	24.2 ± 0.8	18.7 ± 0.6	55.0 ± 1.8
$> 3.50\sigma$	22.3 ± 1.1	3.1 ± 0.1	31.4 ± 1.5	26.7 ± 1.3	38.8 ± 1.8
$> 4.00\sigma$	0.0 ± 0.0	4.7 ± 0.3	36.4 ± 2.3	32.6 ± 2.0	26.4 ± 1.6

Table 3.48: Output versus input flux density statistics for the uniform noise region of the SSA13 wide area field, for signal-to-noise thresholds in the range $> 1.50\sigma$ to $> 4.00\sigma$.

SSA17 field, uniform noise region					
	Output vs. input flux density statistics				
S/N threshold	% noise only	% fainter	% within 1σ errors	% boosted	% confused/ spurious
$> 1.50\sigma$	91.7 ± 1.8	1.7 ± 0.1	29.7 ± 0.6	10.2 ± 0.2	58.5 ± 1.1
$> 2.00\sigma$	51.9 ± 2.2	2.0 ± 0.1	25.6 ± 0.6	16.1 ± 0.4	56.3 ± 1.4
$> 2.50\sigma$	9.0 ± 0.3	2.5 ± 0.1	26.8 ± 0.8	22.0 ± 0.7	48.7 ± 1.5
$> 3.00\sigma$	13.8 ± 0.5	3.4 ± 0.1	29.4 ± 1.1	27.9 ± 1.0	39.2 ± 1.5
$> 3.50\sigma$	20.0 ± 0.9	4.4 ± 0.2	30.3 ± 1.4	31.7 ± 1.4	33.7 ± 1.5
$> 4.00\sigma$	0.0 ± 0.0	5.6 ± 0.3	32.2 ± 1.7	35.3 ± 1.9	26.8 ± 1.4

Table 3.49: Output versus input flux density statistics for the uniform noise region of the SSA17 field, for signal-to-noise thresholds in the range $> 1.50\sigma$ to $> 4.00\sigma$.

SSA22 field, uniform noise region					
	Output vs. input flux density statistics				
S/N threshold	% noise only	% fainter	% within 1σ errors	% boosted	% confused/ spurious
$> 1.50\sigma$	89.1 ± 1.6	4.8 ± 0.1	35.1 ± 0.6	16.9 ± 0.3	43.3 ± 0.8
$> 2.00\sigma$	62.7 ± 1.8	5.4 ± 0.1	31.7 ± 0.6	22.2 ± 0.5	40.8 ± 0.8
$> 2.50\sigma$	11.0 ± 0.3	5.7 ± 0.1	28.5 ± 0.7	28.0 ± 0.7	37.7 ± 0.9
$> 3.00\sigma$	0.0 ± 0.0	5.9 ± 0.2	28.0 ± 0.8	32.4 ± 0.9	33.7 ± 0.9
$> 3.50\sigma$	0.0 ± 0.0	7.2 ± 0.2	26.2 ± 0.8	36.6 ± 1.1	30.0 ± 0.9
$> 4.00\sigma$	0.0 ± 0.0	7.9 ± 0.3	26.9 ± 0.9	39.6 ± 1.4	25.7 ± 0.9

Table 3.50: Output versus input flux density statistics for the uniform noise region of the SSA22 field, for signal-to-noise thresholds in the range $> 1.50\sigma$ to $> 4.00\sigma$.

Lockman Hole deep field, uniform noise region					
	Output vs. input flux density statistics				
S/N threshold	% noise only	% fainter	% within 1σ errors	% boosted	% confused/ spurious
$> 1.50\sigma$	52.2 ± 1.5	5.1 ± 0.2	36.3 ± 1.1	16.7 ± 0.5	41.9 ± 1.2
$> 2.00\sigma$	65.3 ± 1.7	5.5 ± 0.2	33.6 ± 1.1	20.9 ± 0.7	39.9 ± 1.3
$> 2.50\sigma$	58.1 ± 2.2	5.8 ± 0.2	30.8 ± 1.2	26.9 ± 1.0	36.6 ± 1.4
$> 3.00\sigma$	37.5 ± 1.6	6.2 ± 0.3	31.1 ± 1.3	30.5 ± 1.3	32.2 ± 1.4
$> 3.50\sigma$	0.0 ± 0.0	6.5 ± 0.3	29.4 ± 1.4	33.5 ± 1.6	30.6 ± 1.5
$> 4.00\sigma$	0.0 ± 0.0	7.8 ± 0.4	30.1 ± 1.7	33.9 ± 1.9	28.2 ± 1.6

Table 3.51: Output versus input flux density statistics for the uniform noise region of the Lockman Hole deep field, for signal-to-noise thresholds in the range $> 1.50\sigma$ to $> 4.00\sigma$.

Hubble deep field, uniform noise region					
	Output vs. input flux density statistics				
S/N threshold	% noise only	% fainter	% within 1σ errors	% boosted	% confused/ spurious
$> 1.50\sigma$	81.5 ± 2.8	9.8 ± 0.3	45.6 ± 1.6	26.7 ± 0.9	17.9 ± 0.6
$> 2.00\sigma$	53.8 ± 3.0	9.3 ± 0.3	41.9 ± 1.5	30.8 ± 1.1	18.0 ± 0.7
$> 2.50\sigma$	31.1 ± 1.2	9.9 ± 0.4	38.5 ± 1.5	34.5 ± 1.4	17.1 ± 0.7
$> 3.00\sigma$	18.6 ± 0.8	9.5 ± 0.4	35.4 ± 1.5	38.0 ± 1.6	17.1 ± 0.7
$> 3.50\sigma$	21.7 ± 1.0	9.6 ± 0.4	33.3 ± 1.6	40.9 ± 1.9	16.3 ± 0.8
$> 4.00\sigma$	0.0 ± 0.0	10.7 ± 0.5	29.4 ± 1.5	43.1 ± 2.2	16.8 ± 0.8

Table 3.52: Output versus input flux density statistics for the uniform noise region of the Hubble deep field field, for signal-to-noise thresholds in the range $> 1.50\sigma$ to $> 4.00\sigma$.

(2000), who used their raw 14h field counts to produce 5 simulations of this field. They reported an integral completeness of $\sim 90\%$ at the $S_{850} > 3\,\mathrm{mJy}$ based on a 3σ catalogue, which is rather higher than that implied from this analysis (integral completeness $\sim 60\%$ at $S_{850} > 4\,\mathrm{mJy}$ based on objects retrieved at $> 3.00\sigma$). This discrepancy may be explained as a combination of 2 effects. The first is in the source counts model used. Eales et al. (2000) used the raw $850\,\mu\mathrm{m}$ counts from the 14h field to create the simulated images. They also, however, reported the flux-boosting effect when comparing their output and input catalogues, quoting a median factor of 1.44, albeit with a large scatter about this value. This means that the input source counts will on average have overestimated the real input counts by a factor of 1.44, and this may in turn have affected the completeness estimate. The second, and probably dominant point, is that the two source extraction mechanisms differ, leading to different source lists and different significances for those sources common to both. Appoximately 50% of the sources reported as $> 3\sigma$ by Eales et al., were recovered at $< 3.00\sigma$ using the simultaneous maximum-likelihood fit developed in Chapter 2. If one instead compares with the completeness values at $> 2.00\sigma$ or $> 2.50\sigma$ from these simulations, the completenss level is closer to 70%, which is slightly more inkeeping with that of Eales et al. (2000).

Hughes & Gaztañaga (2000) have also performed more sophisticated Monte Carlo simulations of SCUBA surveys, as part of a broader investigation into the effects of confusion and noise on submillimetre surveys in general, for both existing and planned instruments and telescope facilities. They incorporated a clustering component into the simulations by employing an N-body simulation

with 200^3 particles in a $600h^{-1}$ Mpc box, produced with the same matter power spectrum as that measured for the APM Survey galaxies (Gaztañaga & Baugh, 1998, and references therein), which was then replicated to cover the total extent of the survey. The local IRAS 60 μm luminosity function (Saunders et al. 1990) was interpolated to longer wavelengths, and a model of pure luminosity evolution of the form $(1+z)^3$ for $0 < z < 2.2$, $(1+2.2)^3$ for $2.2 < z < 6$ and an exponential cutoff for $z > 6$ was assumed to account for the star formation histories. An Arp 220 SED was assumed throughout. The simulations of Hughes & Gaztañaga (2000) find the same effects of confusion and noise on the expected number counts as those simulations presented in this thesis. Their mock images of comparable size and depth to the "SCUBA 8 mJy Survey" fields (Lockman Hole East wide area and ELAIS N2) imply that a count-correction factor of $\sim 50\%$ for a S/N > 3 catalogue at $S_{850} > 8$ mJy is required, which is in keeping with the quantities presented in Tables 3.21 and 3.23, again implying a large quantity of either boosted or spurious / confused sources. This affects the brighter flux-limited surveys more, due to the steep decline in galaxy counts and therefore increased contribution of the measured counts due to noise.

Chapter 4

The SCUBA 8 mJy Survey

This Chapter describes the results of the "SCUBA 8 mJy Survey", currently the largest of the deep 850 μm blank field surveys to be completed. The first section describes the motivation for the fields selected, as well as the general observing strategy. In Section 2 the 850 μm source lists are presented, and in Section 3 the number counts at bright submillimetre fluxes are calculated using the corrections for incompleteness and boosting derived from the extensive simulations in Chapter 3. Section 4.4 discusses constraints on the redshifts of the SCUBA population based on the evolution of the far-infrared to submillimetre spectral index with redshift, and Section 4.5 uses these results to estimate the star formation rates and dust masses of these bright SCUBA sources. Star formation rate densities and co-moving number densities are discussed in Sections 4.6 and 4.7 respectively. Finally, the first attempt at measuring the clustering strength of the bright 850 μm population is presented in Section 4.8.

4.1 Survey Strategy and Observations

The "SCUBA 8 mJy Survey" is divided between two fields; the Lockman Hole East (centred at RA 10:52:08.82, DEC +57:21:33.8) and ELAIS N2 (centred at RA 16:36:48.85, DEC +41:01:48.5). These fields both lie in regions of low galactic cirrus emission (Schlegel, Finkbeiner & Davis 1998), and have a vast quantity of multi-wavelength data available for follow-up studies. They were also selected to coincide with deep Infrared Space Observatory (ISO) surveys at 6.7, 15, 90 and 175 μm (Lockman Hole East – Elbaz et al. 1999, Kawara et al. 1998; ELAIS N2 – Oliver et al. 2000, Serjeant et al. 2000, Efstathiou et al. 2000a).

Pilot observations of the Lockman Hole East and ELAIS N2 fields began in

March 1998 and July 1998 respectively, using SCUBA (Holland et al. 1999) on the JCMT in jiggle-mapping mode. A 30 arcsecond chop throw was chosen in order to optimise the sky subtraction, with the chop direction fixed in celestial co-ordinates. In order to avoid bands of higher cirrus emission in the ELAIS N2 region, the shape of this field was designed to be a parallelogram with the long axis lying in the direction 48° east of north. Consequently, in order to ensure that the chop remained within the boundaries, the position angle of the chop throw was also selected to be 48° east of north. There were no such issues in the Lockman Hole, and a 30 arcsecond chop throw lying directly in the north-south direction was chosen.

The preliminary observing strategy was to build up a linear strip in each field by overlapping SCUBA jiggle-maps, staggered by half the width of the array. The data collected from the pilot Lockman Hole East run in March 1998 were composed of a series of jiggle-maps, forming a deep strip at the centre of the survey area with $\sigma_{850} \simeq 1.6$ mJy/beam. In subsequent observing runs, the strategy was modified to that of an overlapping 'tripod' positioning scheme (illustrated in Figure 4.1), with three offset grids of hexagonally-close-packed pointings. The overall integration time was also reduced by a factor of ~ 2 to make more efficient use of the allocated observing time, resulting in each point on the sky being observed for a total of 3.0 hours, yielding a typical noise level of $\sigma_{850} \simeq 2.5$ mJy/beam. In order to give near homogeneous sky noise across the final coadded map, high and low airmasses were evenly distributed throughout. A total area of 280 arcmin^2 was mapped, with around 220 arcmin^2 receiving the full integration time (ie. the uniform noise regions comprising the fully observed central regions of the images). I was present at the JCMT for approximately 50% of the survey observations.

Prior to 15th December 1999, the observations were made using the narrow-band 850/450 μm filters. The majority of the observations carried out after this date made use of the more sensitive wide-band 850/450 μm filters. Since the central wavelength of the 850 μm filter did not change by more than 1 μm, the data taken with the wide- and narrow-band filters were directly combined in producing the final images.

Skydips were carried out, on average, every $1.5 - 2$ hrs, and pointings every $1.0 - 1.5$ hrs. The observations were conducted in dry weather conditions under the constraint $\tau_{225\mathrm{GHz}} < 0.10$, and with the majority of the jiggle-maps taken in conditions $0.06 < \tau_{225\mathrm{GHz}} < 0.08$. Primary/secondary calibration observations were taken at the start and end of every shift, with additional beam maps of the

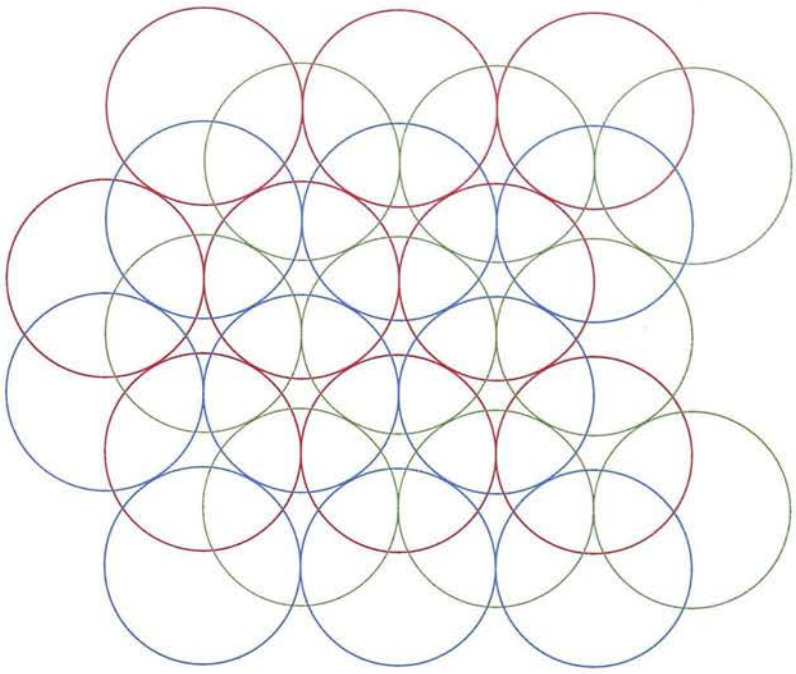

Figure 4.1: The 'tripod' positioning scheme for 9 neighbouring grid positions, as employed in the vast majority of observations for the "SCUBA 8 mJy Survey". The red, green and blue circles correspond to the 1st, 2nd and 3rd pointings for each of the grid positions.

pointing source (0923+392 in the case of the Lockman Hole East, and 3C345 in the case of ELAIS N2) being made every 3-4 hours to provide tertiary flux-density calibration.

4.2 850 μm Source Lists

The data were reduced and analysed by the methods described in Chapter 2. Sources down to a significance level of $> 3.00\sigma$ at 850 μm are listed in Table 4.1 for ELAIS N2 and Table 4.2 for the Lockman Hole East, ranked in order of formal significance as determined from the maximum-likelihood source extraction technique described in Section 2.5. Column 1 gives the source number in order of decreasing signal-to-noise. Columns 2 and 3 give the right ascension and declination of the source in J2000 coordinates. Column 4 gives the simultaneously fitted 850 μm flux densities of the sources. The error includes a 10% calibration error combined in quadrature. Column 5 gives the measured signal-to-noise ratio of the source from the simultaneously fitted model. Column 6 defines the noise region in which the source was found; 'deep' corresponds to the deep central strip in the Lockman Hole, 'central' corresponds to the parts of the map which have seen the full integration time (outside of the deep area) and have roughly uniform

noise, and 'edge' corresponds to the rather noisier non-uniform regions near the perimeter which have not seen the full integration time. Column 7 gives any previous reference to the 850 μm source. Reference S02 is an abbreviation for Scott et al. (2002) in which an earlier analysis was published. Column 8 gives the previously recorded signal-to-noise ratio where applicable, and Column 9 gives the distance between the listed and previously referenced positions. The listings given in italics at the bottom of the tables correspond to previously referenced sources with S/N $>$ 3.00 in Scott et al. (2002), which did not meet this criteria in this analysis.

Figures 4.2 and 4.3 show the beam-sized (14.5" FWHM) Gaussian convolved survey maps at 850 μm for ELAIS N2 and the Lockman Hole East respectively, with each of the sources identified with signal-to-noise ratio $>$ 3.00 circled. Those sources with signal-to-noise ratio $>$ 4.00 are circled in red, sources with signal-to-noise ratio in the range 3.50 – 3.99 are circled in blue, and those objects with signal-to-noise ratio in the range 3.00 – 3.49 are circled in green. The numbering corresponds to the signal-to-noise ranking given in Column 1 of Tables 4.1 and 4.2 for ELAIS N2 and the Lockman Hole respectively.

The simulations described in Chapter 3 suggest that some fraction of those detections listed may be the result of confusion of faint sources and noise, the level of contamination increasing as the signal-to-noise threshold is lowered. In the deep and central regions of the two maps, as many as 20 – 25% of sources above a signal-to-noise threshold of 4.00 may be spurious / confused, this fraction increasing to 30 – 40% at $> 3.50\sigma$ and perhaps as high as 50 – 60% for S/N $>$ 3.00. These quantities are significantly higher in the regions of non-uniform noise towards the edge of the maps, with a majority of detections at these significances failing to be identified with a single source at least half as bright as the retrieved flux density, and these sources must therefore be considered the least secure.

Reassuringly, however, deep radio imaging of the survey areas (to a $1\sigma_{\rm rms}$ depth of 10 and 20 μJy/beam at 1.4 GHz for the Lockman Hole East and ELAIS N2 respectively; Ivison et al. (2002)) has securely identified 18 of the original 36 $> 3.50\sigma$ 850 μm sources published in Scott et al. (2002) with a probability < 0.05 that the radio detection is not associated with the submillimetre source. A further 8 of these objects were identified as having potentially significant radio counterparts, albeit not at the formal probability < 0.05 level, thus putting an absolute upper limit of 50% on the spurious fraction at $> 3.50\sigma$, with a more likely limit of $< 30\%$, which is in line with the simulation results. Since the publication

of Ivison et al. (2002), further 1.4 GHz data have been obtained in the Lockman Hole region taking the $1\sigma_{\rm rms}$ depth down to $\sim 5\,\mu$Jy/beam and revealing radio counterparts to a greater proportion of the submillimetre sources. Based on the up-to-date Lockman Hole 850 μm source list given in Table 4.2, 6/11, 9/19 and 15/40 sources have been robustly detected ($> 4\sigma$) in the radio images for signal-to-noise thresholds of 4.00, 3.50 and 3.00 at 850 μm. In addition, potential radio identifications exist for a further 2, 5 and 14 submillimetre sources at $> 4.00\sigma$, $> 3.50\sigma$ and $> 3.00\sigma$ respectively. The remaining objects which have no obvious radio counterpart are either at very high redshift ($z > 3$) and hence invisible even in this ultra-deep radio imaging, or the result of confusion and noise. This deeper imaging also modifies the likely fraction of spurious / confused sources to a limit of $< 25\%$ for the sources detected at $> 3.50\sigma$. Further details of the 1.4 GHz VLA imaging are published in Ivison et al. (2002) and discussed in Section 4.4.

	RA (J2000)	DEC (J2000)	S_{850} /mJy	S/N	Noise Region	Previous Reference	Prev. S/N	Sep. /arcsec
01	16:37:04.29	+41:05:30.9	11.1 ± 1.7	8.54	central	S02 (N2.01)	8.59	0.9
02	16:36:58.62	+41:05:24.9	11.0 ± 1.9	6.92	central	S02 (N2.02)	6.27	1.3
03	16:36:58.18	+41:04:39.9	9.5 ± 1.8	6.02	central	S02 (N2.03)	5.86	2.1
04	16:36:50.04	+40:57:33.0	8.3 ± 1.8	5.20	central	S02 (N2.04)	5.18	0.5
05	16:36:39.36	+40:56:38.9	9.1 ± 2.4	4.14	central	S02 (N2.07)	4.07	1.0
06	16:37:04.25	+40:55:44.9	9.2 ± 2.4	4.12	central	S02 (N2.06)	4.13	0.6
07	16:36:35.66	+40:55:56.9	8.4 ± 2.2	4.10	central	S02 (N2.05)	4.16	1.3
08	16:37:02.50	+41:01:22.9	6.1 ± 1.7	4.00	central	S02 (N2.12)	3.65	0.1
09	16:37:07.97	+40:59:30.9	6.0 ± 1.6	3.94	central			
10	16:36:51.37	+41:05:06.0	6.5 ± 1.8	3.90	central	S02 (N2.17)	3.50	0.3
11	16:36:22.41	+40:57:04.8	9.2 ± 2.6	3.84	edge	S02 (N2.09)	3.76	0.2
12	16:37:07.46	+41:02:36.9	6.2 ± 1.7	3.84	central	S02 (N2.30)	3.13	0.5
13	16:36:49.34	+41:04:17.0	7.7 ± 2.2	3.73	central	S02 (N2.20)	3.48	0.7
14	16:36:58.78	+40:57:32.9	5.0 ± 1.4	3.71	central	S02 (N2.08)	3.82	0.2
15	16:36:44.48	+40:58:38.0	7.3 ± 2.1	3.66	central	S02 (N2.11)	3.67	0.2
16	16:36:48.81	+40:55:54.0	5.5 ± 1.6	3.65	central	S02 (N2.10)	3.69	0.1
17	16:36:31.25	+40:55:46.9	6.4 ± 1.9	3.64	central	S02 (N2.13)	3.56	0.6
18	16:37:04.27	+41:01:06.9	6.4 ± 1.9	3.62	central			
19	16:36:19.68	+40:56:22.7	11.2 ± 3.3	3.55	edge	S02 (N2.14)	3.55	0.4
20	16:37:10.10	+41:00:16.8	5.1 ± 1.5	3.54	central	S02 (N2.15)	3.52	1.1
21	16:36:59.41	+40:59:57.9	8.1 ± 2.5	3.50	central			
22	16:37:19.47	+41:01:37.7	12.4 ± 3.8	3.46	edge	S02 (N2.23)	3.45	0.5
23	16:36:27.90	+40:54:03.9	13.2 ± 4.1	3.42	edge	S02 (N2.22)	3.46	0.1
24	16:36:48.27	+41:03:52.0	7.0 ± 2.2	3.25	central	S02 (N2.27)	3.25	0.3
25	16:36:34.50	+40:57:23.9	6.4 ± 2.0	3.30	central			
26	16:36:57.11	+40:59:36.0	7.6 ± 2.4	3.28	central			
27	16:37:12.23	+41:02:57.8	5.1 ± 1.6	3.27	central			
28	16:37:10.54	+41:00:48.8	4.6 ± 1.5	3.26	central	S02 (N2.21)	3.47	0.5
29	16:36:26.89	+41:02:22.8	10.9 ± 3.5	3.24	edge	S02 (N2.24)	3.43	0.2
30	16:36:33.96	+41:01:36.9	11.8 ± 3.8	3.22	edge			
31	16:36:39.79	+41:00:33.9	5.9 ± 2.0	3.14	central	S02 (N2.32)	3.07	0.2
32	16:36:36.51	+41:05:17.9	11.8 ± 4.0	3.13	edge			
33	16:36:24.07	+40:59:34.8	10.4 ± 3.5	3.12	central	S02 (N2.29)	3.14	0.4
34	16:36:53.66	+41:00:49.0	7.2 ± 2.4	3.11	central			
35	16:36:44.83	+40:56:51.0	5.7 ± 1.9	3.10	central	S02 (N2.35)	3.02	0.3
36	16:36:45.44	+41:04:52.0	5.6 ± 1.9	3.08	central			
37	16:36:35.90	+41:01:37.9	9.3 ± 3.2	3.06	central	S02 (N2.19)	3.49	0.1
38	16:36:32.02	+41:00:04.9	9.2 ± 3.1	3.06	central	S02 (N2.26)	3.26	0.2
39	16:36:53.14	+41:03:46.0	5.7 ± 2.0	3.05	central			
40	16:37:08.62	+41:04:48.9	4.3 ± 1.5	3.05	central			
41	16:36:25.57	+41:00:35.8	7.8 ± 2.7	3.04	central			
42	16:36:52.87	+41:02:52.0	3.9 ± 1.3	3.03	central	S02 (N2.36)	3.00	0.3
43	16:36:27.00	+40:58:14.8	6.8 ± 2.4	3.02	central	S02 (N2.34)	3.05	0.2
44	16:37:01.81	+41:06:22.9	6.1 ± 2.1	3.01	edge			
45	16:37:09.13	+41:01:59.9	4.3 ± 1.5	3.01	central			
	16:36:50.48	*+40:58:54.0*	*4.6 ± 1.6*	*2.90*	*central*	S02 (N2.33)	3.06	0.2
	16:36:28.21	*+41:01:41.9*	*6.8 ± 2.5*	*2.88*	*central*	S02 (N2.31)	3.07	1.5
	16:36:47.21	*+41:08:48.0*	*4.0 ± 1.9*	*2.14*	*central*	S02 (N2.28)	3.24	0.1
	16:36:18.34	*+40:59:11.7*	*10.5 ± 5.2*	*2.07*	*edge*	S02 (N2.25)	3.37	0.5
	16:36:51.99	*+41:05:54.0*	*6.8 ± 3.6*	*1.93*	*edge*	S02 (N2.16)	3.51	4.0
	16:36:11.36	*+40:59:25.6*	*13.3 ± 11.8*	*1.13*	*edge*	S02 (N2.18)	3.49	0.6

Table 4.1: 850 μm source list for the ELAIS N2 field of the "SCUBA 8 mJy Survey".

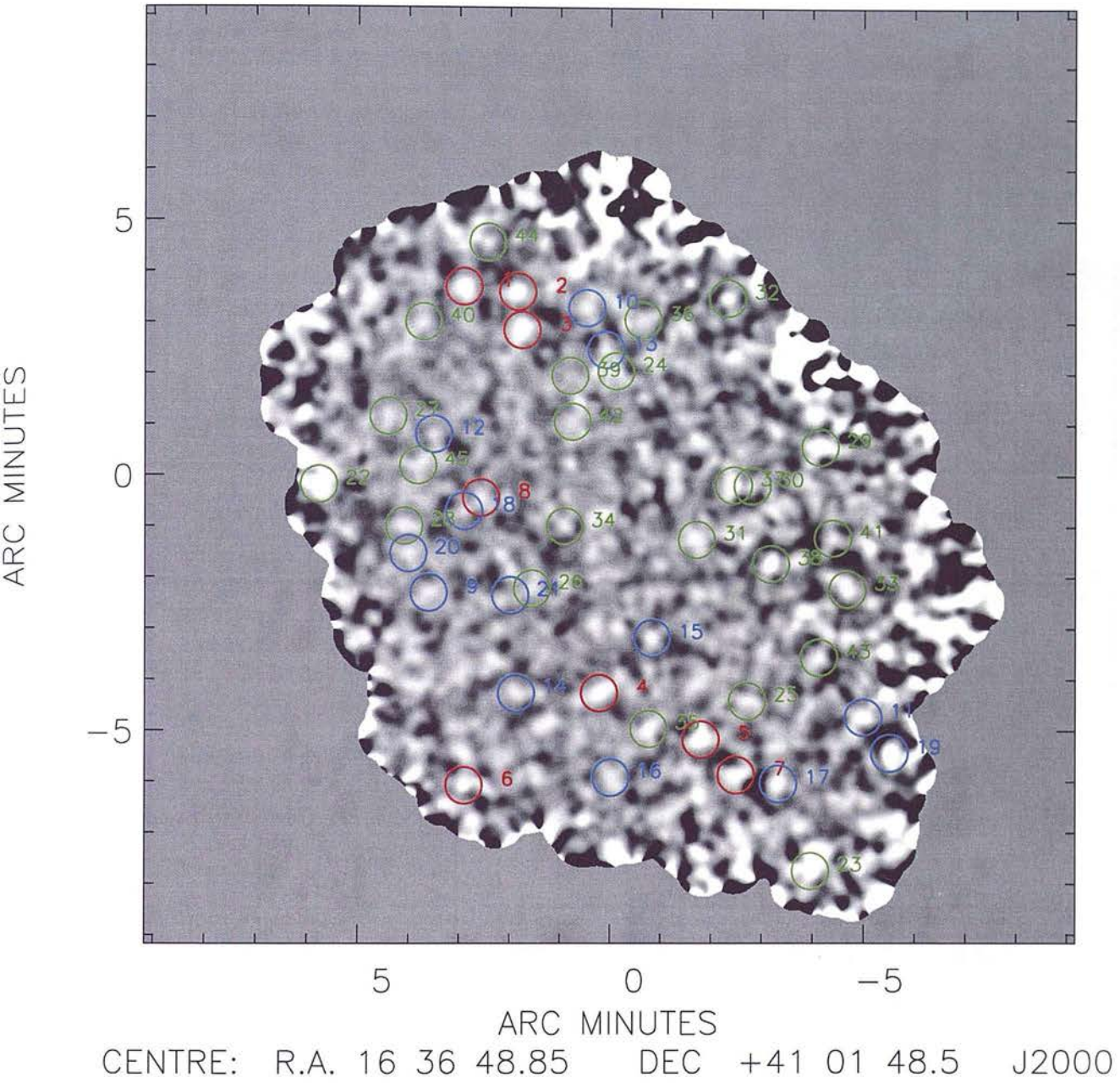

Figure 4.2: The 850 μm image of the ELAIS N2 field, smoothed with a beam-size Gaussian (14.5 arcsecond FWHM). The numbered circles highlight those sources found at a significance of > 3.00; the red circles are those sources with S/N > 4.00, the blue circles those sources with $3.50 <$ S/N < 3.99, and the green circles those detections with $3.00 <$ S/N < 3.49. The labelling corresponds to the numbers in Table 4.1.

	RA (J2000)	DEC (J2000)	S_{850} /mJy	S/N	Noise Region	Previous Reference	Prev. S/N	Sep. /arcsec
01	10:52:01.33	+57:24:43.3	9.6 ± 1.6	7.68	deep	S02 (LH.01)	8.10	0.6
02	10:52:38.21	+57:24:35.1	11.0 ± 2.3	5.33	central	S02 (LH.02)	5.22	0.9
03	10:51:58.39	+57:18:00.3	7.9 ± 1.7	5.31	deep	S02 (LH.03)	5.06	1.0
04	10:52:04.05	+57:25:29.3	7.8 ± 1.8	4.88	deep	S02 (LH.04)	5.03	1.4
05	10:52:30.39	+57:22:13.2	10.8 ± 2.6	4.58	central	S02 (LH.06)	4.50	2.1
06	10:52:22.71	+57:19:32.3	14.0 ± 3.4	4.52	central	S02 (LH.09)	4.20	0.3
07	10:51:51.54	+57:26:35.2	8.0 ± 2.0	4.45	deep	S02 (LH.07)	4.50	0.4
08	10:51:59.60	+57:24:21.3	4.8 ± 1.2	4.26	deep	S02 (LH.08)	4.38	3.3
09	10:51:59.26	+57:17:18.3	8.0 ± 2.1	4.12	deep	S02 (LH.05)	4.57	0.4
10	10:51:42.39	+57:24:45.1	12.0 ± 3.2	4.04	central	S02 (LH.10)	4.18	0.1
11	10:51:53.82	+57:18:47.3	6.7 ± 1.8	4.01	deep	S02 (LH.27)	3.38	0.3
12	10:52:16.78	+57:19:23.3	10.1 ± 2.8	3.80	central	S02 (LH.17)	3.55	0.3
13	10:51:33.57	+57:26:41.0	9.5 ± 2.7	3.73	central	S02 (LH.13)	3.69	0.2
14	10:52:07.77	+57:19:07.3	5.6 ± 1.6	3.71	deep	S02 (LH.12)	4.01	0.6
15	10:51:30.46	+57:20:37.9	12.0 ± 3.5	3.70	edge	S02 (LH.11)	4.01	1.1
16	10:52:36.37	+57:25:15.1	5.7 ± 1.7	3.67	central			
17	10:52:04.30	+57:27:01.3	9.2 ± 2.7	3.64	central	S02 (LH.14)	3.61	2.3
18	10:52:05.67	+57:20:53.3	4.6 ± 1.4	3.52	deep	S02 (LH.22)	3.61	0.4
19	10:52:24.58	+57:21:19.3	11.7 ± 3.5	3.50	central	S02 (LH.15)	3.60	0.3
20	10:52:27.18	+57:22:21.2	12.1 ± 3.7	3.40	central			
21	10:52:37.67	+57:20:30.1	9.8 ± 3.1	3.38	edge	S02 (LH.20)	3.51	0.3
22	10:51:46.97	+57:24:51.2	7.1 ± 2.2	3.38	central	S02 (LH.23)	3.48	0.3
23	10:52:28.07	+57:25:09.2	5.8 ± 1.8	3.37	central	S02 (LH.16)	3.56	10.4
24	10:52:03.94	+57:20:07.3	4.0 ± 1.3	3.36	deep	S02 (LH.31)	3.24	0.4
25	10:51:48.36	+57:21:48.2	12.1 ± 3.8	3.34	central			
26	10:52:09.87	+57:20:40.3	9.0 ± 2.8	3.33	central	S02 (LH.34)	3.16	0.4
27	10:52:34.57	+57:20:02.1	10.0 ± 3.2	3.29	central	S02 (LH.28)	3.31	0.3
28	10:51:42.89	+57:24:12.1	11.0 ± 3.6	3.26	central	S02 (LH.24)	3.47	0.1
29	10:52:01.71	+57:19:16.3	4.0 ± 1.3	3.23	deep	S02 (LH.21)	3.50	0.3
30	10:51:59.99	+57:20:39.3	4.2 ± 1.4	3.21	deep	S02 (LH.32)	3.22	0.3
31	10:52:27.28	+57:19:06.2	7.7 ± 2.5	3.20	central	S02 (LH.26)	3.31	0.3
32	10:52:34.51	+57:25:34.1	4.1 ± 1.4	3.18	central			
33	10:52:10.86	+57:24:13.3	8.4 ± 2.8	3.17	central			
34	10:51:33.81	+57:19:29.0	7.8 ± 2.6	3.12	central	S02 (LH.33)	3.20	0.1
35	10:51:55.77	+57:23:12.3	4.0 ± 1.3	3.12	deep	S02 (LH.18)	3.55	0.6
36	10:51:23.29	+57:20:33.8	13.9 ± 4.7	3.09	edge			
37	10:52:29.57	+57:26:20.2	4.7 ± 1.6	3.09	central	S02 (LH.19)	3.54	1.6
38	10:52:41.14	+57:21:47.1	14.3 ± 4.9	3.06	edge			
39	10:52:03.45	+57:16:54.3	7.9 ± 2.7	3.06	central	S02 (LH.36)	3.00	0.5
40	10:51:52.56	+57:22:29.2	4.4 ± 1.5	3.06	deep			
	10:52:42.21	*+57:18:28.0*	10.0 ± 3.5	*2.99*	*edge*	S02 (LH.30)	3.25	0.1
	10:52:16.43	*+57:25:04.3*	5.0 ± 1.8	*2.95*	*central*	S02 (LH.29)	3.30	2.7
	10:52:36.03	*+57:18:20.1*	10.5 ± 3.8	*2.91*	*edge*	S02 (LH.25)	3.46	0.3
	10:51:57.61	*+57:26:03.3*	6.5 ± 2.3	*2.90*	*central*	S02 (LH.35)	3.02	0.3

Table 4.2: 850 μm source list for the Lockman Hole East field of the "SCUBA 8 mJy Survey".

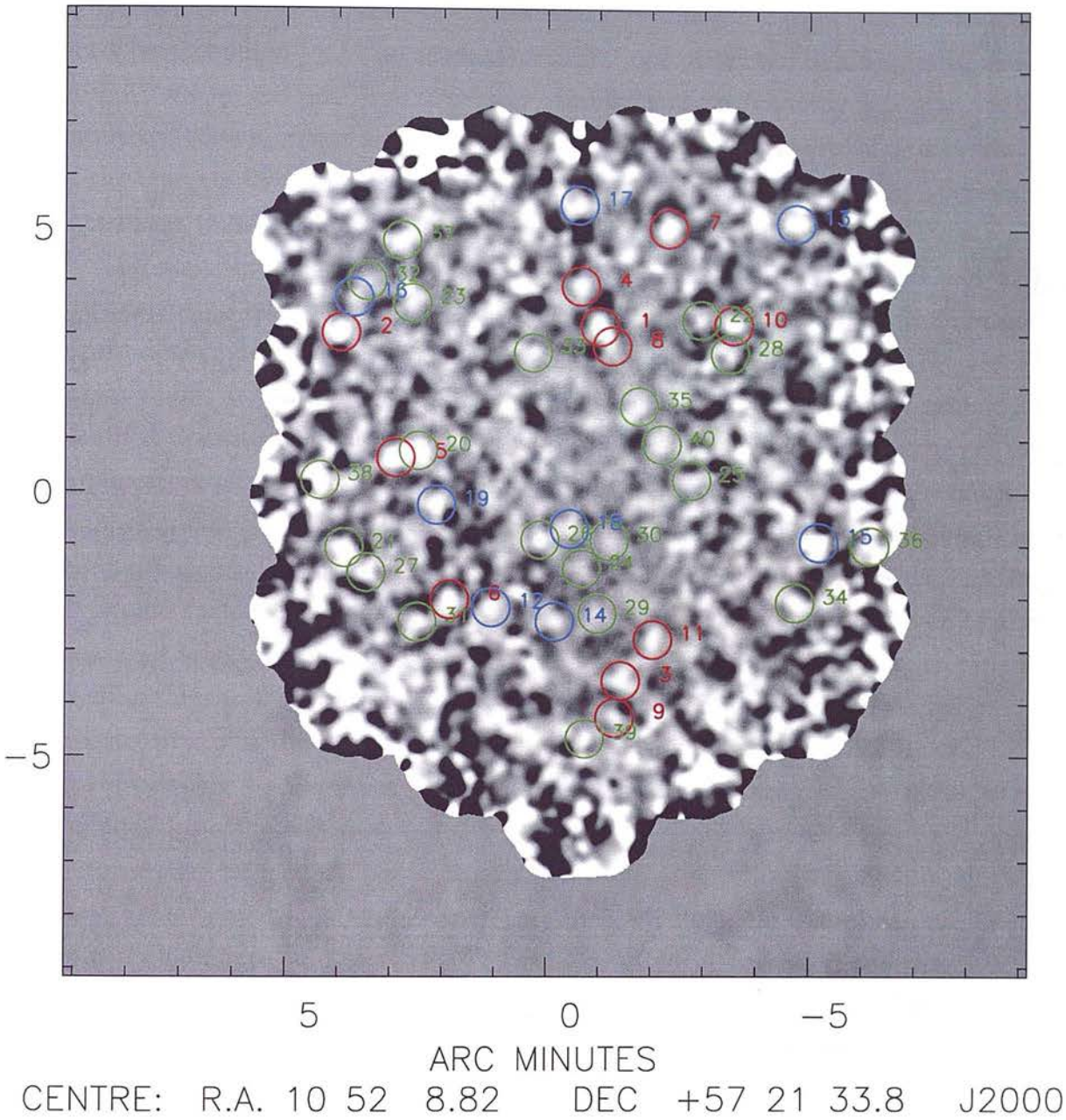

Figure 4.3: The 850 μm image of the Lockman Hole East field, smoothed with a beam-size Gaussian (14.5 arcsecond FWHM). The numbered circles highlight those sources found at a significance of > 3.00; the red circles are those sources with S/N > 4.00, the blue circles those sources with $3.50 <$ S/N < 3.99, and the green circles those detections with $3.00 <$ S/N < 3.49. The labelling corresponds to the numbers in Table 4.2.

4.3 Number Counts

In order to obtain the best estimate of the number counts at 850 μm, the effects of flux-density boosting, incompleteness and contamination from spurious sources must be accounted for. The extensive simulations presented in Chapter 3, using both a "one in, one out" source recovery test with the real survey fields, and fully simulated 850 μm maps, showed that the raw number counts are an overestimate of the true number counts - that is to say that the effect of flux-density boosting is stronger than the effect of incompleteness.

The observed flux-densities of the $> 3.50\sigma$ sources (as in Tables 4.1 and 4.2) were corrected using the best-fit models to the output versus input flux-density ratios, determined from the "one in, one out" simulations conducted on the actual survey maps. It is important to note that these corrected flux-densities cannot be assumed to be accurate for any *individual* source, but can successfully correct for the boosting effect in a statistical manner when general properties of the 850 μm source population as a whole, such as number counts, are to be considered. The steep exponential nature of the output-to-input flux-density ratio means that the correction factors become less accurate at fainter levels; a small decrease in the measured brightness in the region of the faint flux-density limit for a given signal-to-noise threshold may lead to a significant difference in the boost-corrected input flux density. For this reason, any sources requiring a correction factor of > 1.5 (corresponding to the point where differential completeness was $\sim 20\%$) were excluded from the corrected number counts. The simulation results for the non-uniform edge regions showed a large scatter and severe boosting factors and so these areas (and hence any sources contained within them) were also excluded from the number count analysis. The number of boost-corrected sources in bins 0.5 mJy wide, for $5.5 - 6.0$, $6.0 - 6.5$, and so on up to $12.0 - 12.5$ mJy were then amended for completeness using the best-fit differential completeness results from the "one in, one out" source retrieval simulations. The cumulative number densities were then obtained by summing the number of sources in the bins down to the required flux-density threshold, and dividing by the relevant area of uniform noise to which sources with that input flux density were detected.

The applied correction factors were determined from a one-by-one source input and reclamation process using the real survey images, and so are independent of source-count models. One cannot, however, attempt to correct for the presence of fake sources without making some assumption about the background counts.

Flux density /mJy	Raw 850 μm source counts $N(>S)\mathrm{deg}^{-2}$	Corrected 850 μm source counts $N(>S)\mathrm{deg}^{-2}$
5.5	700 ± 130	600^{+130}_{-220}
6.0	650 ± 130	520^{+120}_{-200}
6.5	540 ± 120	390^{+100}_{-150}
7.0	490 ± 110	$300^{+\ 90}_{-130}$
7.5	460 ± 110	$300^{+\ 90}_{-130}$
8.0	$380 \pm\ 90$	$250^{+\ 80}_{-110}$
8.5	$240 \pm\ 70$	$170^{+\ 80}_{-\ 80}$
9.0	$240 \pm\ 70$	$140^{+\ 60}_{-\ 70}$
9.5	$160 \pm\ 50$	$120^{+\ 50}_{-\ 60}$
10.0	$130 \pm\ 50$	$90^{+\ 50}_{-\ 50}$
10.5	$110 \pm\ 40$	$40^{+\ 30}_{-\ 30}$
11.0	$70 \pm\ 30$	$20^{+\ 20}_{-\ 20}$
11.5	$50 \pm\ 30$	$20^{+\ 20}_{-\ 20}$
12.0	$30 \pm\ 20$	$20^{+\ 20}_{-\ 20}$
12.5	$20 \pm\ 20$	$20^{+\ 20}_{-\ 20}$

Table 4.3: The 850 μm source counts per square degree based on sources with S/N > 3.50 in both survey maps, and excluding those detected in the non-uniform noise regions. Column 1 gives the flux density and column 2 the cumulative raw counts per square degree with the Poisson error. Column 3 gives the cumulative corrected counts per square degree, the upper error corresponding to the Poisson error, and the lower error accounting for both the Poisson error and the presence of spurious sources based on the simulation data.

Consequently, the estimated number of spurious sources has been combined in quadrature with the $1\sigma_{\mathrm{rms}}$ Poisson error, rather than being applied directly to the derived source-count values. Table 4.3 gives the raw and amended counts per square degree.

Although the "SCUBA 8 mJy Survey" was undertaken with the aim of constraining the brighter end of the 850 μm number counts, it has in fact achieved the most accurate determination to date of the sub-mm source counts down to $S_{850} \simeq 5.5$ mJy. The corrected source counts are plotted in Figure 4.4 (solid diamonds), and it can be seen that the number of sources per square degree derived from the "SCUBA 8 mJy Survey" are a factor of 2 to 3 higher than the CUDSS and Hawaii survey values. The most likely explanation for this discrepancy is that it is due to small number statistics in the smaller submillimetre surveys rather than a real steepening of the source counts at > 5 mJy. One would in fact *expect this to be the case* if bright SCUBA sources were generally clustered on scales of a few arcminutes, as is tentatively suggested by the two point autocorrelation functions and nearest neighbour analyses in Sections 4.8, 5.2.1 and 5.2.2, since there

is a greater probability of centring a small blank field survey in a region of lower source density. The "SCUBA 8 mJy Survey" covers 260 arcmin^2 of sky, twice the area of both the 'Canada UK Deep Sub-millimetre Survey (CUDSS)' (Eales et al. 2000, Webb et al. 2003a), and 'Hawaii Survey' (Barger et al. 1998, Barger, Cowie & Sanders 1999), making it less susceptible to arcmin-scale clustering and thus better able to constrain the number counts at brighter flux densities. At 8 mJy, Blain et al. (1999) suggest a rather higher count of $800 \pm 600 \mathrm{deg}^{-2}$ than the "8 mJy Survey" value of $250^{+80}_{-100} \mathrm{deg}^{-2}$. Their result, however, is derived from a series of small deep surveys which make use of gravitational lensing from intervening clusters, in order to access the faintest counts. This anomalously high value may again be due to small number statistics, but could also be the result of strong rather than weak lensing effects on some of the sources, thus leading to an inaccurate correction factor being applied to the retrieved flux densities. At flux densities > 10 mJy the "8 mJy Survey" also inevitably becomes limited by the lower surface density of brighter sources. In a similar manner to the source counts of Eales et al. and Barger et al. beyond 6 mJy, the "8 mJy Survey" counts at 11 and 12 mJy suggest a steepening of the counts slope towards brighter fluxes. At this time there is insufficient data to say whether this steepening is real or not. Borys et al. (2002) reported a number count of $164^{+78}_{-59} \mathrm{deg}^{-2}$ at 12 mJy, based on a similar sized survey to the "8 mJy Survey" suggesting that this may again be a statistical rather than a real effect, although it should be noted that they had problems with their calibration.

The source counts accumulated across all of the submillimetre surveys (as shown in Figure 4.4) are consistent with a population of high-redshift ($z > 1$, dusty, star-forming galaxies, analogous to the local ULIRGs. Strong evolution of the 850μm luminosity function is required to produce a model consistent with the observed number counts. The upper solid and dashed lines in the figure show the predicted source counts based on the 60μm luminosity function of Saunders et al. (1990), interpolated to 850μm assuming an Arp 200 type spectral energy distribution (dust temperature $T_d \sim 40$K, emissivity $\beta \sim 1.2$), with pure luminosity evolution of the form $(1+z)^3$ out to a redshift $z = 2$ (and simply frozen beyond), for the cosmologies ($\Omega_M = 1.0$, $\Omega_\Lambda = 0.0$) and ($\Omega_M = 0.3$, $\Omega_\Lambda = 0.7$). The dot-dash and dot-dot dash assume a more complicated, but arguably more realistic luminosity evolution of the form $L(z) = L(0)(1+z)^{3/2}\mathrm{sech}^2[\mathrm{b}\ \ln(1+z) - \mathrm{c}]\cosh^2\mathrm{c}$, consistent with models of cosmic chemical evolution, for cosmologies ($\Omega_M = 1.0, \Omega_\Lambda = 0.0$) and ($\Omega_M = 0.3, \Omega_\Lambda = 0.7$) respectively, and assuming a dust tem-

perature of 37K and dust emissivity index of $\beta = 1.2$ (Jameson et al. 1999, Smail et al. 2002). The lower solid and dashed lines show the predicted source counts using the same luminosity function but without any luminosity evolution. Such a model is inconsistent with the measured number counts by $2 - 3$ orders of magnitude, which simply serves to re-emphasise the extent of the evolution in the starburst population uncovered by SCUBA.

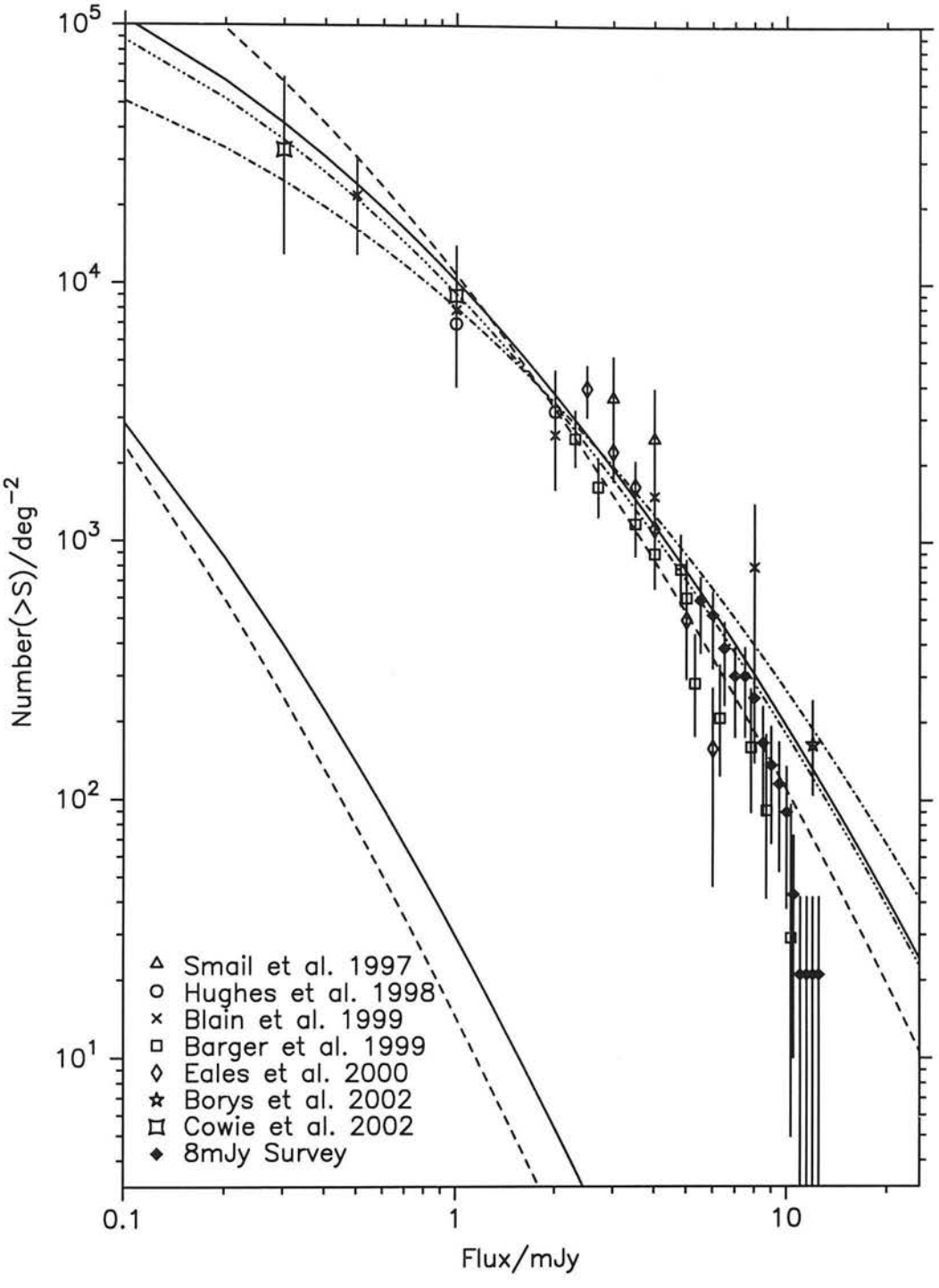

Figure 4.4: Cumulative 850 μm source counts. The solid diamonds show the results from the 'SCUBA 8 mJy Survey', corrected for the effects of flux density boosting and incompleteness. The upper solid and dashed curves are predicted number counts, based on the 60 μm luminosity function of Saunders et al. (1990), assuming a dust temperature of 40 K, a dust emissivity index of $\beta = 1.2$, and pure luminosity evolution of the form $L(z) = L(0)(1+z)^3$ out to $z = 2$ (beyond which the luminosity function is simply frozen), for cosmologies ($\Omega_{\rm M} = 1.0, \Omega_\Lambda = 0.0$) and ($\Omega_{\rm M} = 0.3, \Omega_\Lambda = 0.7$) respectively. The lower solid and dashed curves show the number counts predicted by the same models if no luminosity evolution is included. The dot-dash and dot-dot dash assume a more complicated, but arguably more realistic luminosity evolution of the form $L(z) = L(0)(1+z)^{3/2}{\rm sech}^2[{\rm b}\ \ln(1+z) - {\rm c}]\cosh^2{\rm c}$, for cosmologies ($\Omega_{\rm M} = 1.0, \Omega_\Lambda = 0.0$) and ($\Omega_{\rm M} = 0.3, \Omega_\Lambda = 0.7$) respectively, and assuming a dust temperature of 37 K and dust emissivity index of $\beta = 1.2$ (Jameson et al. 1999, Smail et al. 2002).

4.4 Redshift Estimation

The extremely faint nature of the optical / near-infrared counterparts to submillimetre sources makes spectroscopic redshift determination impractical for all but a handful of sources, even with the latest generation of 8 or 10m ground-based optical telescopes. In fact, given the large SCUBA beam-size (14.5" FWHM at 850 μm) obtaining the correct identification on which to place a slit is by no means trivial. The potential identifications originally proposed for the most significant Hubble Deep Field source (Hughes et al. 1998, Downes et al. 1999), for example, have recently been shown to be incorrect following the discovery of an extremely faint ($K \simeq 23.5$) and red ($I - K > 5.2$) object (Dunlop et al. 2003b) lensed by one of the initally suggested counterparts. Instead, more subtle techniques such as photometric redshift estimates and the radio-to-submillimetre spectral index must be used.

In Fox et al. (2002), the $S_{850\mu m}/S_{450\mu m}$, $S_{850\mu m}/S_{175\mu m}$ and $S_{850\mu m}/S_{1.2mm}$ flux density ratios were used to obtain redshift constraints for 19 of the most significantly detected 850μm sources based on a range of model SEDs from Efstathiou et al. (2000b). In all but 1/19 cases, the redshifts of the 850 μm sources were constrained to lie at $z > 1$, with approximately 50% constrained to $z > 2$.

More recently, Ivison et al. (2002) used deep 1.4 GHz observations taken with the VLA ($1\sigma_{\rm rms} = 5\,\mu$Jy/beam in the Lockman Hole East, and $1\sigma_{\rm rms} = 10\,\mu$Jy/beam in ELAIS N2) to constrain the redshifts of those sources listed in Scott et al. (2002) with S/N > 3.50, based on the radio-to-submillimetre spectral index (Carilli & Yun, 1999, 2000). This method is based on the tight correlation observed in local star-forming galaxies between the radio continuum emission arising from relativistic electrons accelerated in supernova remnant shocks, and thermal dust emission from reprocessed star light (Condon 1992). Figure 4.5 (taken from Condon 1992) shows the FIR-radio correlation for strong sources selected at $\lambda = 60\,\mu$m from the revised IRAS bright galaxy sample (Soifer et al. 1989), and not containing any known active galactic nucleii, or partially free-free absorbed systems.

If the radio-FIR correlation holds independently of redshift, then climbing the steep Rayleigh-Jeans tail of the thermal dust emission leads to the radio-to-submillimetre spectral index evolving strongly with redshift. This is illustrated in Figure 4.6, for the SEDs of the local starburst galaxies M82 and Arp 220. The dashed lines represnt the 1.4 GHz - 850 μm spectral index at redshift $z = 0$ and

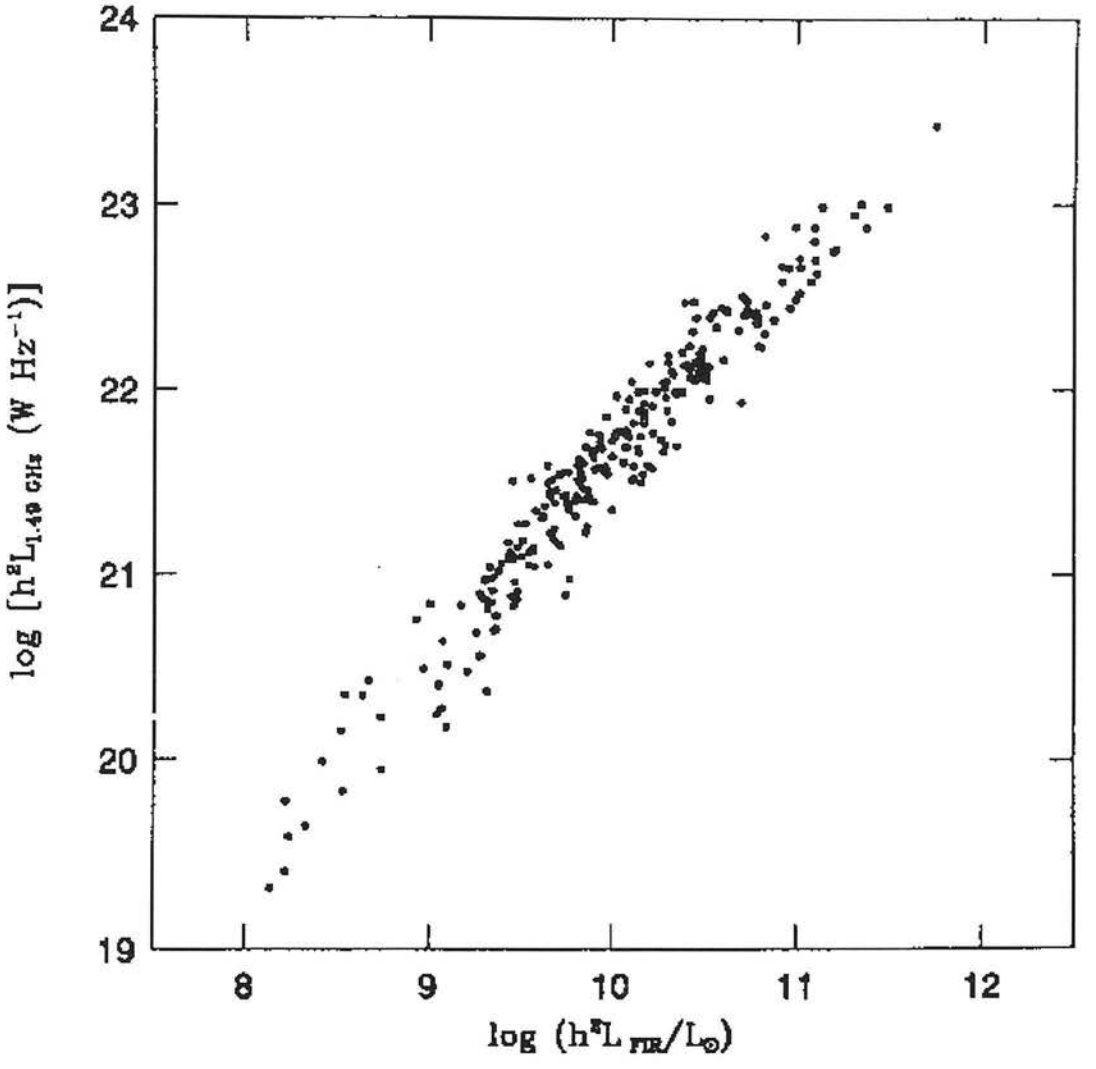

Figure 4.5: The FIR-radio correlation for strong sources selected at $\lambda = 60\,\mu$m from the revised IRAS bright galaxy sample (Soifer et al. 1989), and not containing any known AGN. The figure is taken from Condon (1992).

the solid lines represent the spectral index as would be measured if the galaxies were placed at redshift $z = 3$.

The accuracy of the redshift estimator begins to drop beyond $z \simeq 2$, due to the decrease in the gradient of the Rayleigh-Jeans tail on approaching the spectral turnover, and hence a decrease in the change of the radio-to-submillimetre flux density ratio for a fixed redshift increment. Other important factors affecting the accuracy of the redshift estimates are the presence of an active galactic nucleus (AGN) and inverse Compton losses off the microwave background.

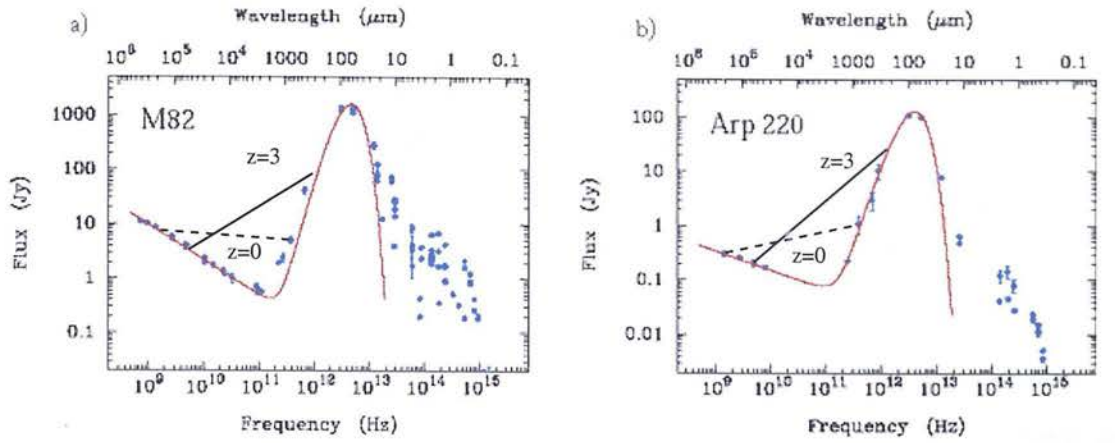

Figure 4.6: SEDs of the local starburst galaxies (a) M82 and (b) Arp 220. The dashed lines represnt the 1.4 GHz - 850 μm spectral index at redshift $z = 0$ and the solid lines represent the spectral index as would be measured if the galaxies were placed at redshift $z = 3$.

If the submillimetre source contains an AGN, there will be additional radio synchrotron emission from the active nucleus. The presence of an AGN may also contribute to the heating of the dust, however, studies of ULIRGs (Sanders & Mirabel 1996) and HLIRGs (Farrah et al. 2002) in the more local universe have implied that even when an AGN is present, the dominant source of submillimetre emission is dust heated by a cirumnuclear starburst rather than the active core. The overall effect of a radio-loud AGN is, therefore, to decrease the radio-to-submillimetre spectral index and hence underestimate the source redshift. The fraction of SCUBA sources containing an AGN is as yet poorly constrained. Multiwavelength follow-up of the "SCUBA Cluster Lens Survey" (Ivison et al. 2000a, Smail et al. 2002) has produced clear evidence for an active nucleus in at least 4 (possibly 5) out of 15 submillimetre galaxies ($\simeq 30\%$). Deep X-ray observations of the "SCUBA 8 mJy Survey" fields with XMM (Lockman Hole; Hasinger et. al. 2001) and Chandra (ELAIS N2; Manners et al. 2003) have identified 4/36 of the most significant submillimetre sources with obscured AGN ($\simeq 10\%$; Almaini et al. 2003, Ivison et al. 2002).

Conversely, "quenching" of the radio continuum emission by inverse Compton losses off the microwave background would artificially increase the redshift estimate for any very high redshift galaxies $z > 6$. The energy density of the microwave background increases as $(1 + z)^4$, which at $z \simeq 6$, corresponds to the energy density in a magnetic field of about 100 μGauss - comparable to the expected interstellar magnetic fields found in starburst nucleii (Condon et al. 1991,

Carilli et al. 1998).

One of the main problems in trying to determine the redshift distribution of the SCUBA population is the contamination from spurious sources. The effect of comological dimming is sufficiently strong at radio wavelengths that even such powerful starbursts as those studied here in the "SCUBA 8 mJy Survey" are unlikely to be identified in these extremely deep radio images if they lie at redshifts $z > 3$. The lack of a radio counterpart, therefore, could mean that the SCUBA source is at $z > 3$, but alternatively could mean that the source is spurious in which case the fraction of high redshift objects would be over-estimated. In order to ascertain which sources were most likely to be spurious, Ivison et al. (2002) analysed the trend in the cumulative proportion of SCUBA sources identified in the deep radio images against signal-to-noise ratio at 850 μm, flux density at 850 μm, and local 850 μm noise level (Figure 4.7), for the original 3.50σ list in Scott et al. (2002) . They found that the 6/36 SCUBA sources with $\sigma_{850\mu m} > 3$ mJy did not appear to match the same trend in radio identification fraction as the other 30 objects with S/N > 3.50, and furthermore none had counterparts at 1.4 GHz. Although it remains plausible that some of these 6 sources are real and lie at very high redshift, they were not included in the subsequent redshift analysis, and so the estimated redshift distribution may be considered conservative in this respect.

The effect of flux-density boosting may also affect the redshift distribution to some extent, skewing it towards slightly higher redshifts, however, this problem is much less serious. To give an idea of the size of likely errors in the redshift estimate arising from boosting, consider a SCUBA source with an Arp 220 type SED for which the inferred radio-submillimetre spectral index implies a redshift of $\simeq 2.5$ based on the measured 850 μm flux density. If the retrieved flux density over-estimated the true value by a factor of 1.2, then this redshift estimate of $z \simeq 2.5$ would be in excess by $\delta z = 0.1$. Similarly, for flux-boosting factors of 1.5 and 2.0, this redshift estimate would be in excess by $\delta z = 0.3$ and 0.5 respectively. These errors in redshift estimate due to flux-boosting are comparable in size to the error arising from the choice of SED (Carilli & Yun, 2000).

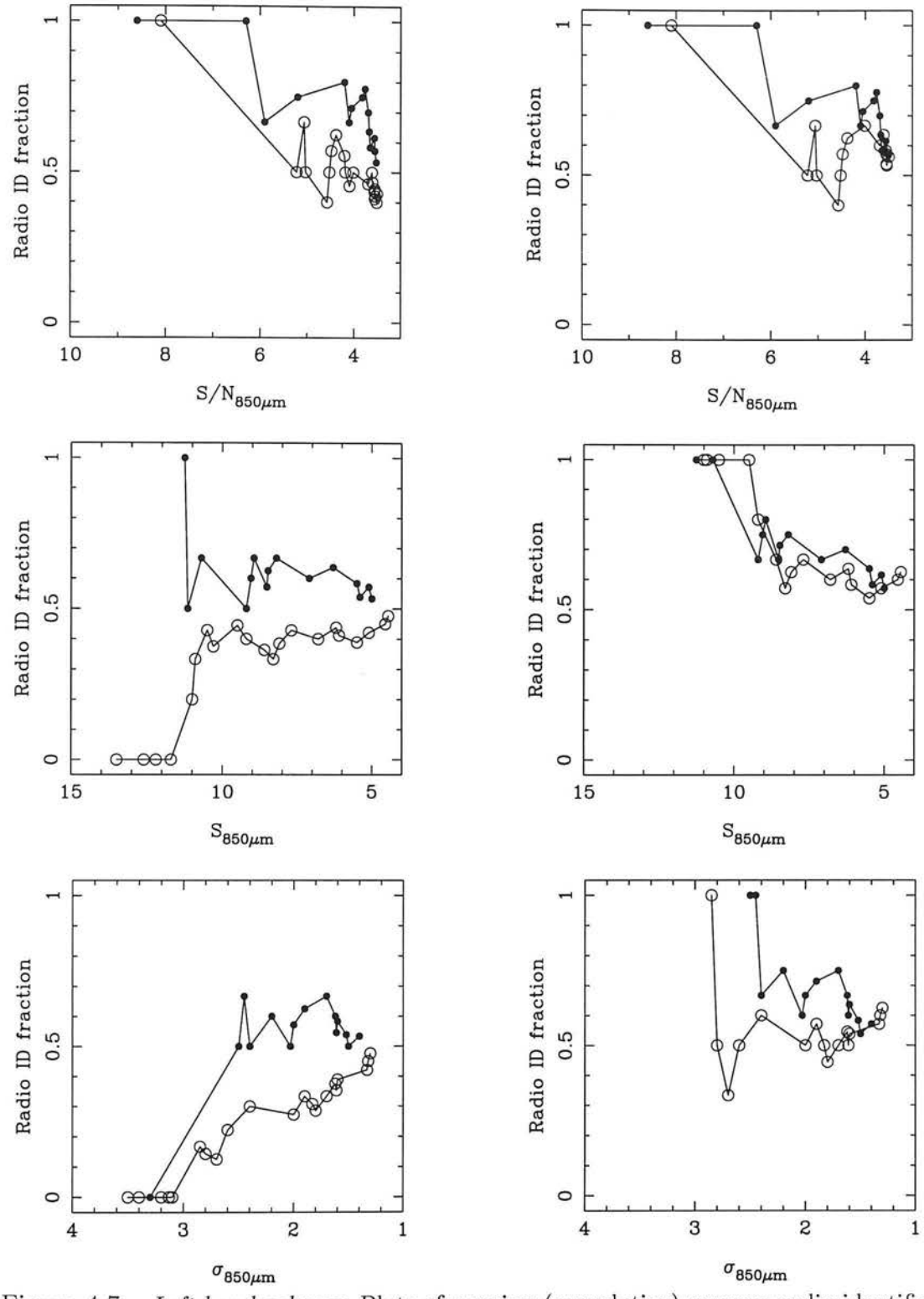

Figure 4.7: *Left hand column:* Plots of running (cumulative) average radio-identified fraction for the Lockman Hole East submm sample (open circles) and the ELAIS N2 submm sample (filled circles) against submm signal-to-noise ratio (top), 850 μm flux density (middle) and local 850 μm noise (bottom). The unexpected failure to identify the radio counterparts to the four brightest Lockman submm sources, obvious in the middle plot, is shown in the bottom plot to be due to the fact that all these sources were extracted from the noisiest regions of the original submm maps. Based on the bottom-left plot, Ivison et al. (2002) have rejected all 6 sources with $\sigma_{850} > 3$ mJy from the sample on the basis that they are probably produced by source confusion/noise. *Right hand column:* Same plots after removal of the 6 unreliable sources. The observed trends are now more sensible and statistically consistent between both fields, asymptoting to a final radio identification rate of 60%. This figure is taken from Ivison et al. (2002).

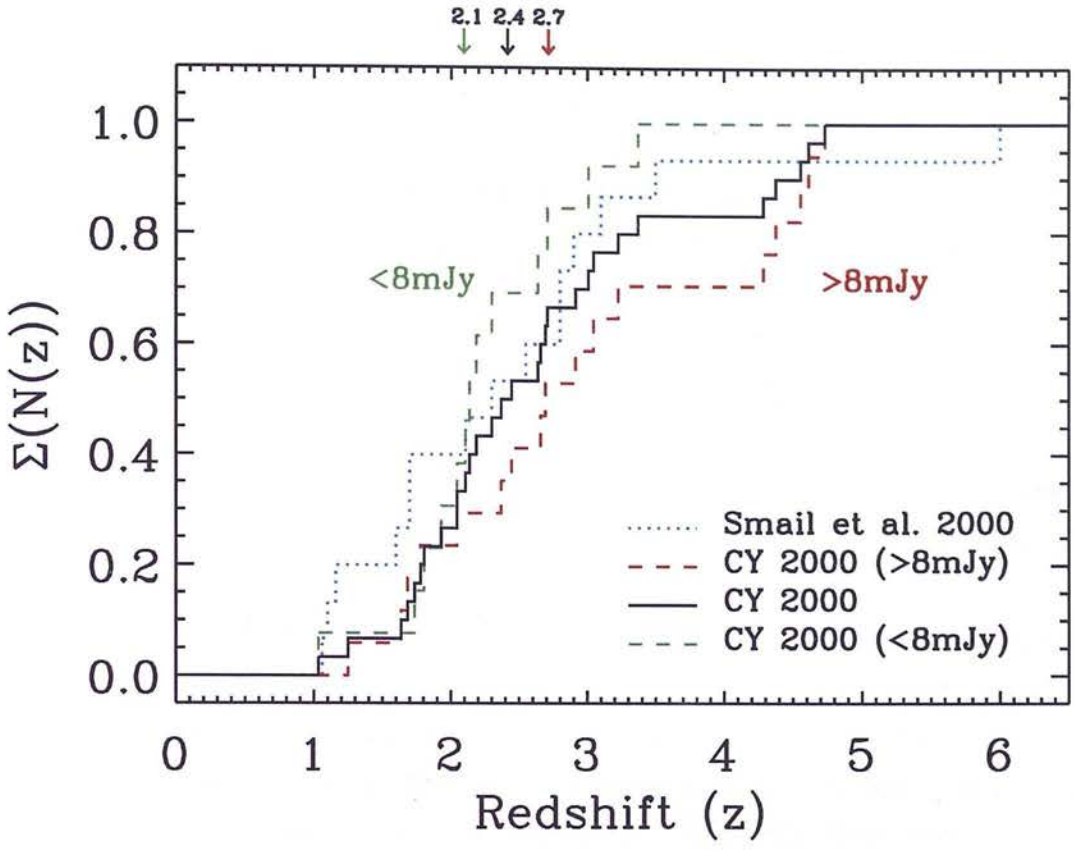

Figure 4.8: Cumulative redshift distribution, $\Sigma N(z)$, of the 8 mJy sample as deduced from the spectral index between 1.4 GHz and 850 μm using the Carilli & Yun (2000) redshift estimator (solid black). For comparison, $\Sigma N(z)$ for the complete SCUBA lens survey by Smail et al. (2000, 2002) has also been plotted (dotted blue). $\Sigma N(z)$ for ≥ 8 and ≤ 8 mJy submm sources are plotted as red and green dashed lines, respectively (again assuming the Carilli & Yun model). This figure is taken from Ivison et al. (2002).

Dunne, Clements & Eales (2000b) and Rengarajan & Takeuchi (2001) have also analysed this technique, using data from the SCUBA Local Universe Galaxy Survey (SLUGS; Dunne et al. (2000a)). Redshift estimates from all three radio-submillimetre correlations are presented in Ivison et al. (2002). The median redshift estimates were 2.0, 2.4 and 3.2 for the Dunne, Clements & Eales (2000b), Carilli & Yun (2000), and Rengarajan & Takeuchi (2001) techniques respectively, with the Carilli & Yun model predicting that there are no sources at $z < 1$, 23% of the sources lie in the range $1 < z < 2$, 43% lie at $2 < z < 3$ and 34% are at $z > 3$. Figure 4.8 (taken from Ivison et al. 2002) shows the cumulative redshift distribution, $\Sigma N(z)$, for the $30 > 3.50\sigma$ SCUBA sources considered in Ivison et al. (2002; solid black line). For comparison, $\Sigma N(z)$ for the complete SCUBA lens survey by Smail et al. (2000, 2002) has also been plotted (dotted blue), and

$\Sigma N(z)$ for ≥ 8 and $\leq 8\,\mathrm{mJy}$ submm sources from the "8 mJy Survey" sample are plotted as red and green dashed lines, respectively (again assuming the Carilli & Yun model).

Interestingly, the brighter SCUBA population ($S_{850} > 8\,\mathrm{mJy}$) appears to have a higher median redshift of $z_{\mathrm{med}} \simeq 2.7$ than the fainter sources ($S_{850} < 8\,\mathrm{mJy}$; $z_{\mathrm{med}} \simeq 2.1$). One possible explanation for the trend is a bias in the radio flux measurements due to resolving out emission from the larger sources. If the more luminous submm sources have larger angular sizes then there may be a weak trend in the radio measurements which would make these appear to have higher submm / radio spectral indices and hence higher inferred redshifts. Ivison et al., however, estimate that this would result in a maximum reduction of 20% in the radio flux and therefore only a modest change in the spectral indices ($\delta\alpha \sim 0.03$). The more likely explanation is that this trend reflects differing behaviour in the intrinsically low- and high- luminosity SCUBA populations. In addition to the 1.4 GHz to 850 μm spectral index being sensitive to the redshift of the source, it is also dependent on the shape of the thermal dust emission SED (and hence the assumed temperature and emissivity index of the dust). There are thus several possible causes of this trend. Firstly, the radio-to-submm spectral index may be reflecting differences in the form of the SED with intrinsic luminosity, a more luminous source having a higher dust temperature, or alternatively a lower emissivity index. This scenario would seem unlikely to be a dominant factor given the very small amount of scatter in the far-IR / radio correlation locally (Condon 1992) and the work of the Dunne, Clements & Eales (2000b) on the SCUBA local Universe Galaxy Survey, although it is perhaps worth noting that these works apply to galaxies with FIR luminosities in the range $L_{\mathrm{FIR}} = 10^9 - 10^{11}\,L_{\odot}$, one or two orders of magnitude fainter than the galaxies studied here. Another possibility is that this reflects a bias in submillimetre surveys in favour of colder objects at a given L_{FIR} and z. Finally the trend could be exactly what it appears, specifically that the more luminous submillimetre sources are generally located at higher redshifts than their less luminous counterparts. If this final scenario is indeed the case, it would suggest very strong luminosity evolution in the submillimetre selected galaxy population, out to high redshifts.

4.5 Star Formation Rates and Dust Masses

The fine balance between cosmological dimming and a strong negative K-correction (arising from the steep spectral index of thermal dust emission longwards of the peak), leads to an almost uniform sensitivity to objects between redshifts $z = 1$ and $z = 8$ when observing at a wavelength of 850 μm. Consequently, even without knowledge of the precise redshift of a submillimetre source, estimates of the FIR luminosity, star formation rate and dust mass can be made, provided the redshift of the source can be constrained to $z > 1$. The dependence of these quantities on redshift for an 8 mJy source with an SED like that of the local extreme starburst Arp 220 (assuming optically thin greybody emssion with a dust temperature of 42.2K and emissivity index 1.2 (Dunne et al. 2000a)) may be seen in Figures 4.9 to 4.12, for both an $\Omega_M = 0.3$, $\Omega_\Lambda = 0.7$ (blue line) and $\Omega_M = 1.0$, $\Omega_\Lambda = 0.0$ (red line) cosmology. One can readily see that for a given cosmology, there is almost no dependence of any of these quantities on the redshift of the source.

The most important effect on estimating star formation rates and dust masses from an 850 μm flux density is the spectral energy distribution of the source. The thermal dust emission is usually described by an optically thin greybody approximation with a single dust temperature and emissivity index. This is a fairly simplistic approach, as in principle the dust will be at a range of temperatures, which depends on the local radiation field. Observations of spiral galaxies, for example, have shown that at least two components, a warm and a cold ($T_d < 20$ K), are necessary to explain the dust emission from FIR to millimetre wavelengths (eg. Guélin et al. 1993; Chini et al. 1995, Alton et al. 1998). However, given the limited SED information available on the high redshift SCUBA sources (i.e. the fact that there is only one flux density measurement at FIR to millimetre wavelengths) there is little point in introducing a multi-temperature model. Therefore, the approach which I have taken to estimate the luminosities, star formation rates and dust masses is to use a single SED template, based on a single temperature optically thin greybody.

The 850 μm luminosity in the source's rest frame is then given by

$$L_{\nu_{850\mu m}} = \frac{S_{850\mu m} D^2}{(1+z)^{2+\beta}} \left(\frac{e^{\frac{hc(1+z)}{kT_d \lambda_{850\mu m}}} - 1}{e^{\frac{hc}{kT_d \lambda_{850\mu m}}} - 1} \right) \tag{4.1}$$

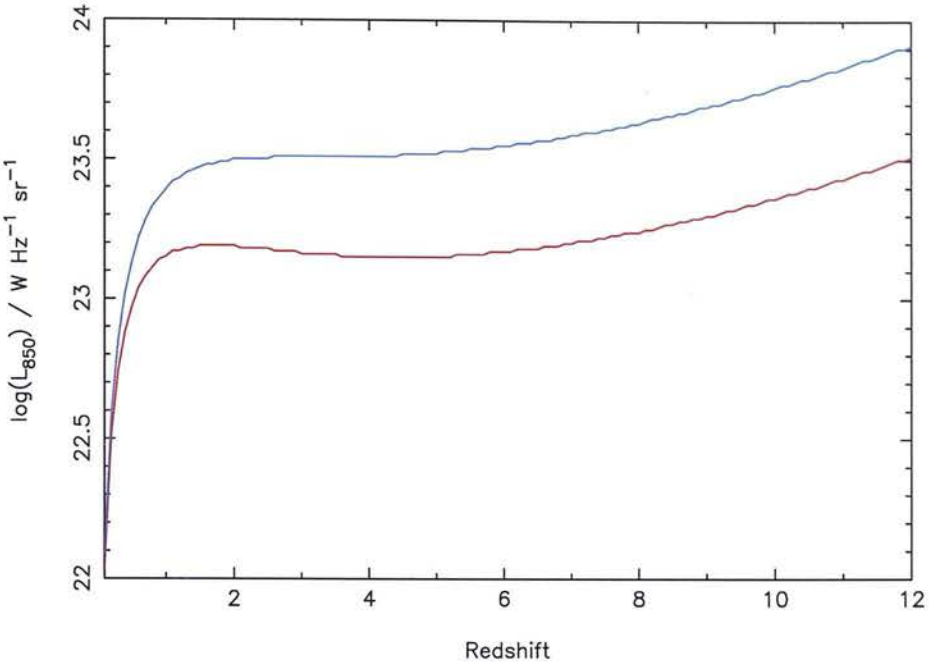

Figure 4.9: The dependence of the 850 μm luminosity on redshift for an 8 mJy source, assuming an Arp 220 SED with dust temperature 42.2K and emissivity index 1.2 (Dunne et al. 2000a). The blue line shows the dependence on redshift in an $\Omega_M = 0.3$, $\Omega_\Lambda = 0.7$ cosmology, whereas the red line shows the dependence on redshift in an $\Omega_M = 1.0$, $\Omega_\Lambda = 0.0$ cosmology.

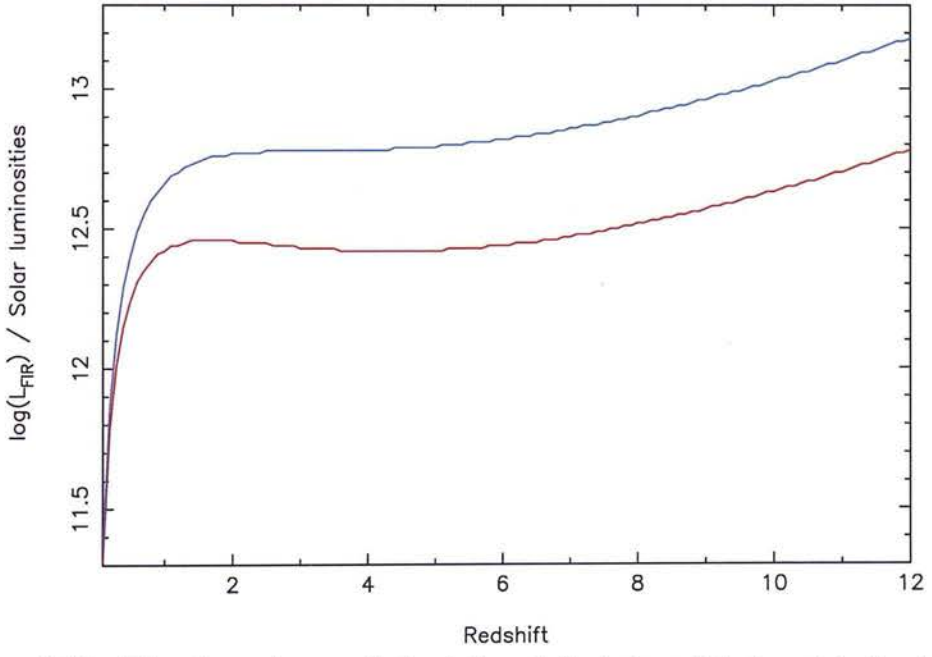

Figure 4.10: The dependence of the inferred far-infrared bolometric luminosity on redshift for an 8 mJy source, assuming an Arp 220 SED with dust temperature 42.2K and emissivity index 1.2 (Dunne et al. 2000a). The blue line shows the dependence on redshift in an $\Omega_M = 0.3$, $\Omega_\Lambda = 0.7$ cosmology, whereas the red line shows the dependence on redshift in an $\Omega_M = 1.0$, $\Omega_\Lambda = 0.0$ cosmology.

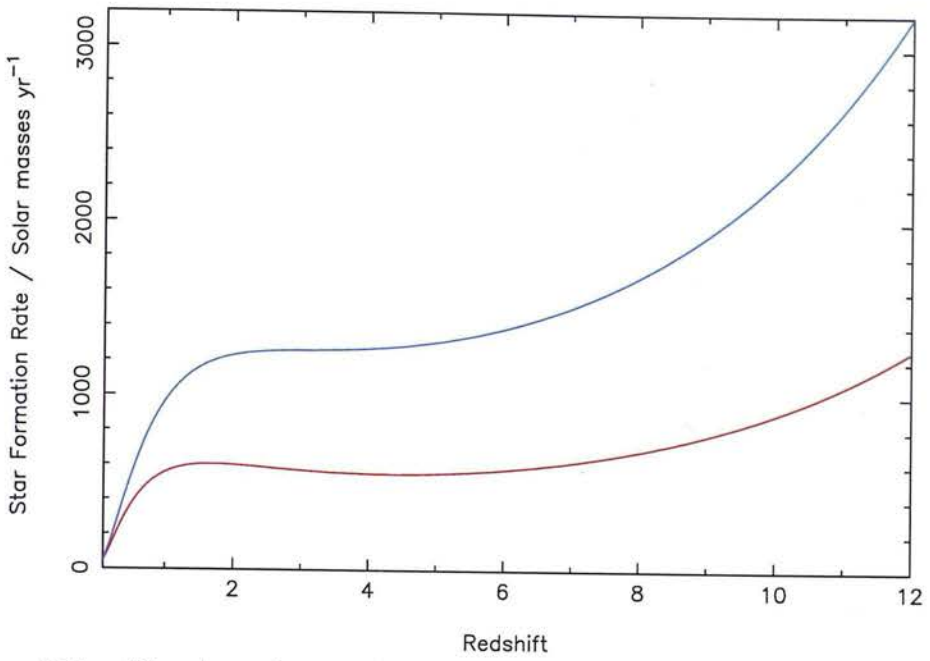

Figure 4.11: The dependence of the star formation rate on redshift for an 8 mJy source, assuming an Arp 220 SED with dust temperature 42.2K and emissivity index 1.2 (Dunne et al. 2000a). The blue line shows the dependence on redshift in an $\Omega_M = 0.3$, $\Omega_\Lambda = 0.7$ cosmology, whereas the red line shows the dependence on redshift in an $\Omega_M = 1.0$, $\Omega_\Lambda = 0.0$ cosmology.

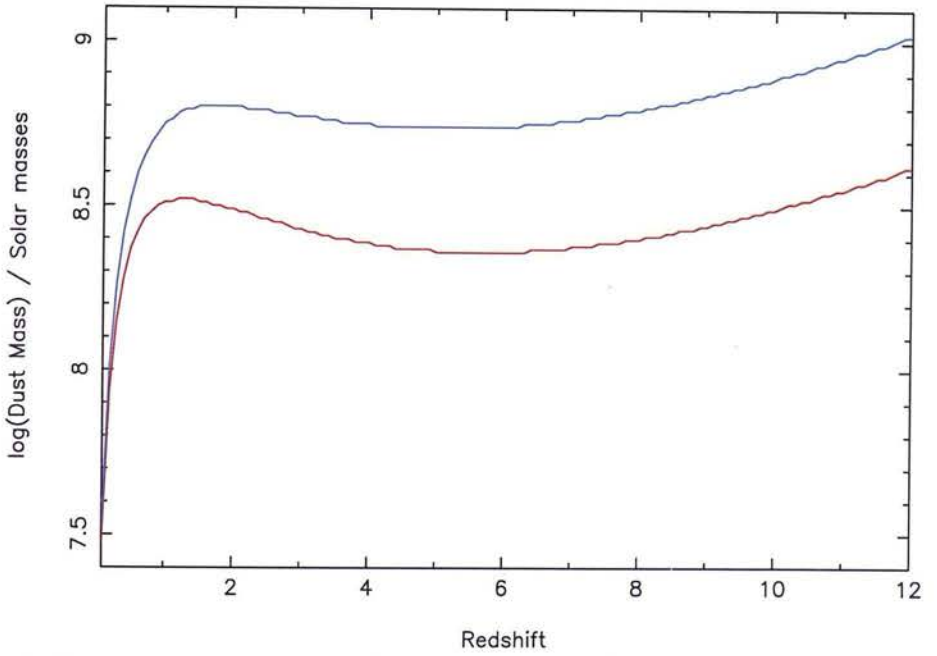

Figure 4.12: The dependence of the dust mass on redshift for an 8 mJy source, assuming an Arp 220 SED with dust temperature 42.2K and emissivity index 1.2 (Dunne et al. 2000a). The blue line shows the dependence on redshift in an $\Omega_M = 0.3$, $\Omega_\Lambda = 0.7$ cosmology, whereas the red line shows the dependence on redshift in an $\Omega_M = 1.0$, $\Omega_\Lambda = 0.0$ cosmology.

where $L_{\nu_{850\mu m}}$ is the 850 μm luminosity in terms of power per unit frequency interval per unit solid angle, $S_{850\mu m}$ is the 850 μm flux density, D is the proper distance, T_d is the dust temperature and β is the dust emissivity index.
The far-infrared bolometric luminosity is determined by integrating the monochromatic luminosity measurements with respect to frequency, over the far-infrared waveband.

$$L_{FIR} = \int_{FIR} L_\nu d\nu \tag{4.2}$$

In practice, however, this quantity is actually well approximated by interpolating $L_{\nu_{850\mu m}}$ to $\nu_{60\,\mu m}$ using the relation,

$$L_{\nu_{60\mu m}} = L_{\nu_{850\mu m}} \left(\frac{850}{60}\right)^{(3+\beta)} \left(\frac{e^{hc/kT\lambda_{850\mu m}} - 1}{e^{hc/kT\lambda_{60\mu m}} - 1}\right) \tag{4.3}$$

where $L_{\nu_{60\mu m}}$ is the 60 μm luminosity in terms of power per unit frequency interval per unit solid angle, and then assuming isotropic emission

$$L_{FIR} \simeq 4\pi L_{\nu_{60\mu m}} \nu_{60\mu m} \tag{4.4}$$

The data from the SCUBA Local Universe Galaxy Survey (SLUGS) of Dunne et al. (2000a) suggests that this approximation is valid to within 0.1 dex. The far-infrared luminosity provides a measure of the current SFR of massive stars. In regions of intense star formation, dust is heated primarily by the embedded O and B stars which evolve rapidly and dispense their surrounding material on similarly short time-scales ($\sim 10^7$ yr, Wang 1991), hence the rate of dust production is proportional to the star formation rate. The star formation rate may be calculated to within a factor of a few, by means of

$$SFR = \epsilon 10^{-10} \frac{L_{FIR}}{L_\odot} M_\odot yr^{-1} \tag{4.5}$$

The value of ϵ is uncertain to within a factor of ~ 3 (Scoville & Young 1983, Thronson & Telesco 1986, Rowan-Robinson et al. 1997, Rowan-Robinson 2000), the main sources of error arising from uncertainties in the initial mass function (IMF), the fraction of optical/UV light absorbed by the dust, and the time-scale of the burst. I have assumed a value of $\epsilon = 2.1$ (Thronson & Telesco 1986), which falls roughly in the middle of the range, incorporating a burst of O,B, and A type star-formation over $\sim 2 \times 10^6$ yr, and assumes a Salpeter IMF. It was also assumed that all of the optical/UV radiation was absorbed and re-radiated thermally by the surrounding dust.

	RA (J2000)	DEC (J2000)	S_{850} /mJy	$\log(L_{850})$ /W Hz^{-1} sr^{-1}	Inferred $\log(L_{FIR})$ /$L_\odot$
01	16:37:04.29	+41:05:30.9	11.1 ± 1.7	$23.65^{+0.06}_{-0.07}$ ($23.32^{+0.06}_{-0.07}$)	$12.92^{+0.06}_{-0.07}$ ($12.59^{+0.06}_{-0.07}$)
02	16:36:58.62	+41:05:24.9	11.0 ± 1.9	$23.64^{+0.07}_{-0.08}$ ($23.32^{+0.07}_{-0.08}$)	$12.91^{+0.07}_{-0.08}$ ($12.59^{+0.07}_{-0.08}$)
03	16:36:58.18	+41:04:39.9	9.5 ± 1.8	$23.58^{+0.08}_{-0.09}$ ($23.25^{+0.08}_{-0.09}$)	$12.85^{+0.08}_{-0.09}$ ($12.52^{+0.08}_{-0.09}$)
04	16:36:50.04	+40:57:33.0	8.3 ± 1.8	$23.52^{+0.09}_{-0.11}$ ($23.19^{+0.09}_{-0.11}$)	$12.79^{+0.09}_{-0.11}$ ($12.46^{+0.09}_{-0.11}$)
05	16:36:39.36	+40:56:38.9	9.1 ± 2.4	$23.56^{+0.10}_{-0.13}$ ($23.23^{+0.10}_{-0.13}$)	$12.83^{+0.10}_{-0.13}$ ($12.50^{+0.10}_{-0.13}$)
06	16:37:04.25	+40:55:44.9	9.2 ± 2.4	$23.56^{+0.10}_{-0.13}$ ($23.24^{+0.10}_{-0.13}$)	$12.84^{+0.10}_{-0.13}$ ($12.51^{+0.10}_{-0.13}$)
07	16:36:35.66	+40:55:56.9	8.4 ± 2.2	$23.53^{+0.10}_{-0.13}$ ($23.20^{+0.10}_{-0.13}$)	$12.80^{+0.10}_{-0.13}$ ($12.47^{+0.10}_{-0.13}$)
08	16:37:02.50	+41:01:22.9	6.1 ± 1.7	$23.39^{+0.11}_{-0.14}$ ($23.06^{+0.11}_{-0.14}$)	$12.66^{+0.11}_{-0.14}$ ($12.33^{+0.11}_{-0.14}$)
09	16:37:07.97	+40:59:30.9	6.0 ± 1.6	$23.38^{+0.10}_{-0.13}$ ($23.05^{+0.10}_{-0.13}$)	$12.65^{+0.10}_{-0.13}$ ($12.32^{+0.10}_{-0.13}$)
10	16:36:51.37	+41:05:06.0	6.5 ± 1.8	$23.41^{+0.11}_{-0.14}$ ($23.09^{+0.11}_{-0.14}$)	$12.68^{+0.11}_{-0.14}$ ($12.36^{+0.11}_{-0.14}$)
11	16:36:22.41	+40:57:04.8	9.2 ± 2.6	$23.56^{+0.11}_{-0.14}$ ($23.24^{+0.11}_{-0.14}$)	$12.84^{+0.11}_{-0.14}$ ($12.51^{+0.11}_{-0.14}$)
12	16:37:07.46	+41:02:36.9	6.2 ± 1.7	$23.39^{+0.11}_{-0.14}$ ($23.07^{+0.11}_{-0.14}$)	$12.66^{+0.11}_{-0.14}$ ($12.34^{+0.11}_{-0.14}$)
13	16:36:49.34	+41:04:17.0	7.7 ± 2.2	$23.49^{+0.11}_{-0.15}$ ($23.16^{+0.11}_{-0.15}$)	$12.76^{+0.11}_{-0.15}$ ($12.43^{+0.11}_{-0.15}$)
14	16:36:58.78	+40:57:32.9	5.0 ± 1.4	$23.30^{+0.11}_{-0.14}$ ($22.97^{+0.11}_{-0.14}$)	$12.57^{+0.11}_{-0.14}$ ($12.24^{+0.11}_{-0.14}$)
15	16:36:44.48	+40:58:38.0	7.3 ± 2.1	$23.46^{+0.11}_{-0.15}$ ($23.14^{+0.11}_{-0.15}$)	$12.73^{+0.11}_{-0.15}$ ($12.41^{+0.11}_{-0.15}$)
16	16:36:48.81	+40:55:54.0	5.5 ± 1.6	$23.34^{+0.11}_{-0.15}$ ($23.01^{+0.11}_{-0.15}$)	$12.61^{+0.11}_{-0.15}$ ($12.29^{+0.11}_{-0.15}$)
17	16:36:31.25	+40:55:46.9	6.4 ± 1.9	$23.41^{+0.11}_{-0.15}$ ($23.08^{+0.11}_{-0.15}$)	$12.68^{+0.11}_{-0.15}$ ($12.35^{+0.11}_{-0.15}$)
18	16:37:04.27	+41:01:06.9	6.4 ± 1.9	$23.41^{+0.11}_{-0.15}$ ($23.08^{+0.11}_{-0.15}$)	$12.68^{+0.11}_{-0.15}$ ($12.35^{+0.11}_{-0.15}$)
19	16:36:19.68	+40:56:22.7	11.2 ± 3.3	$23.65^{+0.11}_{-0.15}$ ($23.32^{+0.11}_{-0.15}$)	$12.92^{+0.11}_{-0.15}$ ($12.59^{+0.11}_{-0.15}$)
20	16:37:10.10	+41:00:16.8	5.1 ± 1.5	$23.31^{+0.11}_{-0.15}$ ($22.98^{+0.11}_{-0.15}$)	$12.58^{+0.11}_{-0.15}$ ($12.25^{+0.11}_{-0.15}$)
21	16:36:59.41	+40:59:57.9	8.1 ± 2.5	$23.51^{+0.12}_{-0.16}$ ($23.18^{+0.12}_{-0.16}$)	$12.78^{+0.12}_{-0.16}$ ($12.45^{+0.12}_{-0.16}$)
22	16:37:19.47	+41:01:37.7	12.4 ± 3.8	$23.69^{+0.12}_{-0.16}$ ($23.37^{+0.12}_{-0.16}$)	$12.96^{+0.12}_{-0.16}$ ($12.64^{+0.12}_{-0.16}$)
23	16:36:27.90	+40:54:03.9	13.2 ± 4.1	$23.72^{+0.12}_{-0.16}$ ($23.40^{+0.12}_{-0.16}$)	$12.99^{+0.12}_{-0.16}$ ($12.67^{+0.12}_{-0.16}$)
24	16:36:48.27	+41:03:52.0	7.0 ± 2.2	$23.45^{+0.12}_{-0.16}$ ($23.12^{+0.12}_{-0.16}$)	$12.72^{+0.12}_{-0.16}$ ($12.39^{+0.12}_{-0.16}$)
25	16:36:34.50	+40:57:23.9	6.4 ± 2.0	$23.41^{+0.12}_{-0.16}$ ($23.08^{+0.12}_{-0.16}$)	$12.68^{+0.12}_{-0.16}$ ($12.35^{+0.12}_{-0.16}$)
26	16:36:57.11	+40:59:36.0	7.6 ± 2.4	$23.48^{+0.12}_{-0.16}$ ($23.16^{+0.12}_{-0.16}$)	$12.75^{+0.12}_{-0.16}$ ($12.43^{+0.12}_{-0.16}$)
27	16:37:12.23	+41:02:57.8	5.1 ± 1.6	$23.31^{+0.12}_{-0.16}$ ($22.98^{+0.12}_{-0.16}$)	$12.58^{+0.12}_{-0.16}$ ($12.25^{+0.12}_{-0.16}$)
28	16:37:10.54	+41:00:48.8	4.6 ± 1.5	$23.26^{+0.12}_{-0.17}$ ($22.94^{+0.12}_{-0.17}$)	$12.53^{+0.12}_{-0.17}$ ($12.21^{+0.12}_{-0.17}$)
29	16:36:26.89	+41:02:22.8	10.9 ± 3.5	$23.64^{+0.12}_{-0.17}$ ($23.31^{+0.12}_{-0.17}$)	$12.91^{+0.12}_{-0.17}$ ($12.58^{+0.12}_{-0.17}$)
30	16:36:33.96	+41:01:36.9	11.8 ± 3.8	$23.67^{+0.12}_{-0.17}$ ($23.35^{+0.12}_{-0.17}$)	$12.94^{+0.12}_{-0.17}$ ($12.62^{+0.12}_{-0.17}$)
31	16:36:39.79	+41:00:33.9	5.9 ± 2.0	$23.37^{+0.13}_{-0.18}$ ($23.05^{+0.13}_{-0.18}$)	$12.64^{+0.13}_{-0.18}$ ($12.32^{+0.13}_{-0.18}$)
32	16:36:36.51	+41:05:17.9	11.8 ± 4.0	$23.67^{+0.13}_{-0.18}$ ($23.35^{+0.13}_{-0.18}$)	$12.94^{+0.13}_{-0.18}$ ($12.62^{+0.13}_{-0.18}$)
33	16:36:24.07	+40:59:34.8	10.4 ± 3.5	$23.62^{+0.13}_{-0.18}$ ($23.29^{+0.13}_{-0.18}$)	$12.89^{+0.13}_{-0.18}$ ($12.56^{+0.13}_{-0.18}$)
34	16:36:53.66	+41:00:49.0	7.2 ± 2.4	$23.46^{+0.12}_{-0.18}$ ($23.13^{+0.12}_{-0.18}$)	$12.73^{+0.12}_{-0.18}$ ($12.40^{+0.12}_{-0.18}$)
35	16:36:44.83	+40:56:51.0	5.7 ± 1.9	$23.36^{+0.12}_{-0.18}$ ($23.03^{+0.12}_{-0.18}$)	$12.63^{+0.12}_{-0.18}$ ($12.30^{+0.12}_{-0.18}$)
36	16:36:45.44	+41:04:52.0	5.6 ± 1.9	$23.35^{+0.13}_{-0.18}$ ($23.02^{+0.13}_{-0.18}$)	$12.62^{+0.13}_{-0.18}$ ($12.29^{+0.13}_{-0.18}$)
37	16:36:35.90	+41:01:37.9	9.3 ± 3.2	$23.57^{+0.13}_{-0.18}$ ($23.24^{+0.13}_{-0.18}$)	$12.84^{+0.13}_{-0.18}$ ($12.51^{+0.13}_{-0.18}$)
38	16:36:32.02	+41:00:04.9	9.2 ± 3.1	$23.56^{+0.13}_{-0.18}$ ($23.24^{+0.13}_{-0.18}$)	$12.84^{+0.13}_{-0.18}$ ($12.51^{+0.13}_{-0.18}$)
39	16:36:53.14	+41:03:46.0	5.7 ± 2.0	$23.36^{+0.13}_{-0.19}$ ($23.03^{+0.13}_{-0.19}$)	$12.63^{+0.13}_{-0.19}$ ($12.30^{+0.13}_{-0.19}$)
40	16:37:08.62	+41:04:48.9	4.3 ± 1.5	$23.23^{+0.13}_{-0.19}$ ($22.91^{+0.13}_{-0.19}$)	$12.50^{+0.13}_{-0.19}$ ($12.18^{+0.13}_{-0.19}$)
41	16:36:25.57	+41:00:35.8	7.8 ± 2.7	$23.49^{+0.13}_{-0.18}$ ($23.17^{+0.13}_{-0.18}$)	$12.76^{+0.13}_{-0.18}$ ($12.44^{+0.13}_{-0.18}$)
42	16:36:52.87	+41:02:52.0	3.9 ± 1.3	$23.19^{+0.12}_{-0.18}$ ($22.87^{+0.12}_{-0.18}$)	$12.46^{+0.12}_{-0.18}$ ($12.14^{+0.12}_{-0.18}$)
43	16:36:27.00	+40:58:14.8	6.8 ± 2.4	$23.43^{+0.13}_{-0.19}$ ($23.11^{+0.13}_{-0.19}$)	$12.70^{+0.13}_{-0.19}$ ($12.38^{+0.13}_{-0.19}$)
44	16:37:01.81	+41:06:22.9	6.1 ± 2.1	$23.39^{+0.13}_{-0.18}$ ($23.06^{+0.13}_{-0.18}$)	$12.66^{+0.13}_{-0.18}$ ($12.33^{+0.13}_{-0.18}$)
45	16:37:09.13	+41:01:59.9	4.3 ± 1.5	$23.23^{+0.13}_{-0.19}$ ($22.91^{+0.13}_{-0.19}$)	$12.50^{+0.13}_{-0.19}$ ($12.18^{+0.13}_{-0.19}$)

Table 4.4: 850 μm and inferred FIR luminosities for the ELAIS N2 sources, assuming an Arp 220 SED with $T_d = 42.2$ K and $\beta = 1.2$ (Dunne et al. 2000a). $z = 2.4$ was assumed (the median value taken from Ivison et al. (2002) using the Carilli and Yun (2000) radio-submm spectral index redshift estimates). Errors represent the error on the flux density. The left hand quantities are for an $\Omega_M = 0.3$, $\Omega_\Lambda = 0.7$ cosmology, and the right hand quantities are for an $\Omega_M = 1.0$, $\Omega_\Lambda = 0.0$ cosmology. $H_0 = 67 \mathrm{kms}^{-1}\mathrm{Mpc}^{-1}$.

	RA (J2000)	DEC (J2000)	S_{850} /mJy	$\log(L_{850})$ /W Hz^{-1} sr^{-1}	Inferred $\log(L_{FIR})$ /$L_\odot$
01	10:52:01.33	+57:24:43.3	9.6 ± 1.6	$23.58^{+0.07}_{-0.08}$ ($23.26^{+0.07}_{-0.08}$)	$12.85^{+0.07}_{-0.08}$ ($12.53^{+0.07}_{-0.08}$)
02	10:52:38.21	+57:24:35.1	11.0 ± 2.3	$23.64^{+0.08}_{-0.10}$ ($23.32^{+0.08}_{-0.10}$)	$12.91^{+0.08}_{-0.10}$ ($12.59^{+0.08}_{-0.10}$)
03	10:51:58.39	+57:18:00.3	7.9 ± 1.7	$23.50^{+0.08}_{-0.11}$ ($23.17^{+0.08}_{-0.11}$)	$12.77^{+0.08}_{-0.11}$ ($12.44^{+0.08}_{-0.11}$)
04	10:52:04.05	+57:25:29.3	7.8 ± 1.8	$23.49^{+0.09}_{-0.11}$ ($23.17^{+0.09}_{-0.11}$)	$12.76^{+0.09}_{-0.11}$ ($12.44^{+0.09}_{-0.11}$)
05	10:52:30.39	+57:22:13.2	10.8 ± 2.6	$23.63^{+0.09}_{-0.12}$ ($23.31^{+0.09}_{-0.12}$)	$12.90^{+0.09}_{-0.12}$ ($12.58^{+0.09}_{-0.12}$)
06	10:52:22.71	+57:19:32.3	14.0 ± 3.4	$23.75^{+0.09}_{-0.12}$ ($23.42^{+0.09}_{-0.12}$)	$13.02^{+0.09}_{-0.12}$ ($12.69^{+0.09}_{-0.12}$)
07	10:51:51.54	+57:26:35.2	8.0 ± 2.0	$23.50^{+0.10}_{-0.12}$ ($23.18^{+0.10}_{-0.12}$)	$12.77^{+0.10}_{-0.12}$ ($12.45^{+0.10}_{-0.12}$)
08	10:51:59.60	+57:24:21.3	4.8 ± 1.2	$23.28^{+0.10}_{-0.12}$ ($22.96^{+0.10}_{-0.12}$)	$12.55^{+0.10}_{-0.12}$ ($12.23^{+0.10}_{-0.12}$)
09	10:51:59.26	+57:17:18.3	8.0 ± 2.1	$23.50^{+0.10}_{-0.13}$ ($23.18^{+0.10}_{-0.13}$)	$12.77^{+0.10}_{-0.13}$ ($12.45^{+0.10}_{-0.13}$)
10	10:51:42.39	+57:24:45.1	12.0 ± 3.2	$23.68^{+0.10}_{-0.13}$ ($23.35^{+0.10}_{-0.13}$)	$12.95^{+0.10}_{-0.13}$ ($12.62^{+0.10}_{-0.13}$)
11	10:51:53.82	+57:18:47.3	6.7 ± 1.8	$23.43^{+0.10}_{-0.14}$ ($23.10^{+0.10}_{-0.14}$)	$12.70^{+0.10}_{-0.14}$ ($12.37^{+0.10}_{-0.14}$)
12	10:52:16.78	+57:19:23.3	10.1 ± 2.8	$23.61^{+0.11}_{-0.14}$ ($23.28^{+0.11}_{-0.14}$)	$12.88^{+0.11}_{-0.14}$ ($12.55^{+0.11}_{-0.14}$)
13	10:51:33.57	+57:26:41.0	9.5 ± 2.7	$23.58^{+0.11}_{-0.15}$ ($23.25^{+0.11}_{-0.15}$)	$12.85^{+0.11}_{-0.15}$ ($12.52^{+0.11}_{-0.15}$)
14	10:52:07.77	+57:19:07.3	5.6 ± 1.6	$23.35^{+0.11}_{-0.15}$ ($23.02^{+0.11}_{-0.15}$)	$12.62^{+0.11}_{-0.15}$ ($12.29^{+0.11}_{-0.15}$)
15	10:51:30.46	+57:20:37.9	12.0 ± 3.5	$23.68^{+0.11}_{-0.15}$ ($23.35^{+0.11}_{-0.15}$)	$12.95^{+0.11}_{-0.15}$ ($12.62^{+0.11}_{-0.15}$)
16	10:52:36.37	+57:25:15.1	5.7 ± 1.7	$23.36^{+0.11}_{-0.15}$ ($23.03^{+0.11}_{-0.15}$)	$12.63^{+0.11}_{-0.15}$ ($12.30^{+0.11}_{-0.15}$)
17	10:52:04.30	+57:27:01.3	9.2 ± 2.7	$23.56^{+0.11}_{-0.15}$ ($23.24^{+0.11}_{-0.15}$)	$12.84^{+0.11}_{-0.15}$ ($12.51^{+0.11}_{-0.15}$)
18	10:52:05.67	+57:20:53.3	4.6 ± 1.4	$23.26^{+0.12}_{-0.16}$ ($22.94^{+0.12}_{-0.16}$)	$12.53^{+0.12}_{-0.16}$ ($12.21^{+0.12}_{-0.16}$)
19	10:52:24.58	+57:21:19.3	11.7 ± 3.5	$23.67^{+0.11}_{-0.15}$ ($23.34^{+0.11}_{-0.15}$)	$12.94^{+0.11}_{-0.15}$ ($12.61^{+0.11}_{-0.15}$)
20	10:52:27.18	+57:22:21.2	12.1 ± 3.7	$23.68^{+0.12}_{-0.16}$ ($23.36^{+0.12}_{-0.16}$)	$12.95^{+0.12}_{-0.16}$ ($12.63^{+0.12}_{-0.16}$)
21	10:52:37.67	+57:20:30.1	9.8 ± 3.1	$23.59^{+0.12}_{-0.17}$ ($23.27^{+0.12}_{-0.17}$)	$12.86^{+0.12}_{-0.17}$ ($12.54^{+0.12}_{-0.17}$)
22	10:51:46.97	+57:24:51.2	7.1 ± 2.2	$23.45^{+0.12}_{-0.16}$ ($23.13^{+0.12}_{-0.16}$)	$12.72^{+0.12}_{-0.16}$ ($12.40^{+0.12}_{-0.16}$)
23	10:52:28.07	+57:25:09.2	5.8 ± 1.8	$23.36^{+0.12}_{-0.16}$ ($23.04^{+0.12}_{-0.16}$)	$12.63^{+0.12}_{-0.16}$ ($12.31^{+0.12}_{-0.16}$)
24	10:52:03.94	+57:20:07.3	4.0 ± 1.3	$23.20^{+0.12}_{-0.17}$ ($22.88^{+0.12}_{-0.17}$)	$12.47^{+0.12}_{-0.17}$ ($12.15^{+0.12}_{-0.17}$)
25	10:51:48.36	+57:21:48.2	12.1 ± 3.8	$23.68^{+0.12}_{-0.16}$ ($23.36^{+0.12}_{-0.16}$)	$12.95^{+0.12}_{-0.16}$ ($12.63^{+0.12}_{-0.16}$)
26	10:52:09.87	+57:20:40.3	9.0 ± 2.8	$23.56^{+0.12}_{-0.16}$ ($23.23^{+0.12}_{-0.16}$)	$12.83^{+0.12}_{-0.16}$ ($12.50^{+0.12}_{-0.16}$)
27	10:52:34.57	+57:20:02.1	10.0 ± 3.2	$23.60^{+0.12}_{-0.17}$ ($23.27^{+0.12}_{-0.17}$)	$12.87^{+0.12}_{-0.17}$ ($12.55^{+0.12}_{-0.17}$)
28	10:51:42.89	+57:24:12.1	11.0 ± 3.6	$23.64^{+0.12}_{-0.17}$ ($23.32^{+0.12}_{-0.17}$)	$12.91^{+0.12}_{-0.17}$ ($12.59^{+0.12}_{-0.17}$)
29	10:52:01.71	+57:19:16.3	4.0 ± 1.3	$23.20^{+0.12}_{-0.17}$ ($22.88^{+0.12}_{-0.17}$)	$12.47^{+0.12}_{-0.17}$ ($12.15^{+0.12}_{-0.17}$)
30	10:51:59.99	+57:20:39.3	4.2 ± 1.4	$23.22^{+0.12}_{-0.18}$ ($22.90^{+0.12}_{-0.18}$)	$12.49^{+0.12}_{-0.18}$ ($12.17^{+0.12}_{-0.18}$)
31	10:52:27.28	+57:19:06.2	7.7 ± 2.5	$23.49^{+0.12}_{-0.17}$ ($23.16^{+0.12}_{-0.17}$)	$12.76^{+0.12}_{-0.17}$ ($12.43^{+0.12}_{-0.17}$)
32	10:52:34.51	+57:25:34.1	4.1 ± 1.4	$23.21^{+0.13}_{-0.18}$ ($22.89^{+0.13}_{-0.18}$)	$12.48^{+0.13}_{-0.18}$ ($12.16^{+0.13}_{-0.18}$)
33	10:52:10.86	+57:24:13.3	8.4 ± 2.8	$23.53^{+0.12}_{-0.18}$ ($23.20^{+0.12}_{-0.18}$)	$12.80^{+0.12}_{-0.18}$ ($12.47^{+0.12}_{-0.18}$)
34	10:51:33.81	+57:19:29.0	7.8 ± 2.6	$23.49^{+0.12}_{-0.18}$ ($23.17^{+0.12}_{-0.18}$)	$12.76^{+0.12}_{-0.18}$ ($12.44^{+0.12}_{-0.18}$)
35	10:51:55.77	+57:23:12.3	4.0 ± 1.3	$23.20^{+0.12}_{-0.17}$ ($22.88^{+0.12}_{-0.17}$)	$12.47^{+0.12}_{-0.17}$ ($12.15^{+0.12}_{-0.17}$)
36	10:51:23.29	+57:20:33.8	13.9 ± 4.7	$23.74^{+0.13}_{-0.18}$ ($23.42^{+0.13}_{-0.18}$)	$13.01^{+0.13}_{-0.18}$ ($12.69^{+0.13}_{-0.18}$)
37	10:52:29.57	+57:26:20.2	4.7 ± 1.6	$23.27^{+0.13}_{-0.18}$ ($22.95^{+0.13}_{-0.18}$)	$12.54^{+0.13}_{-0.18}$ ($12.22^{+0.13}_{-0.18}$)
38	10:52:41.14	+57:21:47.1	14.3 ± 4.9	$23.76^{+0.13}_{-0.18}$ ($23.43^{+0.13}_{-0.18}$)	$13.03^{+0.13}_{-0.18}$ ($12.70^{+0.13}_{-0.18}$)
39	10:52:03.45	+57:16:54.3	7.9 ± 2.7	$23.50^{+0.13}_{-0.18}$ ($23.17^{+0.13}_{-0.18}$)	$12.77^{+0.13}_{-0.18}$ ($12.44^{+0.13}_{-0.18}$)
40	10:51:52.56	+57:22:29.2	4.4 ± 1.5	$23.24^{+0.13}_{-0.18}$ ($22.92^{+0.13}_{-0.18}$)	$12.51^{+0.13}_{-0.18}$ ($12.19^{+0.13}_{-0.18}$)

Table 4.5: 850 μm and inferred far infrared bolometric luminosities for the Lockman Hole sources, assuming an Arp 220 SED with dust temperature 42.2K and emissivity index 1.2 (Dunne et al. 2000a). A redshift of 2.4 was assumed (the median value taken from Ivison et al. (2002) using the Carilli and Yun (2000) radio-submm spectral index redshift estimates). Errors represent the error on the flux density. The left hand quantities are for an $\Omega_M = 0.3$, $\Omega_\Lambda = 0.7$ cosmology, and the right hand quantities (enclosed in brackets) are for an $\Omega_M = 1.0$, $\Omega_\Lambda = 0.0$ cosmology. $H_0 = 67 \mathrm{kms}^{-1}\mathrm{Mpc}^{-1}$.

	RA (J2000)	DEC (J2000)	S_{850} /mJy	SFR /$M_\odot$ yr^{-1}	log(Dust Mass) /$M_\odot$
01	16:37:04.29	+41:05:30.9	11.1 ± 1.7	1734 ± 265 (817 ± 125)	$8.93^{+0.06}_{-0.07}$ ($8.61^{+0.06}_{-0.07}$)
02	16:36:58.62	+41:05:24.9	11.0 ± 1.9	1718 ± 296 (810 ± 139)	$8.93^{+0.07}_{-0.08}$ ($8.60^{+0.07}_{-0.08}$)
03	16:36:58.18	+41:04:39.9	9.5 ± 1.8	1484 ± 281 (699 ± 132)	$8.86^{+0.08}_{-0.09}$ ($8.54^{+0.08}_{-0.09}$)
04	16:36:50.04	+40:57:33.0	8.3 ± 1.8	1296 ± 281 (611 ± 132)	$8.81^{+0.09}_{-0.11}$ ($8.48^{+0.09}_{-0.11}$)
05	16:36:39.36	+40:56:38.9	9.1 ± 2.4	1421 ± 374 (670 ± 176)	$8.85^{+0.10}_{-0.13}$ ($8.52^{+0.10}_{-0.13}$)
06	16:37:04.25	+40:55:44.9	9.2 ± 2.4	1437 ± 374 (677 ± 176)	$8.85^{+0.10}_{-0.13}$ ($8.52^{+0.10}_{-0.13}$)
07	16:36:35.66	+40:55:56.9	8.4 ± 2.2	1312 ± 343 (618 ± 162)	$8.81^{+0.10}_{-0.13}$ ($8.48^{+0.10}_{-0.13}$)
08	16:37:02.50	+41:01:22.9	6.1 ± 1.7	952 ± 265 (449 ± 125)	$8.67^{+0.11}_{-0.14}$ ($8.35^{+0.11}_{-0.14}$)
09	16:37:07.97	+40:59:30.9	6.0 ± 1.6	937 ± 249 (441 ± 117)	$8.66^{+0.10}_{-0.13}$ ($8.34^{+0.10}_{-0.13}$)
10	16:36:51.37	+41:05:06.0	6.5 ± 1.8	1015 ± 281 (478 ± 132)	$8.70^{+0.11}_{-0.14}$ ($8.37^{+0.11}_{-0.14}$)
11	16:36:22.41	+40:57:04.8	9.2 ± 2.6	1437 ± 406 (677 ± 191)	$8.85^{+0.11}_{-0.14}$ ($8.52^{+0.11}_{-0.14}$)
12	16:37:07.46	+41:02:36.9	6.2 ± 1.7	968 ± 265 (456 ± 125)	$8.68^{+0.11}_{-0.14}$ ($8.35^{+0.11}_{-0.14}$)
13	16:36:49.34	+41:04:17.0	7.7 ± 2.2	1202 ± 343 (567 ± 162)	$8.77^{+0.11}_{-0.15}$ ($8.45^{+0.11}_{-0.15}$)
14	16:36:58.78	+40:57:32.9	5.0 ± 1.4	781 ± 218 (368 ± 103)	$8.59^{+0.11}_{-0.14}$ ($8.26^{+0.11}_{-0.14}$)
15	16:36:44.48	+40:58:38.0	7.3 ± 2.1	1140 ± 328 (537 ± 154)	$8.75^{+0.11}_{-0.15}$ ($8.42^{+0.11}_{-0.15}$)
16	16:36:48.81	+40:55:54.0	5.5 ± 1.6	859 ± 249 (405 ± 117)	$8.63^{+0.11}_{-0.15}$ ($8.30^{+0.11}_{-0.15}$)
17	16:36:31.25	+40:55:46.9	6.4 ± 1.9	999 ± 296 (471 ± 139)	$8.69^{+0.11}_{-0.15}$ ($8.37^{+0.11}_{-0.15}$)
18	16:37:04.27	+41:01:06.9	6.4 ± 1.9	999 ± 296 (471 ± 139)	$8.69^{+0.11}_{-0.15}$ ($8.37^{+0.11}_{-0.15}$)
19	16:36:19.68	+40:56:22.7	11.2 ± 3.3	1749 ± 515 (825 ± 243)	$8.94^{+0.11}_{-0.15}$ ($8.61^{+0.11}_{-0.15}$)
20	16:37:10.10	+41:00:16.8	5.1 ± 1.5	796 ± 234 (375 ± 110)	$8.59^{+0.11}_{-0.15}$ ($8.27^{+0.11}_{-0.15}$)
21	16:36:59.41	+40:59:57.9	8.1 ± 2.5	1265 ± 390 (596 ± 184)	$8.80^{+0.12}_{-0.16}$ ($8.47^{+0.12}_{-0.16}$)
22	16:37:19.47	+41:01:37.7	12.4 ± 3.8	1937 ± 593 (913 ± 279)	$8.98^{+0.12}_{-0.16}$ ($8.65^{+0.12}_{-0.16}$)
23	16:36:27.90	+40:54:03.9	13.2 ± 4.1	2062 ± 640 (972 ± 302)	$9.01^{+0.12}_{-0.16}$ ($8.68^{+0.12}_{-0.16}$)
24	16:36:48.27	+41:03:52.0	7.0 ± 2.2	1093 ± 343 (515 ± 162)	$8.73^{+0.12}_{-0.16}$ ($8.41^{+0.12}_{-0.16}$)
25	16:36:34.50	+40:57:23.9	6.4 ± 2.0	999 ± 312 (471 ± 147)	$8.69^{+0.12}_{-0.16}$ ($8.37^{+0.12}_{-0.16}$)
26	16:36:57.11	+40:59:36.0	7.6 ± 2.4	1187 ± 374 (559 ± 176)	$8.77^{+0.12}_{-0.16}$ ($8.44^{+0.12}_{-0.16}$)
27	16:37:12.23	+41:02:57.8	5.1 ± 1.6	796 ± 249 (375 ± 117)	$8.59^{+0.12}_{-0.16}$ ($8.27^{+0.12}_{-0.16}$)
28	16:37:10.54	+41:00:48.8	4.6 ± 1.5	718 ± 234 (338 ± 110)	$8.55^{+0.12}_{-0.17}$ ($8.22^{+0.12}_{-0.17}$)
29	16:36:26.89	+41:02:22.8	10.9 ± 3.5	1702 ± 546 (802 ± 257)	$8.92^{+0.12}_{-0.17}$ ($8.60^{+0.12}_{-0.17}$)
30	16:36:33.96	+41:01:36.9	11.8 ± 3.8	1843 ± 593 (869 ± 279)	$8.96^{+0.12}_{-0.17}$ ($8.63^{+0.12}_{-0.17}$)
31	16:36:39.79	+41:00:33.9	5.9 ± 2.0	921 ± 312 (434 ± 147)	$8.66^{+0.13}_{-0.18}$ ($8.33^{+0.13}_{-0.18}$)
32	16:36:36.51	+41:05:17.9	11.8 ± 4.0	1843 ± 624 (869 ± 294)	$8.96^{+0.13}_{-0.18}$ ($8.63^{+0.13}_{-0.18}$)
33	16:36:24.07	+40:59:34.8	10.4 ± 3.5	1624 ± 546 (766 ± 257)	$8.90^{+0.13}_{-0.18}$ ($8.58^{+0.13}_{-0.18}$)
34	16:36:53.66	+41:00:49.0	7.2 ± 2.4	1124 ± 374 (530 ± 176)	$8.74^{+0.12}_{-0.18}$ ($8.42^{+0.12}_{-0.18}$)
35	16:36:44.83	+40:56:51.0	5.7 ± 1.9	890 ± 296 (419 ± 139)	$8.64^{+0.12}_{-0.18}$ ($8.32^{+0.12}_{-0.18}$)
36	16:36:45.44	+41:04:52.0	5.6 ± 1.9	874 ± 296 (412 ± 139)	$8.63^{+0.13}_{-0.18}$ ($8.31^{+0.13}_{-0.18}$)
37	16:36:35.90	+41:01:37.9	9.3 ± 3.2	1452 ± 499 (685 ± 235)	$8.86^{+0.13}_{-0.18}$ ($8.53^{+0.13}_{-0.18}$)
38	16:36:32.02	+41:00:04.9	9.2 ± 3.1	1437 ± 484 (677 ± 228)	$8.85^{+0.13}_{-0.18}$ ($8.52^{+0.13}_{-0.18}$)
39	16:36:53.14	+41:03:46.0	5.7 ± 2.0	890 ± 312 (419 ± 147)	$8.64^{+0.13}_{-0.19}$ ($8.32^{+0.13}_{-0.19}$)
40	16:37:08.62	+41:04:48.9	4.3 ± 1.5	671 ± 234 (316 ± 110)	$8.52^{+0.13}_{-0.19}$ ($8.19^{+0.13}_{-0.19}$)
41	16:36:25.57	+41:00:35.8	7.8 ± 2.7	1218 ± 421 (574 ± 198)	$8.78^{+0.13}_{-0.18}$ ($8.45^{+0.13}_{-0.18}$)
42	16:36:52.87	+41:02:52.0	3.9 ± 1.3	609 ± 203 (287 ± 95)	$8.48^{+0.12}_{-0.18}$ ($8.15^{+0.12}_{-0.18}$)
43	16:36:27.00	+40:58:14.8	6.8 ± 2.4	1062 ± 374 (500 ± 176)	$8.72^{+0.13}_{-0.19}$ ($8.39^{+0.13}_{-0.19}$)
44	16:37:01.81	+41:06:22.9	6.1 ± 2.1	952 ± 328 (449 ± 154)	$8.67^{+0.13}_{-0.18}$ ($8.35^{+0.13}_{-0.18}$)
45	16:37:09.13	+41:01:59.9	4.3 ± 1.5	671 ± 234 (316 ± 110)	$8.52^{+0.13}_{-0.19}$ ($8.19^{+0.13}_{-0.19}$)

Table 4.6: Star formation rates and dust masses for the ELAIS N2 sources, assuming an Arp 220 SED with $T_d = 42.2$ K and $\beta = 1.2$ (Dunne et al. 2000a). $z = 2.4$ was assumed (the median value taken from Ivison et al. (2002) using the Carilli and Yun (2000) radio-submm spectral index redshift estimates). Errors represent the error on the flux density. The left hand quantities are for an $\Omega_M = 0.3$, $\Omega_\Lambda = 0.7$ cosmology, and the right hand quantities are for an $\Omega_M = 1.0$, $\Omega_\Lambda = 0.0$ cosmology. $H_0 = 67 \mathrm{kms}^{-1}\mathrm{Mpc}^{-1}$.

	RA (J2000)	DEC (J2000)	S_{850} /mJy	SFR /$M_\odot$ yr^{-1}	log(Dust Mass) /$M_\odot$
01	10:52:01.33	+57:24:43.3	9.6 ± 1.6	1499 ± 249 (707 ± 117)	$8.87^{+0.07}_{-0.08}$ ($8.54^{+0.07}_{-0.08}$)
02	10:52:38.21	+57:24:35.1	11.0 ± 2.3	1718 ± 359 (810 ± 169)	$8.93^{+0.08}_{-0.10}$ ($8.60^{+0.08}_{-0.10}$)
03	10:51:58.39	+57:18:00.3	7.9 ± 1.7	1234 ± 265 (581 ± 125)	$8.78^{+0.08}_{-0.11}$ ($8.46^{+0.08}_{-0.11}$)
04	10:52:04.05	+57:25:29.3	7.8 ± 1.8	1218 ± 281 (574 ± 132)	$8.78^{+0.09}_{-0.11}$ ($8.45^{+0.09}_{-0.11}$)
05	10:52:30.39	+57:22:13.2	10.8 ± 2.6	1687 ± 406 (795 ± 191)	$8.92^{+0.09}_{-0.12}$ ($8.59^{+0.09}_{-0.12}$)
06	10:52:22.71	+57:19:32.3	14.0 ± 3.4	2187 ± 531 (1031 ± 250)	$9.03^{+0.09}_{-0.12}$ ($8.71^{+0.09}_{-0.12}$)
07	10:51:51.54	+57:26:35.2	8.0 ± 2.0	1249 ± 312 (589 ± 147)	$8.79^{+0.10}_{-0.12}$ ($8.46^{+0.10}_{-0.12}$)
08	10:51:59.60	+57:24:21.3	4.8 ± 1.2	749 ± 187 (353 ± 88)	$8.57^{+0.10}_{-0.12}$ ($8.24^{+0.10}_{-0.12}$)
09	10:51:59.26	+57:17:18.3	8.0 ± 2.1	1249 ± 328 (589 ± 154)	$8.79^{+0.10}_{-0.13}$ ($8.46^{+0.10}_{-0.13}$)
10	10:51:42.39	+57:24:45.1	12.0 ± 3.2	1874 ± 499 (883 ± 235)	$8.97^{+0.10}_{-0.13}$ ($8.64^{+0.10}_{-0.13}$)
11	10:51:53.82	+57:18:47.3	6.7 ± 1.8	1046 ± 281 (493 ± 132)	$8.71^{+0.10}_{-0.14}$ ($8.39^{+0.10}_{-0.14}$)
12	10:52:16.78	+57:19:23.3	10.1 ± 2.8	1577 ± 437 (743 ± 206)	$8.89^{+0.11}_{-0.14}$ ($8.56^{+0.11}_{-0.14}$)
13	10:51:33.57	+57:26:41.0	9.5 ± 2.7	1484 ± 421 (699 ± 198)	$8.86^{+0.11}_{-0.15}$ ($8.54^{+0.11}_{-0.15}$)
14	10:52:07.77	+57:19:07.3	5.6 ± 1.6	874 ± 249 (412 ± 117)	$8.63^{+0.11}_{-0.15}$ ($8.31^{+0.11}_{-0.15}$)
15	10:51:30.46	+57:20:37.9	12.0 ± 3.5	1874 ± 546 (883 ± 257)	$8.97^{+0.11}_{-0.15}$ ($8.64^{+0.11}_{-0.15}$)
16	10:52:36.37	+57:25:15.1	5.7 ± 1.7	890 ± 265 (419 ± 125)	$8.64^{+0.11}_{-0.15}$ ($8.32^{+0.11}_{-0.15}$)
17	10:52:04.30	+57:27:01.3	9.2 ± 2.7	1437 ± 421 (677 ± 198)	$8.85^{+0.11}_{-0.15}$ ($8.52^{+0.11}_{-0.15}$)
18	10:52:05.67	+57:20:53.3	4.6 ± 1.4	718 ± 218 (338 ± 103)	$8.55^{+0.12}_{-0.16}$ ($8.22^{+0.12}_{-0.16}$)
19	10:52:24.58	+57:21:19.3	11.7 ± 3.5	1827 ± 546 (861 ± 257)	$8.95^{+0.11}_{-0.15}$ ($8.63^{+0.11}_{-0.15}$)
20	10:52:27.18	+57:22:21.2	12.1 ± 3.7	1890 ± 578 (891 ± 272)	$8.97^{+0.12}_{-0.16}$ ($8.64^{+0.12}_{-0.16}$)
21	10:52:37.67	+57:20:30.1	9.8 ± 3.1	1530 ± 484 (721 ± 228)	$8.88^{+0.12}_{-0.17}$ ($8.55^{+0.12}_{-0.17}$)
22	10:51:46.97	+57:24:51.2	7.1 ± 2.2	1109 ± 343 (523 ± 162)	$8.74^{+0.12}_{-0.16}$ ($8.41^{+0.12}_{-0.16}$)
23	10:52:28.07	+57:25:09.2	5.8 ± 1.8	906 ± 281 (427 ± 132)	$8.65^{+0.12}_{-0.16}$ ($8.32^{+0.12}_{-0.16}$)
24	10:52:03.94	+57:20:07.3	4.0 ± 1.3	624 ± 203 (294 ± 95)	$8.49^{+0.12}_{-0.17}$ ($8.16^{+0.12}_{-0.17}$)
25	10:51:48.36	+57:21:48.2	12.1 ± 3.8	1890 ± 593 (891 ± 279)	$8.97^{+0.12}_{-0.16}$ ($8.64^{+0.12}_{-0.16}$)
26	10:52:09.87	+57:20:40.3	9.0 ± 2.8	1405 ± 437 (662 ± 206)	$8.84^{+0.12}_{-0.16}$ ($8.51^{+0.12}_{-0.16}$)
27	10:52:34.57	+57:20:02.1	10.0 ± 3.2	1562 ± 499 (736 ± 235)	$8.89^{+0.12}_{-0.17}$ ($8.56^{+0.12}_{-0.17}$)
28	10:51:42.89	+57:24:12.1	11.0 ± 3.6	1718 ± 562 (810 ± 265)	$8.93^{+0.12}_{-0.17}$ ($8.60^{+0.12}_{-0.17}$)
29	10:52:01.71	+57:19:16.3	4.0 ± 1.3	624 ± 203 (294 ± 95)	$8.49^{+0.12}_{-0.17}$ ($8.16^{+0.12}_{-0.17}$)
30	10:51:59.99	+57:20:39.3	4.2 ± 1.4	656 ± 218 (309 ± 103)	$8.51^{+0.12}_{-0.18}$ ($8.18^{+0.12}_{-0.18}$)
31	10:52:27.28	+57:19:06.2	7.7 ± 2.5	1202 ± 390 (567 ± 184)	$8.77^{+0.12}_{-0.17}$ ($8.45^{+0.12}_{-0.17}$)
32	10:52:34.51	+57:25:34.1	4.1 ± 1.4	640 ± 218 (302 ± 103)	$8.50^{+0.13}_{-0.18}$ ($8.17^{+0.13}_{-0.18}$)
33	10:52:10.86	+57:24:13.3	8.4 ± 2.8	1312 ± 437 (618 ± 206)	$8.81^{+0.12}_{-0.18}$ ($8.48^{+0.12}_{-0.18}$)
34	10:51:33.81	+57:19:29.0	7.8 ± 2.6	1218 ± 406 (574 ± 191)	$8.78^{+0.12}_{-0.18}$ ($8.45^{+0.12}_{-0.18}$)
35	10:51:55.77	+57:23:12.3	4.0 ± 1.3	624 ± 203 (294 ± 95)	$8.49^{+0.12}_{-0.17}$ ($8.16^{+0.12}_{-0.17}$)
36	10:51:23.29	+57:20:33.8	13.9 ± 4.7	2171 ± 734 (1023 ± 346)	$9.03^{+0.13}_{-0.18}$ ($8.70^{+0.13}_{-0.18}$)
37	10:52:29.57	+57:26:20.2	4.7 ± 1.6	734 ± 249 (346 ± 117)	$8.56^{+0.13}_{-0.18}$ ($8.23^{+0.13}_{-0.18}$)
38	10:52:41.14	+57:21:47.1	14.3 ± 4.9	2233 ± 765 (1053 ± 360)	$9.04^{+0.13}_{-0.18}$ ($8.72^{+0.13}_{-0.18}$)
39	10:52:03.45	+57:16:54.3	7.9 ± 2.7	1234 ± 421 (581 ± 198)	$8.78^{+0.13}_{-0.18}$ ($8.46^{+0.13}_{-0.18}$)
40	10:51:52.56	+57:22:29.2	4.4 ± 1.5	687 ± 234 (324 ± 110)	$8.53^{+0.13}_{-0.18}$ ($8.20^{+0.13}_{-0.18}$)

Table 4.7: Star formation rates and dust masses for the Lockman Hole sources, assuming an Arp 220 SED with dust temperature 42.2K and emissivity index 1.2 (Dunne et al. 2000a). A redshift of 2.4 was assumed (the median value taken from Ivison et al. (2002) using the Carilli and Yun (2000) radio-submm spectral index redshift estimates). Errors represent the error on the flux density. The left hand quantities are for an $\Omega_M = 0.3$, $\Omega_\Lambda = 0.7$ cosmology, and the right hand quantities (enclosed in brackets) are for an $\Omega_M = 1.0$, $\Omega_\Lambda = 0.0$ cosmology. $H_0 = 67 \mathrm{kms}^{-1}\mathrm{Mpc}^{-1}$.

In calculating the mass of dust present in each source, it is assumed that the submillimetre continuum is the result of optically-thin thermal emission from the heated dust grains, with no additional contribution from bremsstrahlung or synchrotron radiation. The dust mass M_d is then determined directly by the relation

$$M_d = \frac{S_{850\mu m} D^2 (1+z)}{\kappa_d^{rest} B(\nu^{rest}, T_d)} \tag{4.6}$$

where $S_{850\mu m}$ is the observed flux density, D is the proper distance, κ_d^{rest} is the rest-frequency mass absorption coefficient, and $B(\nu^{rest}, T_d)$ is the rest-frequency value of the Planck function from dust grains radiating at temperature T_d. For more information regarding this equation, see Section 1.4 in the Introduction. The main uncertainty in determining the dust mass M_d is the uncertainty in the rest-frequency mass absorption coefficient κ_d^{rest}. The values given in the literature span almost an order of magnitude, from $\kappa_d(850\mu m) \simeq 0.04\,m^2kg^{-1}$ (Draine & Lee 1984), $\kappa_d(850\mu m) = 0.07 \pm 0.02\,m^2kg^{-1}$ (James et al. 2002), to $\kappa_d(850\mu m) \simeq 0.3\,m^2kg^{-1}$ (Mathis & Whiffen 1989), depending on the size, shape, mass and composition of the dust grains, as well as how the dust is distributed ie. if the grains stick together or are spread fairly diffusely. In order to minimise the error on the dust mass estimates, I have adopted the same approach as Hughes, Dunlop & Rawlings (1997), using their average value of $\kappa_d(800\mu m) = 0.15 \pm 0.09\,m^2kg^{-1}$, and interpolating to other submillimetre wavelengths by assuming $\kappa_d \propto \lambda^{-1.5}$ (at 850μm the average value is equivalent to $\kappa_d(850\mu m) = 0.14 \pm 0.08\,m^2kg^{-1}$). A different choice of $\kappa_d(850\mu m)$ would be expected to change the dust mass estimates by factors of up to $\sim 2-3$.

One of the best studied starburst galaxies in the local universe is the ultraluminous infrared galaxy (ULIRG) Arp 220. This galaxy is an extreme starburst ($L_{FIR} = 10^{12}\,L_\odot$, $SFR = 300\,M_\odot yr^{-1}$) and has a very steep rest frame mid- to far-IR spectrum. Chapman et al. (2003a) have shown that it describes the spectral energy distribution of the high-redshift ($z > 1$) SCUBA population fairly well on average. Dunne et al. (2000a) find a best fit dust temperature $T_d = 42.2\,K$ and emissivity index $\beta = 1.2$, which is in good agreemant with Lisenfeld, Isaak & Hills (2000) who found a slightly larger best fit dust temperature $T_d = 45\,K$ and emissivity index $\beta = 1.2$. Adopting the values of Dunne et al. (2000a), and assuming that all of the recovered sources lie at $z = 2.4$ (the median redshift given in Ivison et al. (2002) based on the Carilli & Yun (2000) radio-to-submillimetre spectral index redshift estimator), Tables 4.4 to 4.7 give estimates for the 850 μm luminosity,

far-infrared luminosity, star formation rates and dust masses using the calculations given above. The un-bracketted quantities assume an $\Omega_M = 0.3$, $\Omega_\Lambda = 0.7$ cosmology with $H_0 = 67\,kms^{-1}Mpc^{-1}$, and those values enclosed in bracketts assuming an Einstein-de Sitter cosmology ($H_0 = 67 kms^{-1}Mpc^{-1}$). The inferred star formation rates range from several hundred to several thousand solar masses per year, exceeding even that of the extreme local starburst Arp220. For an 8 mJy source in an $\Omega_M = 0.3$, $\Omega_\Lambda = 0.7$, the star formation rate is $\simeq 1200\,M_\odot yr^{-1}$ (approximately 4 times that of Arp 220). This star-forming activity, however, is very heavily obscured by $10^8 - 10^9\,M_\odot$ of dust, implying gas reservoirs of $10^{10} - 10^{11}\,M_\odot$.

Figures 4.13 to 4.19 show how these results would vary for an 8 mJy source, placed at a redshift $z = 2.4$, for a broad range of dust temperatures and emissivity indices, and for both of the adopted cosmologies. Increasing the dust temperature T_d has the effect of shifting the spectral peak to higher frequencies, allowing the negative K-correction to counteract the cosmological dimming over a larger range in redshift. Increasing the dust emissivity index β has the effect of steepening the Rayleigh-Jeans tail, thus increasing the strength of the negative K-correction. If one considers the most extreme combinations of dust temperature and emissivity shown in these plots ie. ($T_d = 30\,K$, $\beta = 1.0$ and $T_d = 50\,K$, $\beta = 2.0$), there is a huge variation in the range of FIR luminosities and SFRs by up to two orders of magnitude. However, such extreme combinations are unphysical descriptions of the SEDs of the known classes of object. Dunne et al. (2000a) investigated a sample of local galaxies in the "SCUBA Local Universe Galaxy Survey" (SLUGS). The sample was selected from the IRAS bright galaxy catalogue, which is complete to a flux density of $S_{60\mu m} > 5.24\,Jy$. The criteria for selecting the objects were declination limits of $-10° < \delta < 50°$ (so that the objects could be reached from the JCMT in Hawaii), and a velocity $> 1900\,km\ s^{-1}$ to try and ensure that the galaxies fitted within the SCUBA field of view. A total of 104 galaxies satisfied these conditions, spread across an area of $\simeq 10400\,sq°$, and so this subset is largely unbiased, containing examples of all known classes of object. Dunne et al. (2000a) found a sample mean and standard deviation for the best fitting dust temperature of $T_d = 35.6 \pm 4.9\,K$, and for the dust emissivity index $\beta = 1.3 \pm 0.2$, suggesting that the SED shapes are actually quite similar. Furthermore, those objects fitted with extreme dust temperatures, tended to be balanced with the extreme emissivity indices, but in such a manner as to counteract the effect of the high / low temperature fit eg. NGC 5371 had best fit values of $T_d = 25.4\,K$ and $\beta = 1.9$, whereas NGC 4418 had best fit values of $T_d = 55.4\,K$ and $\beta = 0.9$.

If instead of using an Arp 220 SED, the mean dust temperature and emissivity index from the SLUGS had been adopted, in an $\Omega_M = 0.3$, $\Omega_\Lambda = 0.7$ cosmology $L_{850\mu m}$ would remain the same to within $\simeq 2\%$, L_{FIR} and the SFR would decrease by a factor of 1.7, and the estimated dust mass would increase by a factor of 1.3.

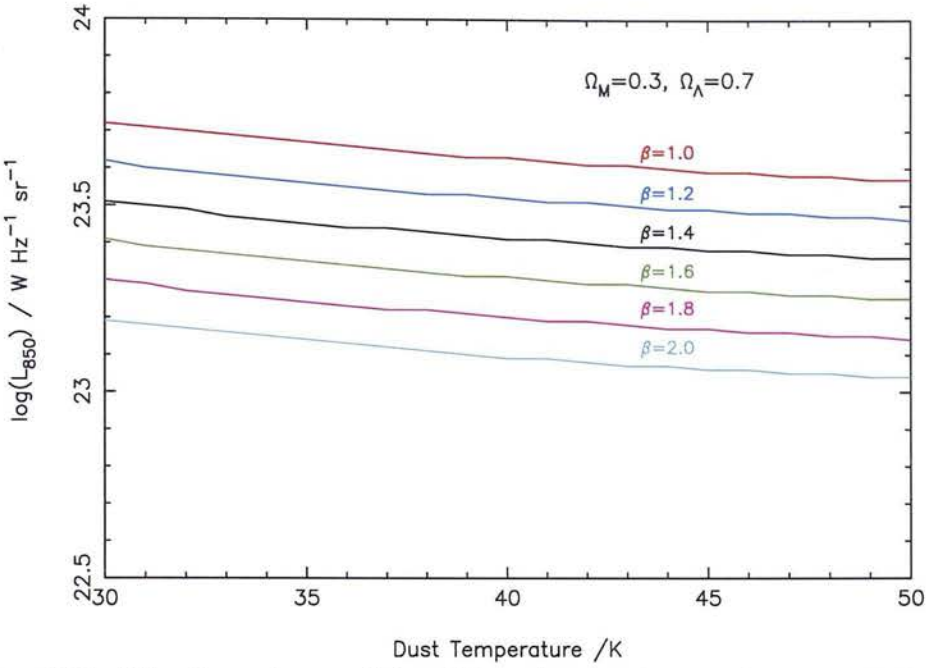

Figure 4.13: The dependence of the 850 μm luminosity on dust temperature for an 8 mJy source, assuming the source lies at $z = 2.4$ in an $\Omega_M = 0.3$, $\Omega_\Lambda = 0.7$ cosmology. Optically thin greybody emission is assumed. The red, blue, black, green, magenta and cyan solid lines are for dust emissivity indexes of 1.0, 1.2, 1.4, 1.6, 1.8 and 2.0 respectively.

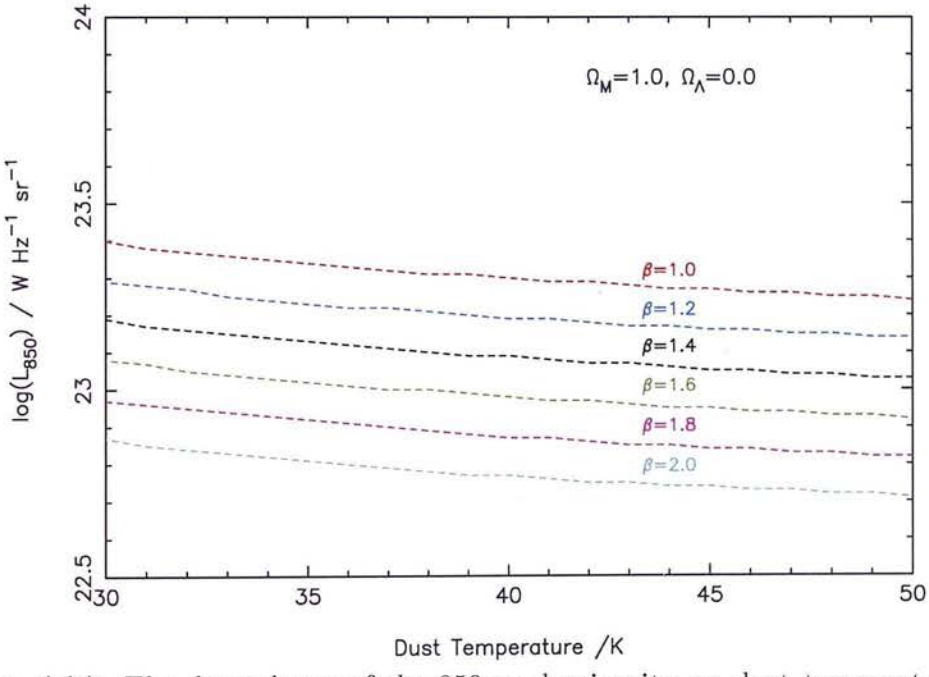

Figure 4.14: The dependence of the 850 μm luminosity on dust temperature for an 8 mJy source, assuming the source lies at $z = 2.4$ in an $\Omega_M = 1.0$, $\Omega_\Lambda = 0.0$ cosmology. Optically thin greybody emission is assumed. The red, blue, black, green, magenta and cyan dashed lines are for dust emissivity indexes of 1.0, 1.2, 1.4, 1.6, 1.8 and 2.0 respectively.

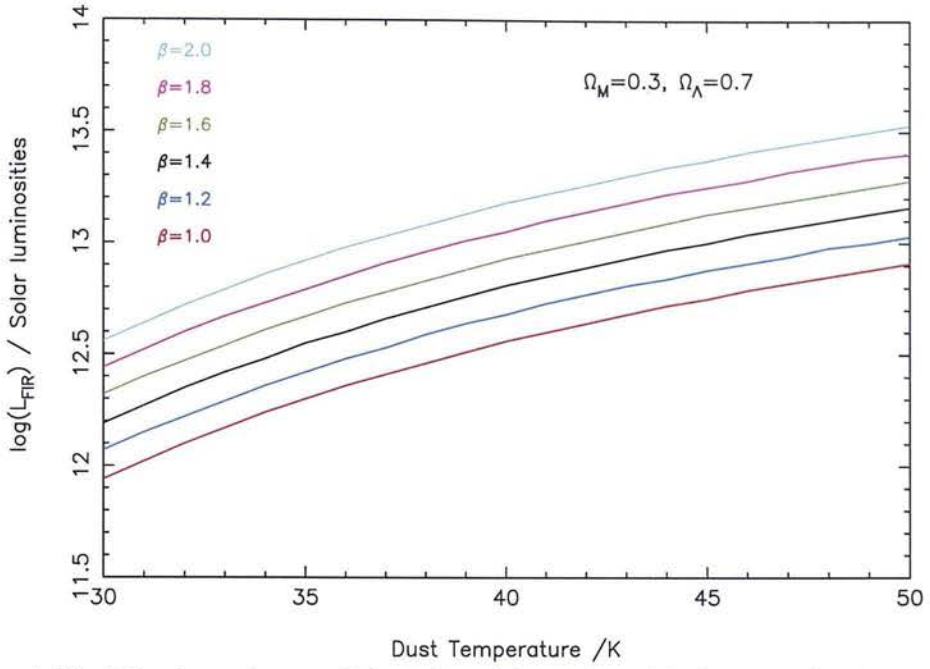

Figure 4.15: The dependence of the inferred far-infrared bolometric luminosity on dust temperature for an 8 mJy source, assuming the source lies at $z = 2.4$ in an $\Omega_{\rm M} = 0.3$, $\Omega_\Lambda = 0.7$ cosmology. Optically thin greybody emission is assumed. The red, blue, black, green, magenta and cyan solid lines are for dust emissivity indexes of 1.0, 1.2, 1.4, 1.6, 1.8 and 2.0 respectively.

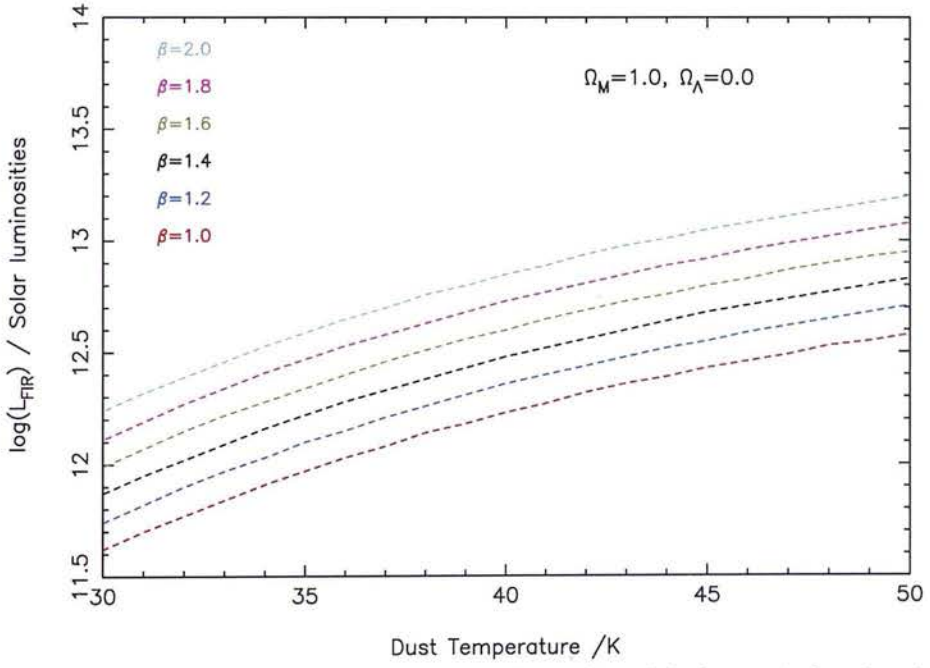

Figure 4.16: The dependence of the inferred far-infrared bolometric luminosity on dust temperature for an 8 mJy source, assuming the source lies at $z = 2.4$ in an $\Omega_{\rm M} = 1.0$, $\Omega_\Lambda = 0.0$ cosmology. Optically thin greybody emission is assumed. The red, blue, black, green, magenta and cyan dashed lines are for dust emissivity indexes of 1.0, 1.2, 1.4, 1.6, 1.8 and 2.0 respectively.

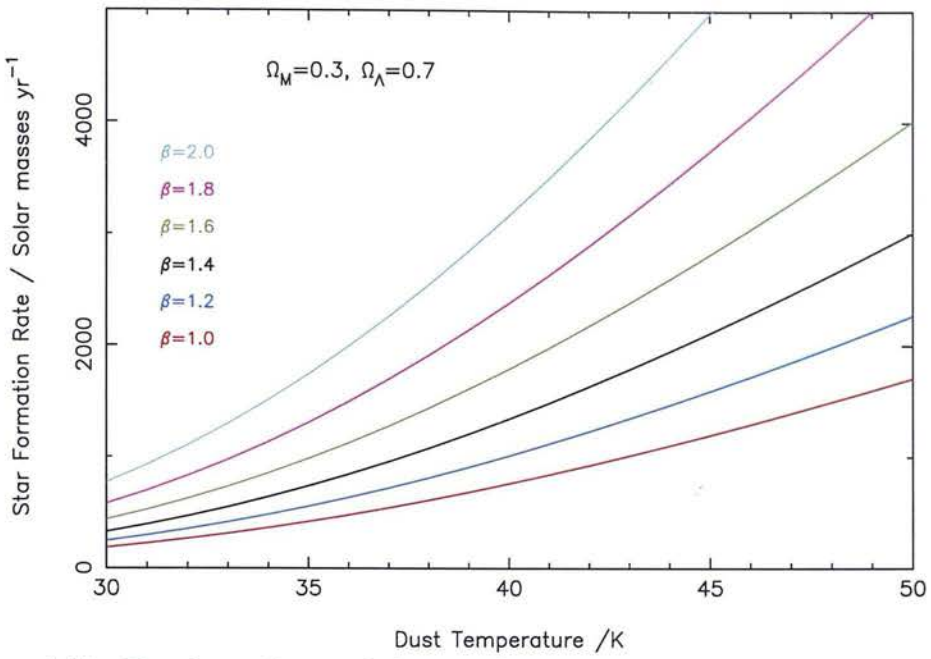

Figure 4.17: The dependence of the star formation rate on dust temperature for an 8 mJy source, assuming the source lies at $z = 2.4$ in an $\Omega_M = 0.3$, $\Omega_\Lambda = 0.7$ cosmology. Optically thin greybody emission is assumed. The red, blue, black, green, magenta and cyan solid lines are for dust emissivity indexes of 1.0, 1.2, 1.4, 1.6, 1.8 and 2.0 respectively.

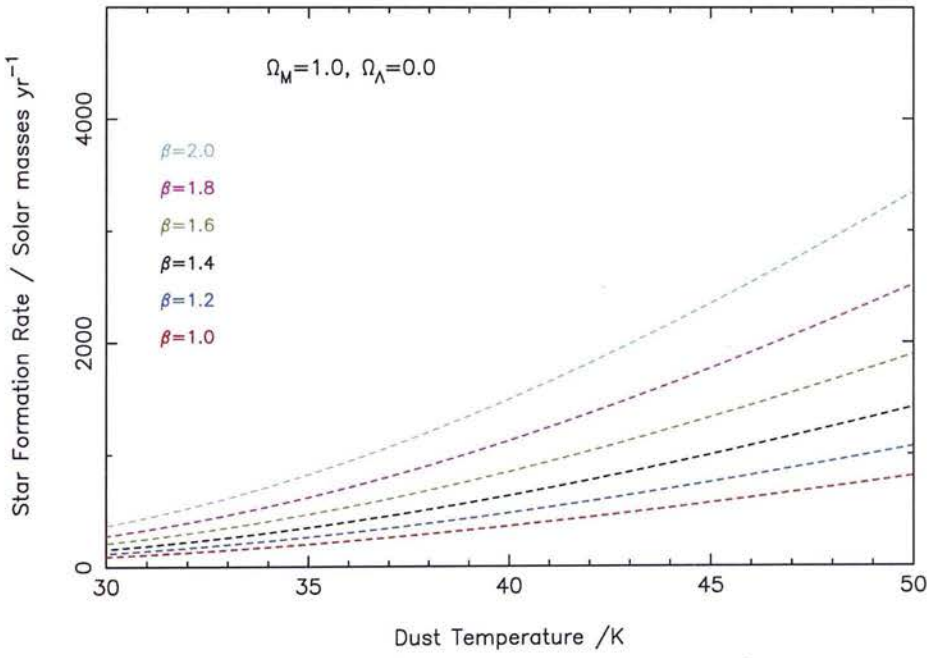

Figure 4.18: The dependence of the star formation rate on dust temperature for an 8 mJy source, assuming the source lies at $z = 2.4$ in an $\Omega_M = 1.0$, $\Omega_\Lambda = 0.0$ cosmology. Optically thin greybody emission is assumed. The red, blue, black, green, magenta and cyan dashed lines are for dust emissivity indexes of 1.0, 1.2, 1.4, 1.6, 1.8 and 2.0 respectively.

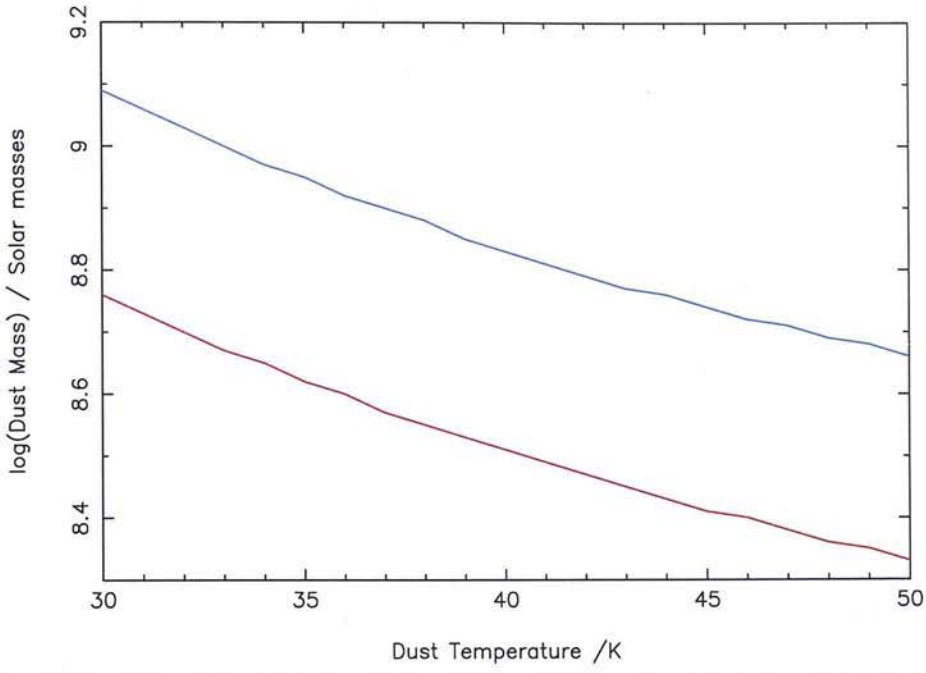

Figure 4.19: The dependence of the dust mass on dust temperature for an 8 mJy source, assuming the source lies at $z = 2.4$. The blue line shows an $\Omega_{\rm M} = 0.3$, $\Omega_\Lambda = 0.7$ cosmology, whereas the red line shows an $\Omega_{\rm M} = 1.0$, $\Omega_\Lambda = 0.0$ cosmology. In this estimate of the dust mass, there is no dependence on the dust emissivity.

Redshift range	Co-moving SFR density ($\Omega_M = 0.3$, $\Omega_\Lambda = 0.7$) $/M_\odot$ yr^{-1} Mpc^{-3}	Co-moving SFR density ($\Omega_M = 1.0$, $\Omega_\Lambda = 0.0$) $/M_\odot$ yr^{-1} Mpc^{-3}
$1-3$	0.019	0.031
$1-4$	0.012	0.021
$1-5$	0.009	0.017
$2-3$	0.035	0.062
$2-4$	0.018	0.033
$2-5$	0.012	0.023
$3-4$	0.037	0.070
$3-5$	0.019	0.038

Table 4.8: The co-moving star formation rate density of sources brighter than 8 mJy, detected with S/N > 3.50, using the uniform noise regions of the two survey areas and assuming that all of these sources lie within the redshift range given in column 1. Column 2 assumes an $\Omega_M = 0.3$, $\Omega_\Lambda = 0.7$ cosmology, and column 3 assumes an Einstein de Sitter cosmology. $H_0 = 67$ kms^{-1}Mpc^{-1} was adopted for both cosmologies.

4.6 Star Formation Rate densities

The 19 sources brighter than 8 mJy, with S/N > 3.50 and located in the uniform noise regions of the survey maps, account for $\simeq 10\%$ of the submillimetre background observed by COBE-FIRAS (Puget et al. 1996, Fixsen et al. 1998, Hauser et al. 1998). Table 4.8 shows the inferred star formation rate density for a variety of redshift bands, and for both of our adopted cosmologies. These bright SCUBA sources alone imply a high-redshift star formation rate density (SFRD) in the range $\simeq 0.01 - 0.07 M_\odot$ yr^{-1} Mpc^{-3} , comparable to that observed in the optical/UV (Steidel et al. 1999). Assuming that the whole of the submillimtere background may be attributed to starlight reprocessed by dust, this would imply a high-redshift SFRD in the range $\simeq 0.1 - 0.7 M_\odot$ yr^{-1} Mpc^{-3}, varying only by a factor of $3-4$ on the adopted redshift band for a given choice of cosmology.

These results agree very well with Barger, Cowie & Richards (2000) who considered the contribution to the SFRD of sources brighter than 6 mJy, and determined completeness corrected SFRDs $\simeq 0.1-0.4$ $M_\odot$yr^{-1}Mpc^{-3} in the redshift range $1 < z < 3$, and $\simeq 0.1 - 0.7$ $M_\odot$yr^{-1}Mpc^{-3} in the redshift range $3 < z < 6$. In contrast to the marked decline in the SFRD at $z > 1$ originally implied by optical/UV observations (Madau et al. 1996), submillimetre surveys suggest that the SFRD is either steady or gently increasing to perhaps as far back as $z = 5$. Current redshift constraints (Ivison et al. 2002, Dunlop 2001a and references within) suggest that $< 25\%$ of luminous (> 4 mJy) submillimetre sources lie at

$z < 2$, and that the median redshift of this population is $z_{\rm med} \simeq 2-3$. A peak in the SFRD around this epoch would not be unexpected given the strong correlation between black-hole and spheroid mass found at low redshift (Kormendy & Gebhardt 2001, Mclure & Dunlop 2002) and the peak in optical emission from powerful quasars at $z \simeq 2.5$ (Schmidt, Schneider, & Gunn 1995). However, improved redshift constraints are required to establish when the co-moving SFRD reached a maximum.

4.7 Co-moving number density of 8 mJy sources

As explained in Section 4.4, although accurate redshifts for the submillimetre sources uncovered in this survey are currently lacking, existing constraints mean that one can be very confident that virtually all of them lie at $z > 1$, and indeed can be reasonably confident that the majority lie at $z > 2$ (Dunlop 2001a, Fox et al. 2002, Ivison et al. 2002). It is thus still possible to make a meaningful estimate of the co-moving number density of bright ($S_{850\mu{\rm m}} > 8\,{\rm mJy}$) sub-mm sources at high redshift implied by the number counts derived from this survey. The results of this calculation, for a variety of assumed redshift bands, are summarized in Table 4.9 (again for the two standard assumed alternative cosmologies). From this table it can be seen that the co-moving number density of dust-enshrouded starburst galaxies with star formation rates $> 1000\ {\rm M_{\odot}yr^{-1}}$ lies in the range $\simeq 1 - 10 \times 10^{-5}\,{\rm Mpc^{-3}}$ in very good agreement with Lilly et al. (1999), Barger, Cowie & Sanders (1999), and Barger, Cowie & Richards (2000). In a similar manner to the co-moving SFRD, this result depends only weakly (a factor of 3–4) on the precise choice of assumed redshift band for the sources, for a given choice of cosmology. Adopting the now strongly-favoured flat, Λ-dominated cosmology leads to the conclusion that the co-moving number density of dust-enshrouded starburst galaxies with star formation rates $> 1000\ {\rm M_{\odot}yr^{-1}}$ is $\simeq 1 \times 10^{-5}\ {\rm Mpc^{-3}}$.

This is an interesting number. It is over an order of magnitude smaller than the number density of galaxies brighter than $L^{\star}$ in the present-day universe, as inferred from the K-band luminosity function (Glazebrook et al. 1995; Cowie et al. 1995; Gardner et al. 1997; Szokoly et al. 1998; Kochanek et al. 2001), but is an order of magnitude greater than the co-moving number density of bright optical QSOs ($M_V < -24$) at $z \simeq 2-3$ (Warren, Hewett & Osmer 1995).

With reference to the present-day K-band luminosity function, a co-moving number density of $1 \times 10^{-5}\ {\rm Mpc^{-3}}$ corresponds to a galaxy luminosity $1 - 1.5$

Redshift range	Co-moving no. density ($\Omega_M = 0.3$, $\Omega_\Lambda = 0.7$) /Mpc^{-3}	Co-moving no. density ($\Omega_M = 1.0$, $\Omega_\Lambda = 0.0$) /Mpc^{-3}
$1-3$	1.20×10^{-5}	4.20×10^{-5}
$1-4$	0.80×10^{-5}	2.93×10^{-5}
$1-5$	0.61×10^{-5}	2.32×10^{-5}
$2-3$	2.25×10^{-5}	8.52×10^{-5}
$2-4$	1.15×10^{-5}	4.52×10^{-5}
$2-5$	0.80×10^{-5}	3.20×10^{-5}
$3-4$	2.37×10^{-5}	9.61×10^{-5}
$3-5$	1.24×10^{-5}	5.13×10^{-5}

Table 4.9: The co-moving number density of sources brighter than 8 mJy, detected with S/N > 3.50, using the uniform noise regions of the two survey areas and assuming that all of these sources lie within the redshift range given in column 1. Column 2 assumes an Einstein-de Sitter cosmology, and column 3 assumes $\Omega_M = 0.3$, $\Omega_\Lambda = 0.7$. $H_0 = 67$ kms^{-1}Mpc^{-1} was adopted for both cosmologies.

magnitudes brighter than $L^\star$, or equivalently to galaxies $3-4$ times more massive than an evolved $L^\star$ galaxy. In this regime the present-day galaxy population is completely dominated by massive ellipticals (Kochanek et al. 2001). Interestingly the hosts of present-day FRII radio sources, and the more luminous radio-quiet quasars are also confined to this same high-mass regime (Dunlop 2001b, Dunlop et al. 2003a).

Thus, if one wants to attempt to link the high-redshift population of very luminous (i.e. SFR $\simeq$ 1000 M$_\odot$yr^{-1}) dust-enshrouded starburst galaxies to a low-redshift population, purely on the basis of number-density coincidence, then the simplest connection is that the bright SCUBA galaxies are the progenitors of present-day massive ellipticals with stellar masses $\simeq 10^{12}$M$_\odot$. This is not unreasonable, given that such objects require star-formation to be sustained at $\simeq$ 1000 M$_\odot$yr^{-1} for $\simeq$ 1 Gyr to assemble their present-day stellar populations (eg. Dunlop et al. 1996, Spinrad et al. 1997, Dunlop 1998, Jimenez et al. 1999). It is also consistent with the discovery that bright SCUBA detections of (comparably massive) radio galaxies are largely confined to $z > 2$ (Archibald et al. 2001).

If the luminous submillimetre SCUBA sources uncovered by this survey are indeed the progenitors of the present-day massive elliptical population (Dunlop 2001c), and if, as current evidence suggests, the majority of bright sub-mm sources lie at $z > 2$ (Dunlop 2001a), then one might reasonably expect to find a comparably-numerous population of passively-evolving massive ellipticals at intermediate redshifts. One way to search for such a population is via surveys de-

signed to detect extremely red objects (EROs), such as that recently undertaken by Daddi et al. (2000, 2002). One can obtain a rough estimate of the co-moving number density of passively-evolving massive ellipticals at intermediate redshifts by considering the surface density of EROs in the Daddi et al. survey with $R - K > 5.3$ (setting a lower redshift boundary of $z \simeq 1$) and $K < 18.5$ (setting an approximate upper redshift boundary of $z \simeq 2$ for ellipticals of comparable mass to bright radio galaxies - Jarvis et al. (2001)). The surface density of such objects is $\simeq 0.1$ per sq. arcmin ($\equiv 350$ per sq. degree), very similar to the surface density found here for > 8 mJy SCUBA sources. For the appropriate redshift band $1 < z < 2$ this surface density converts into a co-moving number density of 3×10^{-5} Mpc^{-3} assuming $\Omega_M = 0.3$, $\Omega_\Lambda = 0.7$ which, as can be seen from Table 4.9, agrees with the co-moving number density of bright SCUBA sources to within a factor of 2 or 3 (depending on the choice of assumed redshift band for the SCUBA sources).

This numerical coincidence provides further circumstantial evidence for an evolutionary path for *all* massive ellipticals which mirrors that which has been already largely established for massive radio galaxies (Archibald et al. 2001; Willott et al. 2001; Jimenez et al. 1999), i.e.

SCUBA source at $z \geq 2.5 \rightarrow$
ERO at $z \simeq 1.5 \rightarrow$
$3 - 4L^\star$ evolved elliptical at $z = 0$

A key test of this picture will be to establish whether or not the bright SCUBA sources display comparable or even stronger *spatial* clustering than the EROs, for which Daddi et al. (2000) report $r_0 \simeq 11\,h^{-1}$Mpc (for objects with $R-K > 5$). As described in the next Section, there is tantalyzing evidence of angular clustering in the 8 mJy survey, but it is clear that a substantially larger sub-mm survey (approaching 1 degree in size) will be required to settle this issue.

4.8 Clustering analysis

If the bright 850 μm sources are indeed the progenitors of massive elliptical galaxies then they should be strongly clustered, an inevitable result of gravitational collapse from Gaussian initial density fluctuations since the rare high-mass peaks are strongly biased with respect to the mass. There is a great deal of evidence to support the presence of this bias at high redshift. The correlations of Lyman-break galaxies at $z \simeq 3$ (Steidel et al. 1999) are almost identical to those of present-day field galaxies, even though the mass must have been much more uniform at early times. Furthermore, the correlations increase with UV luminosity (Giavalisco & Dickinson 2001) reaching scale lengths of $r_0 \simeq 7.5h^{-1}$ Mpc - approximately 1.5 times the present-day value. In the case of luminous proto-ellipticals an even stronger bias is expected since one is selecting not just massive galaxies but those that have collapsed particularly early in order to generate the oldest stellar populations. This is suggested by studies of the local Universe which have shown that early-type galaxies are much more clustered than late-type galaxies (eg. Guzzo et al. 1997, Willmer et al. 1998), and more recently by the findings of Daddi et al. (2000) who have investigated the clustering properties of extremely red objects (EROs). They detect a strong clustering signal of the EROs which is about an order of magnitude larger than the clustering of $K-$selected field galaxies, and also report a smooth trend of increasing clustering amplitude with increasing $R-K$ colour, reaching $r_0 \simeq 11h^{-1}$ Mpc for $R-K>5$. These results are probably the strongest evidence to date that the largest fraction of EROs is composed of ellipticals at $z>1$. There are already some hints of strong clustering in the bright sub-mm population from the discovery of a strong excess of bright SCUBA sources around high-redshift AGN (Ivison et al. 2000b). Motivated by this result, and the potential connection with the intermediate-redshift EROs discussed above, I have made the first attempt to quantify the strength of clustering in the two survey fields via calculation of angular 2-point correlation functions based on the $>3.50\sigma$ sources for each of the two fields. Using the S/N >3.50 catalogue provides a reasonable balance between having a reasonable number of sources to work with, but without too much contamination from spurious / confused sources which can "wash out" the correlation signal.

A catalogue of randomly placed fake sources was created for each of the survey fields, assuming a uniform source density in the first instance ie. the number of sources appearing in the catalogue $\propto$ the area of the field. Since the Lockman

Hole East and ELAIS N2 are virtually the same size this meant that almost the same number of sources were located in each field and 5000 fake sources were generated for each field within the boundaries of the real data. Although, the positions were allocated randomly, the Gaussian convolved noise maps were used to weight the number density of sources across the image, since a larger density of sources above a specified signal-to-noise threshold would be expected in regions of lower noise. In practice, this meant dividing the full image into a series of sub-images, 20 arcseconds by 20 arcseconds in size, and calculating the mean noise level in each of these grid sections. For sources brighter than $\simeq 5\,\mathrm{mJy}$, the number of sources expected above a constant signal-to-noise threshold increases approximately as $\mathrm{No.}(> \mathrm{S}_{850\mu\mathrm{m}}) \propto \mathrm{S}_{850\mu\mathrm{m}}^{-1.5}$, and consequently the relative number of sources in each sub-image scales as $\langle\mathrm{noise}\rangle^{-1.5}$. The fake source positions were then allocated according to a Poisson distribution, masking any positions which were covered by a negative sidelobe accompanying a significant source in the real survey data. If the number of fake sources included in the catalogue is very much larger than the number recovered from the real data (as is the case here), this is in essence equivalent to choosing positions by combining the results from source extraction on a series of fully simulated survey fields.

The angular correlation function $\mathrm{w}(\theta)$ is the projection of the spatial function on the sky and is defined in terms of the joint probability $\delta\mathrm{P}$ of finding two galaxies separated by an angular distance θ with respect to that expected for a random distribution

$$\delta\mathrm{P} = \mathrm{N}^2[1 + \mathrm{w}(\theta)]\delta\Omega_1\delta\Omega_2 \tag{4.7}$$

where $\delta\Omega_1$ and $\delta\Omega_2$ are elements of solid angle, and N is the mean surface density of objects. If $\mathrm{w}(\theta) = 0$ the distribution is homgeneous. A positive $\mathrm{w}(\theta)$, therefore, corresponds to an over-density of sources separated by distance θ.

There are a variety of possible estimators for $w(\theta)$ as a function of pair-count ratios. Following Landy & Szalay (1993), I have adopted the estimator:

$$\mathrm{w}(\theta) = \frac{(\mathrm{DD} - 2\mathrm{DR} + \mathrm{RR})}{\mathrm{RR}} \tag{4.8}$$

in which the variance is minimised to almost Poisson level. DD is the number of distinct data pairs in the real image within a bin covering a specified range of θ, DR is the number of cross-pairs between the real and mock catalogues within the same range of θ, and RR is the number of random-random pairs. DR and RR are normalised with respect to the total number of data-data pairs from the real image.

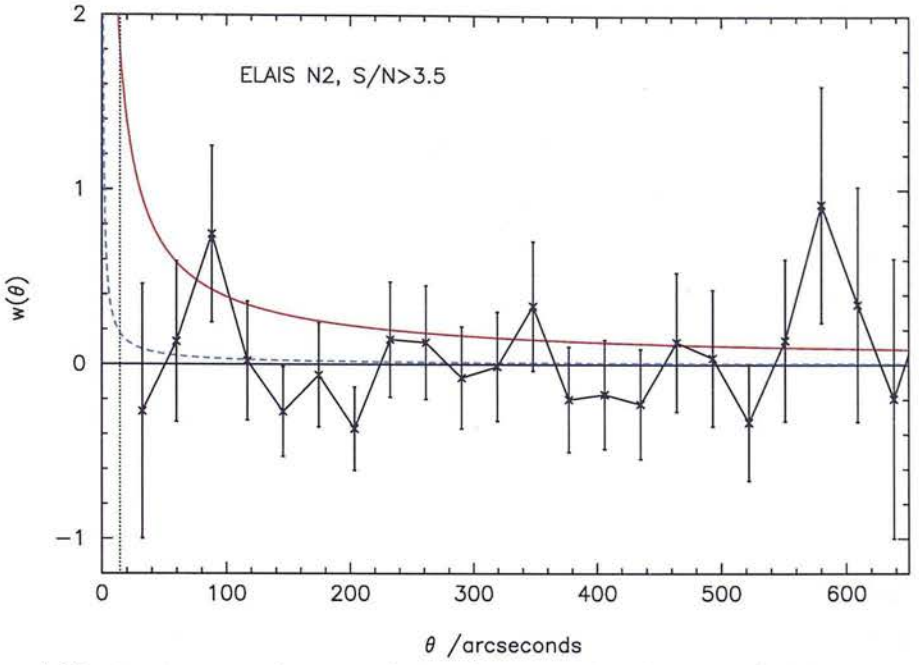

Figure 4.20: 2-point angular correlation function for the ELAIS N2 survey field. The red (solid) power-law line indicates the correlation function found by Daddi et al. (2000) for EROs with $R-K > 5$ and $K < 18.5$, and the blue (dashed) power-law line indicates the correlation function found by Giavalisco et al. (1998) for Lyman break galaxies at $z \sim 3$.

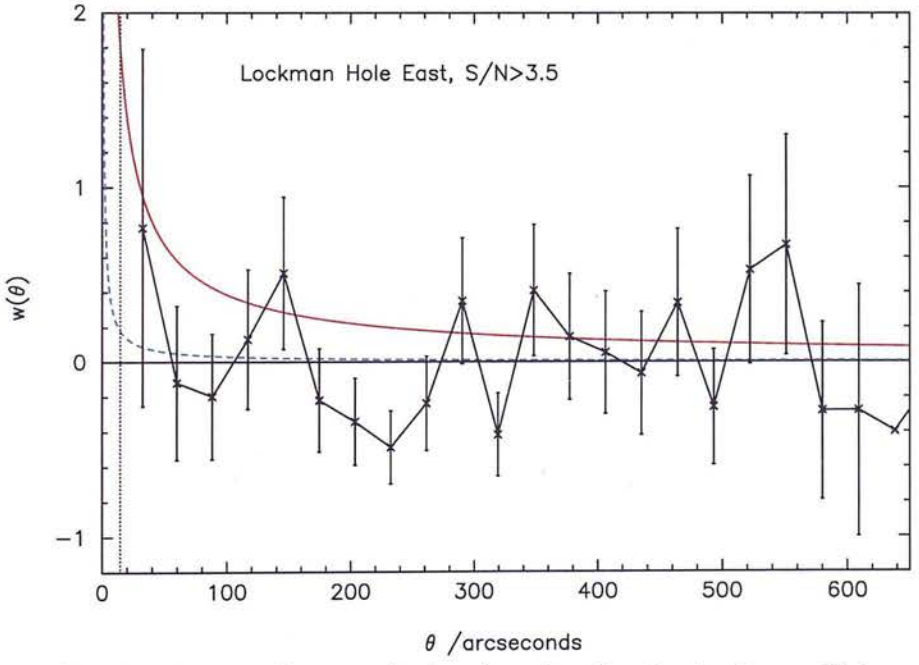

Figure 4.21: 2-point angular correlation function for the Lockman Hole survey field. The red (solid) power-law line indicates the correlation function found by Daddi et al. (2000) for EROs with $R - K > 5$ and $K < 18.5$, and the blue (dashed) power-law line indicates the correlation function found by Giavalisco et al. (1998) for Lyman break galaxies at $z \sim 3$.

The angular correlation functions for sources with S/N > 3.50 in the two individual fields may be seen in Figures 4.20 and 4.21. A bin size of twice the beam (29.0 arceconds) has been used and the error bars are 1σ Poisson errors ($= (1 + \mathrm{w}(\theta)) \times \sqrt{< \mathrm{DD} >}$ for each bin). Any sources marked as "edge" in Tables 4.1 and 4.2 were excluded from this analysis since these are the least secure. The red (solid) line represents the angular correlation function measured by Daddi et al. (2000) for EROs with $R - K > 5$ and $K < 18.5$ and the blue (dashed) power-law line indicates the correlation function found by Giavalisco et al. (1998) for Lyman break galaxies at $z \sim 3$. The vertical dotted line is the size of the SCUBA beam (14.5") and defines the limit of resolution of the SCUBA images. There is very tentative evidence of clustering on scales of $1 - 2$ arcmin in both of the survey fields, but most particularly, and somewhat stronger, in the ELAIS N2 region. Referring to Figure 4.2, one can in fact see by eye that the most significant (S/N > 3.50) sources in ELAIS N2 do not conform to a homogeneous distribution across the field - rather there are two apparent concentrations of 850 μm sources in the top left and bottom right of the image, approximately at RA 16:37:00, DEC +41:05:00, and RA 16:36:30, DEC +40:56:00 respectively, with an apparent under-density of sources in the intervening regions. A second peak in $\mathrm{w}(\theta)$ at $\simeq$ 600 arcseconds (the distance between these over-densities), and a trough at $\simeq$ 400 arcseconds are seen to reflect this "by eye" distribution.

Very interestingly, the same large-scale inhomogeneities are found in the Chandra X-ray image of the ELAIS N2 region (Almaini et al. 2003), although the coincidence of X-ray and SCUBA sources is small (< 10%). Almaini et al. (2003) report a 4.3σ excess of SCUBA-Chandra source pairs in the first 100 arcseconds, over that determined from cross-correlating the Chandra positions with a random catalogue. This would suggest that the Chandra and SCUBA sources represent slightly different stages in galaxy evolution, but that they trace the same large scale structure. If this is indeed the case, then combining the submillimetre and X-ray datasets yields a combined angular auto-correlation function very similar to that observed by Daddi et al. (2000) for EROs with $R - K > 5$ and $K < 18.5$ shown in Figure 4.22 (Almaini et al. 2003). As a note of caution here, this plot combines 17 SCUBA sources (the original > 3.50σ ELAIS N2 catalogue published in Scott et al. (2002)), and 72 high-redshift X-ray sources, hence it is largely dominated by the Chandra population.

Combining the Lockman Hole East and ELAIS N2 submillimetre data, the angular correlation functions for all S/N > 3.50 sources and those S/N > 3.50

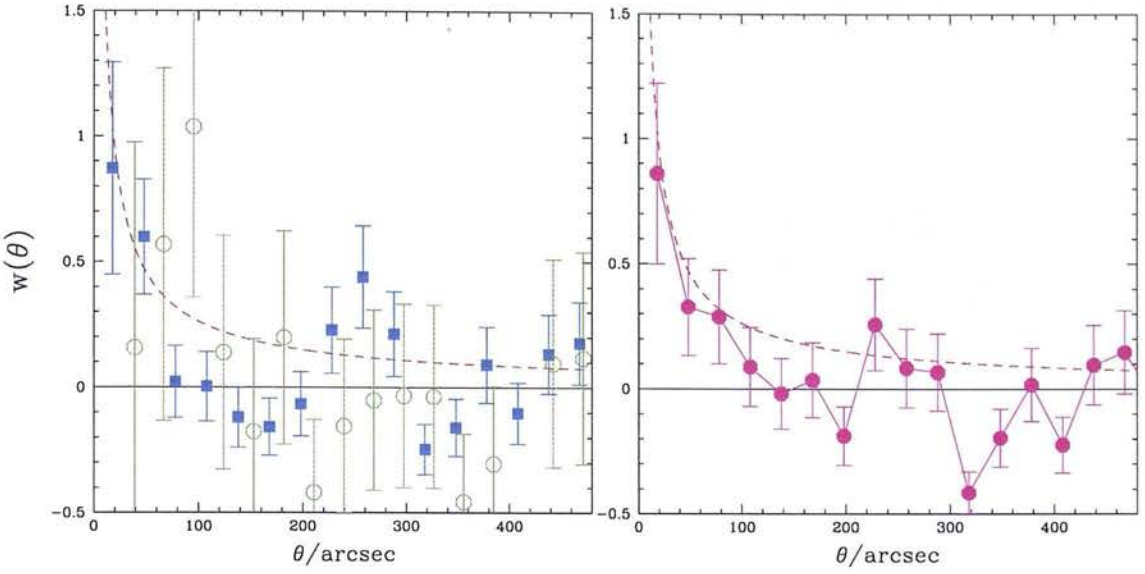

Figure 4.22: In the left-hand plot, the green circles show the original angular correlation function determined for the 17 SCUBA sources with S/N > 3.50 in the ELAIS N2 field, as published in Scott et al. (2002) The blue squares show the angular correlation function for the 72 high redshift Chandra sources in the ELAIS N2 field (Almaini et al. 2003). In the right-hand plot the magenta circles show the combined angular correlation function for both the submillimetre and X-ray sources. In both plots the red (dashed) power-law line represents the angular correlation function measured by Daddi et al. (2000) for EROs with $R-K > 5$ and $K < 18.5$. Error bars are 1σ Poisson errors. This plot is taken from Almaini et al. (2003).

with $S_{850\mu m} > 6$ mJy are shown in Figures 4.23 and 4.24. It can be seen that the combined clustering signal from the bright SCUBA sources appears to be stronger than that from the full S/N > 3.50 catalogue. There are two possible explanations for this observation. Firstly, by applying a flux density limit of $S_{850\mu m} \geq 6$ mJy, only the most massive haloes with the strongest bias are included and this is a real effect. A more pessimistic interpretation, however, is that the sources fainter than 6 mJy are generally at lower significance and hence have a greater probability of being spurious/confused. Contamination from a fraction f of randomly positioned spurious sources would be expected to reduce the measured angular correlation function in all bins by $(1 - f)^2$. If the contamination is largely from fainter confused sources, the reduction in signal would likely be less since one might expect the fainter SCUBA population to exhibit some level of clustering, albeit not as strong.

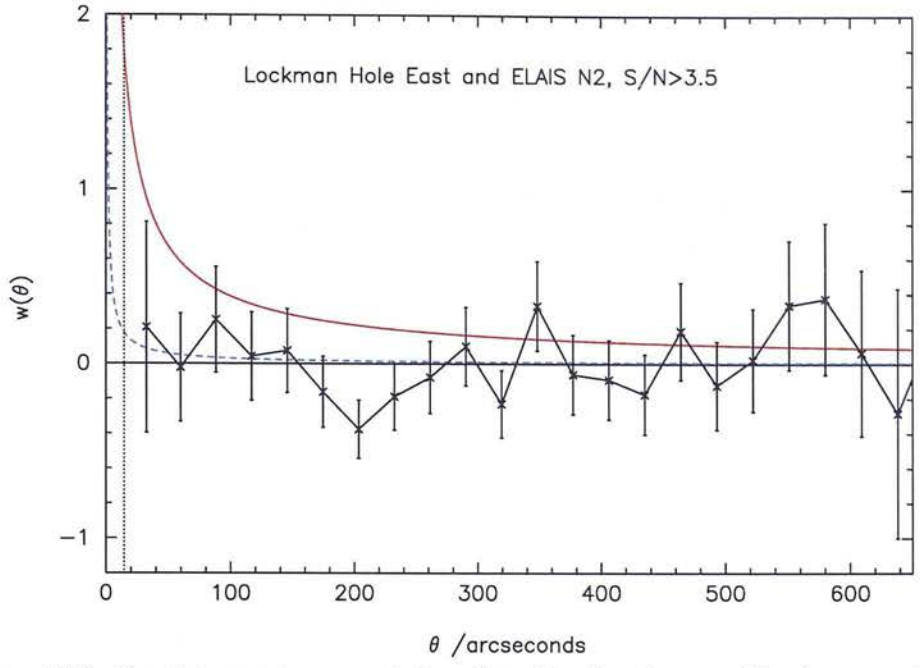

Figure 4.23: 2-point angular correlation function for the combined survey fields. The red (solid) power-law line indicates the correlation function found by Daddi et al. (2000) for EROs with $R-K > 5$ and $K < 18.5$, and the blue (dashed) power-law line indicates the correlation function found by Giavalisco et al. (1998) for Lyman break galaxies at $z \sim 3$.

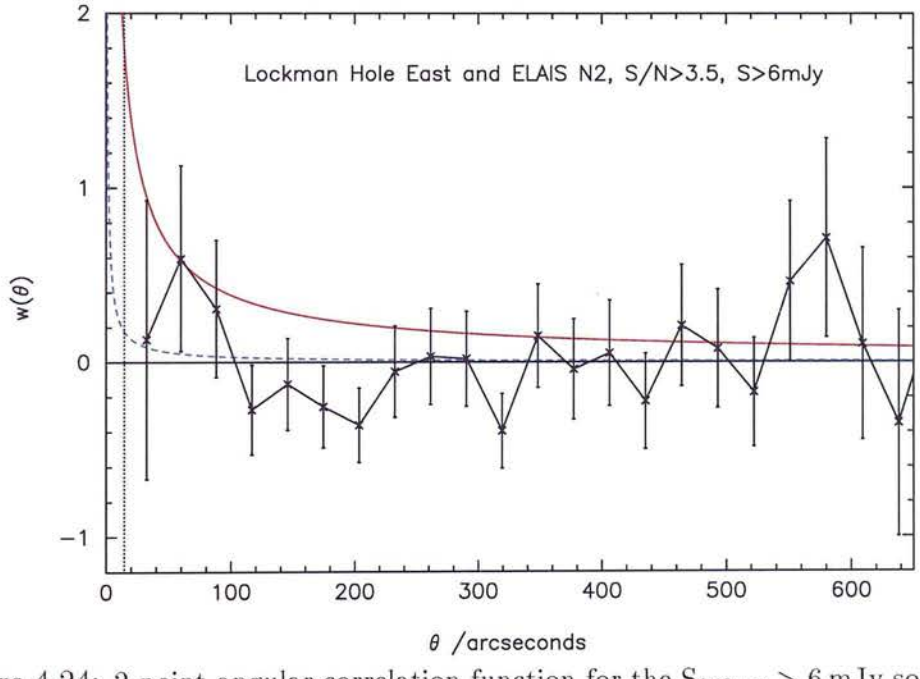

Figure 4.24: 2-point angular correlation function for the $S_{850\mu m} > 6$ mJy sources from the combined survey fields. The red (solid) power-law line indicates the correlation function found by Daddi et al. (2000) for EROs with $R - K > 5$ and $K < 18.5$, and the blue (dashed) power-law line indicates the correlation function found by Giavalisco et al. (1998) for Lyman break galaxies at $z \sim 3$.

It is clear from Figures 4.20 to 4.24 that due to small-number statistics, this first attempt at a direct measure of the clustering of bright sub-mm sources has proved inconclusive. However, this should not be taken as evidence that the SCUBA sources are unclustered. In fact, as illustrated in these figures, it is worth noting that these correlation functions are certainly still consistent with the strong clustering signal detected for EROs by Daddi et al. (2000). Clearly a much larger survey ($\sim$ 0.5 square degrees) will be required to obtain a meaningful measurement of the strength of clustering in the bright submillimetre population. Near complete redshift information may also be required to quantify the extent to which any clustering signal will be partially erased by projection through a wide range in redshift. For example, suppose that the bright SCUBA population spans a relatively wide range in redshift $2 < z < 5$ whereas, as argued above, the bright EROs are confined to the redshift range $1 < z < 2$. In that case, if the strength of the spatial clustering in the two populations was the same, $w(\theta)$ as measured from SCUBA images would be expected to be $1.6 - 1.9$ times smaller (depending on choice of cosmology) than that which has been measured for EROs. In the next chapter I combine data from all existing blank field surveys to try to obtain better constraints on the strength of clustering of the bright submillimetre population.

Chapter 5

A Combined Re-analysis of Existing Blank Field SCUBA Surveys

Over the past six years, a series of complementary deep 850 μm surveys (eg. Smail et al. 1997, Hughes et al. 1998, Barger et al. 1998, Barger et al. 1999, Blain et al. 1999, Eales et al. 2000, Scott et al. 2002, Borys et al. 2002, Webb et al. 2003a, Cowie et al. 2002) carried out using SCUBA on the JCMT have successfully resolved the bulk of the far-infrared (FIR) extragalactic background into discrete sources, revealing a population of heavily dust-enshrouded high-redshift galaxies undergoing an intense period of massive star-forming activity. These surveys vary in size and depth from ultra-deep surveys exploiting gravitational lensing from intervening clusters to study the very faintest submm sources (Smail et al. 1997, Cowie et al. 2002), through small and deep blank field surveys such as the HDF (6 sq. arcmin to a uniform noise level of $1\sigma_{\rm rms} \simeq 0.5$ mJy/beam; Hughes et al. 1998, Serjeant et al. 2003), to moderate area and comparatively shallower blank field surveys such as the "SCUBA 8-mJy Survey" (a total of 260 sq. arcmins to a uniform noise level of $1\sigma_{\rm rms} \simeq 2.5$ mJy/beam; Scott et al. 2002) which is the largest and most successful of these surveys to date, in terms of the number of significant sources recovered.

Results from the "8 mJy Survey" are presented in detail in Chapter 4. Here I present a re-analysis of several other 850 μm blank field surveys; namely the "Canada UK Deep Submillimetre Survey (CUDSS)", the "Hawaii Flanking Fields Survey", and the "Hubble Deep Field Survey" (pencil beam only) using the same data reduction and simulation techniques as applied to the "8-mJy Survey" and described in Chapters 2 and 3. The raw data were downloaded from the Canadian

Astronomy Data Centre (CADC). Revised source lists and comparisons with previous reductions are presented in Section 5.1. The combined datasets are then used to provide the first significant detection of the strong clustering of the bright ($> 5\,$mJy) SCUBA population (Section 5.2) (by means of angular 2-point correlation functions and nearest-neighbour analyses), as well as the most accurate analysis of the 850 μm source counts to date (Section 5.3).

5.1 Comparative Source Lists

5.1.1 The "Canada UK Deep Submillimetre Survey"

The "Canada UK Deep Submillimetre Survey (CUDSS)" (Eales et al. 1999, Lilly et al. 1999, Gear et al. 2000, Eales et al. 2000, Webb et al. 2003a), covers a total of $\simeq$ 130 sq. arcmin over 4 regions of sky, selected to coincide with areas observed in the "Canada-France Redshift Survey (CFRS)" (Lilly et al. 1995). The 03-Hour field is composed of a deep pencil beam area ($\simeq$ 8 sq. arcmin in size, $\sigma_{850} = 1.1\,$mJy/beam; Eales et al. 1999, Lilly et al. 1999), embedded in a wider-area, shallower map covering an additional 55 sq. arcmin with a typical rms noise level of $\sigma_{850} = 1.8\,$mJy/beam (Webb et al. 2003a). The 14-Hour field (Eales et al. 2000) is similar in size, the uniform noise region covering approximately 57 sq. arcmin, but to a slightly deeper uniform noise level of $\sigma_{850} = 1.5\,$mJy/beam. The 10-Hour and 22-Hour fields (Eales et al. 1999, Lilly et al. 1999) are small in area, each having a uniform noise region of $\simeq$ 7 sq. arcmin, with rms noise levels of $\sigma_{850} = 1.3$ and $1.5\,$mJy/beam respectively.

The data were originally reduced independently by the Cardiff and Toronto groups, using the standard SURF procedures described in Chapter 2. They made additional attempts to improve the quality of the final map, firstly by allowing the residual sky removal to be a linear function of position (i.e. a planar fit was applied rather than a D.C. offset), and secondly by examining the Fourier-transform of each bolometer's measured signal to search for non-white noise profiles (although Eales et al. (2000) reported this produced negligible improvements to the final regridded images). The chop throw in all cases was fixed at 30 arcsec in an east-west direction as observed on the sky. Source extraction was carried out by convolving a normalised template of the full beam-profile, constructed from the many observations of Uranus taken thoughout the lifetime of this survey, with the raw survey maps. The "CUDSS" team used a method of noise modelling

which is in effect quite similar to the way in which the noise maps were created in the IDL reduction of the "SCUBA 8 mJy Survey". They began with the basic assumption that the noise on any bolometer was independent of the noise on every other bolometer, and then measured the standard deviation of the intensities for each bolometer in units of one hour (the length of each CUDSS pointing). Artificial data were then created by replacing the real data with the output of a Gaussian random-number generator with the same standard deviation as the real data, re-running the sky subtraction and clipping routines from the SURF package to account for any non-Gaussian nature arising from these processes, and finally rescaling the mock data so that it had the same standard deviation as the real data. In total, 1000 simulated maps were generated, each of which was convolved with the beam template as was the real data. The final noise maps were produced by measuring the standard deviation of these convolved maps, pixel by pixel.

As previously stated in Chapter 2, the method of convolving the raw images with the normalised point spread function (PSF) is formally the best method of source-extraction, provided that the sources are all well separated from one another. It does, however, run into difficulties when dealing with partially confused sources, a problem which is likely to be fairly common, as inferred from the ELAIS N2 image (Section 4.2) and the clustering analyses of Section 5.2. In the "SCUBA 8 mJy Survey" the problem of confusion was tackled by means of a maximum-likelihood fit of the beam template to all potential sources simultaneously using the raw data. Eales et al. (2000) instead addressed the problem of confusion by attempting a deconvolution with the CLEAN algorithm (Hogbom 1974). They created an initial list of possible sources based on the beam-convolved signal image divided by the Gaussian generated noise image, then iteratively CLEANed the raw data in boxes centred on the positions of the potential sources. For each source the information from CLEAN was then used to remove all other possible sources from the raw image, before again carrying out a convolution with the beam template on this new map, and dividing by the noise to measure the signal-to-noise ratio.

Comparative source lists for detections with S/N $>$ 3.00 from the two different reductions and source extraction procedures are given in Tables 5.1 to 5.4. Column 1 gives the source number in order of decreasing signal-to-noise ratio as derived from the new IDL-reduction and simultaneous maximum-likelihood source extraction method, and corresponds to the labelling of the circled sources

in Figs. 5.1 to 5.4. The red circles are those sources with S/N $>$ 4.00, the blue circles those sources with 3.50 $<$ S/N $<$ 3.99, and the green circles those detections with 3.00 $<$ S/N $<$ 3.49. Columns 2 and 3 give the right ascension and declination of the source in J2000 coordinates. Column 4 gives the simultaneously fitted 850 μm flux densities of the sources. The error includes a 10% calibration error combined in quadrature. Column 5 gives the measured signal-to-noise ratio of the source from the simultaneously-fitted model. Column 6 defines the noise region in which the source was found; 'deep' corresponds to the deep pencil-beam surveys which constitute part of a wider-area and somewhat shallower image, 'central' corresponds to the parts of the map which have seen the full integration time (outside of the deep area), and 'edge' corresponds to the rather noisier regions near the perimeter which have not seen the full integration time. Column 7 gives any previous reference to the 850 μm source. Reference E99 is an abbreviation for Eales et al. (1999), E00 is an abbreviation for Eales et al. (2000), and W03 is an abbreviation for Webb et al. (2003a). The presence of a * indicates that a previous reduction found more than one source here, whereas in my reduction I found only one. Column 8 gives the previously recorded signal-to-noise ratio where applicable, and Column 9 gives the distance between the listed and previously referenced positions. The table listings given in italics correspond to previously referenced sources with S/N $>$ 3.00, which did not meet this criterion in this analysis.

As can be seen from comparing the two different reduction and source extraction procedures, a majority of the most highly significant objects ($> 4.00\sigma$) identified in the initial CUDSS analyses are also recovered here, but as one considers detections at decreasing signal-to-noise ratios, the two catalogues increasingly diverge. In the 03-Hour field, I find all but 3 of their 12 $> 4.00\sigma$ sources at better than $> 3.00\sigma$. In addition I have detected a further 3 previously unpublished sources at better than $> 4.00\sigma$. Dropping down the list to lower significances, however, the resulting source catalogues of significant ($> 3.00\sigma$) detections are actually markedly different, in particular only a handful of objects are common to both lists for 3.00 $<$ S/N $<$ 4.00. That is not to say that all detections under a signal-to-noise ratio of 3.00 are spurious, simply that there is a rapidly increasing probability of contamination from fake sources on decreasing the signal-to-noise threshold. A few of those objects identified at $> 3.00\sigma$ by the original analysis of Webb et al. (2003a) fall only just short of this criterion in this new analysis adding some credibility to their reality. In the 14-Hour field, the top 5 sources

identified by Eales et al. (2000) are also securely recovered as the top 5 detections in this analysis. Again, on dropping to lower signal-to-noise ratios the two catalogues diverge. Only a further 5 of the remaining 14 objects detected by Eales et al. (2000) at $> 3.00\sigma$ are recovered by this criterion in this maximum-likelihood analysis, although a few of these objects fall only just below this threshold. For those potential sources common to both catalogues, the combination of the IDL-reduction and simultaneous maximum-likelihood source extraction algorithm provide much more conservative values of the signal-to-noise ratio, in most cases by $1 - 2\sigma$. At this stage it is not possible to say which of the two reduction algorithms is the more accurate. The deep radio imaging of the "SCUBA 8 mJy Survey" fields (Ivison et al. 2002) has provided quite a stringent test of the IDL-reduction and the simultaneous maximum-likelihood source extraction algorithm technique, robustly detecting 50% of the bright SCUBA sources uncovered in the "8 mJy Survey", and less significantly detecting a further 20% of the objects, suggesting a 30% upper limit on the contamination from spurious / confused sources. A similar analysis of the CUDSS fields, however, is unlikely to be very informative regarding a comparison of the two independent source lists, since the CUDSS fields are smaller and deeper than the "8 mJy Survey" fields, designed with the aim of studying less bright SCUBA sources in the range $3\,\mathrm{mJy} < S_{850} < 6\,\mathrm{mJy}$, and hence only the very brightest (and most significant of the CUDSS sources) are likely to be detected in a radio image even at a depth of $\sigma_{1.4\mathrm{GHz}} = 5\,\mu\mathrm{Jy/beam}$.

	RA (J2000)	DEC (J2000)	S_{850} /mJy	S/N	Noise Region	Previous Reference	Prev. S/N	Sep. /arcsec
01	03:02:43.84	+00:09:52.6	7.0 ± 1.4	5.90	central	W03 (03h.19)	3.2	1.8
02	03:02:36.04	+00:08:16.6	3.4 ± 0.8	4.89	deep	W03 (03h.06)	5.4	1.3
03	03:02:42.84	+00:07:57.6	3.6 ± 0.9	4.61	deep	W03 (03h.02)	6.7	3.9
04	03:02:40.77	+00:09:20.6	6.9 ± 1.7	4.51	central			
05	03:02:31.17	+00:08:18.6	4.8 ± 1.2	4.31	central	W03 (03h.03)	6.4	5.1
06	03:02:56.57	+00:08:08.6	7.0 ± 1.8	4.21	central	W03 (03h.24)	3.0	3.5
07	03:02:47.31	+00:09:21.6	4.7 ± 1.3	4.18	central			
08	03:02:53.51	+00:07:52.6	9.0 ± 2.3	4.16	central			
09	03:02:44.51	+00:06:53.6	5.6 ± 1.5	4.14	central	W03 (03h.04)	6.2	2.2
10	03:02:44.31	+00:08:16.6	4.0 ± 1.0	4.14	central	W03 (03h.05)	5.8	5.3
11	03:02:44.64	+00:06:37.6	6.0 ± 1.6	4.03	central	W03 (03h.01)	7.4	3.4
12	03:02:29.04	+00:09:03.6	5.3 ± 1.5	3.87	central			
13	03:02:41.51	+00:10:46.6	9.8 ± 2.8	3.81	central			
14	03:02:35.64	+00:06:09.6	7.9 ± 2.2	3.79	central	W03 (03h.07)	5.3	2.2
15	03:02:27.84	+00:06:45.6	6.0 ± 1.8	3.63	central	W03 (03h.15)*	3.5	7.8
						W03 (03h.27)*	3.0	13.5
16	03:02:53.11	+00:09:41.6	4.8 ± 1.4	3.50	central	W03 (03h.20)	3.2	3.3
17	03:02:25.31	+00:10:17.6	7.2 ± 2.2	3.49	central			
18	03:02:40.97	+00:06:44.6	3.0 ± 0.9	3.48	deep			
19	03:02:53.51	+00:06:23.6	7.3 ± 2.2	3.47	central	W03 (03h.23)	3.0	10.9
20	03:02:25.97	+00:09:06.6	6.3 ± 1.9	3.47	central	W03 (03h.14)	3.5	3.0
21	03:02:58.17	+00:06:07.6	13.9 ± 4.3	3.44	edge			
22	03:02:52.44	+00:08:58.6	4.3 ± 1.4	3.32	central	W03 (03h.10)	4.5	1.4
23	03:02:43.51	+00:10:51.6	9.0 ± 2.9	3.23	central			
24	03:02:48.24	+00:08:03.6	3.9 ± 1.3	3.15	central			
25	03:02:45.11	+00:09:53.6	4.0 ± 1.3	3.14	central			
26	03:02:52.97	+00:11:21.6	6.2 ± 2.1	3.08	central	W03 (03h.11)	4.0	1.1
27	03:02:30.51	+00:08:50.6	4.8 ± 1.6	3.07	central			
28	03:02:40.31	+00:11:42.6	6.5 ± 2.2	3.04	central			
29	03:02:55.37	+00:09:49.6	5.3 ± 1.8	3.03	central			
30	03:02:35.71	+00:12:05.6	7.2 ± 2.5	3.00	central			
	03:02:35.91	*+00:09:57.6*	*3.7 ± 1.3*	*2.97*	*central*	W03 (03h.13)	3.8	4.4
	03:02:38.77	*+00:10:27.6*	*5.2 ± 1.9*	*2.80*	*central*	W03 (03h.12)	4.0	1.9
	03:02:26.24	*+00:06:18.6*	*4.8 ± 1.9*	*2.67*	*central*	W03 (03h.08)	5.0	2.3
	03:02:26.11	*+00:08:17.6*	*3.8 ± 1.5*	*2.66*	*central*	W03 (03h.21)	3.1	3.4
	03:02:32.77	*+00:10:20.6*	*4.0 ± 1.7*	*2.51*	*central*	W03 (03h.18)	3.3	5.8
	03:02:31.37	*+00:10:33.6*	*4.5 ± 2.0*	*2.33*	*central*	W03 (03h.17)	3.4	5.2
	03:02:34.97	*+00:09:16.6*	*3.4 ± 1.5*	*2.33*	*central*	W03 (03h.26)	3.0	4.5
	03:02:28.31	*+00:10:19.6*	*3.5 ± 1.7*	*2.09*	*central*	W03 (03h.09)	4.6	8.9
	03:02:35.44	*+00:08:51.6*	*2.3 ± 1.1*	*2.08*	*central*	W03 (03h.16)	3.4	9.5
	03:02:39.17	*+00:06:14.6*	*2.2 ± 1.3*	*1.77*	*central*	W03 (03h.22)	3.1	12.5
	03:02:38.11	*+00:11:10.6*	*2.9 ± 2.4*	*1.22*	*central*	W03 (03h.25)	3.0	8.2

Table 5.1: 850 μm source list for the 03h field of the "Canada-UK Deep Submillimetre Survey".

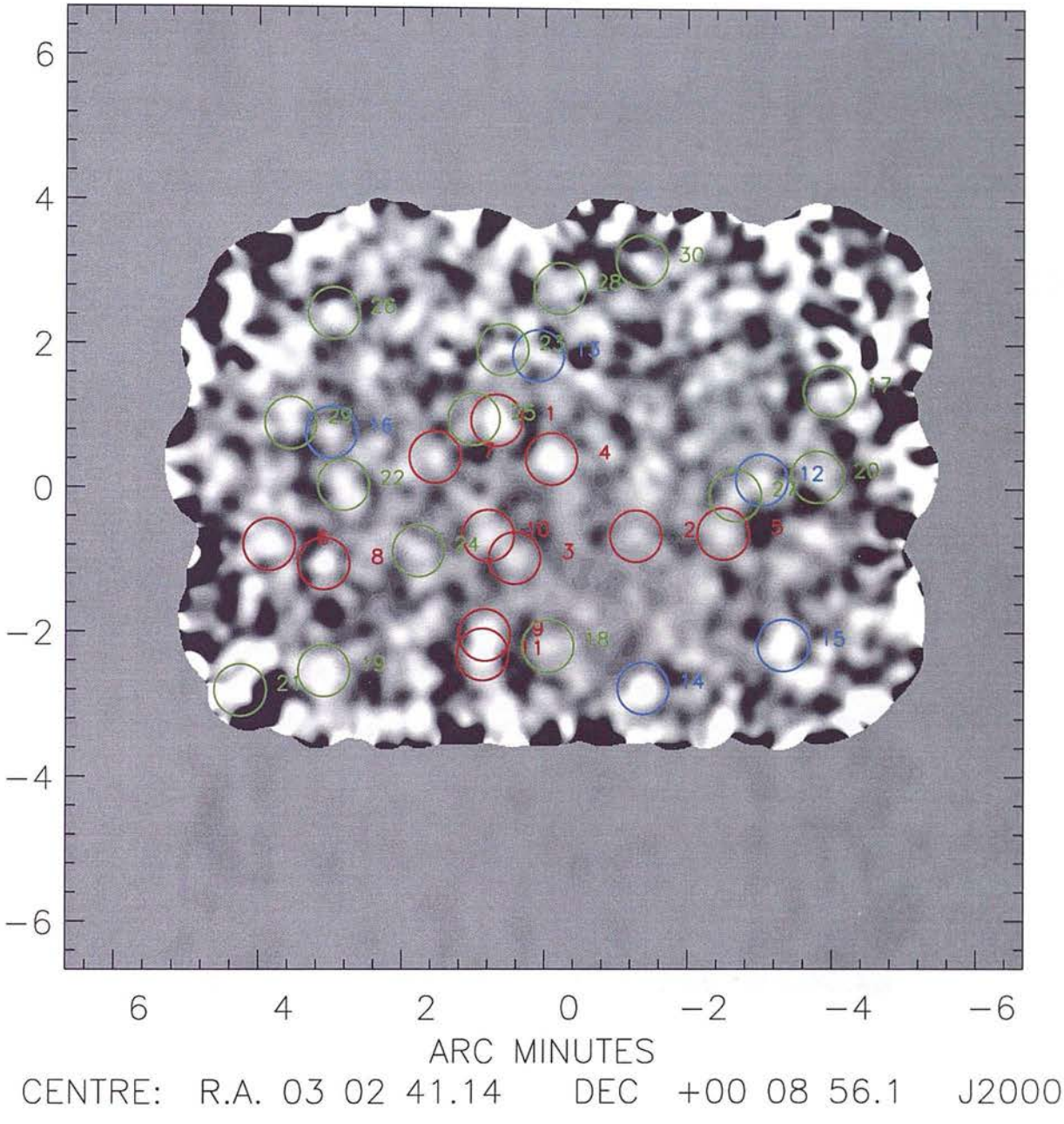

Figure 5.1: The 850 μm image of the CUDSS 03-Hour field, smoothed with a beam-size Gaussian (14.5 arcsec FWHM). The numbered circles highlight those sources found at a significance of > 3.00; the red circles are those sources with S/N > 4.00, the blue circles those sources with $3.50 <$ S/N < 3.99, and the green circles those detections with $3.00 <$ S/N < 3.49. The labelling corresponds to the numbers in Table 5.1.

	RA (J2000)	DEC (J2000)	S_{850} /mJy	S/N	Noise Region	Previous Reference	Prev. S/N	Sep. /arcsec
01	10:00:36.86	+25:14:56.9	3.3 ± 1.1	3.12	central	E99 (10h.B)*	5.0	3.4
						E99 (10h.C)*	3.8	15.9
						E99 (10h.D)*	3.6	15.0
	10:00:38.12	*+25:14:51.9*	*2.8 ± 1.0*	*2.79*	*central*	E99 (10h.A)	6.1	2.1

Table 5.2: 850 μm source list for the 10h field of the "Canada-UK Deep Submillimetre Survey".

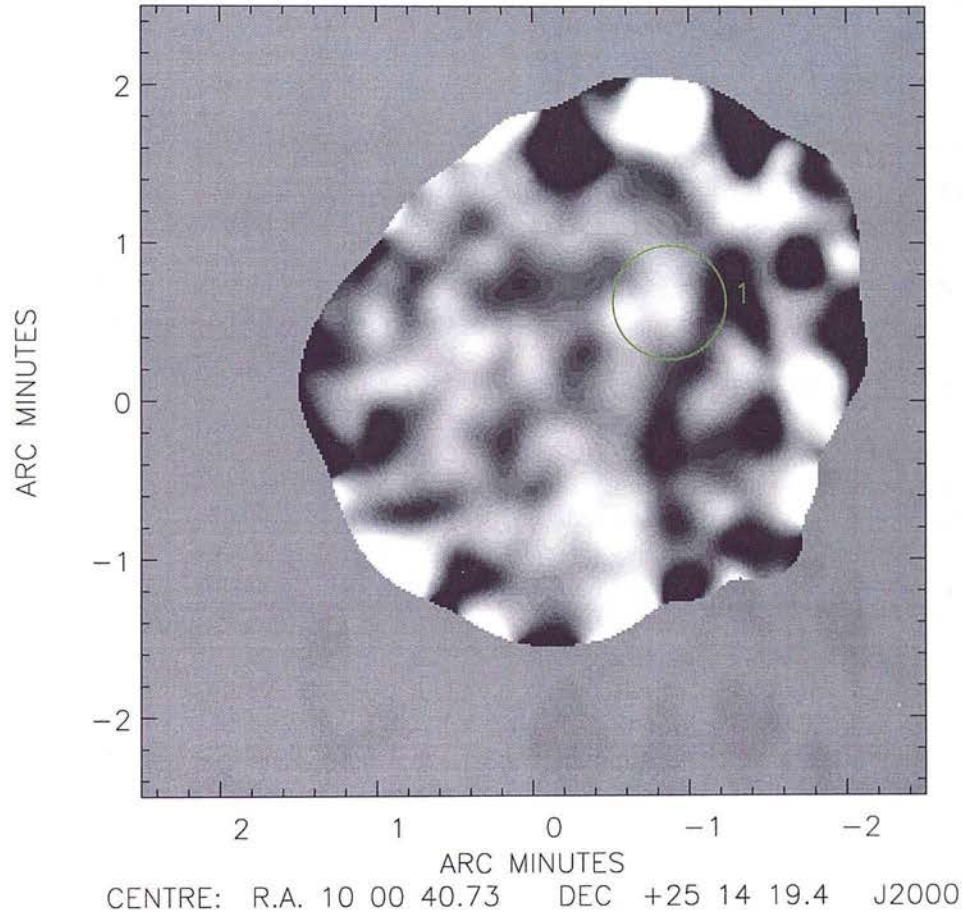

Figure 5.2: The 850 μm image of the CUDSS 10-Hour field, smoothed with a beam-size Gaussian (14.5 arcsec FWHM). The numbered circles highlight those sources found at a significance of > 3.00; the red circles are those sources with S/N > 4.00, the blue circles those sources with $3.50 <$ S/N < 3.99, and the green circles those detections with $3.00 <$ S/N < 3.49. The labelling corresponds to the numbers in Table 5.2.

	RA (J2000)	DEC (J2000)	S_{850} /mJy	S/N	Noise Region	Previous Reference	Prev. S/N	Sep. /arcsec
01	14:17:40.03	+52:29:07.0	8.5 ± 1.4	7.62	central	E00 (14h.01)	10.1	2.1
02	14:17:51.86	+52:30:32.0	6.0 ± 1.1	6.01	central	E00 (14h.02)	6.3	2.1
03	14:18:00.61	+52:28:20.0	7.2 ± 1.5	5.45	central	E00 (14h.03)	5.4	3.6
04	14:17:43.21	+52:28:16.0	5.7 ± 1.4	4.57	central	E00 (14h.04)	5.3	2.0
05	14:18:07.51	+52:28:22.9	5.8 ± 1.4	4.42	central	E00 (14h.05)	4.5	2.3
06	14:17:38.05	+52:32:50.0	4.9 ± 1.4	3.90	central			
07	14:18:09.39	+52:32:02.9	5.4 ± 1.5	3.76	central			
08	14:18:12.91	+52:33:21.9	9.3 ± 2.7	3.71	edge			
09	14:17:56.03	+52:32:59.0	3.7 ± 1.1	3.59	central			
10	14:17:36.07	+52:33:15.0	4.1 ± 1.2	3.47	central			
11	14:17:42.22	+52:30:31.0	3.7 ± 1.1	3.46	central	E00 (14h.18)	3.0	4.5
12	14:17:45.61	+52:33:23.0	3.9 ± 1.2	3.37	central			
13	14:17:46.93	+52:29:20.0	4.2 ± 1.3	3.31	central			
14	14:17:25.02	+52:30:41.9	9.0 ± 2.9	3.25	edge	E00 (14h.17)	3.3	4.5
15	14:17:35.11	+52:28:53.0	4.5 ± 1.4	3.25	central			
16	14:18:03.26	+52:32:29.0	3.7 ± 1.2	3.20	central			
17	14:17:47.25	+52:32:36.0	3.3 ± 1.1	3.19	central	E00 (14h.11)	3.5	2.4
18	14:17:42.66	+52:30:04.0	4.5 ± 1.5	3.14	central			
19	14:17:35.53	+52:32:11.0	3.2 ± 1.1	3.14	central			
20	14:18:08.71	+52:28:00.9	4.4 ± 1.5	3.13	central	E00 (14h.09)	4.1	4.1
21	14:18:03.68	+52:29:33.9	3.1 ± 1.0	3.05	central	E00 (14h.10)	3.5	5.0
22	14:17:48.13	+52:32:51.0	3.4 ± 1.2	3.04	central			
23	14:17:43.42	+52:32:46.0	3.9 ± 1.3	3.01	central			
	14:17:41.57	*+52:28:27.0*	3.7 ± 1.3	*2.96*	*central*	E00 (14h.13)	3.4	3.9
	14:18:11.68	*+52:30:05.9*	5.7 ± 2.0	*2.90*	*central*	E00 (14h.19)	3.0	2.5
	14:18:12.44	*+52:29:13.9*	6.3 ± 2.4	*2.77*	*central*	E00 (14h.16)	3.7	6.3
	14:18:09.28	*+52:31:01.9*	4.1 ± 1.6	*2.61*	*central*	E00 (14h.14)	3.3	6.0
	14:18:01.61	*+52:30:28.0*	3.3 ± 1.3	*2.56*	*central*	E00 (14h.08)	4.0	13.8
	14:17:56.45	*+52:29:12.0*	3.0 ± 1.2	*2.50*	*central*	E00 (14h.06)	4.2	5.2
	14:18:05.21	*+52:28:55.9*	3.3 ± 1.4	*2.41*	*central*	E00 (14h.12)	3.4	0.9
	14:17:29.53	*+52:28:17.9*	4.2 ± 1.9	*2.26*	*central*	E00 (14h.15)	3.1	2.4
	14:18:01.60	*+52:29:44.0*	1.8 ± 1.0	*1.76*	*central*	E00 (14h.07)	3.2	6.8

Table 5.3: 850 μm source list for the 14h field of the "Canada-UK Deep Submillimetre Survey".

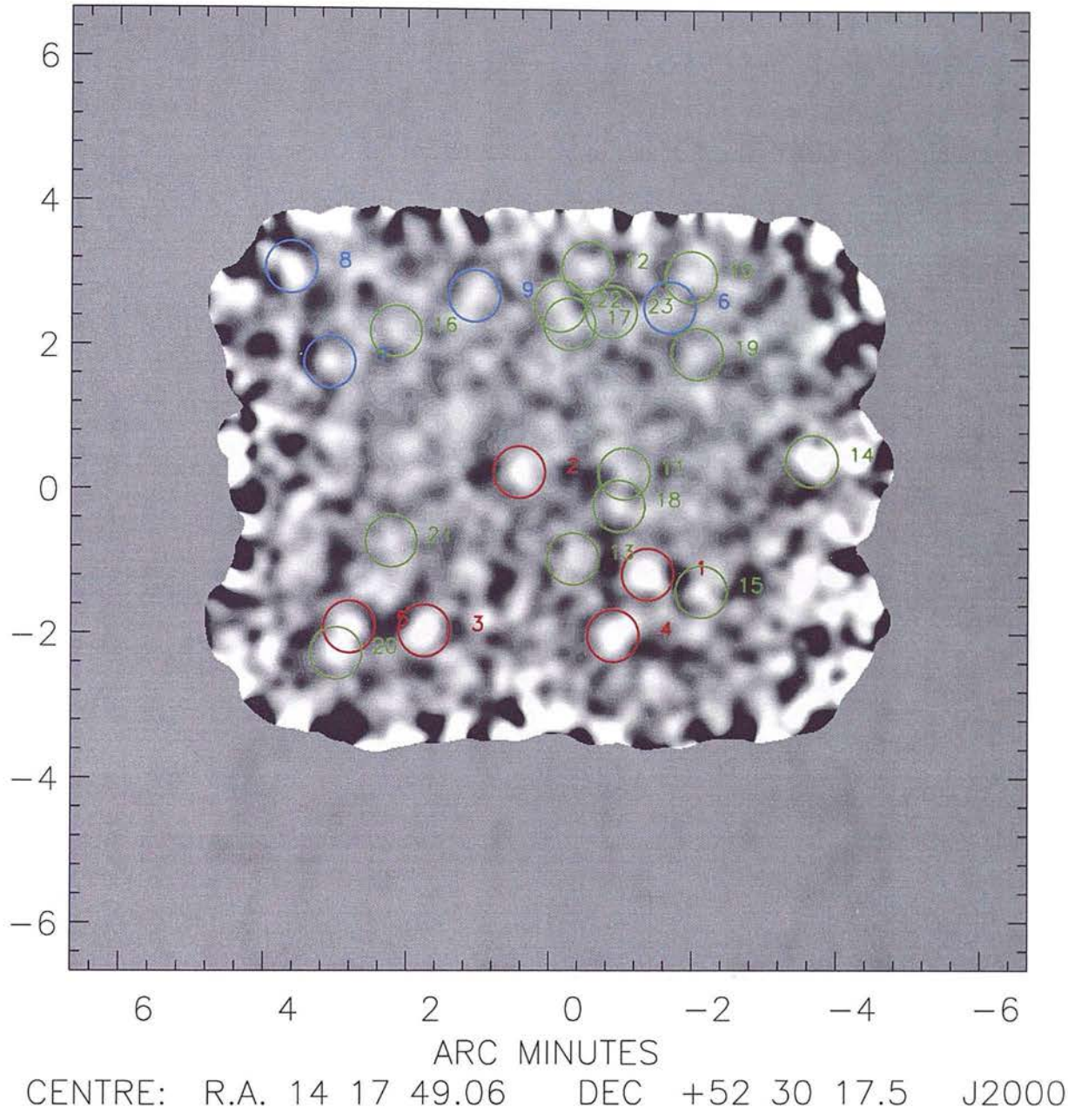

Figure 5.3: The 850 μm image of the CUDSS 14-Hour field, smoothed with a beam-size Gaussian (14.5 arcsec FWHM). The numbered circles highlight those sources found at a significance of > 3.00; the red circles are those sources with S/N > 4.00, the blue circles those sources with $3.50 <$ S/N < 3.99, and the green circles those detections with $3.00 <$ S/N < 3.49. The labelling corresponds to the numbers in Table 5.3.

	RA (J2000)	DEC (J2000)	S_{850} /mJy	S/N	Noise Region	Previous Reference	Prev. S/N	Sep. /arcsec
01	22:17:59.18	+00:17:36.9	5.6 ± 1.3	4.62	central			
02	22:17:59.18	+00:18:22.9	4.8 ± 1.3	4.14	central			
03	22:17:55.58	+00:17:36.9	3.6 ± 1.1	3.36	central			

Table 5.4: 850 μm source list for the 22h field of the "Canada-UK Deep Submillimetre Survey".

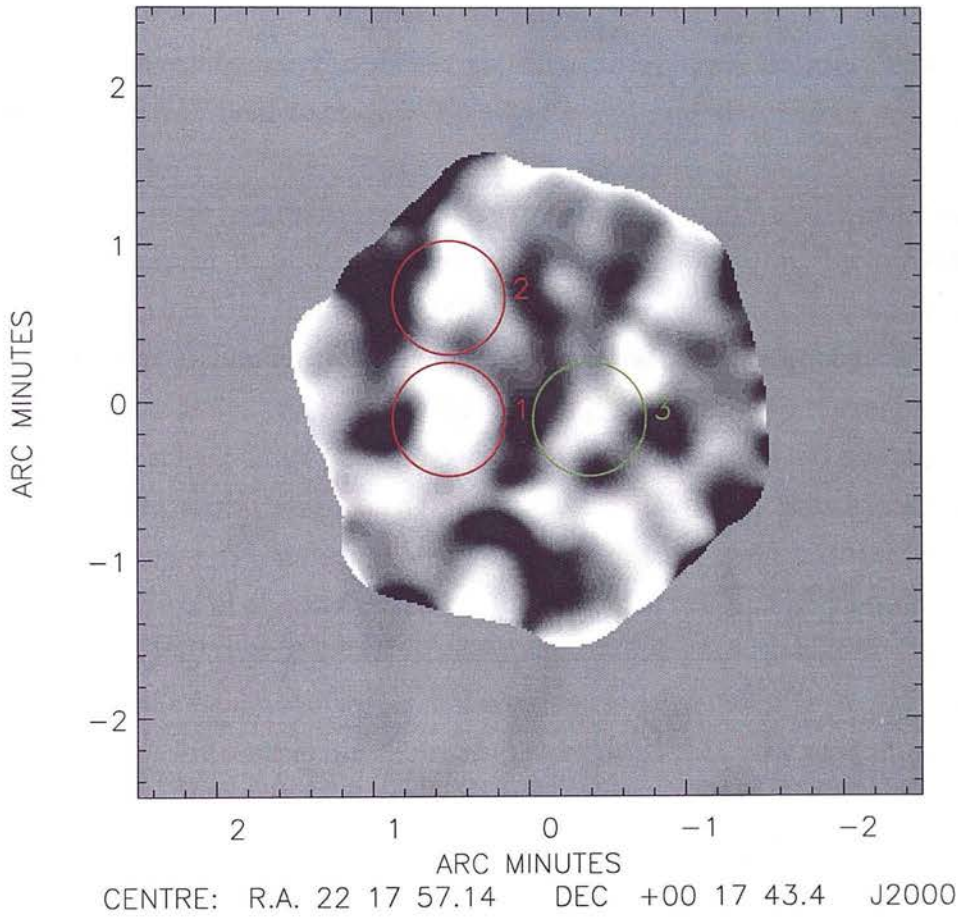

Figure 5.4: The 850 μm image of the CUDSS 22-Hour field, smoothed with a beam-size Gaussian (14.5 arcsec FWHM). The numbered circles highlight those sources found at a significance of > 3.00; the red circles are those sources with S/N > 4.00, the blue circles those sources with $3.50 <$ S/N < 3.99, and the green circles those detections with $3.00 <$ S/N < 3.49. The labelling corresponds to the numbers in Table 5.4.

5.1.2 The "Hawaii Flanking Fields Survey"

The "Hawaii Flanking Fields Survey (HFFS)" (Barger et al. 1998, Barger, Cowie & Sanders 1999, Barger, Cowie & Richards 2000), covers a total of $\simeq$ 110 sq. arcmin over 4 regions of sky. The Lockman Hole deep field is a small pencil beam map (Barger et al. 1998), covering approximately of $\simeq$ 8 sq. arcmin of sky to an rms noise level of $\sigma_{850} = 0.8\,\mathrm{mJy/beam}$. The SSA13 field is composed of a deep pencil beam area ($\simeq$ 8 sq. arcmin in size, $\sigma_{850} = 0.7\,\mathrm{mJy/beam}$; Barger et al. 1998), embedded in a wider-area, shallower map covering an additional 45 sq. arcmin with a typical rms noise level of $\sigma_{850} = 2.5\,\mathrm{mJy/beam}$ (Barger, Cowie & Sanders 1999). The SSA17 and SSA22 fields (Barger, Cowie & Sanders 1999) both have regions of uniform noise covering approximately 20 sq. arcmin of sky, the SSA17 field to $\sigma_{850} = 1.6\,\mathrm{mJy/beam}$, and the SSA22 field to $\sigma_{850} = 0.9\,\mathrm{mJy/beam}$.

The data were originally reduced using the standard SURF pipeline as described in Chapter 2, and source extraction was carried out by convolving the signal maps with the beam. In order to determine the absolute noise levels, Barger, Cowie & Sanders (1999) first eliminated any significant sources (estimated to be at the $\geq 2.8\sigma$ level) by subtracting appropriately normalised versions of the beam profile. They then placed beam-sized apertures at random positions on the residual signal map, using the standard deviation between the enclosed pixels to estimate the noise. These values were then used to iteratively adjust the normalization of the variance array values, until the dispersion of the signal-to-noise ratio was approximately one. As previously mentioned in Chapter 2, it is not clear that using the variance arrays output from SURF in this manner is a valid method for measuring the noise values, and this may explain some of the discrepancies between the resulting catalogues.

Comparative source lists for detections with S/N > 3.00 from the two different reductions and source extraction procedures are given in Tables 5.5 to 5.8. Column 1 gives the source number in order of decreasing signal-to-noise ratio as derived from the new IDL-reduction and simultaneous maximum-likelihood source extraction method, and corresponds to the labelling of the circled sources in Figs. 5.5 to 5.8. The red circles are those sources with S/N > 4.00, the blue circles those sources with 3.50 < S/N < 3.99, and the green circles those detections with 3.00 < S/N < 3.49. Columns 2 and 3 give the right ascension and declination of the source in J2000 coordinates. Column 4 gives the simultaneously

fitted 850 μm flux densities of the sources. The error includes a 10% calibration error combined in quadrature. Column 5 gives the measured signal-to-noise ratio of the source from the simultaneously fitted model. Column 6 defines the noise region in which the source was found; 'deep' corresponds to the deep pencil-beam surveys which constitute part of a wider-area and somewhat shallower image, 'central' corresponds to the parts of the map which have seen the full integration time (outside of the deep area), and 'edge' corresponds to the rather noisier regions near the perimeter which have not seen the full integration time. In one case, a source previously identified by Barger, Cowie & Sanders (1999) has been marked with 'bad bol.' as this region appears to have been observed with a bad bolometer, hence the "source" is most likely to be an artefact of SURF's attempt to interpolate between neighbouring areas of good quality data. Column 7 gives any previous reference to the 850 μm source. Reference B99 is an abbreviation for Barger, Cowie & Sanders (1999). Column 8 gives the previously recorded signal-to-noise ratio where applicable, and Column 9 gives the distance between the listed and previously referenced positions. The table listings given in italics correspond to previously referenced sources with S/N $>$ 3.00, which did not meet this criterion in this analysis.

The two reduction and source-extraction algorithms again produce quite different results. There is no clear trend in the variations between the independent measurements of signal-to-noise for those sources detected significantly in both analyses; in some cases the SURF reduction yields a higher signal-to-noise estimate whereas for other sources the situation is reversed. The IDL-based reduction and maximum likelihood algorithm has identified nearly twice as many peaks at the $> 3.00\sigma$ level as the original catalogue of Barger, Cowie & Sanders (1999), including all of their original $> 4.00\sigma$ objects. The most discrepant of the fields is the wide-area SSA13 field, which has particulaly uneven noise when compared to all of the other survey fields and it is most likely because of this that only 2/5 of the original detections could be identified at S/N $>$ 3.00. In the deep part of the SSA13 field, however, the top two original sources are detected at better than 5.00σ in this analysis. In the SSA22 field, all 5 of the $> 3.00\sigma$ detected by Barger, Cowie & Sanders (1999) are recovered, with firm agreement on the top 2 sources at better than 4.00σ in both catalogues.

	RA (J2000)	DEC (J2000)	S_{850} /mJy	S/N	Noise Region	Previous Reference	Prev. S/N	Sep. /arcsec
01	10:34:02.05	+57:46:27.1	4.9 ± 0.9	6.45	central	B99 (LH.1)	5.1	2.1
02	10:33:55.80	+57:45:10.1	2.6 ± 0.7	3.79	central			
	10:33:55.42	*+57:47:38.1*	*2.0 ± 0.8*	2.59	*central*	B99 (LH.2)	3.3	10.6

Table 5.5: 850 μm source list for the Lockman Hole Field of the "Hawaii Flanking Fields Survey".

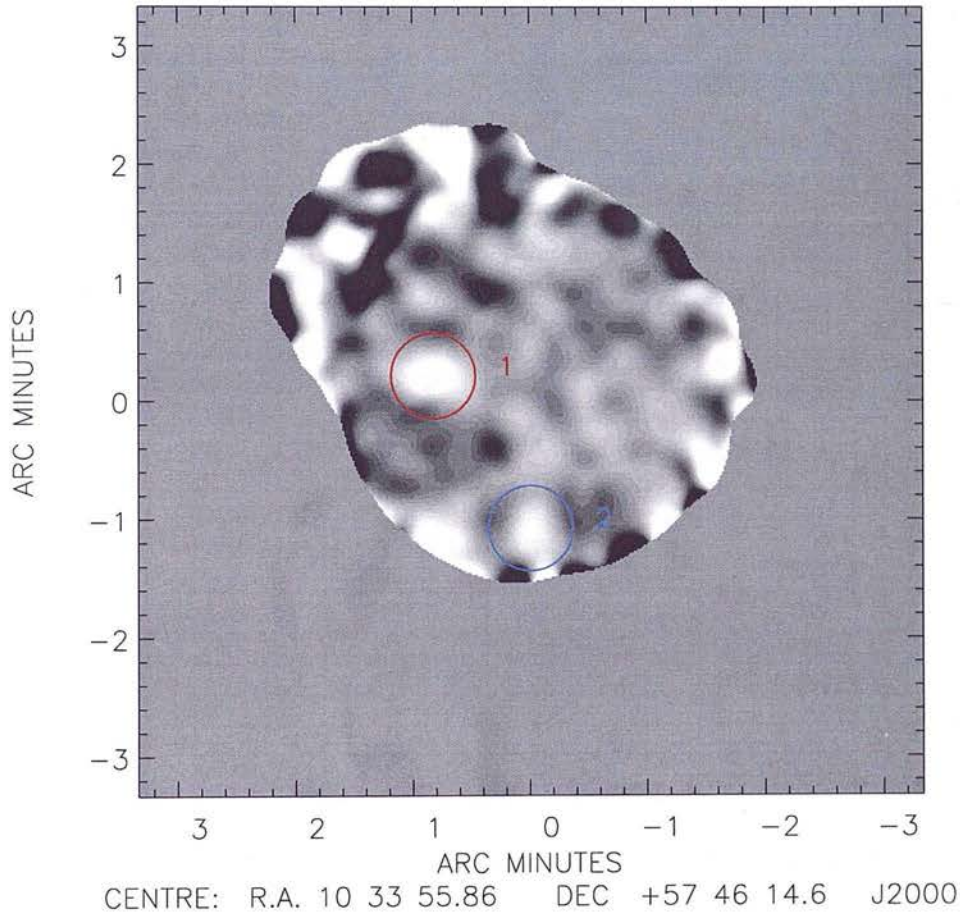

Figure 5.5: The 850 μm image of the Lockman Hole field from the HFF Survey, smoothed with a beam-size Gaussian (14.5 arcsec FWHM). The numbered circles highlight those sources found at a significance of > 3.00; the red circles are those sources with S/N > 4.00, the blue circles those sources with $3.50 <$ S/N < 3.99, and the green circles those detections with $3.00 <$ S/N < 3.49. The labelling corresponds to the numbers in Table 5.5.

	RA (J2000)	DEC (J2000)	S_{850} /mJy	S/N	Noise Region	Previous Reference	Prev. S/N	Sep. /arcsec
01	13:12:31.82	+42:44:28.6	3.6 ± 0.7	6.52	deep	B99 (SSA13.1)	4.7	3.4
02	13:12:13.94	+42:37:00.7	10.2 ± 2.2	5.19	central			
03	13:12:27.56	+42:45:01.5	2.8 ± 0.6	5.08	deep	B99 (SSA13.2)	3.8	6.0
04	13:12:19.93	+42:39:30.7	6.1 ± 1.6	4.22	central			
05	13:12:08.51	+42:38:19.7	7.0 ± 1.9	4.03	central			
06	13:12:25.00	+42:39:56.7	7.8 ± 2.1	4.01	central	B99 (SSA13.6)	3.4	1.3
07	13:12:25.82	+42:39:38.7	8.7 ± 2.5	3.75	central			
08	13:12:17.66	+42:42:51.7	7.4 ± 2.1	3.66	central			
09	13:12:22.29	+42:45:00.7	2.7 ± 0.8	3.65	deep			
10	13:12:13.94	+42:39:49.7	5.9 ± 1.8	3.43	central			
11	13:12:31.26	+42:40:22.7	8.1 ± 2.5	3.41	central			
12	13:12:05.79	+42:38:52.7	10.2 ± 3.2	3.36	central			
13	13:12:14.40	+42:43:33.7	10.1 ± 3.2	3.34	central			
14	13:12:27.28	+42:41:54.7	6.6 ± 2.1	3.33	central	B99 (SSA13.7)	3.3	13.9
15	13:12:04.88	+42:37:51.7	10.2 ± 3.4	3.18	central			
16	13:12:33.71	+42:40:22.6	7.9 ± 2.6	3.18	central			
17	13:12:28.99	+42:40:14.7	7.1 ± 2.4	3.14	central			
18	13:12:11.22	+42:42:20.7	5.9 ± 2.0	3.14	central			
19	13:12:27.27	+42:38:59.7	9.1 ± 3.1	3.03	central			
	13:12:18.66	*+42:38:25.7*	*4.0 ± 1.4*	*2.99*	*central*	B99 (SSA13.5)	3.3	12.8
	13:12:25.65	*+42:43:48.5*	*1.6 ± 0.6*	*2.69*	*deep*	B99 (SSA13.3)	3.2	1.6
	13:12:05.95	*+42:44:37.7*	*1.5 ± 3.2*	*0.49*	*edge*	B99 (SSA13.9)	3.4	10.1
	n/a	*n/a*	*n/a*	*n/a*	*bad bol.*	B99 (SSA13.8)	3.5	*n/a*
	n/a	*n/a*	*n/a*	*n/a*	*edge*	B99 (SSA13.4)	3.3	*n/a*

Table 5.6: 850 μm source list for the SSA13 Field of the "Hawaii Flanking Fields Survey".

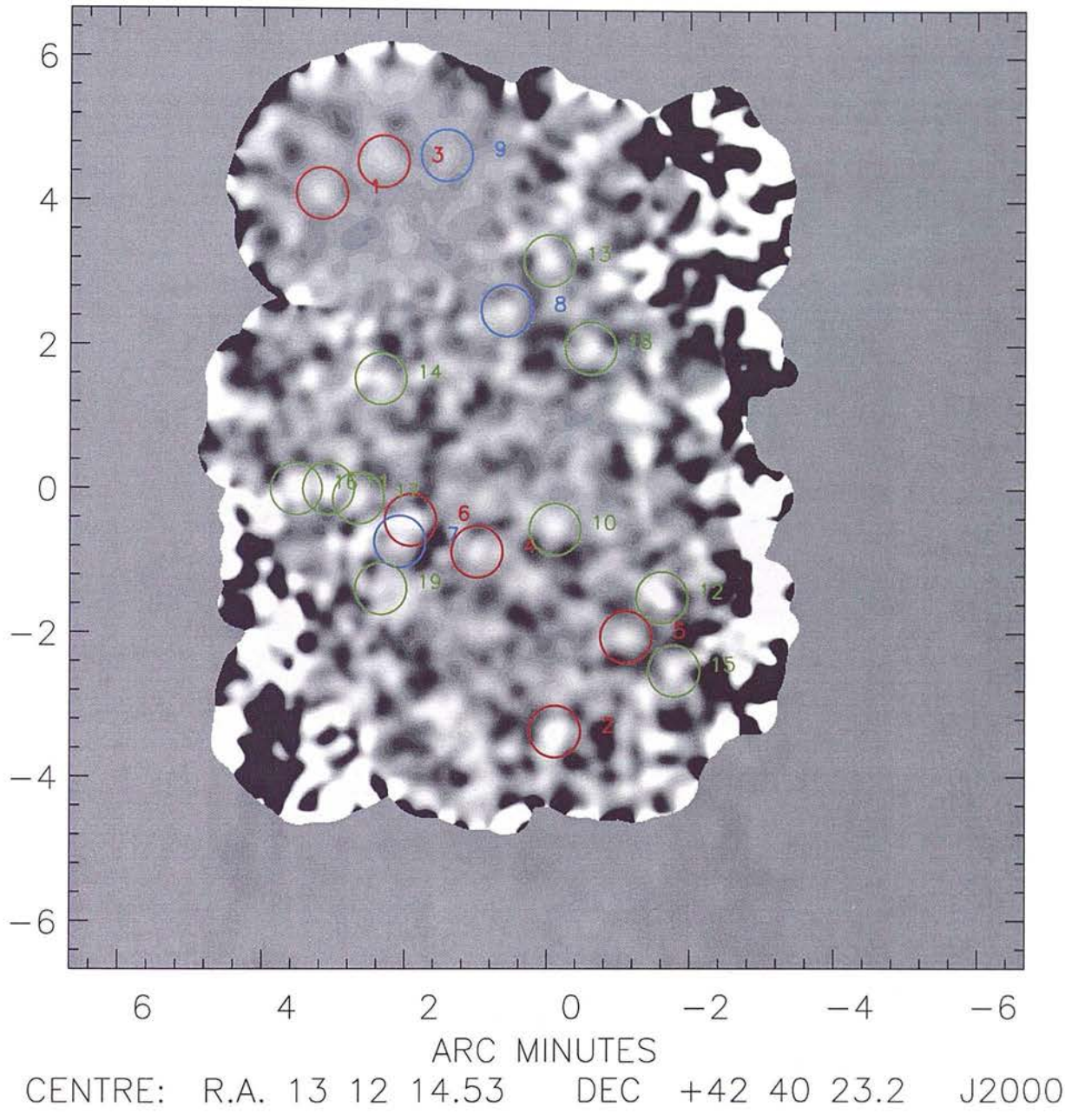

Figure 5.6: The 850 μm image of the SSA13 field from the HFF Survey, smoothed with a beam-size Gaussian (14.5 arcsec FWHM). The numbered circles highlight those sources found at a significance of > 3.00; the red circles are those sources with S/N $>$ 4.00, the blue circles those sources with $3.50 <$ S/N < 3.99, and the green circles those detections with $3.00 <$ S/N < 3.49. The labelling corresponds to the numbers in Table 5.6.

	RA (J2000)	DEC (J2000)	S_{850} /mJy	S/N	Noise Region	Previous Reference	Prev. S/N	Sep. /arcsec
01	17:06:37.03	+43:55:31.8	3.2 ± 1.0	3.51	central	B99 (SSA17.3)	3.7	2.0
02	17:06:29.53	+43:55:08.8	4.0 ± 1.2	3.36	central			
03	17:06:25.08	+43:57:40.8	5.6 ± 1.8	3.33	central	B99 (SSA17.1)	4.2	2.0
04	17:06:32.86	+43:54:05.8	5.1 ± 1.7	3.16	central	B99 (SSA17.4)	3.6	3.4
	17:06:25.55	*+43:54:39.8*	3.1 ± 1.4	*2.35*	*central*	B99 (SSA17.2)	3.9	0.6
	17:06:20.37	*+43:54:09.8*	2.6 ± 2.6	*1.02*	*edge*	B99 (SSA17.5)	3.1	5.8

Table 5.7: 850 μm source list for the SSA17 Field of the "Hawaii Flanking Fields Survey".

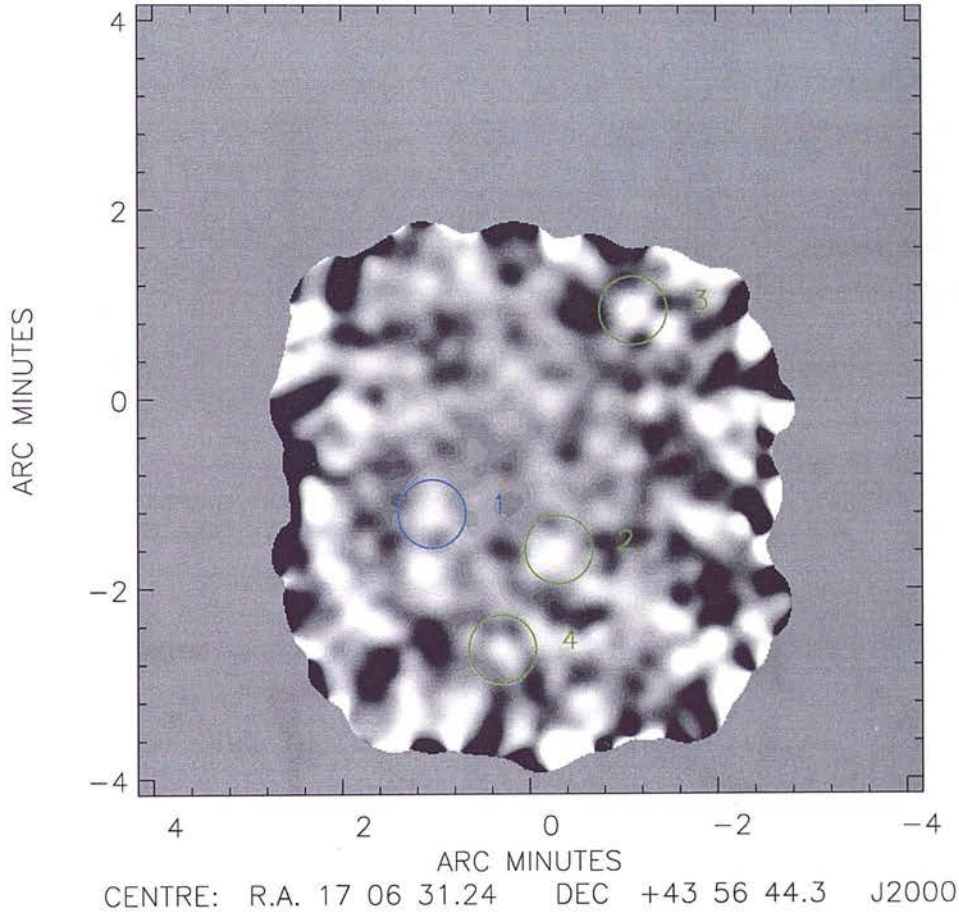

Figure 5.7: The 850 μm image of the SSA17 field from the HFF Survey, smoothed with a beam-size Gaussian (14.5 arcsec FWHM). The numbered circles highlight those sources found at a significance of > 3.00; the red circles are those sources with S/N $>$ 4.00, the blue circles those sources with $3.50 <$ S/N < 3.99, and the green circles those detections with $3.00 <$ S/N < 3.49. The labelling corresponds to the numbers in Table 5.7.

	RA (J2000)	DEC (J2000)	S_{850} /mJy	S/N	Noise Region	Previous Reference	Prev. S/N	Sep. /arcsec
01	22:17:33.96	+00:13:53.4	4.7 ± 0.8	6.97	central	B99 (SSA22.1)	6.9	2.2
02	22:17:35.03	+00:15:36.4	2.7 ± 0.7	4.29	central	B99 (SSA22.2)	5.3	5.1
03	22:17:31.23	+00:16:07.4	3.1 ± 0.8	4.04	central			
04	22:17:41.56	+00:16:04.4	3.7 ± 1.0	3.96	central	B99 (SSA22.5)	3.1	7.0
05	22:17:40.90	+00:14:56.4	3.0 ± 0.8	3.92	central			
06	22:17:35.96	+00:15:56.4	2.5 ± 0.7	3.77	central	B99 (SSA22.3)	4.0	13.1
07	22:17:37.36	+00:16:21.4	3.6 ± 1.0	3.75	central			
08	22:17:29.30	+00:13:57.4	2.6 ± 0.7	3.66	central			
09	22:17:19.96	+00:15:25.4	8.1 ± 2.7	3.22	edge			
10	22:17:33.43	+00:16:13.4	2.4 ± 0.8	3.11	central			
11	22:17:33.76	+00:15:42.4	1.8 ± 0.6	3.10	central	B99 (SSA22.4)	3.6	3.6
12	22:17:41.03	+00:13:32.4	3.2 ± 1.1	3.08	central			

Table 5.8: 850 μm source list for the SSA22 Field of the "Hawaii Flanking Fields Survey".

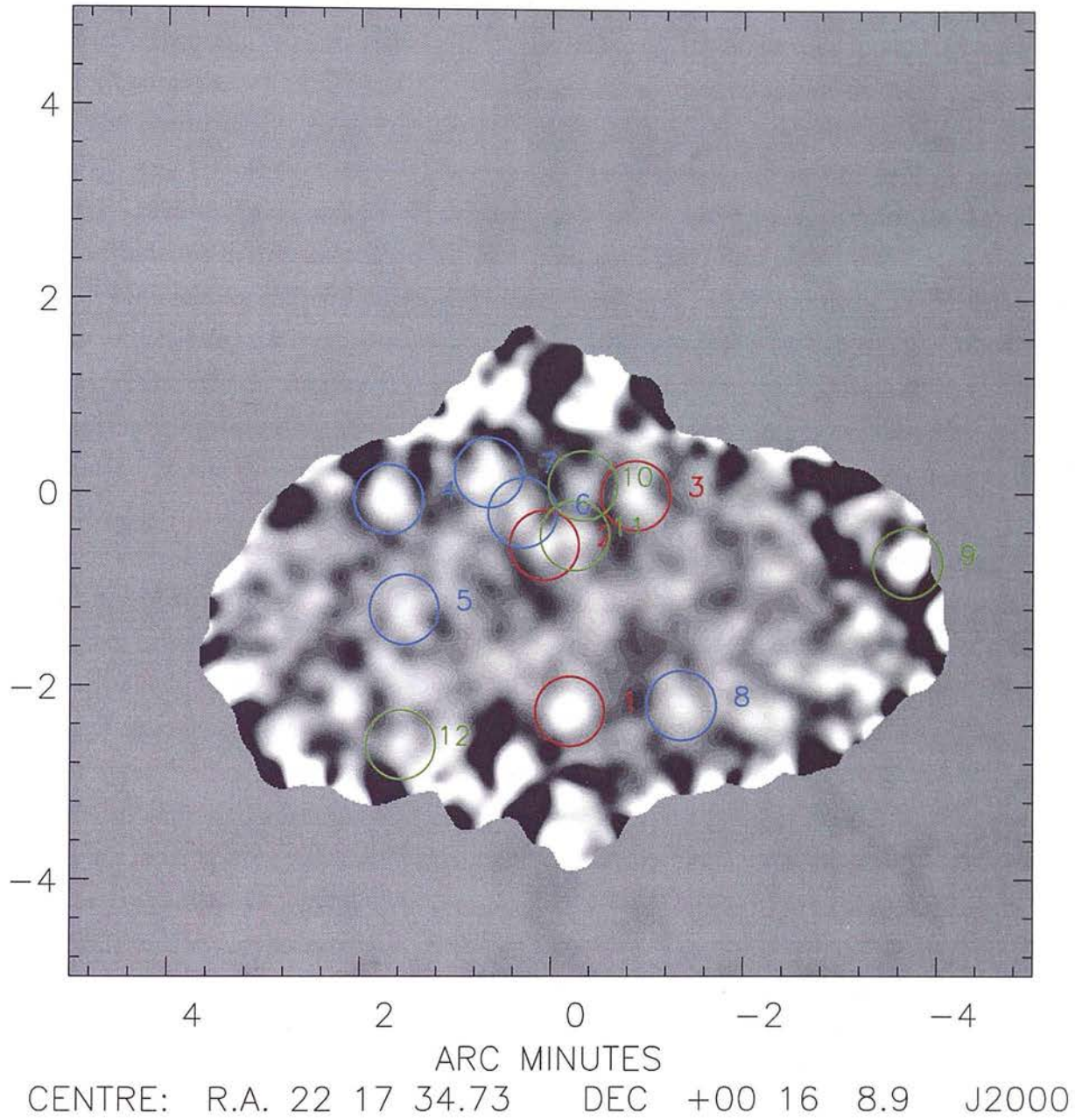

Figure 5.8: The 850 μm image of the SSA22 field from the HFF Survey, smoothed with a beam-size Gaussian (14.5 arcsec FWHM). The numbered circles highlight those sources found at a significance of > 3.00; the red circles are those sources with S/N $>$ 4.00, the blue circles those sources with $3.50 <$ S/N < 3.99, and the green circles those detections with $3.00 <$ S/N < 3.49. The labelling corresponds to the numbers in Table 5.8.

5.1.3 The "Hubble Deep Field Survey"

The Hubble Deep field is the deepest of the submillimetre surveys, covering approximately 6 square arcminutes of sky down to the confusion level of $\sigma_{850} = 0.5\,\mathrm{mJy/beam}$. It differs slightly from the other SCUBA surveys in that two different chop throws of 30" and 45", both fixed in celestial coordinates, were applied to the observations, each for approximately half of the integration time. Both SURF and IDL reductions have previously been carried out on this field (Hughes et al. 1998 and Serjeant et al. 2003 respectively), but the maximum-likelihood simultaneous-fitting algorithm has not been used previously.

Comparative source lists for detections with S/N > 3.00 from the three different reductions and source extraction procedures are given in Table 5.9. Column 1 gives the source number corresponding to the labelling on Figure 5.9, in order of decreasing signal-to-noise. Columns 2 and 3 give the right ascension and declination of the source in J2000 coordinates. Column 4 gives the simultaneously fitted 850 μm flux densities of the sources. The error includes a 10% calibration error combined in quadrature. Column 5 gives the measured signal-to-noise ratio of the source from the simultaneously fitted model. Column 6 defines the noise region in which the source was found; 'central' corresponds to the parts of the map which have seen the full integration time (outside of the deep area), and 'edge' corresponds to the rather noisier regions near the perimeter which have not seen the full integration time. Column 7 gives any previous reference to the 850 μm source. Reference H98 is an abbreviation for Hughes et al. (1998), and Serj03 is an abbreviation for Serjeant et al. (2003). The presence of a * indicates that Hughes et al. (1998) deconvolved two sources here, whereas Serjeant et al. (2003) and my own reduction extracted only one. Column 8 gives the previously recorded signal-to-noise ratio where applicable, and column 9 gives the distance between the listed and previously referenced positions. The table listings given in italics correspond to previously referenced sources with S/N > 3.00, which did not meet this criteria in this analysis.

Two of the newly detected "sources" presented in Serjeant et al. may be real, but since they are located on / beyond the edge of the map to the extent that they do not peak in the region where there is actual data in the smoothed signal map, there is a strong possibility that in fact these objects are simply edge artefacts. However, two new sources which have eluded previous analyses, have been recovered at the S/N > 3.50 level.

	RA (J2000)	DEC (J2000)	S_{850} /mJy	S/N	Noise Region	Previous Reference	Prev. S/N	Sep. /arcsec
01	12:36:52.01	+62:12:27.0	5.5 ± 0.7	12.13	central	H98 (HDF.1)	14.0	2.2
						Serj03 (HDF.1)	15.3	1.6
02	12:36:56.59	+62:12:06.0	3.6 ± 0.6	7.06	central	H98 (HDF.2)	5.4	2.3
						Serj03 (HDF.2)	7.6	2.6
03	12:36:53.16	+62:13:55.0	2.7 ± 0.6	4.79	central	Serj03 (HDF.8)	3.5	0.8
04	12:36:50.58	+62:13:18.0	2.1 ± 0.5	4.35	central	H98 (HDF.4)*	4.6	2.6
						H98 (HDF.5)*	4.2	9.9
						Serj03 (HDF.4&5)	5.1	n/a
05	12:36:44.87	+62:11:40.0	2.9 ± 0.8	3.87	central			
06	12:37:03.17	+62:13:04.0	2.8 ± 0.8	3.66	central			
	12:36:44.00	*+62:13:09.0*	*1.2 ± 0.6*	*2.13*	*central*	H98 (HDF.3)	5.0	7.5
						Serj03 (HDF.3)	2.1	2.9
	n/a	*n/a*	*n/a*	*n/a*	*edge*	Serj03 (HDF.6)	3.8	*n/a*
	n/a	*n/a*	*n/a*	*n/a*	*edge*	Serj03 (HDF.7)	3.7	*n/a*

Table 5.9: 850 μm source list for the "Hubble Deep Field Survey".

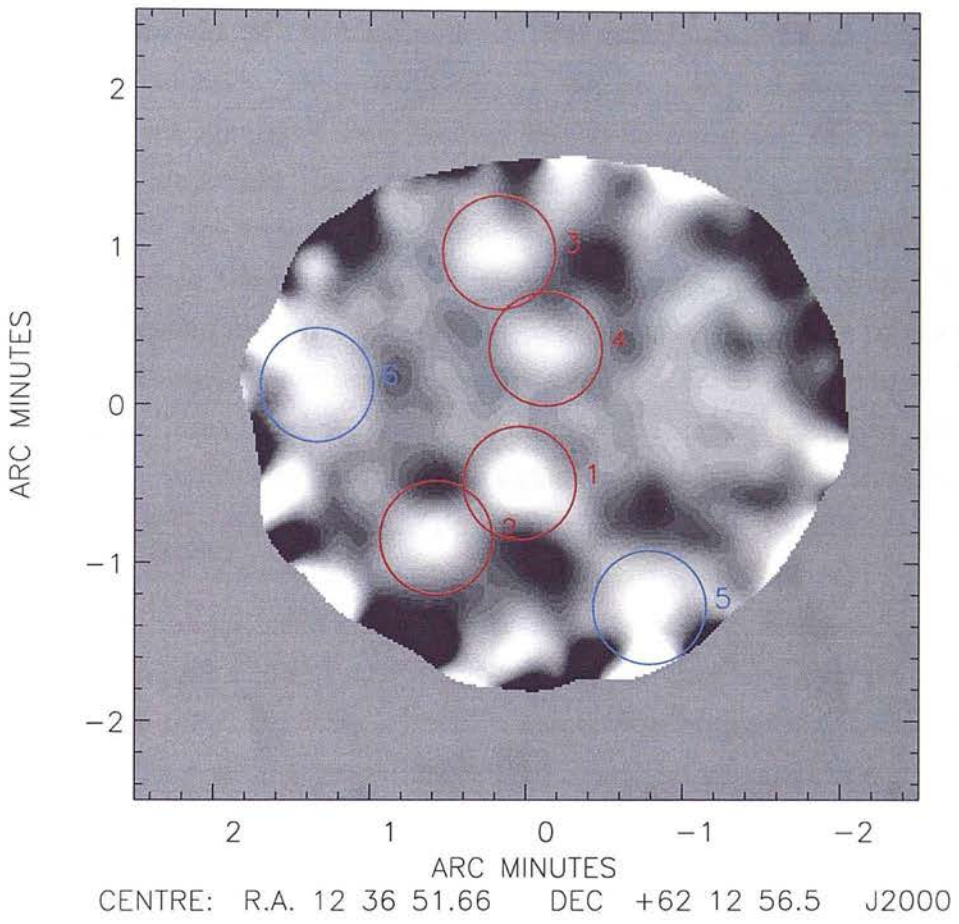

Figure 5.9: The 850 μm image of the Hubble Deep field smoothed with a beam-size Gaussian (14.5 arcsec FWHM). The numbered circles highlight those sources found at a significance of > 3.00; the red circles are those sources with S/N > 4.00, the blue circles those sources with $3.50 <$ S/N < 3.99, and the green circles those detections with $3.00 <$ S/N < 3.49. The labelling corresponds to the numbers in Table 5.9.

5.2 Clustering of the bright (> 5 mJy) SCUBA population

5.2.1 Angular correlation functions

In Chapter 4, a 2-point angular correlation analysis performed on the "SCUBA 8 mJy Survey" fields yielded the first tentative indications of strong clustering amongst the bright SCUBA population, but was limited by the small number of significant sources. Here, the analysis has been extended to include bright SCUBA sources identified significantly in this re-reduction of the other blank field surveys, such that the master catalogue contains detections from approximately double the area of sky of the "8 mJy Survey" alone. Mock catalogues were generated in the same manner as before, with the number of fake objects contained in each field's random catalogue chosen to be directly proportional to the area of the image (number in mock catalogue = $0.01 \times$ Area(/arcsec^2)), so as to reflect a uniform number density across the sky. The wider area fields which dominate this analysis are still largely signal-to-noise limited at these flux densities, and hence there is an increasing probability of finding significant detections in deeper regions of the maps. This was accounted for as before, by splitting the map into sub-images, each containing a quantity of fake detections weighted by the mean noise but allowed random positions according to a Poisson distribution within the sub-map. Detections lying in non-uniform regions of the maps in both the real and fake catalogues were omitted from the correlation function calculations, and positions falling on locations of negative sidelobes in the real data were masked. The angular correlation function was again calculated using the expression

$$\mathrm{w}(\theta) = \frac{(\mathrm{DD} - 2\mathrm{DR} + \mathrm{RR})}{\mathrm{RR}} \tag{5.1}$$

Although combining all existing blank field survey data together does increase the number of sources on which a correlation function can be based, the numbers are still fairly small. Above a signal-to-noise ratio of 3.50, there are a total of 53 sources detected brighter than 5 mJy, of which 51 may be used in a correlation function analysis (the other 2 are lone sources in two of the deep single SCUBA pointing fields). This number increases to 104 sources brighter than 5 mJy at $> 3.00\sigma$, of which 100 may be used in a correlation function analysis. However, this will also increase the contribution from spurious sources in the catalogue and may therefore dilute the measured signal. Figures 5.10 and 5.11 show the

directly measured angular correlation data points for detections brighter than 5 mJy, with 1σ Poisson error bars, and for signal-to-noise thresholds of > 3.50 and > 3.00 respectively. The bin-size used in both plots is 29 arcseconds (twice the beam-size). Rather surprisingly, there is little change in the proportion of excess pairs between corresponding data points in the first 100 arcseconds of the two plots. The Gaussian-convolved noise images did not imply that there was anything unusual about the survey data in regions of higher than average 3.00σ source density, indicating that elevated noise where there is a concentration of significant detections is unlikely to be the cause. There are two likely explanations as to why the signal from the $> 3.50\sigma$ catalogue is not diluted in the $> 3.00\sigma$ plot. Firstly, the simulation results in Chapter 3, which made estimates of the fraction of spurious / confused sources at various signal-to-noise thresholds, have been pessimistic. It is difficult to generate accurate realisations of the SCUBA maps on which to make estimates of contamination in a source catalogue due to confusion and noise without knowing the clustering properties of the SCUBA population in the first place, and the fact that there is very little difference in the proportion of excess pairs on scales of ~ 1 arcminute between the two signal-to-noise datasets may be suggesting that most of the $3.00 - 3.49\sigma$ sources are real. Perhaps a more likely scenario, however, is that the clustering properties of the SCUBA population are strong over a significant range of flux densities, and thus detections arising from the confusion of faint objects are more likely to be found on the same scale and in the vicinity of the real bright SCUBA sources. The major difference between the > 3.00 and $> 3.50\sigma$ plots is the size of the Poisson error bars. As one might expect, the error bars are a factor of $\sim \sqrt{2}$ smaller in Figure 5.11, reflecting the increase by a factor of 2 of the number of sources considered, increasing the significance of the number of excess pairs contained in the first 3 bins (14.5 - 101.5 arcseconds) from 2.5 to 3.7σ.

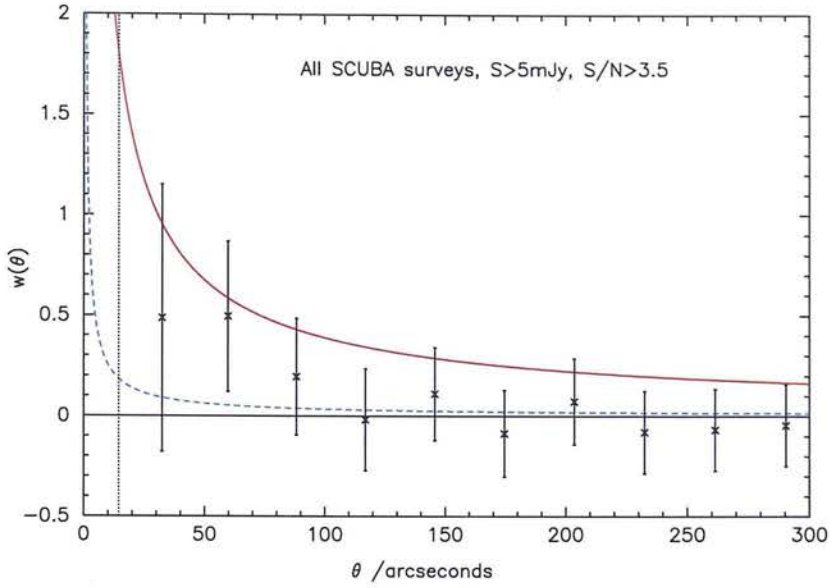

Figure 5.10: 2-point angular correlation function for sources brighter than 5 mJy, detected at a significance of $> 3.50\sigma$, over all of the survey fields. The error bars are 1σ Poisson errors. The red (solid) power-law line indicates the correlation function found by Daddi et al. (2000) for EROs with $R - K > 5$ and $K < 18.5$, and the blue (dashed) power-law line indicates the correlation function found by Giavalisco et al. (1998) for Lyman break galaxies at $z \sim 3$. The vertical dotted line indicates the size of the JCMT beam at 850 μm.

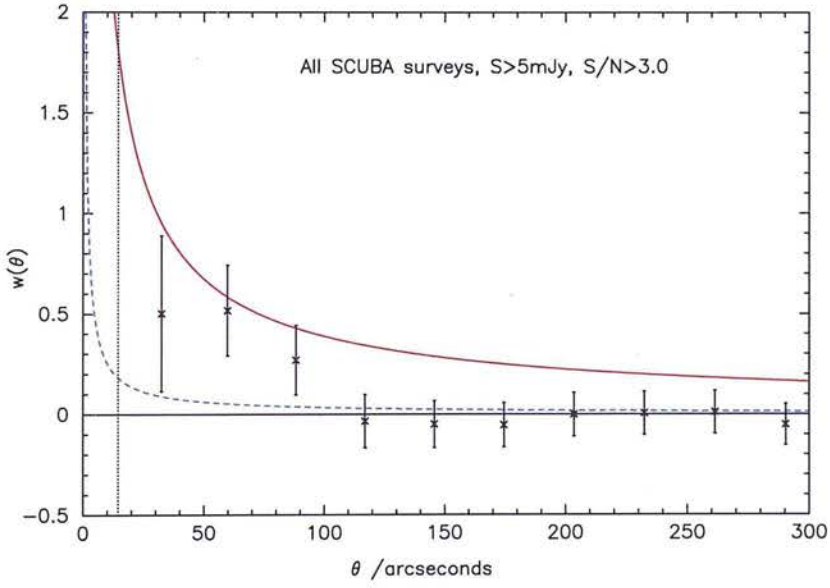

Figure 5.11: 2-point angular correlation function for sources brighter than 5 mJy, detected at a significance of $> 3.00\sigma$, over all of the survey fields. The error bars are 1σ Poisson errors. The red (solid) power-law line indicates the correlation function found by Daddi et al. (2000) for EROs with $R - K > 5$ and $K < 18.5$, and the blue (dashed) power-law line indicates the correlation function found by Giavalisco et al. (1998) for Lyman break galaxies at $z \sim 3$. The vertical dotted line indicates the size of the JCMT beam at 850 μm.

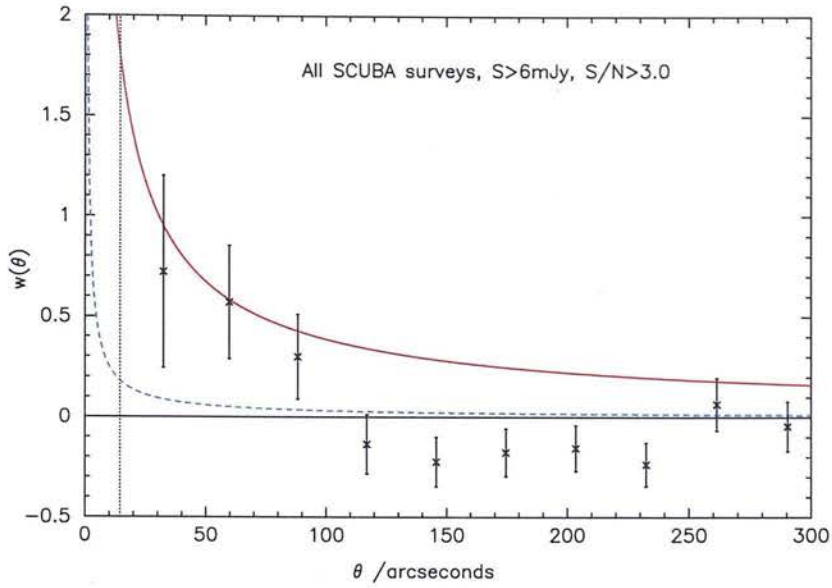

Figure 5.12: 2-point angular correlation function for sources brighter than 6 mJy, detected at a significance of $> 3.00\sigma$, over all of the survey fields. The error bars are 1σ Poisson errors. The red (solid) power-law line indicates the correlation function found by Daddi et al. (2000) for EROs with $R - K > 5$ and $K < 18.5$, and the blue (dashed) power-law line indicates the correlation function found by Giavalisco et al. (1998) for Lyman break galaxies at $z \sim 3$.The vertical dotted line indicates the size of the JCMT beam at 850 μm.

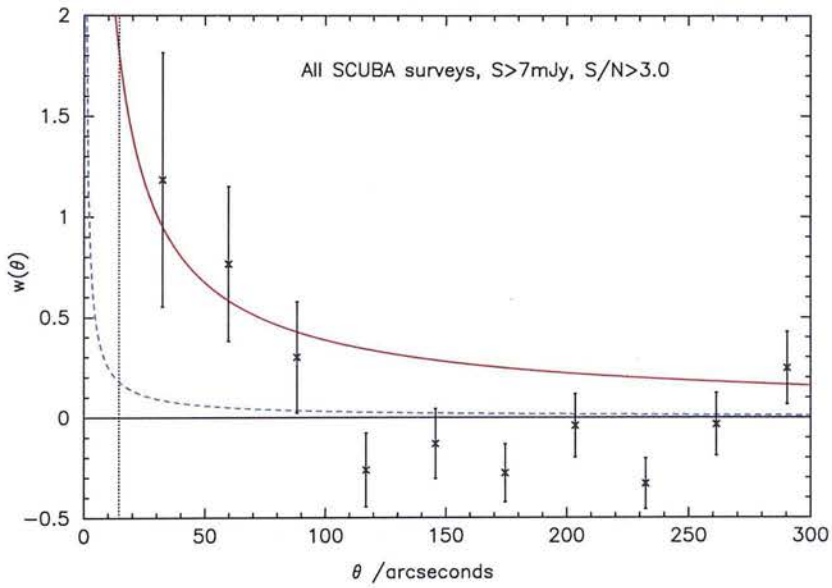

Figure 5.13: 2-point angular correlation function for sources brighter than 7 mJy, detected at a significance of $> 3.00\sigma$, over all of the survey fields. The error bars are 1σ Poisson errors. The red (solid) power-law line indicates the correlation function found by Daddi et al. (2000) for EROs with $R - K > 5$ and $K < 18.5$, and the blue (dashed) power-law line indicates the correlation function found by Giavalisco et al. (1998) for Lyman break galaxies at $z \sim 3$.The vertical dotted line indicates the size of the JCMT beam at 850 μm.

Cutting at higher flux densities decreases the number of sources available for producing a 2-point angular correlation function even further, thus using the smaller "safer" catalogue of sources above a signal-to-noise threshold of 3.50 leads to tentative but non-significant measures of the clustering strength above the noise level. Instead, the analysis has been repeated using the full $> 3.00\sigma$ source lists for flux density cut-offs of > 6 and $> 7\,$mJy shown in Figures 5.12 and 5.13 respectively, pushing the available data to its limits. It should be noted that these flux density thresholds are the raw values as measured directly from the maps and should therefore not be taken as "absolute" because of the boosting effects described in Chapter 3. However, it is fair to say that cutting at $S_{850} > 7\,$mJy defines a set of objects with generally higher star formation rates than cutting at $S_{850} > 5\,$mJy and so Figures 5.11 to 5.12 can still be used to look for any trends in clustering strength with increasing flux density. For comparison, the number of excess pairs within ~ 100 arcseconds of each other in the real data when compared to a random distribution is significant at the 3.3σ level for $S_{850\mu m} > 6\,$mJy, and at the 3.5σ level for $S_{850\mu m} > 7\,$mJy.

For all three flux density limits, the measured correlation functions indicate a clustering strength much larger than that measured by Giavalisco et al. (1998) for Lyman-break galaxies at $z \simeq 3$ (the blue dashed lines in the figures), even given the rather large error bars on the SCUBA data points. Could the apparent difference in clustering strength simply be due to projection effects over redshift space? The Lyman-break technique uses colour selection to identify high-redshift galaxies through multi-band imaging across the 1216Å line and the 912Å Lyman break. At $z > 2.5$ the Lyman limit is redshifted far enough into the optical window to be observable in broad-band ground-based photometry. By placing filters on either side of the redshifted Lyman limit one can find high-redshift objects by their strong spectral breaks. Giavalisco et al. (1998) used a custom photometric system, U_nGR (Steidel & Hamilton 1993) optimized for selecting Lyman-break galaxies with $z \simeq 3$. By the nature of this method, 90% of the galaxies they used were confined to the redshift range $2.6 < z < 3.4$, with none at $z < 2.2$. The redshift range of the bright SCUBA population used in these calculations of angular correlation functions is much more uncertain, but Ivison et al. (2002) have suggested a median redshift of $z = 2.4$ based on the radio-to-submillimetre spectral indices (Carilli & Yun, 1999 & 2000), with inferred redshifts spanning the range of $z \simeq 1 - 4$. Therefore, unless the bright SCUBA population occupies a very much narrower redshift band than implied by the radio-to-submillimetre

spectral indices the dilution of the angular clustering signal by projection over redshift cannot be the reason for the large difference in clustering strength.

Instead, this contrast in clustering properties implies that the Lyman-break galaxies and bright SCUBA sources are sampling two different stages or mass domains in galaxy formation (see also Barger, Cowie & Richards 2000, Webb et al. 2003b). The stronger clustering exhibited by the bright 850 μm sources suggests that these objects are tracing the rarest high-mass peaks of the Gaussian initial density fluctuations and are the progenitors of the most massive ellipticals, whereas the weaker clustering of the Lyman-break galaxies indicates a weaker bias with respect to mass, detecting the formation of smaller disk or bulge systems. The strength of clustering, however, is consistent with that measured by Daddi et al. (2000) for extremely red objects (EROs) with $K < 18.5$ and $R - K > 5$ (the red solid lines in the figures), perhaps suggesting an evolutionary sequence from SCUBA source to ERO. The numerical coincidence between the co-moving number densities of EROs and that estimated for bright SCUBA sources is also in line with this idea (Chapter 4).

Attempts have been made to fit a standard power-law describing the angular correlation function to the data points shown in Figures 5.10 to 5.13. The fit is slightly complicated by the fact that the global number density is unknown and must be estimated from the sample to hand. Hence,

$$(1 + \mathrm{w_{true}}(\theta)) = (1 + \mathrm{w_{obs}}(\theta)) \left(\frac{\bar{\mathrm{n}}}{< \mathrm{n} >}\right)^2 \tag{5.2}$$

where $\mathrm{w}(\theta)_{\mathrm{true}}$ is the true correlation function, $\mathrm{w}(\theta)_{\mathrm{obs}}$ is the observed correlation function, $\bar{\mathrm{n}}$ is the mean number density of sources and $< \mathrm{n} >$ is the global number density of sources. One can rewrite the observed mean number density $\bar{\mathrm{n}}$ in terms of a pertubation δn on the global number density $< \mathrm{n} >$ (ie. $\bar{\mathrm{n}} =< \mathrm{n} > \pm \delta \mathrm{n}$), such that in averaging over a set of sky areas the size of the sample

$$(1 + \mathrm{w_{true}}(\theta)) = (1 + \mathrm{w_{obs}}(\theta))(1 + \sigma^2) \tag{5.3}$$

where σ^2 is the rms surface density variation. The final effect is very nearly to subtract a constant from $\mathrm{w_{true}}(\theta)$ when plotting the observed 2-point angular correlation function. If the real correlation functions take the power-law form $\mathrm{w_{true}}(\theta) = \mathrm{A}\theta^{-\delta}$ and one rewrites the integral constraint in terms of the amplitude multiplied by a constant (ie. $\sigma^2 = \mathrm{A} \times \mathrm{C}$), then

$$\mathrm{w_{obs}}(\theta) = \frac{\mathrm{A}(\theta^{-\delta} - \mathrm{C})}{(1 + \mathrm{AC})} \tag{5.4}$$

One can then either determine the values of A, δ and C by allowing them all to be free parameters in a minimised χ^2 fit, or alternatively one can estimate the integral constraint by doubly integrating an assumed true $w(\theta)$ over the field area Ω,

$$AC = \frac{1}{\Omega^2} \int \int w(\theta) d\Omega_1 d\Omega_2 \tag{5.5}$$

This can be done numerically using the random-random correlation, such that

$$C = \frac{\sum N_{rr}(\theta)\theta^{-\delta}}{\sum N_{rr}(\theta)} \tag{5.6}$$

Both of these methods have been attempted for all four sets of data points. However, the large error bars and scatter in the data points beyond the first 3 fairly robust data point measurements (out to $\sim$ 100 arcseconds) means that these combined observations are insufficient with which to obtain a meaningful fit. The indication is certainly that the bright SCUBA population does strongly cluster on scales of a few arcmin, but a much larger SCUBA survey, approaching 0.5 square degrees (4 times the area covered here) is required to obtain a meaningful measure of the correlation power-law slope and scale length.

5.2.2 Nearest-neighbour analyses

An alternative method for measuring the strength of clustering is a nearest-neighbour analysis. This procedure measures the distribution of the separations between each source and its closest neighbour as compared to what one would expect from a random distribution, and is sometimes more informative in deciding whether sources are clustered when dealing with small datasets like these.

The nearest-neighbour distributions for the bright SCUBA sources were measured from the S/N > 3.00 datasets, for flux density thresholds of $S_{850} > 5$, > 6, and > 7 mJy as measured directly from the raw maps (i.e. no corrections for flux-boosting effects have been applied). One can readily weight any uncharacteristically deep areas of an image for calculating a 2-point angular correlation function by creating a large mock catalogue of randomly positioned sources, equivalent to a combined catalogue from conducting many simulations, but which has the local number density of detections in any given region weighted according to the number counts and the noise (see Chapter 4). A nearest neighbour distribution, however, requires mock images with the same source number density as the actual survey fields. In this analysis 100 mock catalogues for each individual field were

generated, the positions allocated randomly according to a Poisson distribution and constrained to lie within the boundaries of the original survey data. This was done separately for the three flux density thresholds, each fake source list containing the same number of $> 3.00\sigma$ sources as the real image. Histograms of the number of nearest neighbours against nearest-neighbour separation are shown in Figures 5.14, 5.15 and 5.16 for flux density cut-offs of 5, 6 and 7 mJy respectively, using bins the size of the SCUBA beam (14.5 arcseconds). The histograms of the real nearest-neighbour distributions are shown by red (solid) lines, and the distributions from combining the mock source catalogues are illustrated by the blue (dashed) lines, normalised according to the total number of real source pairings.

In all three plots there is a clear excess of bright 850 μm sources separated from their nearest neighbour at $\sim$ 50 arcsec. This is most noticeable in the $S_{850} > 7$ mJy histogram (Figure 5.16) where there are 51 nearest neighbour pairs compared to 36 expected within the first $\sim$ 100 arcseconds (a statistical excess at the 2.5σ level), and 34 nearest-neighbour pairs compared to 16 expected within the first $\sim$ 50 arcseconds (a statistical excess at the 4.5σ level).

A Kolmogorov-Smirnov test is a simple method for testing the probability that two distributions are identical. The test statistic, D, is defined as the maximum absolute difference between an observed (S_o) and an expected (S_e) normalised cumulative distribution, in this case applied to the cumulative fraction of nearest-neighbour pairs with angular separation:

$$D = \max |S_o(\theta) - S_e(\theta)| \tag{5.7}$$

If the measured D value exceeds a critical value when compared to the known sampling distribution for D appropriate to the number of data points, then the two distributions may be rejected as being the same at that level of significance.

As shown in Table 5.10, the distributions of $> 3.00\sigma$ sources brighter than > 5 and > 6 mJy were rejected as being consistent with a random distribution at the 95% confidence level, and the sources brighter than > 7 mJy were inconsistent with a random distribution at better than the 99% confidence level. Overall this again suggests that the bright SCUBA population are strongly clustered on scales of ~ 1 arcmin.

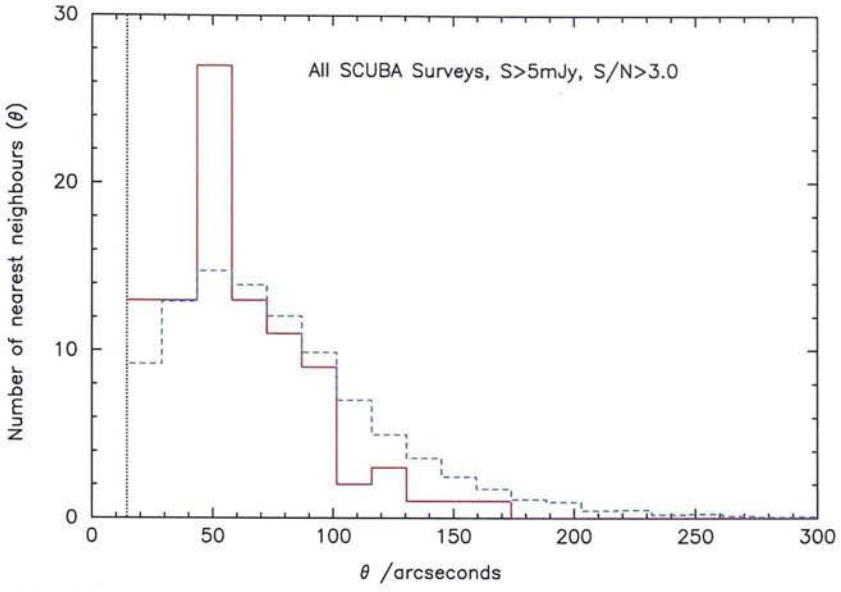

Figure 5.14: Nearest-neighbour analysis for sources brighter than 5 mJy, detected at a significance of $> 3.00\sigma$ over all of the survey fields.The vertical dotted line indicates the size of the JCMT beam at 850 μm. The red (solid) line shows the distribution of nearest-neighbour pairs for the actual dataset, whereas the blue (dashed) line shows the expected nearest-neighbour histogram for the same surface density of sources when distributed randomly. The probability that the two distributions are the same is < 0.05.

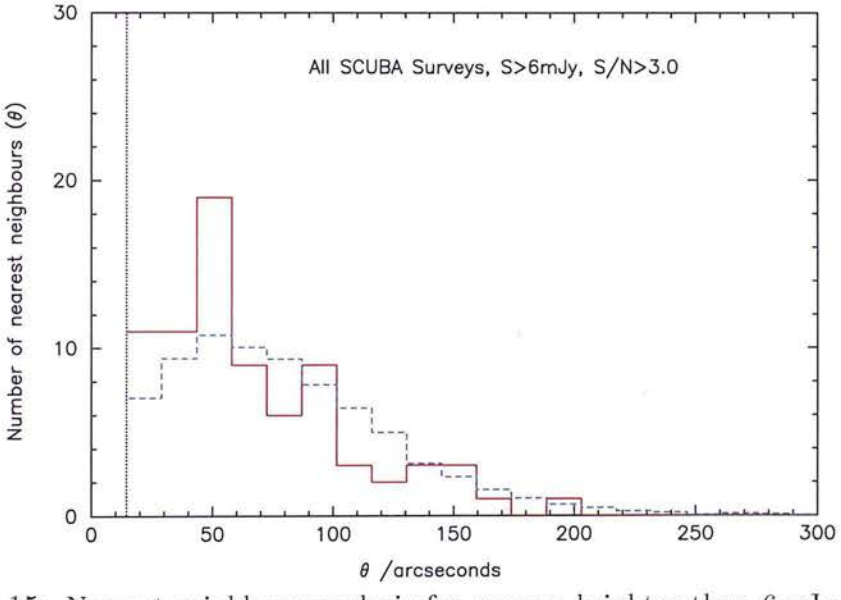

Figure 5.15: Nearest-neighbour analysis for sources brighter than 6 mJy, detected at a significance of $> 3.00\sigma$ over all of the survey fields.The vertical dotted line indicates the size of the JCMT beam at 850 μm. The red (solid) line shows the distribution of nearest-neighbour pairs for the actual dataset, whereas the blue (dashed) line shows the expected nearest-neighbour histogram for the same surface density of sources when distributed randomly. The probability that the two distributions are the same is < 0.05.

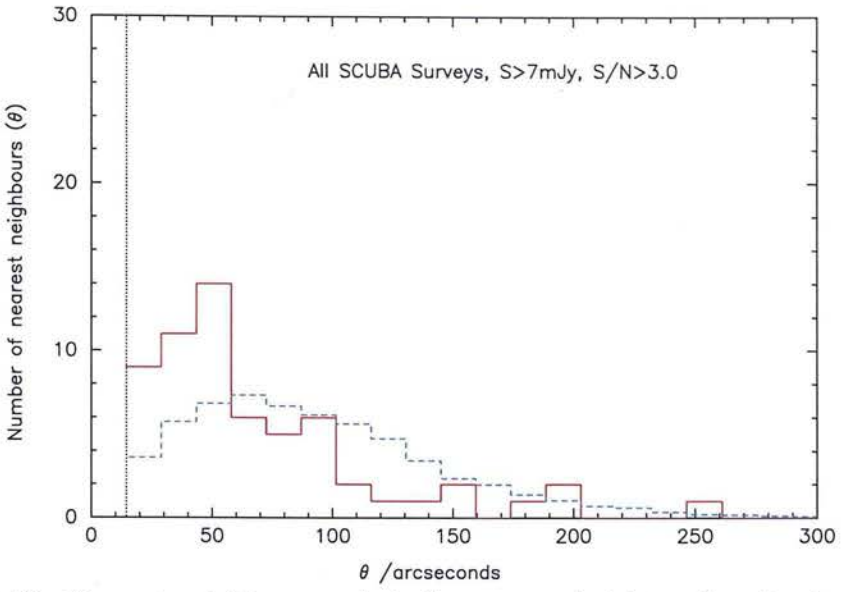

Figure 5.16: Nearest-neighbour analysis for sources brighter than 7 mJy, detected at a significance of $> 3.00\sigma$ over all of the survey fields.The vertical dotted line indicates the size of the JCMT beam at 850 μm. The red (solid) line shows the distribution of nearest-neighbour pairs for the actual dataset, whereas the blue (dashed) line shows the expected nearest-neighbour histogram for the same surface density of sources when distributed randomly. The probability that the two distributions are the same is < 0.01.

Flux density threshold	D	θ_D /arcsec	Number sources	P(D)
> 5 mJy	0.1587	82.6	100	< 0.05
> 6 mJy	0.1659	65.5	78	< 0.05
> 7 mJy	0.2898	65.5	61	< 0.01

Table 5.10: Results of applying a Kolmogorov-Smirnov test to the cumulative fraction of nearest-neighbour pairs. Column 1 gives the flux density cutoff as measured from the raw images. Column 2 gives the maximum absolute difference between the observed and expected normalised cumulative distributions, D, and the nearest-neighbour separation at which this occurs is given in Column 3. Column 4 gives the probability that the two distributions are the same.

5.3 Combined Number Counts

As discussed in Chapter 4, the cumulative number counts differ quite markedly between the various surveys at bright flux densities ($> 5\,\mathrm{mJy}$). This is not surprising given the small area of sky observed by each individual survey and the low number density of bright sources, particularly given the evidence presented in Sections 5.2.1 and 5.2.2 implying that the bright SCUBA population has a tendency to cluster strongly on arcmin scales. Here, the sources detected with a signal-to-noise ratio > 3.50 from my reanalysis of the CUDSS, Hawaii and HDF surveys have been combined with those identified in the 8 mJy Survey, to produce the most accurate number counts to date, from $2 - 12.5\,\mathrm{mJy}$ at $0.5\,\mathrm{mJy}$ intervals. The regions of non-uniform noise towards the edge of the maps and any sources they contained were excluded. The simulations described in Section 3.2 were used to correct for the effects of flux-density boosting and incompleteness on a field by field basis, in the same way as applied to the 8 mJy Survey number counts. Estimating the level of contamination from spurious / confused sources, however, requires the generation of fully simulated images. The accuracy of such images is hampered by the lack of knowledge regarding the clustering properties of the SCUBA population down to the faintest flux density levels. The approach taken is fully described in Section 3.3 and summarised in brief here. The best fit source counts model to the incompleteness and boosting corrected data was used to determine the number of sources observed at 0.1 mJy levels, assuming that *all* of the raw $> 3.50\sigma$ detection were real. Each of these sources was positioned randomly according to a Poisson distribution i.e. assuming no clustering. Applying the simultaneous maximum-likelihood source-extraction algorithm to the fully simulated maps, the fraction of spurious / confused sources (defined as having no input source at least half as bright as the output flux density) at a significance of $> 3.50\sigma$ was found to be about 30%. This number is in line with the upper limit placed on the confused / spurious fraction from deep radio follow-up of the "8 mJy Survey" fields. The raw and corrected cumulative number counts are given in Table 5.11 along with 1σ Poisson error bars (calculated from the square root of the number of detections on which the source count was based). The estimated 30% fraction of spurious / confused sources has been combined in quadrature with the lower Poisson error bar in the corrected number counts.

Flux density /mJy	Raw 850 μm source counts $N(>S)\mathrm{deg}^{-2}$	Corrected 850 μm source counts $N(>S)\mathrm{deg}^{-2}$
2.0	2880 ± 310	$3920^{+\ 550}_{-1120}$
2.5	1680 ± 180	$2140^{+\ 320}_{-\ 620}$
3.0	1080 ± 120	$1250^{+\ 200}_{-\ 370}$
3.5	830 ± 100	$680^{+\ 120}_{-\ 200}$
4.0	700 ± 90	$620^{+\ 110}_{-\ 190}$
4.5	700 ± 90	$490^{+\ 90}_{-\ 150}$
5.0	540 ± 70	$380^{+\ 70}_{-\ 120}$
5.5	500 ± 70	$330^{+\ 70}_{-\ 110}$
6.0	420 ± 60	$310^{+\ 60}_{-\ 100}$
6.5	340 ± 60	$230^{+\ 50}_{-\ 80}$
7.0	300 ± 50	$180^{+\ 50}_{-\ 60}$
7.5	260 ± 50	$180^{+\ 50}_{-\ 60}$
8.0	210 ± 40	$150^{+\ 40}_{-\ 60}$
8.5	160 ± 40	$100^{+\ 30}_{-\ 40}$
9.0	130 ± 30	$70^{+\ 30}_{-\ 30}$
9.5	90 ± 30	$60^{+\ 30}_{-\ 30}$
10.0	70 ± 20	$40^{+\ 20}_{-\ 20}$
10.5	60 ± 20	$20^{+\ 10}_{-\ 10}$
11.0	30 ± 20	$10^{+\ 10}_{-\ 10}$
11.5	20 ± 10	$10^{+\ 10}_{-\ 10}$
12.0	20 ± 10	$10^{+\ 10}_{-\ 10}$
12.5	10 ± 10	$10^{+\ 10}_{-\ 10}$

Table 5.11: The 850 μm source counts per square degree based on sources with S/N > 3.50 in all of the survey maps, and excluding those detected in the non-uniform noise regions. Column 1 gives the flux density and column 2 the cumulative raw counts per square degree with the Poisson error. Column 3 gives the cumulative corrected counts per square degree, the upper error corresponding to the Poisson error, and the lower error accounting for both the Poisson error and the presence of spurious sources based on the simulation data.

Figure 5.17 shows the corrected versus the raw number counts at each flux density, together with a dotted line marking the locus of where the raw and corrected counts take the same value. An increase in the cumulative number counts along either axis correponds to a decrease in the flux density threshold. One can see immediately that at brighter flux densities, the effect of boosting is stronger than incompleteness and hence the real number density of sources above a specified flux density threshold is lower than the directly measured value. This may also be implied from an examination of the raw data alone. The area of sky mapped in the "SCUBA 8 mJy Survey" is almost identical to the area of sky mapped by the other deeper surveys combined. At bright flux densities

the deeper surveys are essentially complete and so one can compare the number of detections above a specified signal-to-noise ratio and flux density threshold between the shallower and deeper maps. For a retrieved $S_{850\mu m} > 10\,mJy$ and $S/N > 3.50$, the "SCUBA 8 mJy Survey" identified 8 sources, whereas in all the other surveys only 1 source was found to satisfy this criteria. Similarly, for a retrieved $S_{850\mu m} > 8\,mJy$ and $S/N > 3.50$, the "SCUBA 8 mJy Survey" identified 20 objects, whereas only a total of 5 were found in the other surveys. Given the small area of sky considered, part of the discrepancy between the number of bright sources recovered in the "SCUBA 8 mJy Survey" and the other deeper blank field surveys can be explained by small number statistics but it seems highly unlikely that this is the sole cause. Moving towards fainter flux density thresholds, the increased source density makes incompleteness more of a problem and around the confusion limit of $\sim 3\,mJy$ (where the density of sources is c. 1000 per square degree) the raw and corrected cumulative number counts are approximately the same.

One of the simplest ways of describing the number counts is by carrying out a simple parametric fit of a power-law model to the differential number counts as a function of flux density. The differential number counts at a specific flux density were determined by the difference in cumulative counts between the two values on either side of the data point, divided by the change in flux density, which approximates to a measure of the gradient of a tangent to the cumulative number counts curve at that point. The completeness and boosting corrected number counts were used for this procedure. Following Barger, Cowie & Sanders (1999), a model of the form

$$n(S) = \frac{dN(S)}{dS} = \frac{N_0}{(a + S^{\alpha})} \tag{5.8}$$

was fitted to the data points by means of a minimised χ^2 method, where the values of N_0, a and α were allowed to vary freely. The best fit values for these parameters were $N_0 = 2.67 \times 10^4$, $a = 0.49$ and $\alpha = 3.14$, predicting a total 850 μm background of $3.8 \times 10^4\,mJy\,deg^{-2}$, mid-way between the 850 μm extragalactic values of $3.1 \times 10^4\,mJy\,deg^{-2}$ and $4.4 \times 10^4\,mJy\,deg^{-2}$ as measured from COBE-FIRAS by Puget et al. (1996) and Fixsen et al. (1998) for the lower and upper values respectively. The values of the fitted parameters are in fact very close to the values originally determined by Barger, Cowie & Sanders (1999) who found $N_0 = 3.0 \times 10^4$, $a = 0.5$ and $\alpha = 3.2$. Figure 5.18 shows a plot of the differential number counts against flux density. The solid diamonds represent data from

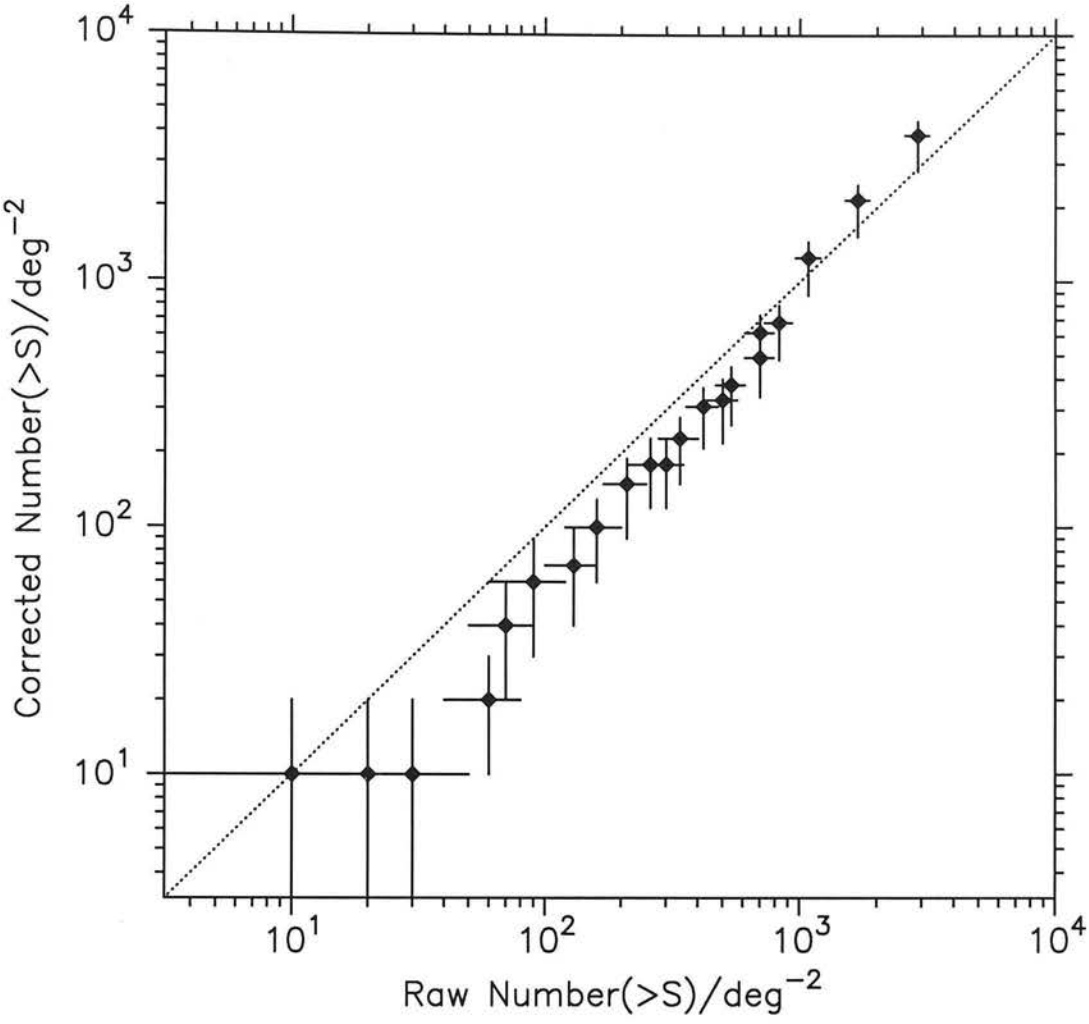

Figure 5.17: Cumulative number counts corrected for the effects of boosting and incompleteness versus the raw number counts. The dotted line marks the case where the raw and corrected cumulative numbers counts are the same. The error bars are as given in Table 5.11.

the combined blank field survey re-analysis only, with 1σ Poisson error bars on the y-axis and a flux density range of 1 mJy on the x-axis, corresponding to the change in flux density between the two data points on either side of the point at which the differential counts has been determined. The open triangles represent data points from the lensing surveys of Blain et al. 1999 and Cowie et al. 2002, and the solid curve is the best fit parametric model. Figures 5.19 and 5.20 show the corrected cumulative number counts, as well as a series of models predicting the 850 μm source counts for an $\Omega_{\rm M} = 0.3$, $\Omega_\Lambda = 0.7$ and an Einstein-de-Sitter cosmology respectively. The black lines are parameterised models, the solid lines following a simple power-law description of the data points and are the same for both figures. The dashed lines represent work by Rowan-Robinson (2000) who

generated best-fit models of the measured far-infrared through to submillimetre number counts, as constrained by the extragalactic background, for a number of assumed cosmologies. In the remaining models (red, blue and green curves), values of dust temperature T_d and emissivity index β based on optically thin greybody emission, were allowed to vary where necessary so that as good a fit as possible could be obtained for the $\Omega_M = 0.3$, $\Omega_\Lambda = 0.7$ cosmology. The correponding models using the same dust temperature and emissivity index are plotted in Figure 5.20 using an Einstein-de-Sitter cosmology, allowing for a direct comparison of the effect of cosmological parameters - no attempt at best fitting these models has been attempted in the latter cumulative counts plot.

The solid black line on both cumulative counts figures is the integrated dN/dS best-fit parametric model given in equation 5.8, providing a good description of the cumulative number counts for $S_{850} < 10\,\mathrm{mJy}$.

Rowan-Robinson (2001) has also taken a parameterised approach to modelling the infrared through to submillimetre counts and backgrounds, in this case by using multiwavelength observational data in these wavelength regimes to place constraints on models made up of four spectral components: infrared cirrus, an M82-like starburst, an Arp220-like starburst and an AGN torus. The model assumes that the evolution of the star formation rate manifests itself as pure luminosity evolution. The models, consistent with infrared and submillimetre counts and backgrounds, showed a flat star formation rate from $z = 1 - 3$, in agreement with other studies of the star formation history such as the HDF (Hughes et al. 1998). The most striking difference between other modelling work and Rowan-Robinson (2001) is the dominant role of the cirrus component at submillimetre wavelengths. The black dashed lines in Figures 5.19 and 5.20 show the best-fit models for the 850 μm counts, for an $\Omega_M = 0.3$, $\Omega_\Lambda = 0.7$ and an Einstein-de-Sitter cosmology respectively. These models appear to be the best-fit of those presented here to the data points over the whole flux density range for either of the assumed cosmologies.

The red lines on the two figures represent a pure luminosity evolution of the form $(1+z)^3$ out to a threshold redshift, and constant thereafter. The solid lines began with the 60 μm luminosity function of Saunders et al. (1990), interpolated to 850 μm assuming an optically thin greybody with a single dust temperature and emissivity index, to describe the far-infrared / submm dust SED. The same values for T_d and β were assumed in calculating the K-correction for consistency. The dashed lines began with the 850 μm luminosity function measured by Dunne et al.

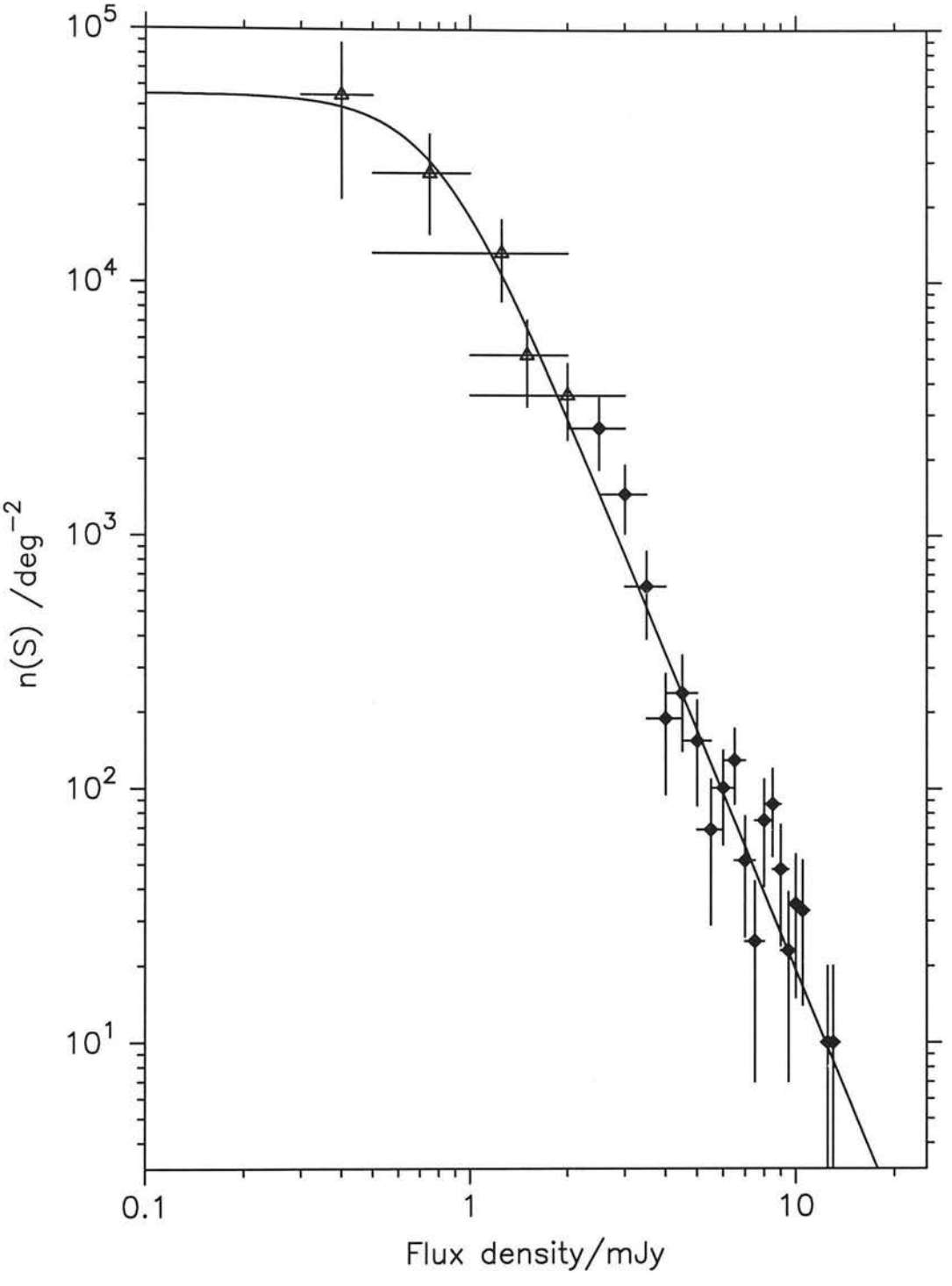

Figure 5.18: A plot of differential number counts vs. flux density. The solid diamonds represent data from the combined blank field survey re-analysis only, with 1σ Poisson error bars on the y-axis, and the flux density range on which the differential count is based marked as an error bar on the x-axis. The open triangles represent data points from the lensing surveys of Blain et al. (1999) and Cowie et al. (2002). The solid curve is a best fit parametric model of the form $n(s) = \frac{N_0}{(a+S^\alpha)}$.

(2000a). A dust temperature of 40 K and emissivity index of $\beta = 1.3$ appeared to best satisfy the data points, using threshold redshifts of $z = 2.0$ and $z = 1.5$ for the Saunders et al. (1990) and Dunne et al. (2000a) based luminosity functions respectively. Using the $\Omega_M = 0.3$, $\Omega_\Lambda = 0.7$ comology, this simple description of luminosity evolution appeared to work well for the interpolated Saunders et al. (1990) 60 μm luminosity function for $S_{850} < 8$ mJy, but predicted too many sources brighter than this. Conversely, using the Dunne et al. (2000a) 850 μm luminosity function, a good fit to the data points was found for $S_{850} > 2$ mJy but overpredicted the number of sources fainter than this by a factor of 2-3.

The solid and dashed blue lines on the source counts plots also assume pure luminosity evolution of the interpolated 60 μm Saunders et al. (1990) and directly measured 850 μm Dunne et al. (2000a) luminosity functions respectively. In this case, however, the luminosity evolution $g(z)$ takes a more realistic form, which is fully compatible with models of cosmic chemical evolution and naturally includes a peak in the evolution function (Jameson et al. 1999, Smail et al. 2002):

$$g(z) = (1+z)^{3/2}\mathrm{sech}^2[b\ln(1+z) - c]\cosh^2 c \qquad (5.9)$$

where best fits values for the parameters b and c based on multiwavelength far-infrared to submillimetre counts and constraints on the probable redshift distribution of the 850 μm population (Smail et al. 2002) are $b = 2.2 \pm 0.1$ and $c = 1.84 \pm 0.1$. Using the $\Omega_M = 0.3$, $\Omega_\Lambda = 0.7$ comology, the interpolated 60 μm luminosity function combined with this description of pure luminosity function fits the data well for $S_{850} < 8$ mJy assuming an optically thin greybody description of the thermal dust emission with parameters $T_d = 39$ K and $\beta = 1.3$. The data points across the whole flux density range are fitted well using the Dunne et al. (2000a) 850 μm luminosity function assuming dust emission parameters of $T_d = 30$ K and $\beta = 1.0$, although it should be noted that this combination of dust temperature and emissivity index does not describe the spectral energy distribution well for any known local galaxies based on the "SCUBA Local Universe Galaxy Survey (SLUGS)" (Dunne et al. 2000a).

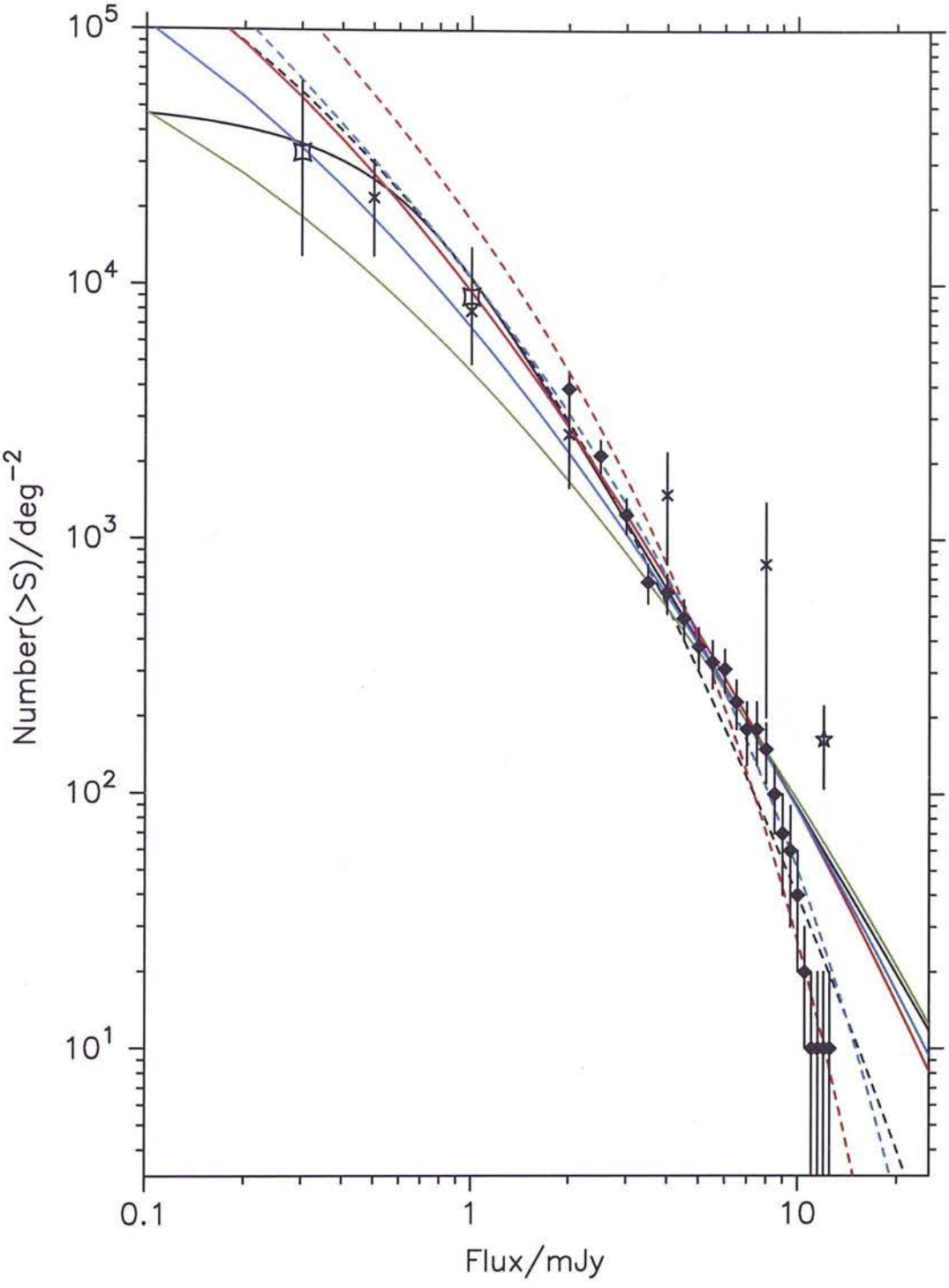

Figure 5.19: A plot of cumulative number counts vs. flux density, along with a series of models assuming an $\Omega_M = 0.3$, $\Omega_\Lambda = 0.7$ cosmology. The solid diamonds represent the cumulative source counts from the completeness and boosting corrected counts derived from the combined blank field survey re-analysis only, with error bars as given in Table 5.11. The crosses and round-edged squares represent data points from the lensing surveys of Blain et al. (1999) and Cowie et al. (2002) respectively, and the star is from Borys et al. (2002). The various models are described in the main text.

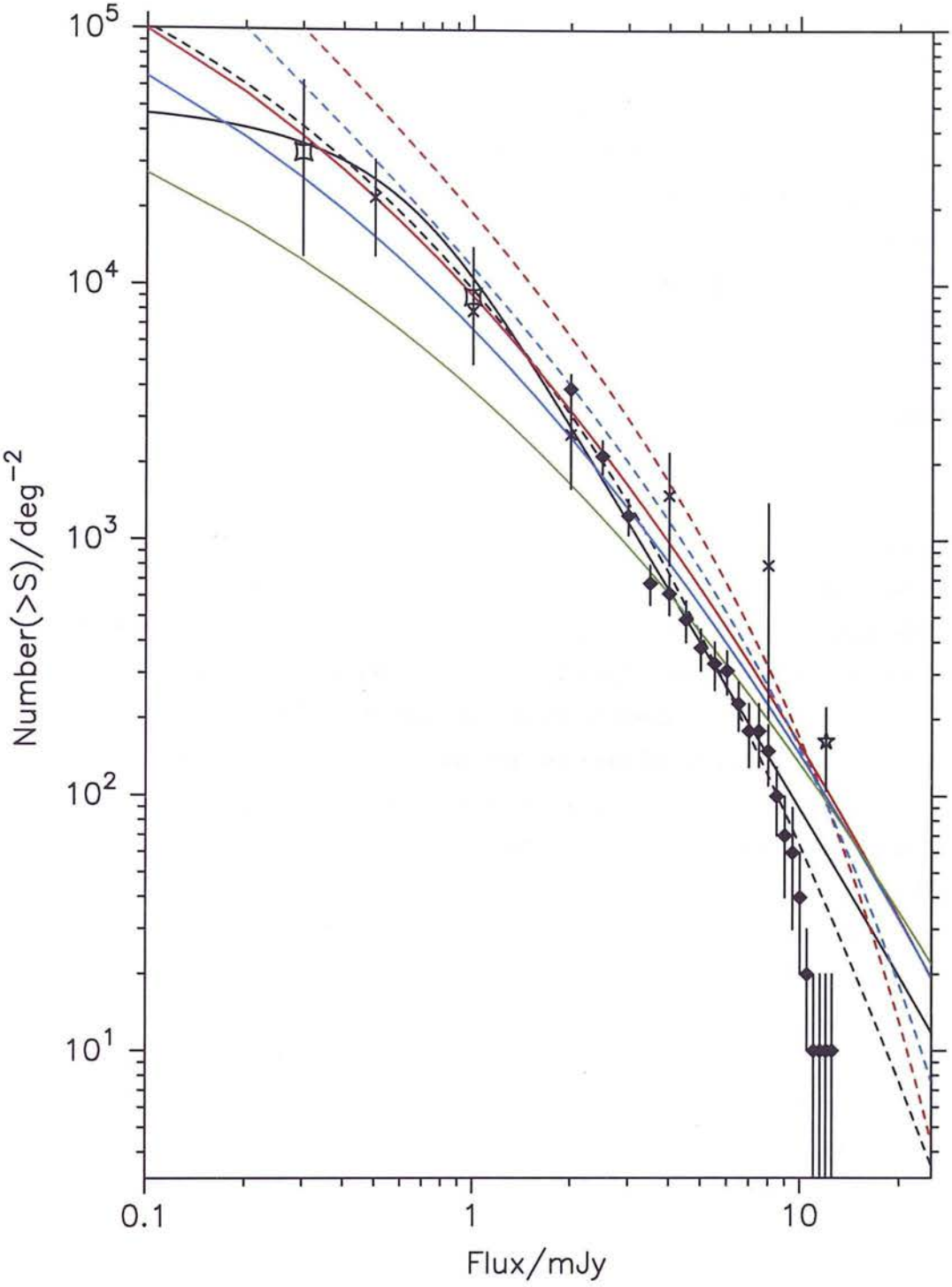

Figure 5.20: A plot of cumulative number counts vs. flux density, along with a series of models assuming an $\Omega_M = 1.0$, $\Omega_\Lambda = 0.0$ cosmology. The solid diamonds represent the cumulative source counts from the completeness and boosting corrected counts derived from the combined blank field survey re-analysis only, with error bars as given in Table 5.11. The crosses and round-edged squares represent data points from the lensing surveys of Blain et al. (1999) and Cowie et al. (2002) respectively, and the star is from Borys et al. (2002). The various models are described in the main text.

The solid green line on both cumulative number counts figures, uses the 60 μm luminosity function of Saunders et al. (1990) combined with luminosity evolution taking the form $(1+z)^4$ up to a threshold redshift $z_{\rm thresh}$, and $(1+z)^{-4}$ thereafter (Chapman et al. 2002a). They find a best fit of $z_{\rm thresh} = 2.6$ for the transitional redshift, based on current constraints on the redshift distribution as well as the source counts. This particular 850 μm counts model has a rather shallower gradient than the others and could only be made to match number counts of this combined re-analysis over the flux density range $\sim 3-7$ mJy for $T_d = 36$ K and a very extreme $\beta = 2.0$ for an $\Omega_M = 0.3$, $\Omega_\Lambda = 0.7$ cosmology. Possibly a higher value of the dust emissivity index could produce a steeper counts model, however, such high values are not observed in in any known class of objects. No satisfactory fit could be obtained beginning with the Dunne et al. (2000a) 850 μm luminosity function. The proposed Chapman et al. (2002a) luminosity evolution does not seem consistent with the blank field survey source counts, although the number counts derived from the lensing survey of Blain et al. 1999 are much shallower, predicting rather higher number densities of bright sources, and could plausibly be fit by this scenario for less extreme values of beta.

In comparing the two figures, one can see that by using an Einstein-de-Sitter cosmology rather than a non-zero Λ-cosmology, keeping all other parameters the same, the predicted number counts are both higher for a given flux-density threshold, and decrease at a slower rate on increasing to higher flux-density cutoffs. The higher overall number counts arise due to the fact that an object of fixed intrinsic luminosity placed at increasing redshifts will appear brighter at 850 μm in an Einstein-de-Sitter cosmology (see Figure 1.2 in the Introduction). The more gentle source counts gradient arises due to an object of fixed intrinsic luminosity experiencing a stronger negative K-correction in an $\Omega_M = 1.0$, $\Omega_\Lambda = 0.0$ cosmology such that it actually appears slightly brighter at 850 μm with increasing redshift beyond $z > 1$, whereas the reverse is true in an $\Omega_M = 0.3$, $\Omega_\Lambda = 0.7$ cosmology.

One particularly interesting feature of this source counts re-analysis is the apparent steepening of the cumulative number counts beyond $S_{850} > 8$ mJy. This could at least in part be due to small number statistics of the brightest sources, however, if real has some important implications. Firstly, it could indicate an intrinsic turn-over in the underlying luminosity function. In turn, this would suggest a very interesting upper limit on the luminosity of a high redshift galaxy, perhaps reflecting an upper limit on the overall mass of the system. This could

place useful constraints on galaxy formation theories. Secondly, a steepening of the source counts could make the SCUBA population much more prone to the effects of gravitational lensing. For weak lensing scenarios, the ratio of the number of observed sources brighter than a flux density threshold to the true number of sources brighter than that flux density threshold is given by

$$\frac{N_{obs}(>S)}{N_{true}(>S)} = \mu^{\gamma-1} \tag{5.10}$$

where μ is the magnification amplitude and γ is the slope of the cumulative source counts. For $1 < S_{850} < 8\,mJy$ the counts slope $\gamma \simeq 2.5$, whereas for $S_{850} > 8\,mJy$ this increases to $\gamma \simeq 5.5$. No attempt has been made to correct the $850\,\mu m$ source counts for the effects of lensing, but there is some evidence to suggest that some blank field sources have been gravitationally lensed. Almaini et al. (2003) found a strong cross-correlation in the ELAIS N2 field between the distribution of SCUBA and Chandra sources even though the coincidence of detections in the submillimetre and X-ray wavelengths was only $\sim 5\%$. One proposed explanation for this effect is that the SCUBA and Chandra sources trace the same large scale structure at high redshift ($z > 1$), however, there also appears to be a similarly strong cross-correlation between the low redshift $I-$band sources and the higher redshift SCUBA and Chandra sources in this field (Almaini et al. in prep) suggesting an alternative explanation may be valid: the SCUBA and Chandra detections may have been magnified in certain regions of the field by the presence of high mass density structure, as traced by the $I-$band imaging, at $z \simeq 0.5$. Chapman et al. (2002b) have also pointed out that some submillimetre sources have apparent counterparts which are optically bright galaxies, $I < 21.5$, lying at modest redshifts, $z < 1$. This could of course be explained by these counterparts being correct, reflecting a population of galaxies which are detected as very cold, luminous submillimetre sources, however, a second explanation for such systems is that the optically bright galaxy is a foreground object acting as a gravitational lens, amplifying the more distant SCUBA galaxy. The detection of luminous molecular CO emission at the redshift of the optically bright galaxy would provide a powerful test to distinguish between these two scenarios. If the latter explanation of gravitational lensing is correct, Chapman et al. (2002b) estimate that up to $3-5\%$ of the $> 10\,mJy$ submillimetre sources detected in blank field surveys could be gravitationally amplified by foreground galaxies.

Gravitational lensing by clusters of galaxies can of course be used to study the fainter submillimetre sources, and this technique has been successfully applied

by Blain et al. (1999) and Cowie et al. (2002) (the data points marked by the crosses and curved-edged squares on Figures 5.19 and 5.20 respectively). The agreement between the source counts derived from the two cluster-lensing surveys is extremely good at flux densities below $S_{850} < 2\,\mathrm{mJy}$, and there is a smooth transition at this point between the faint number counts from the cluster-lensing surveys and the brighter source counts from my combined reanalysis of the blank field surveys. However, the number counts derived by Blain et al. (1999) at 4 and 8 mJy are significantly higher than the combined blank field survey counts presented in Table 5.11. The most likely explanation for this discrepancy is that the numbers quoted by Blain et al. (1999) suffer badly from small number statistics at bright flux densities, their lensing survey being composed of a number of small fields covering a total area of sky of only a few tens of square arcminutes. In comparison, the total area of sky observed by the "8 mJy Survey", "CUDSS", "HDF" and "Hawaii Survey" is 460 square arcminutes, an order of magnitude larger. If the bright SCUBA population does strongly cluster on arcminute scales, as implied by the evidence presented in Section 5.2, this could also affect the bright end of the number counts in small area surveys such as Blain et al. (1999).

The data point marked on Figures 5.19 and 5.20 by a star is determined from a 100 sq. arcmin blank field survey of the Hubble Deep Field, observed using the scan-mapping (raster) mode of SCUBA and the JCMT. The survey reaches a uniform noise level of $1\sigma_{\mathrm{rms}} \simeq 3\,\mathrm{mJy}$ / beam (Borys et al. 2002). One can see immediately that the number counts from my combined reanalysis of other blank field surveys at flux densities in the region of 12 mJy are over an order of magnitude less than the measurement of Borys et al. (2002). It is very unlikely that such a huge discrepancy could be explained by the effects of cosmic variance, even once clustering effects have been taken into account. The effect of flux-boosting may be part of the explanation, although the sources used by Borys et al. for this analysis were retrieved with signal-to-noise ratios > 4, so one would not expect flux-boosting to be entirely responsible for the elevated number density. Borys et al. did, however, have major problems with the calibration of their data, and the source counts in this region are to be very steep. If the '12 mJy' data point of Borys et al. were in fact placed at 8 or 9 mJy (a calibration error of 25-30%) then there would be good agreement between the two analyses.

Overall, the increased accuracy of this new source counts analysis will allow the evolutionary nature, as well as the dust and star-forming properties of the submillimetre population to be studied in much more detail than has been possible

before. This will be particularly useful when combined with knowledge of the redshift distribution of submillimetre sources, which is slowly being built up at the present.

Chapter 6

Conclusions

6.1 Summary

Deep blank-field surveys conducted with SCUBA on the JCMT have successfully resolved $\simeq 30-50\%$ of the far-infrared extragalactic background into discrete sources down to the confusion limit of $S_{850} \simeq 2-3\,\mathrm{mJy}$, with deeper surveys making use of gravitational lensing from intervening massive clusters probing the very faintest submillimetre sources. This has revealed a population of heavily dust-enshrouded galaxies at high redshift ($z > 1$) undergoing a burst of massive star-forming activity. The work presented here is an investigation into the nature of the most luminous 850 μm sources ($S_{850} > 5\,\mathrm{mJy}$), with particular consideration of their link with the formation and evolution of the most massive elliptical galaxies visible in the present-day Universe. Essentially this study is comprised of two parts: firstly the data from the "SCUBA 8 mJy Survey", the largest of the blank field submillimetre surveys completed to date, designed specifically with the aim of identifying the brightest 850 μm sources, and secondly combining this data with a re-analysis of other existing blank field surveys to obtain better constraints on some of the general statistical properties of the SCUBA population. The main results of this thesis can be summarised as follows:

1) Using an alternative IDL-based reduction pipeline (developed by Serjeant et al. 2003) to the standard JCMT SURF procedures, uncorrelated noise images of the survey regions have been produced, allowing for the development of a maximum-likelihood source extraction algorithm which simultaneously measures the statistical significance of every peak in a SCUBA map, leading to properly quantified errors on the flux densities of all potential sources.

2) The "SCUBA 8 mJy Survey" covers $\simeq 260$ square arcminutes of sky to a

depth of $\sigma_{\rm rms} \simeq 2.5\,{\rm mJy/beam}$, evenly split between two areas of low galactic cirrus emission; the Lockman Hole East and ELAIS N2. Applying the source extraction algorithm to these two fields has revealed 19 sources with S/N > 4.00, 40 sources with S/N > 3.50, and 85 sources with S/N > 3.00. The handful of sources detected with S/N > 3.50 alone are able to account for $\sim$ 10% of the observed 850 μm extragalactic background.

3) The steep Rayleigh-Jeans tail of the thermal dust emission allows the radio-to-submillimetre spectral index to be used as a redshift estimator. This method is based on the tight correlation observed in local star-forming galaxies between the radio continuum emission arising from relativistic electrons accelerated in supernova remnant shocks, and thermal dust emission from reprocessed star light. Using deep VLA 1.4 GHz imaging ($\sigma_{\rm rms} \sim 10\,\mu{\rm Jy/beam}$ in ELAIS N2, and $\sigma_{\rm rms} \sim 5\,\mu{\rm Jy/beam}$ in the Lockman Hole East) in combination with the measured 850 μm flux densities of each detection, all sources were constrained to lie at $z > 1$, with > 50% at redshift $z > 2$, and a median redshift of $z_{\rm med} \simeq 2.4$ based on the Carilli & Yun (2000) redshift estimator. A peak in the SFRD around this epoch would not be unexpected given the strong correlation between black-hole and spheroid mass found at low redshift and the peak in optical emission from powerful quasars at $z \simeq 2.5$.

4) The inferred star formation rates of these bright sources range from a few hundred to a few thousand solar masses per year, an 8 mJy source having a star formation rate of $\simeq 1000\,{\rm M_\odot\ yr^{-1}}$, assuming an $\Omega_{\rm M} = 0.3$, $\Omega_\Lambda = 0.7$ cosmology. This is sufficient to form the most massive elliptical galaxies on timescales of $\sim$ 1 Gyr, as appears to be required by a vast array of observational evidence (see the Introduction). The starburst, however, is heavily obscured by approximately $10^8 - 10^9\,{\rm M_\odot}$ of dust.

5) The co-moving number density of high redshift galaxies forming stars at > $1000\,{\rm M_\odot\ yr^{-1}}$ is $\simeq 10^{-5}\,{\rm Mpc^{-3}}$, with only a weak dependence on the precise redshift distribution. This also corresponds to the number density of massive ellipticals with L > 3 − 4L* in the present-day Universe, as well as the co-moving number density of comparably massive, passively-evolving objects in the redshift band $1 < z < 2$ inferred from recent surveys of extremely red objects. This is suggestive of an evolutionary sequence of the form:

SCUBA source at $z \geq 2.5 \rightarrow$
ERO at $z \simeq 1.5 \rightarrow$
$3 - 4L^{\star}$ evolved elliptical at $z = 0$

and can plausibly account for the formation of all present-day massive spheroids.
6) Using extensive Monte Carlo simulations to quantify the effects of completeness, mean output-to-input flux density ratio, and the degree of contamination from spurious / confused sources, the corrected cumulative 850 μm number counts based on a signal-to-noise detection threshold of > 3.50 are lower than that measured directly from the raw data until the source density approaches the confusion limit of SCUBA ($S_{850} \simeq 2 - 3$ mJy) at which point incompleteness is more of an issue and the corrected and uncorrected source counts tend towards the same value. The bright number counts from the "SCUBA 8 mJy Survey" are a factor of 2-3 higher than those derived from other comparatively wide area blank field surveys. In part this could be due to small number statistics, but perhaps more likely is the effect of clustering if the $S_{850} > 5$ mJy sources cluster on scales of a few arcminutes, since there is a higher probability of randomly centring a blank field survey in a region of lower than average source density under these circumstances.
7) Combining the data from the "SCUBA 8 mJy Survey" with other existing blank field surveys, re-reduced and analysed in an identical manner, approximately doubles the area of sky observed with SCUBA in an unbiased manner. The combined datasets allow the determination of the most accurate source counts to date for $S_{850} > 2$ mJy. The differential source counts for $S_{850} < 8$ mJy are well satisfied by a power-law of the form $dN(> S)/dS = N_0/(a + S^{\alpha})$ where the best-fit values of the free parameters were $N_0 = 2.67 \times 10^4$, $a = 0.49$ and $\alpha = 3.14$. If one assumes this is true over the full range of flux densities from the very faint to the very bright, this predicts a total 850 μm background of 3.8×10^4 mJy deg^{-2}, mid-way between the 850 μm extragalactic values of 3.1×10^4 mJy deg^{-2} and 4.4×10^4 mJy deg^{-2}. However, there are some indications that the source counts steepen for $S_{850} > 8$ mJy. This may simply be a result of small number statistics, but is possibly indicative of a high-mass cutoff of the SCUBA population. A steepening of the source counts would also make the bright SCUBA population more prone to the effects of gravitational lensing. More physical models of the source counts, beginning with a local 850 μm luminosity

function, are able to reasonably successfully model the number counts using only strong pure luminosity evolution with redshift, and assuming a single temperature optically thin greybody to represent the thermal spectral energy distribution of the dust with characteristic dust temperatures in the range $30 < T_d < 50\,K$, and emissivity index in the range $1.0 < \beta < 2.0$.

8) Tentative indications that the bright SCUBA population clusters on scales of $1 - 2$ arcminutes may be seen simply "by eye" on examining the distribution of sources in the ELAIS N2 field, although the low source density means that formally the significance level is only $\sim 2\sigma$. However, the full source catalogue derived from combining all of the survey fields contains a sufficient number of significant detections to place more meaningful constraints on the clustering properties of the bright submillimetre population. Measurements of angular correlation functions and nearest neighbour statistics for $S_{850} > 5$, 6, and 7 mJy, imply strong clustering on scales of ~ 1 arcminute at a significance level of $\sim 4\sigma$. The angular correlation functions from the combined data are still not of sufficient quality to obtain a meaningful fit of the form $w(\theta) = A\theta^{-\delta}$ where A and δ are well constrained. However, the data points are in fairly good agreement with the clustering strength measured for extremely red objects by Daddi et al. (2000), again suggesting a link between the SCUBA and ERO populations.

6.2 Future Work

The results from this work have provided a major part of the motivation for a new wide-field extragalactic submillimetre survey, which has now been underway for a year at the JCMT. The aim of this survey is to map 0.5 square degrees of sky, ~ 7 times the total area of the "SCUBA 8 mJy Survey" to a comparable depth of $\sigma_{rms} \simeq 2.5\,mJy/beam$. The area is split over two regions of sky; the Lockman Hole East (a continuation of the 8 mJy Survey), and the Subaru-XMM Deep Field. Based on the 850 μm source counts, a survey of this nature is expected to yield $200-400$ sources detected at the $> 3.5\sigma$ level. The aim of the "SCUBA Half Degree Extragalactic Survey (SHADES)" is to address the following fundamental questions:

- What is the cosmic history of massive dust-enshrouded star-formation activity?
- Are SCUBA sources the progenitors of massive elliptical galaxies?
- What fraction of SCUBA sources harbour a dust-obscured AGN?

In order to address the first question, and to some extent the second, a robust and unbiased redshift estimate is required for every 850 μm source detected by the wide-field SCUBA survey. Optical spectroscopy with the largest ground based facilities has had some limited success in measuring the redshifts of SCUBA sources (Chapman et al. 2003b), however, there are two major problems with this approach. The first issue is that an accurate position is required for positioning the slit, which given the size of the SCUBA beam requires there to be some sort of counterpart in the optical / infrared or radio identification. This immediately places a bias towards the lower end of the redshift scale for the selected objects, since even the deepest radio imaging to date will only detect starburst galaxies out to $z \simeq 3$. Furthermore, the faintness of the counterpart at optical / infrared wavelengths coupled with the large SCUBA beam size means that it is not trivial to identify the real counterpart, and again placing a slit on an object falling within the positional uncertainty of the 850 μm source has potential for selecting a lower-redshift candidate than the real identification, which may be too faint to be detected at that depth of imaging. An alternative approach has been to use the radio-to-submillimetre spectral index as a redshift estimator, however, the accuracy drops of markedly beyond $z \simeq 2$ where the dominant fraction of bright SCUBA sources are believed to lie.

In order to overcome these difficulties, the SHADES JCMT programme is to be complemented by deep observations from BLAST, a 2m-aperture balloon-borne submillimetre telescope designed to observe at 500, 350 and 250 μm, as well as deep VLA and MAMBO coverage at 21 cm and 1.3 mm respectively. Hughes et al. (2002) and Aretxaga et al. (2003) have used Monte Carlo simulations to generate mock catalogues of galaxies in the redshift range $0 < z < 6$ using an evolving 60 μm luminosity function that reproduces the 850 μm counts. The submillimetre flux densities and counts of these mock galaxies were calculated from spectral energy distributions, randomly selected from a library of template starburst galaxies, ULIRGs and AGN encompassing a wide range of dust temperatures. Appropriate observational noise incorporating both calibration and measurement errors was added at each wavelength to produce a realistic scatter in the submillimetre-FIR colour distribution for the mock galaxies. The probability that the colours of the sources measured from the simulated SCUBA-BLAST images could be identified with the colours from the SED of each galaxy in the mock catalogue was calculated, and through a combination of these individual probabilities, an overall redshift probability distribution for each source was gen-

erated. These simulations have indicated that photometric redshift estimates of this type are accurate to better than $\delta z = \pm 0.5$ out to $z > 4$. This complete and unbiased redshift information is sufficient to subdivide the full sample into redshift bins of unit width, which for a dataset comprised of a few hundred sources allows the evolution of the far-infrared luminosity as a function of redshift (and hence dust-obscured star formation rate density) to be delineated.

A second important goal of this survey is to measure the clustering properties of bright submillimetre sources over co-moving scales up to $\sim 10\,\mathrm{Mpc}$. As discussed in earlier chapters, if the bright SCUBA sources are indeed the progenitors of massive spheroids then they should be strongly clustered. This is an inevitable result of the gravitational collapse from Gaussian initial density fluctuations: the rare high-mass peaks are strongly biased with respect to the mass. The angular correlation functions presented in Chapter 5, which are based on < 100 sources with S/N > 3.00 over a number of relatively small fields, have implied that the bright $850\,\mu\mathrm{m}$ population clusters strongly on scales of $\sim 1\,\mathrm{arcminute}$. The significance level of this measurement is only $\sim 4\sigma$ and is insufficient to obtain a definitive power law fit to the data, however, based on this evidence, a sample of 200-400 detections above a signal-to-noise threshold of 3.50 (hence less prone to contamination from spurious / confused sources) in two fields, each approaching 0.25 square degrees in area, should place firm constraints on the form of the angular correlation function. Furthermore, the photometric redshift information can also be factored into the correlation function calculation making it three-dimensional, boosting the significance of the raw angular clustering signal by a factor of $\simeq 3$.

This combination of crude redshift and clustering measurements will provide strong constraints on current theoretical galaxy formation models, as illustrated in Figure 6.1. These two plots represent the simulation results from 6 alternative theoretical models of the submillimetre source population. The left-hand plot shows the measured clustering amplitude and slope, along with error bars on the auto-correlation function parameters based on 50 realizations of each theoretical model and assuming that 200-400 sources are detected at $> 3.50\sigma$, in line with the measured source counts from the "8 mJy Survey" which observed to the same depth at $850\,\mu\mathrm{m}$. The right-hand plot shows the corresponding redshift distribution for each of the models, smoothed from the raw theoretical output by a box-car filter of width $\delta z = 1$, to reflect the redshift resolution available with SCUBA+BLAST photometric redshifts.

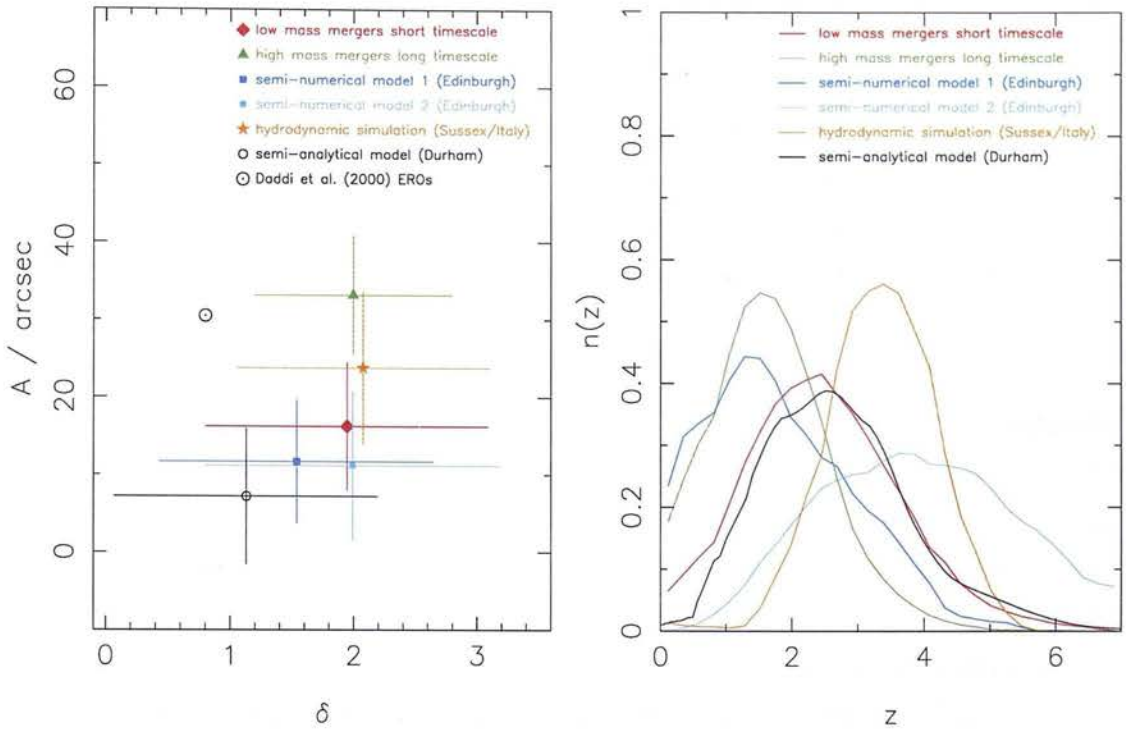

Figure 6.1: Simulated SCUBA / BLAST survey results in terms of measured clustering amplitude and slope (left-hand plot) and source redshift distribution (right-hand plot) as predicted from 6 alternative theoretical models of the submillimetre source population. The error bars on the autocorrelation functions are based on fits to 50 different realizations of each theoretical model, and assume that the survey will detect 200-400 sources at $> 3.50\sigma$, as implied by the source counts from the "8 mJy Survey". The redshift distributions have been smoothed from the raw theoretical output by a box-car filter of width $\delta z = 1$, to reflect the redshift resolution achievable from SCUBA+BLAST photometric redshifts. This figure is taken from the JCMT telescope proposal for SHADES.

Together these two plots demonstrate a number of important points. Firstly, the left-hand figure shows that even with only a few hundred significant sources, this survey is reasonably expected to detect clustering within the SCUBA population. Furthermore, if the bright SCUBA sources show a clustering strength comparable with that of the ERO population (Daddi et al. 2000), as preliminary evidence in Section 5.2 would imply, the detection of the clustering signal will be very significant indeed (see the circled dot on the figure). A second potentially interesting point is that current theoretical scenarios are unable to produce a clustering signal as strong as this. Thirdly, even within these fairly large errors, the clustering amplitude should be recoverable with sufficient accuracy to distinguish between low-mass and high-mass galaxy galaxy mergers (green and

red models). Finally, the power of combining the measured clustering signal with the photometric redshift distribution is able to discriminate between the models. For example, measuring the clustering parameters alone would not be enough to distinguish between the green and orange models on the left-hand plot, but from the right-hand plot, one can see that the redshift distributions for these two scenarios are very different. Conversely, the red and black models have very similar redshift distributions, as seen on the right-hand plot, but the clustering parameters are quite different.

The last of the key aims of this survey is to ascertain what fraction of SCUBA sources harbour a dust-enshrouded but active black hole. This can be achieved by combining the submillimetre data with SIRTF 70 μm observations sensitive to rest-frame mid-infrared emission. Although the early comparisons of SCUBA and Chandra / XMM surveys have shown that X-ray visible active galactic nucleii and submillimetre sources are rarely coincident, Almaini et al. (2003) found that they appeared to trace the same large scale structures on arcminute scales. One possibility is that these two populations represent different relatively short lived evolutionary stages in the formation of massive high redshift objects (eg. Archibald et al. 2002b), but alternatively it is plausible that the majority of SCUBA sources do contain a massive and active black hole which is too heavily obscured to be detected in current X-ray surveys (Fabian 1999). Although SIRTF is neither large enough, nor observes at sufficiently long wavelengths to constrain the redshifts of dust-enshrouded sources (for example, the SIRTF SWIRE Survey would not be able to detect a galaxy with an Arp 220 SED at $z > 3$ even if scaled to $S_{850} \simeq 10\,\mathrm{mJy}$), it should have the sensitivity and beamsize at 70 μm to detect bright SCUBA sources at $z > 3$ if they have a strong mid-infrared component. An object such as Mkn 231, for example, which is known to harbour an obscured active nucleus, is 3 times brighter at $\lambda_{\mathrm{rest}} = 30\,\mu\mathrm{m}$ when compared to Arp 220, and 10 times brighter at $\lambda_{\mathrm{rest}} = 10\,\mu\mathrm{m}$.

In conclusion, the completion of this survey should resolve many of the remaining issues regarding the formation and evolution of massive elliptical galaxies.

Bibliography

[1] Afonso, C., Albert, J.N., Andersen, J., Ansari, R., Aubourg, É., Bareyre, P., Beaulieu, J.P., Blanc, G., Charlot, X., Couchot, F., Coutures, C., Ferlet, R., Fouqué, P., Glicenstein, J.F., Goldman, B., Gould, A., Graff, D., Gros, M., Haissinski, J., Hamadache, C., de Kat, J., Lasserre, T., Le Guillou, L., Lesquoy, É., Loup, C., Magneville, C., Marquette, J.B., Maurice, É Maury, A., Milsztajn, A., Moniez, M., Palanque-Delabrouille, N., Perdereau, O., Prévot, L., Rahal, Y.R., Rich, J., Spiro, M., Tisserand, P., Vidal-Madjar, A., Vigroux, L., Zylberajch, S., 2003, A&A, 400, 951.

[2] Alcock, C., Allsman, R.A., Alves, D.R., Axelrod, T.S., Becker, A.C., Bennett, D.P., Cook, K.H., Drake, A.J., Freeman, K.C., Geha, M., Griest, K., Keller, S.C., Lehner, M.J., Marshall, S.L., Minniti, D., Nelson, C.A., Peterson, B.A., Popowski, P., Pratt, M.R., Quinn, P.J., Stubbs, C.W., Sutherland, W., Tomaney, A.B., Vandehei, T., Welch, D., 2001, ApJS, 136, 419.

[3] Allen, S.W., Schmidt, R.W., Fabian, A.C., 2002a, MNRAS, 334, L11.

[4] Allen, S.W., Schmidt, R.W., Fabian, A.C., 2002b, MNRAS, 335, 256.

[5] Almaini, O., Scott, S.E., Dunlop, J.S., Manners, J.C., Willott, C.J., Lawrence, A., Ivison, R.J., Johnson, O., Blain, A.W., Peacock, J.A., Oliver, S.J., Fox, M.J., Mann, R.G., Pérez-Fournon, I., González-Solares, E., Rowan-Robinson, M., Serjeant, S., Cabrera-Guerra, F., Hughes, D.H., 2003, MNRAS, 338, 303.

[6] Alton, P.B., Trewhella, M., Davies, J.I., Evans, R., Bianchi, S., Gear, W., Thronson, H., Valentijn, E., Witt, A., 1998, A&A, 335, 807.

[7] Archibald, E.N., Dunlop, J.S., Hughes, D.H., Rawlings, S., Eales, S.A., Ivison, R.J., 2001, MNRAS, 323, 417.

[8] Archibald, E.N., Jenness, T., Holland, W.S., Coulson, I.M., Jessop, N.E., Stevens, J.A., Robson, E.I., Tilanus, R.P.J., Duncan, W.D., Lightfoot, J.F., 2002a, MNRAS, 336, 1.

[9] Archibald, E.N., Dunlop, J.S., Jimenez, R., Friaca, A.C.S., McLure, R.J., Hughes, D.H., 2002b, 336, 353.

[10] Aretxaga, I., Hughes, D.H., Chapin, E.L., Gaztañaga, E., Dunlop, J.S., Ivison, R.J., 2003, MNRAS, 342, 759.

[11] Baker, A.J., Lutz, D., Genzel, R., Tacconi, L.J., Lehnert, M.D., 2001, A&A, 372, L37.

[12] Barger, A.J., Cowie, L.L., Sanders, D.B., Fulton, E., Taniguchi, Y., Sato, Y., Kawara, K., Okuda, H., 1998, Nat, 394, 248.

[13] Barger, A.J., Cowie, L.L., Sanders, D.B., 1999, ApJ, 518, L5.

[14] Barger, A.J., Cowie, L.L., Richards, E.A., 2000, AJ, 119, 2092.

[15] Baugh, C.M., Cole, S., Frenk, C.S., 1996, MNRAS, 283, 1361.

[16] Baugh, C.M., Cole, S., Frenk, C.S., Lacey, C.G., 1998, ApJ, 498, 504.

[17] Bender, R., Burstein, D., Faber, S.M., 1993, ApJ, 411, 153.

[18] Bennett, C.L., Halpern, M., Hinshaw, G., Jarosik, N., Kogut, A., Limon, M., Meyer, S.S., Page, L., Spergel, D.N., Tucker, G.S., Wollack, E., Wright, E.L., Barnes, C., Greason, M.R., Hill, R.S., Komatsu, E., Nolta, M.R., Odegard, N., Peiris, H.V., Verde, L., Weiland, J.L., 2003, ApJS, 148, 1.

[19] Bertola, F., Buson, L.M., Zeilinger, W.W., 192, ApJ, 401, L79.

[20] Blain, A.W., Kneib, J.-P., Ivison, R.J., Smail, I., 1999, ApJ, 512, L87.

[21] Borys, C., Chapman, S., Halpern, M., Scott, D., 2002, MNRAS, 330, L63.

[22] Bower, R.G., Lucey, J.R., Ellis, R.S., 1992a, MNRAS, 254, 589.

[23] Bower, R.G., Lucey, J.R., Ellis, R.S., 1992b, MNRAS, 254, 601.

[24] Bouwens, R.J., Illingworth, G.D., Rosati, P., Lidman, C., Broadhurst, T., Franx, M., Ford, H.C., Magee, D., Benítez, N., Blakeslee, J.P., Meurer, G.R., Clampin, M., Hartig, G.F., Ardila, D.R., Bartko, F., Brown, R.A., Burrows, C.J., Cheng, E.S., Cross, N.J.G., Feldman, P.D., Golimowski, D.A., Gronwall, C., Infante, L., Kimble, R.A., Krist, J.E., Lesser, M.P., Martel, A.R., Menanteau, F., Miley, G.K., Postman, M., Sirianni, M., Sparks, W.B., Tran, H.D., Tsvetanov, Z.I., White, R.L., Zheng, W., 2003a, ApJ, 595, 589.

[25] Bouwens, R.J., Broadhurst, T., Illingworth, G., 2003b, ApJ, 593, 640.

[26] Bromm, V., Coppi, P.S., Larson, R.B., 2002, ApJ, 564, 23.

[27] Calzetti, D., 1997, AJ., 113, 162.

[28] Carilli, C.L., Wrobel, J.M., Ulvestad, J.S., 1998, AJ, 115, 928.

[29] Carilli, C.L., Yun, M.S., 1999, ApJ, 513, L13.

[30] Carilli, C.L., Yun, M.S., 2000, ApJ, 530, 618.

[31] Chanamé, J., Gould, A., 2003, ApJ, in press, (astro-ph/0307434).

[32] Chapman, S.C., Lewis, G.F., Helou, G., 2002, in A New Era in Cosmology, ASP Conference Proceedings, Vol. 283. Edited by Nigel Metcalfe and Tom Shanks. ISBN: 1-58381-126-5. San Francisco: Astronomical Society of the Pacific, 2002a., p.373.

[33] Chapman, S.C., Smail, I., Ivison, R.J., Blain, A.W., 2002b, MNRAS, 335, L17.

[34] Chapman, S.C., Barger, A.J., Cowie, L.L., Scott, D., Borys, C., Capak, P., Fomalont, E.B., Lewis, G.F., Richards, E.A., Steffen, A.T., Wilson, G., Yun, M., 2003a, ApJ, 585, 57.

[35] Chapman, S.C., Blain, A.W., Ivison, R.J., Smail, I.R., 2003b, Nat, 422, 695.

[36] Chini, R., Kruegel, E., Lemke, R., Ward-Thompson, D., 1995, A&A, 295, 317.

[37] Condon, J.J., Huang, Z.-P., Yin, Q.F., Thuan, T.X., 1991, ApJ, 378, 65.

[38] Condon, J.J., 1992, ARA&A, 30, 575.

[39] Cowie, L.L., Hu, E.M., Songaila, A., 1995, Nat, 377, 603.

[40] Cowie, L.L., Songaila, A., Barger, A.J., 1999, AJ, 118, 603.

[41] Cowie, L.L., Barger, A.J., Kneib, J.-P.. 2002, AJ, 123, 2197.

[42] Coulson, I., 2000,
`http://www.jach.hawaii.edu/JACpublic/ JCMT/Facility_description/ Pointing/problems.html#new`

[43] Daddi, E., Cimatti, A., Pozzetti, L., Hoekstra, H., Rottgering, H.J.A., Renzini, A., Zamorani, G., Mannucci, F., 2000, A&A, 361, 535.

[44] Daddi, E., Cimatti, A., Broadhurst, T., Renzini, A., Zamorani, G., Mignoli, M., Saracco, P., Fontana, A., Pozzetti, L., Poli, F., Cristiani, S., D'Odorico, S., Giallongo, E., Gilmozzi, R., Menci, N., 2002, A&A, 384, L1.

[45] De Rújula, A., Jetzer, P., Massó, E., 1992, A&A, 254, 99.

[46] Dickinson, M., Stern, D., Giavalisco, M., Ferguson, H.C., Tsvetanov, Z., Chornock, R., Cristiani, S., Dawson, S., Dey, A., Filippenko, A.V., Moustakas, L.A., Nonino, M., Papovich, C., Ravindranath, S., Riess, A., Rosati, P., Spinrad, H., Vanzella, E., 2003, ApJL, submitted, (astro-ph/0309070).

[47] Djorgovski, S., Thompson, D.J., 1992, IAUS, 149, 337.

[48] Donas, J., Deharveng, J.M., Laget, M., Milliard, B., Huguenin, D., 1987, A&,A, 180, 12.

[49] Downes, D., Neri, R., Greve, A., Guilloteau, S., Casoli, F., Hughes, D., Lutz, D., Menten, K.M., Wilner, D.J., Andreani, P., Bertoldi, F., Carilli, C.L., Dunlop, J., Genzel, R., Gueth, F., Ivison, R.J., Mann, R.G., Mellier, Y., Oliver, S., Peacock, J., Rigopoulou, D., Rowan-Robinson, M., Schilke, P., Serjeant, S., Tacconi, L.J., Wright, M., 1999, A&A, 347, 809.

[50] Draine, B.T., Lee, H.M., 1984, ApJ, 285, 89.

[51] Dunlop, J.S., Hughes, D.H., Rawlings, S., Eales, S.A., Ward, M.J., 1994, Nat, 370, 347.

[52] Dunlop, J., Peacock, J., Spinrad, H., Dey, A., Jimenez, R., Stern, D., Windhorst, R., 1996, Nat, 381, 581.

[53] Dunlop, J.S., 1998, in Observational Cosmology with the New Radio Surveys, Proceedings of a Workshop held in Puerto de la Cruz, Tenerife, Canary Islands, Spain, 13-15 January 1997, Dordrecht: Kluwer Academic Publishers, 1998, Astrophysics and space science library (ASSL) Series vol no: 226, ISBN: 0792348850., p.157.

[54] Dunlop, J.S., 2001a, in: FIRSED2000, eds. I.M. van Bemmel, B. Wilkes, & P. Barthel, Elsevier New Astronomy Reviews 45, p. 609, (astro-ph/0101297).

[55] Dunlop, J.S., 2001b, in: QSO Hosts and their Environments, eds. Marquez, I. et al. Kluwer, p. 3, (astro-ph/0103238).

[56] Dunlop, J.S., 2001c, in: Deep Sub-millimetre Surveys, eds. Lowenthal, J. & Hughes, D.H., World Scientific, p. 11, (astro-ph/0011077)

[57] Dunlop, J.S., McLure, R.J., Kukula, M.J., Baum, S.A., O'Dea, C.P., Hughes, D.H., 2003a, MNRAS, 340, 1095.

[58] Dunlop, J.S., McLure, R.J., Yamada, T., Kajisawa, M., Peacock, J.A., Mann, R.G., Hughes, D.H., Aretxaga, I., Muxlow, T.W.B., Richards, A.M.S., Dickinson, M., Ivison, R.J., Smith, G.P., Smail, I., Serjeant, S., Almaini, O., Lawrence, A., 2003b, MNRAS, in press, (astro-ph/0205480).

[59] Dunne, L., Eales, S., Edmunds, M., Ivison, R., Alexander, P., Clements, D.L., 2000a, MNRAS, 315, 115.

[60] Dunne, L., Clements, D.L., Eales, S.A., 2000b, MNRAS, 319, 813.

[61] Dunne, L., Eales, S., 2001, 327, 697.

[62] Eales, S., Lilly, S., Gear, W., Dunne, L., Bond, J.R., Hammer, F., Le Févre, O., Crampton, D., 1999, ApJ, 515, 518.

[63] Eales, S., Lilly, S., Webb, T., Dunne, L., Gear, W., Clements, D., Yun, M., 2000, AJ, 120, 2244.

[64] Edmunds, M.G., 1994, MNRAS, 270, L37.

[65] Efstathiou, A., Oliver, S., Rowan-Robinson, M., Surace, C., Sumner, T., Héraudeau, P., Linden-Vornle, M.J.D., Rigopoulou, D., Serjeant, S., Mann, R.G., Cesarsky, C.J., Danese, L., Franceschini, A., Genzel, R., Lawrence, A.,

Lemke, D., McMahon, R.G., Miley, G., Puget, J.-L., Rocca-Volmerange, B., 2000a, MNRAS, 319, 1169.

[66] Efstathiou, A., Rowan-Robinson, M., Siebenmorgen, R., 2000b, MNRAS, 313, 734.

[67] Elbaz, D., Cesarsky, C.J., Fadda, D., Aussel, H., Désert, F.X., Franceschini, A., Flores, H., Harwit, M., Puget, J.L., Starck, J.L., Clements, D.L., Danese, L., Koo, D.C., Mandolesi, R., 1999, A&A, 351, L37.

[68] Faber, S.M., Gallagher, J.S., 1976, ApJ, 204, 365.

[69] Fabian, A.C., 1999, MNRAS, 308, L39.

[70] Farrah, D., Serjeant, S., Efstathiou, A., Rowan-Robinson, M., Verma, A., 2002, MNRAS, 335, 1163.

[71] Fixsen, D.J., Cheng, E.S., Gales, J.M., Mather, J.C., Shafer, R.A., Wright, E.L., 1996, ApJ, 473, 576.

[72] Fixsen, D.J., Dwek, E., Mather, J.C., Bennel, C.L., Shafer, R.A., 1998, ApJ, 508, 123.

[73] Fox, M.J., Efstathiou, A., Rowan-Robinson, M., Dunlop, J.S., Scott, S., Serjeant, S., Mann, R.G., Oliver, S., Ivison, R.J., Blain, A., Almaini, O., Hughes, D., Willott, C.J., Longair, M., Lawrence, A., Peacock, J.A., 2002, MNRAS, 331, 839.

[74] Fruchter, A.S., Hook, R.N., 2002, PASP, 114, 144.

[75] Gardner, J.P., Sharples, R.M., Frenk, C.S., Carrasco, B.E., 1997, ApJ, 480, L99.

[76] Gaztañaga, E., Baugh, C.M., 1998, MNRAS, 294, 229.

[77] Gear, W.K., Lilly, S.J., Stevens, J.A., Clements, D.L., Webb, T.M., Eales, S.A., Dunne, L., 2000, MNRAS, 316, L51.

[78] Giavalisco, M., Steidel, C.C., Adelberger, K.L., Dickinson, M.E., Pettini, M., Kellogg, M., 1998, ApJ, 503, 543.

[79] Giavalisco, M., Dickinson, M., 2001, ApJ, 550, 177.

[80] Glazebrook, K., Ellis, R., Colless, M., Broadhurst, T., Allington-Smith, J., Tanvir, N., 1995, MNRAS, 273, 157.

[81] Glazebrook, K., Baldry, I.K., Blanton, M.R., Brinkmann, J., Connolly, A., Csabai, I., Fukugita, M., Ivezic, Z., Loveday, J., Meiksin, A., Nichol, R., Peng, E., Schneider, D.P., SubbaRao, M., Tremonti, C., York, D.G., 2003, ApJ, 587, 55.

[82] Guélin, M., Zylka, R., Mezger, P.G., Haslam, C.G.T., Kreysa, E., Lemke, R., Sievers, A.W., 1993, A&A, 279, L37.

[83] Guzzo, L., Strauss, M.A., Fisher, K.B., Giovanelli, R., Haynes, M.P., 1997, ApJ, 489, 37.

[84] Hasinger, G., Altieri, B., Arnaud, M., Barcons, X., Bergeron, J., Brunner, H., Dadina, M., Dennerl, K., Ferrando, P., Finoguenov, A., Griffiths, R.E., Hashimoto, Y., Jansen, F.A., Lumb, D.H., Mason, K.O., Mateos, S., McMahon, R.G., Miyaji, T., Paerels, F., Page, M.J., Ptak, A.F., Sasseen, T.P., Schartel, N., Szokoly, G.P., Trümper, J., Turner, M., Warwick, R.S., Watson, M.G., 2001, A&A, 365, L51.

[85] Hauser, M.G., Arendt, R.G., Kelsall, T., Dwek, E., Odegard, N., Weiland, J.L., Freudenreich, H.T., Reach, W.T., Silverberg, R.F., Moseley, S.H., Pei, Y.C., Lubin, P., Mather, J.C., Shafer, R.A., Smoot, G.F., Weiss, R., Wilkinson, D.T., Wright, E.L., 1998, AJ, 508, 25.

[86] Heavens, A.F., Jimenez, R., Lahav, O., 2000, MNRAS, 317, 965.

[87] Hogbom, J.A., 1974, A&AS, 15, 417.

[88] Holland, W.S., Robson, E.I., Gear, W.K., Cunningham, C.R., Lightfoot, J.F., Jenness, T., Ivison, R.J., Stevens, J.A., Ade, P.A.R., Griffin, M.J., Duncan, W.D., Murphy, J.A., Naylor, D.A., 1999, MNRAS, 303, 659.

[89] Hughes, D.H., Dunlop, J.S., Rawlings, S., 1997, MNRAS, 289, 766.

[90] Hughes, D.H., Dunlop, J.S., Rowan-Robinson, M., Serjeant, S., Blain, A., Mann, R.G., Ivison, R.J., Peacock, J., Efstathiou, A., Gear, W., Oliver, S., Lawrence, A., Longair, M., Goldschmidt, P., Jenness, T., 1998, Nat, 394, 241.

[91] Hughes, D.H., Gaztañaga, 2000, in: Proc. of 33rd ESLAB Symp. "Star formation from the small to the large scale" (F. Favata, A.A. Kaas & A. Wilson eds., ESA SP-445, 2000).

[92] Hughes, D.H., Aretxaga, I., Chapin, E.L., Gaztañaga, E., Dunlop, J.S., Devlin, M.J., Halpern, M., Gundersen, J., Klein, J., Netterfield, C.B., Olmi, L., Scott, D., Tucker, G., 2002, MNRAS, 335, 871.

[93] Ivison, R.J., 1995, MNRAS, 275, L33.

[94] Ivison, R.J., Dunlop, J.S., Hughes, D.H., Archibald, E.N., Stevens, J.A., Holland, W.S., Robson, E.I., Eales, S.A., Rawlings, S., Dey, A., Gear, W.K., 1998, ApJ, 494, 211.

[95] Ivison, R.J., Smail, I., Barger, A.J., Kneib, J.-P., Blain, A.W., Owen, F.N., Kerr, T.H., Cowie, L.L., 2000a, MNRAS, 315, 209.

[96] Ivison, R.J., Dunlop, J.S., Smail, I., Dey, A., Liu, M.C., Graham, J.R., 2000b, ApJ, 542, 27.

[97] Ivison, R.J., Greve, T.R., Smail, I., Dunlop, J.S., Roche, N.D., Scott, S.E., Page, M.J., Stevens, J.A., Almaini, O., Blain, A.W., Willott, C.J., Fox, M.J., Gilbank, D.G., Serjeant, S., Hughes, D.H., 2002, MNRAS, 337, 1.

[98] Iwata, I., Ohta, K., Tamura, N., Ando, M., Wada, S., Watanabe, C., Akiyama, M., Aoki, K., 2003, PASJ, 55, 415.

[99] James, A., Dunne, L., Eales, S., Edmunds, M.G., 2002, MNRAS, 335, 753.

[100] James, P.A., Mobasher, B., 1999, MNRAS, 306, 199.

[101] Jameson, A., Longair, M., Blain, A., 1999, in The Third Stromlo Symposium: The Galactic Halo, eds. Gibson, B.K., Axelrod, T.S. & Putman, M.E., ASP Conference Series Vol. 165, p. 346.

[102] Janssen, M.A., Gulkis, S., 1992, in The infrared and submillimetre sky after COBE; Proceedings of the NATO Advanced Study Institute, Les Houches, France, Mar. 20-30, 1991 (A93-51701 22-90), p.391-408.

[103] Jarvis, M.J., Rawlings, S., Eales, S.A., Blundell, K.M., Willott, C.J., 2001, in: QSO hosts and their environments, eds. Marquez, I. et al., Kluwer.

[104] Jenkins, A., Frenk, C.S., Pearce, F.R., Thomas, P.A., Colberg, J.M., White, S.D.M., Couchman, H.M.P., Peacock, J.A., Efstathiou, G., Nelson, A.H., 1998, ApJ, 499, 20.

[105] Jenness, T., Lightfoot, J.F., 'SURF - SCUBA User Reduction facility v1.1 Users Manual', 1997.

[106] Jenness, T., Lightfoot, J.F., Holland, W.S., 1998, SPIE, 3357, 548.

[107] Jenness, T., 2000, `http://www.jach.hawaii.edu/JACdocs/JCMT/ tr/001/84/index.html`

[108] Jenness, T., Stevens, J.A., Archibald, E.N., Economou, F., Jessop, N.E., Robson, E.I., 2002, MNRAS, 336, 14.

[109] Jimenez, R., Friaca, A.C.S., Dunlop, J.S., Terlevich, R.J., Peacock, J.A., Nolan, L.A., 1999, MNRAS, 305, L16.

[110] Jimenez, R., Padoan, P., Dunlop, J.S., Bowen, D.V., Juvela, M., Matteucci, F., 2000, ApJ, 532, 152.

[111] Jorgensen, I., Franx, M., Hjorth, J., van Dokkum, P.G., 1999, MNRAS, 308, 833.

[112] Kawara, K., Sato, Y., Matsuhara, H., Taniguchi, Y., Okuda, H., Sofue, Y., Matsumoto, T., Wakamatsu, K., Karoji, H., Okamura, S., Chambers, K.C., Cowie, L.L., Joseph, R.D., Sanders, D.B., 1998, A&A, 336, L9.

[113] Kelson, D., van Dokkum, P.G., Franx, M., Illingworth, G.D., Fabrikant, D., 1997, ApJ, 478, L13.

[114] Kennicutt, R.C., 1983, ApJ, 272, 54.

[115] Knox, R.A., Hawkins, M.R.S., Hambly, N.C., 1999, MNRAS, 306, 736.

[116] Kochanek, C.S., Pahre, M.A., Falco, E.E., Huchra, J.P., Mader, J., Jarrett, T.H., Chester, T., Cutri, R., Schneider, S.E., 2001, ApJ, 560, 566.

[117] Kormendy, J., Gebhardt, K., 2001, in: 20th Texas Symposium on Relativistic Astrophysics, eds. Martel, H., Wheeler, J.C., AIP, (astro-ph/0105230).

[118] Kuo, C.-L., Ade, P., Bock, J.J., Daub, M.D., Goldstein, J., Holzapfel, W.L., Lange, A.E., Newcomb, M, Peterson, J.B., Ruhl, J., Runyan, M.C., Torbet, E., 2002, 201st AAS Meeting, 140.04; Bulletin of the American Astronomical Society, 34, 1324.

[119] Lacey, C.G., Ostriker, J.P., 1985, ApJ, 299, 633.

[120] Landy, S.D., Szalay, A.S., 1993, ApJ, 412, 64.

[121] Larson, R.B., 1975, MNRAS, 173, 671.

[122] Larson, R.B., 1999, Star Formation 1999, Proceedings of Star Formation 1999, held in Nagoya, Japan, June 21 - 25, 1999, Editor: T. Nakamoto, Nobeyama Radio Observatory, p. 336-340.

[123] Lees, J.F., Knapp, G.R., Rupen, M.P., Phillips, T.G., 1991, ApJ, 379, 177.

[124] Lilly, S.J., Le Fèvre, O., Crampton, D., Hammer, F., Tresse, L., 1995, ApJ, 455, 50.

[125] Lilly, S.J., Le Fèvre, O., Hammer, F., Crampton, D., 1996, ApJ, 460, L1.

[126] Lilly, S., Eales, S.A., Gear, W.K., Hammer, F., Le Fèvre, O., Crampto5, D., Bond, J.R., Dunne, L., 1999, ApJ, 518, 641.

[127] Lisenfeld, U., Isaak, K.G., Hills, R., 2000, MNRAS, 312, 433.

[128] Madau, P., Ferguson, H.C., Dickinson, M.E., Giavalisco, M., Steidel, C.C., Fruchter, A., 1996, MNRAS, 283, 1388.

[129] Madau, P., Pozzetti, L., Dickinson, M., 1998, ApJ, 498, 106.

[130] Manners, J.C., Johnson, O., Almaini, O., Willott, C.J., Gonzalez-Solares, E., Lawrence, A., Mann, R.G., Perez-Fournon, I., Dunlop, J.S., McMahon, R.G., Oliver, S.J., Rowan-Robinson, M., Serjeant, S., 2003, MNRAS, 343, 293.

[131] Mathis, J.S., Whiffen, G., 1989, ApJ, 341, 808.

[132] McLure, R.J., Dunlop, J.S., 2002, MNRAS, 331, 795.

[133] Moore, B., 1993, ApJ, 413, L93.

[134] Nemiroff, R.J., Norris, J.P., Wickramasinghe, W.A.D.T., Horack, J.M., Kouveliotou, C., Fishman, G.J., Meegan, C.A., Wilson, R.B., Paciesas, W.S., 1993, ApJ, 414, 36.

[135] Oliver, S., Rowan-Robinson, M., Alexander, D.M., Almaini, O., Balcells, M., Baker, A.C., Barcons, X., Barden, M., Bellas-Velidis, I., Cabrera-Guerra, F., Carballo, R., Cesarsky, C.J., Ciliegi, P., Clements, D.L., Crockett, H., Danese, L., Dapergolas, A., Drolias, B., Eaton, N., Efstathiou, A., Egami, E., Elbaz, D., Fadda, D., Fox, M., Franceschini, A., Genzel, R., Goldschmidt, P., Graham, M., Gonzalez-Serrano, J.I., Gonzalez-Solares, E.A., Granato, G.L., Gruppioni, C., Herbstmeier, U., Héraudeau, P., Joshi, M., Kontizas, E., Kontizas, M., Kotilainen, J.K., Kunze, D., La Franca, F., Lari, C., Lawrence, A., Lemke, D., Linden-Vornle, M.J.D., Mann, R.G., Márquez, I., Masegosa, J., Mattila, K., McMahon, R.G., Miley, G., Missoulis, V., Mobasher, B., Morel, T., Norgaard-Nielsen, H., Omont, A., Papadopoulos, P., Perez-Fournon, I., Puget, J.-L., Rigopoulou, D., Rocca-Volmerange, B., Serjeant, S., Silva, L., Sumner, T., Surace, C., Vaisanen, P., van der Werf, P.P., Verma, A., Vigroux, L., Villar-Martin, M., Willott, C.J., 2000, MNRAS, 316, 749.

[136] O'Meara, J.M., Tytler, D., Kirkman, D., Suzuki, N., Prochaska, J.X., Lubin, D., Wolfe, A.M., 2001, ApJ, 552, 718.

[137] Panter, B., Heavens, A.F., Jimenez, R., 2003, MNRAS, 343, 1145.

[138] Pearson, T.J., & The Cosmic Background Imager Collaboration, 2002, 200th AAS Meeting, 06.06; Bulletin of the American Astronomical Society, 34, 9.

[139] Peebles, P.J.E., 2002, in A New Era in Cosmology, eds. N.Metcalfe & T. Shanks, ASP Conf. Ser., p.351.

[140] Perlmutter, S., Aldering, G., Goldhaber, G., Knop, R.A., Nugent, P., Castro, P.G., Deustua, S., Fabbro, S., Goobar, A., Groom, D.E., Hook, I.M., Kim, A.G., Kim, M.Y., Lee, J.C., Nunes, N.J., Pain, R., Pennypacker, C.R., Quimby, R., Lidman, C., Ellis, R.S., Irwin, M., McMahon, R.G., Ruiz-Lapuente, P., Walton, N., Schaefer, B., Boyle, B.J., Filippenko, A.V., Matheson, T., Fruchter, A.S., Panagia, N., Newberg, H.J.M., Couch, W.J., 1999, ApJ., 517, 565.

[141] Pritchet, C.J., Hartwick, F.D.A., 1990, ApJ, 355, 410.

[142] Puget, J.L., Abergel, A., Bernard, J.P., Boulanger, F., Burton, W.B., Desert, F.X., Hatmann, D., 1996, A&A, 308, L5.

[143] Rengarajan, T.N., Takeuchi, T.T., 2001, PASJ, 53, 433.

[144] Renzini, A., Ciotti, L., 1993, ApJ, 416, 49.

[145] Riess, A.G., Filippenko, A.V., Challis, P., Clocchiatti, A., Diercks, A., Garnavich, P.M., Gilliland, R.L., Hogan, C.J., Jha, S., Kirshner, R.P., Leibundgut, B., Phillips, M.M.; Reiss, D., Schmidt, B.P., Schommer, R.A., Smith, R.C., Spyromilio, J., Stubbs, C., Suntzeff, N.B., Tonry, J., 1998, AJ, 116, 1009.

[146] Rowan-Robinson, M., Mann, R.G., Oliver, S.J., Efstathiou, A., Eaton, N., Goldschmidt, P., Mobasher, B., Serjeant, S.B.G., Sumner, T.J., Danese, L., Elbaz, D., Franceschini, A., Egami, E., Kontizas, M., Lawrence, A., McMahon, R., Norgaard-Nielsen, H.U., Perez-Fournon, I., Gonzalez-Serrano, J.I., 1997, MNRAS, 289, 490.

[147] Rowan-Robinson, M., 2000, MNRAS, 316, 885.

[148] Rowan-Robinson, M., 2001, IAUS, 204, 265.

[149] Sandell, G., 1994, MNRAS, 271, 75.

[150] Sanders, D.B., Mirabel, I.F., 1996, ARA&A, 34, 749.

[151] Saunders, W., Rowan-Robinson, M., Lawrence, A., Efstathiou, G., Kaiser, N., Ellis, R.S., Frenk, C.S., 1990, MNRAS, 242, 318.

[152] Sawicki, M., 2000, A&AS, 197, 6504.

[153] Schlegel, D.J., Finkbeiner, D.P., Davis, M., 1998, ApJ, 500, 525.

[154] Schmidt, M., Schneider, D.P., Gunn, J.E., 1995, AJ, 110, 68.

[155] Scott, S.E., Fox, M.J., Dunlop, J.S., Serjeant, S., Peacock, J.A., Ivison, R.J., Oliver, S., Mann, R.G., Lawrence, A., Efstathiou, A., Rowan-Robinson, M., Hughes, D.H., Archibald, E.N., Blain, A., Longair, M., 2002, MNRAS, 331, 817.

[156] Scoville, N.Z., Young, J.S., 1983, ApJ, 265, 148.

[157] Seeds, M.A., 1990, 'Foundations of Astronomy - 1990 Edition', Wadsworth publishing Company.

[158] Serjeant, S., Oliver, S., Rowan-Robinson, M., Crockett, H., Missoulis, V., Sumner, T., Gruppioni, C., Mann, R.G., Eaton, N., Elbaz, D., Clements, D.L., Baker, A., Efstathiou, A., Cesarsky, C., Danese, L., Franceschini, A., Genzel, R., Lawrence, A., Lemke, D., McMahon, R.G., Miley, G., Puget, J.-L., Rocca-Volmerange, B., 2000, MNRAS, 316, 768.

[159] Serjeant, S., Dunlop, J.S., Mann, R.G., Rowan-Robinson, M., Hughes, D., Efstathiou, A., Blain, A., Fox, M., Ivison, R.J., Jenness, T., Lawrence, A., Longair, M., Oliver, S., Peacock, J.A., 2003, MNRAS, 344, 887.

[160] Smail, I., Ivison, R.J., Blain, A.W., 1997, ApJ, 490, L5.

[161] Smail, I., Ivison, R.J., Owen, F.N., Blain, A.W., Kneib, J.-P., 2000, ApJ, 528, 612.

[162] Smail, I., Ivison, R.J., Blain, A.W., Kneib, J.-P., 2002, MNRAS, 331, 495.

[163] Soifer, B.T., Boehmer, L., Neugebauer, G., Sanders, D.B., 1989, AJ, 98, 766.

[164] Spergel, D.N., Verde, L., Peiris, H.V., Komatsu, E., Nolta, M.R., Bennett, C.L., Halpern, M., Hinshaw, G., Jarosik, N., Kogut, A., Limon, M., Meyer, S.S., Page, L., Tucker, G.S., Weiland, J.L., Wollack, E., Wright, E.L., 2003, ApJS, 148, 175.

[165] Spinrad, H., Dey, A., Stern, D., Dunlop, J., Peacock, J., Jimenez, R., Windhorst, R., 1997, ApJ, 484, 581.

[166] Stanford, S.A., Eisenhardt, P.R.M., Dickinson, M., 1998, ApJ, 492, 461.

[167] Stanway, E.R., Bunker, A.J., McMahon, R.G., 2003, MNRAS, 342, 439.

[168] Steidel, C.C., Hamilton, D., 1993, AJ, 101, 2017.

[169] Steidel, C.C., Adelberger, K.L., Giavalisco, M., Dickinson, M., Pettini, M., 1999, ApJ, 519, 1.

[170] Szokoly, G.P., Subbarao, M.U., Connolly, A.J., Mobasher, B., 1998, ApJ, 492, 452.

[171] Tegmark, M., Strauss, M.A., Blanton, M.R., Abazajian, K., Dodelson, S., Sandvik, H., Wang, X., Weinberg, D.H., Zehavi, I., Bahcall, N.A., Hoyle, F., Schlegel, D., Scoccimarro, R., Vogeley, M.S., Berlind, A., Budavari, T., Connolly, A., Eisenstein, D.J., Finkbeiner, D., Frieman, J.A., Gunn, J.E., Hui, L., Jain, B., Johnston, D., Kent, S., Lin, H., Nakajima, R., Nichol, R.C., Ostriker, J.P., Pope, A., Scranton, R., Seljak, U., Sheth, R.K., Stebbins, A., Szalay, A.S., Szapudi, I., Xu, Y., Annis, J., Brinkmann, J., Burles, S., Castander, F.J., Csabai, I., Loveday, J., Doi, M., Fukugita, M., Gillespie, B., Hennessy, G., Hogg, D.W., Ivezić, Ž., Knapp, G.R., Lamb, D.Q., Lee, B.C., Lupton, R.H., McKay, T.A., Kunszt, P., Munn, J.A., O'Connell, L., Peoples, J., Pier, J.R., Richmond, M., Rockosi, C., Schneider, D.P., Stoughton, C., Tucker, D.L., Vanden Berk, D.E., Yanny, B., York, D.G., 2003, Phys. Rev., submitted, (astro-ph/0310723).

[172] Thomas, D., Maraston, C., Bender, R., 2002, in Reviews in Modern Astronomy, Vol. 15, Astronomische Gesellschaft, ed., R.E. Schielicke (astro-ph/0202166).

[173] Thompson, R.I., Weymann, R.J., Storrie-Lombardi, L.J., 2001, ApJ, 546, 694.

[174] Thronson, H., Telesco, C., 1986, ApJ, 309, L79.

[175] Toomre, A., 1997, in the Evolution of Galaxies and Stellar Populations, eds., B.M. Tinsley, R.B. Larson, Yale Univ. Press, p.401.

[176] Treyer, M.A., Ellis, R.S., Milliard, B., Donas, J., Bridges, T.J., 1998, MNRAS, 300, 303.

[177] van Dokkum, P.G., Franx, M., 1996, MNRAS, 281, 985.

[178] van der Werf, P.P., Kraiberg Knudsen, K., Labbé, I., Franx, M., 2001,in: Deep Sub-millimetre Surveys, eds. Lowenthal, J. & Hughes, D.H., World Scientific, (astro-ph/0010459).

[179] Vandenberg, D.A., 1998, 'Globular Cluster Ages: Are They Converging?', in Fundamental Stellar Properties: the Interaction between Observation and Theory, eds., Bedding, T.R., Booth, A.J., Davis, J., IAU Symposium, Kluwer, Dordrecht, p.439.

[180] Verde, L., Peiris, H.V., Spergel, D.N., Nolta, M.R., Bennett, C.L., Halpern, M., Hinshaw, G., Jarosik, N., Kogut, A., Limon, M., Meyer, S.S., Page, L., Tucker, G.S., Wollack, E., Wright, E.L., 2003, ApJS, 148, 195.

[181] Wang, B., 1991, ApJ, 374, 456.

[182] Warren, S.J., Hewett, P.C., Osmer, P.S., 1995, ApJ, 438, 506.

[183] Webb, T.M., Eales, S.A., Lilly, S.J., Clements, D.L., Dunne, L., Gear, W.K., Ivison, R.J., Flores, H., Yun, M., 2003a, ApJ, 587, 41.

[184] Webb, T.M., Eales, S., Foucaud, S., Lilly, S.J., McCracken, H., Adelberger, K., Steidel, C., Shapley, A., Clements, D.L., Dunne, L., Le Fèvre, O., Brodwin, M., Gear, W., 2003b, ApJ, 582, 6.

[185] White, S.D.M., Rees, M.J., 1978, ApJ, 183, 341.

[186] Willmer, C.N.A., da Costa, L.N., Pellegrini, P.S., 1998, AJ, 115, 869.

[187] Willott, C.J., Rawlings, S., Blundell, K.M., 2001, MNRAS, 324, 1.

[188] Yoo, J., Chanamé J., Gould, A., 2003, ApJ, in press, (astro-ph/0307437).

[189] York, D.G., Adelman, J., Anderson, J.E. Jr., Anderson, S.F., Annis, J., Bahcall, N.A., Bakken, J.A., Barkhouser, R., Bastian, S., Berman, E., Boroski, W.N., Bracker, S., Briegel, C., Briggs, J.W., Brinkmann, J., Brunner, R., Burles, S., Carey, L., Carr, M.A., Castander, F.J., Chen, B., Colestock, P.L., Connolly, A.J., Crocker, J.H., Csabai, I., Czarapata, P.C., Davis, J.E., Doi, M., Dombeck, T., Eisenstein, D., Ellman, N., Elms, B.R., Evans, M.L., Fan, X., Federwitz, G.R., Fiscelli, L., Friedman, S., Frieman, J.A., Fukugita, M., Gillespie, B., Gunn, J.E., Gurbani, V.K., de Haas, E., Haldeman, M., Harris, F.H., Hayes, J., Heckman, T.M., Hennessy, G.S., Hindsley, R.B., Holm, S., Holmgren, D.J., Huang, C., Hull, C., Husby, D., Ichikawa, S.-I., Ichikawa, T., Ivezic, Z., Kent, S., Kim, R.S.J., Kinney, E., Klaene, M., Kleinman, A.N., Kleinman, S., Knapp, G.R., Korienek, J., Kron, R.G., Kunszt, P.Z., Lamb, D.Q., Lee, B., Leger, R.F., Limmongkol, S., Lindenmeyer, C., Long, D.C., Loomis, C., Loveday, J., Lucinio, R., Lupton, R.H., MacKinnon, B., Mannery, E.J., Mantsch, P.M., Margon, B., McGehee, P., McKay, T.A., Meiksin, A., Merelli, A., Monet, D.G., Munn, J.A., Narayanan, V.K., Nash, T., Neilsen, E., Neswold, R., Newberg, H.J., Nichol, R.C., Nicinski, T., Nonino, M., Okada, N., Okamura, S.,

Ostriker, J.P., Owen, R., Pauls, A.G., Peoples, J., Peterson, R.L., Petravick, D., Pier, J.R., Pope, A., Pordes, R., Prosapio, A., Rechenmacher, R., Quinn, T.R., Richards, G.T., Richmond, M.W., Rivetta, C.H., Rockosi, C.M., Ruthmansdorfer, K., Sandford, D., Schlegel, D.J., Schneider, D.P., Sekiguchi, M. Sergey, G., Shimasaku, K., Siegmund, W.A., Smee, S., Smith, J.A., Snedden, S., Stone, R., Stoughton, C., Strauss, M.A., Stubbs, C., SubbaRao, M., Szalay, A.S., Szapudi, I., Szokoly, G.P., Thakar, A.R., Tremonti, C., Tucker, D.L., Uomoto, A., Vanden Berk, D., Vogeley, M.S., Waddell, P., Wang, S.-I., Watanabe, M., Weinberg, D.H., Yanny, B., Yasuda, N., 2000, AJ, 120, 1579.

[190] Zeldovich, Y.B., 1967, J.E.T.P.Lett., 6, 316.

[191] Ziegler, B.L., Saglia, R.P., Bender, R., Belloni, P., Greggio, L., Seitz, S., 1999, A&A, 346, 13.